



BERGISCHE
UNIVERSITÄT
WUPPERTAL

Modelling the Material Behaviour of Concrete with Polypropylene Fibres under Tunnel Fire and its Influence on the Structural Analysis

**Dissertation zur Erlangung eines Doktorgrades
(Dr.-Ing.)**

in der
Fakultät für Architektur und Bauingenieurwesen
der
Bergischen Universität Wuppertal

vorgelegt von
Omid Pouran
aus Teheran

Wuppertal 2019

Die Dissertation kann wie folgt zitiert werden:

urn:nbn:de:hbz:468-20190612-103823-6

[<http://nbn-resolving.de/urn/resolver.pl?urn=urn%3Anbn%3Ade%3A468-20190612-103823-6>]

DOI: 10.25926/1x4b-6253

[<https://doi.org/10.25926/1x4b-6253>]

Contents

Symbols and Notations.....	I
Abbreviations	VII
Glossary of Strain and Stress Components	VIII
Summary	XI
Zusammenfassung.....	XII
Introduction.....	XIV
1 Fire Design.....	1
1.1 Compartment and Tunnel Fires.....	3
1.2 Nominal Fire Curves for Compartments and Road Tunnels	3
1.3 Thermal Analysis of an Element of Tunnel Structure vs. Residential Structure.....	4
1.4 Fire Design according to EUROCODE 2's Concept	5
1.5 Advanced Calculation Method.....	7
2 Fire Action and Development of Temperature Fields	9
2.1 Temperature Difference over a Cross-section in Fire Situation and Determination of Absolute Temperature Values	9
2.2 Determination of Functions for Heat Transfer Coefficient	15
2.3 Determination of Functions for Cross-section Coefficient	18
2.4 Evaluation of Temperature Values in Tunnel Members	18
2.5 Summary	18
3 Concrete Material Model at Elevated Temperatures	21
3.1 Explicit and Implicit Models.....	21
3.2 Strains and Modulus of Elasticity from Steady-state Tests.....	23
3.2.1 Instantaneous-stress-related Strain.....	23
3.2.2 Steady-state Creep	26
3.3 Strains from Transient Tests	27
3.3.1 Transient-creep Strain for Drying Specimen	27
3.3.2 Mechanical-induced Strain at Elevated Temperatures.....	28
3.4 Strain Components and Influential Parameters	29
3.4.1 Thermal Strain	29
3.4.2 Mechanical-induced Strain at Elevated Temperatures.....	32
3.4.3 Elastic Strain	32

4	Compressive Strength and Residual Strength of Concrete	34
4.1	Compressive Strength	34
4.2	Parameters Affecting the Compressive Strength.....	35
4.2.1	Effects of Load Level during Heating-up Stage on High and Normal-strength Concrete.....	35
4.2.2	Heating Rate and Other Parameters	39
4.3	Spalling of High-strength Concrete (HSC)	40
4.3.1	Mechanisms of Explosive Spalling.....	40
4.3.2	Influence of Heating Rate on Spalling during Tests	41
4.4	Residual Compressive Strength	42
4.4.1	Residual Compressive Strength after Cooled Down to Ambient Temperature	43
4.4.2	Residual Compressive Strength after Cooled Down to a Specified Temperature	45
5	Influence of Polypropylene Fibres on Material Properties of Concrete Exposed to Elevated Temperatures	46
5.1	Thermal Strain.....	46
5.2	Mechanical-induced Strain at Elevated Temperatures	47
5.3	Modulus of Elasticity	47
5.4	Relative Porosity	50
5.5	Mass Loss.....	50
5.6	Compressive Strength	51
5.7	Residual Compressive Strength	52
5.8	Strain at Peak Stress	53
5.9	Stress-strain Curves.....	53
6	Tests and Mixture Characteristics.....	55
6.1	Design Mix.....	55
6.2	Properties of Specimens.....	55
6.3	Batches	56
6.4	Curing.....	56
6.4.1	Mass and Moisture Content of Oven-dried Specimens.....	58
6.4.2	Accelerated Curing and Moisture Content of Cylinder Specimens	58
6.4.3	Curing and Moisture Content of Prisms	58

7	Compression Tests at Ambient Temperatures and Thermal Considerations.....	61
7.1	Compressive Strength and Stress-strain Tests.....	61
7.1.1	Compressive Strength Results	61
7.1.2	Stress-strain Results	62
7.2	Modulus of Elasticity Tests.....	63
8	Calibration of Test Results at Elevated Temperatures.....	65
8.1	General.....	65
8.2	Scaling Factor for Free Thermal Elongation Based on Proposed Method.....	66
8.3	Different Assumptions to Evaluate Scaling Factors.....	68
8.4	Compressive Steady-state Tests at Elevated Temperatures	70
8.4.1	Equivalent Modulus of Elasticity for Calibration Tests at Ambient Temperature.....	72
8.4.2	Equivalent Modulus of Elasticity of Steady-state Tests at Elevated Temperatures Based on 1 st Proposed Method	73
8.4.3	Calibration of Steady-state Tests Based on 2 nd Proposed Method.....	75
8.5	Calibration of Transient Tests with a Specified Constant Applied Load Level Based on 1 st Proposed Method	79
9	Tests at Elevated Temperatures	82
9.1	Test Program	82
9.2	Temperature Measurements	84
9.3	Heating Rate and Thermal Incompatibilities.....	86
9.4	Relative Compressive Strength	86
9.5	Relative Compressive Strength of Pre-loaded Tests	89
9.6	Stress-strain Curves from Tests.....	89
9.7	Explicit Modulus of Elasticity from Cyclic Tests.....	89
9.8	Residual Compressive Strength after the Specimen Is Cooled Down to Ambient Temperature	94
9.9	Residual Compressive Strength after Specimen Is Cooled Down to a Specified Temperature.....	95
9.10	Thermal Strains	96
9.11	Total Transient Strains with Different Load Levels.....	97
9.12	Strains and Relative Strains at Peak Stress Values for Specimens with Different Load Levels.....	99
9.13	Strains at Peak Stress Values for Specimens Cooled Down to Specified Temperatures	99
9.14	Proposing a Constitutive Implicit Model for Concrete with Polypropylene Fibres.....	102
9.14.1	Strain at Maximum Stress for an Implicit Model.....	102
9.14.2	Stress-strain.....	102

9.14.3 Modulus of Elasticity	105
9.14.4 Modified EN 1992-1-2 Stress-strain Model for Concrete with Polypropylene Fibres	106
10 Structural Analysis of a Cut-and-cover Tunnel under ZTV-ING Fire Using Finite Element Method	109
10.1 General	109
10.2 Structural Mechanics	110
10.3 Beam Theory according to Euler-Bernoulli and Timoshenko	111
10.4 An Insight into Finite Element Method	112
10.4.1 Finite Element Analysis Using Nonlinear Material Properties	116
10.4.2 Analysis Using Nonlinear Material Properties for Fibre or Layered Elements	117
10.5 Design of a Reinforced Concrete Beam	117
10.5.1 At Ambient Temperatures according to EN 1992-1-1	117
10.5.2 Fire Design: Simplified Calculation Method or Level 2 to EN 1992-1-2	118
10.5.3 Fire Design: Advanced Calculation Method or Level 3 to EN 1992-1-2	119
10.6 Analysis of Structure Using Beam Elements in SOFiSTiK	123
10.6.1 Material Nonlinear Fibre Beam Analysis for Fire Situation	123
10.6.2 Benchmark Examples for Fibre Beams Exposed to Elevated Temperatures in SOFiSTiK	124
10.7 Further Proposed Examples of Fibre Beams Exposed to Elevated Temperatures in SOFiSTiK	126
10.8 Case Studies for Straight Fibre Beams at Elevated Temperatures Using SOFiSTiK	130
10.8.1 Single-span Beam under Transverse Loading and Exposed to Fire (Cases 1-4)	130
10.8.2 Two-span Beam under Transverse Loading and One Span Exposed to Fire (Case 5)	130
10.8.3 Two-span Beam under Transverse Loading and One Span Exposed to Fire with 20% Strength Reduction (Case 6)	130
10.9 Analysis of a Two-cell-cut-and-cover Tunnel Exposed to Fire	133
10.10 Tunnel Structure at the Beginning of Fire	135
10.11 Physical Nonlinear Structural Analysis of Tunnel for Fire Situation Using SOFiSTiK	137
11 Conclusions and Outlook	142
Bibliography	145
Normative References	150
Annex A: One-dimensional Heat Transfer in a Wall	151
Annex B: Spalling of Cylinder Specimens under Uniaxial Compressive Load	153
Annex C: Mass Loss of Batches	158

Annex D: Stress-strain Curves at Ambient Temperature	160
Annex E: Characteristics of Cylinder Tests	163
Annex F: Results of Temperature Measurements for the Prisms	165
Annex G: Thermal Incompatibilities in Specimens with Polypropylene Fibres under Heating	168
G.1 Introduction	168
G.2 Thermal Analysis and Transient Heat Transfer	168
G.3 Boundary Conditions	168
G.4 Thermal Analysis of Cylinder Specimen	170
G.5 Stress Analysis of Cylinder	171
G.6 Restraint Forces Using Volume Model	172
G.7 Variation in Stress Distribution using Fibre-enhanced-quadrilateral-plate Elements	174
Annex H: Cross-section and System Variable States for the Reinforced Concrete Beams under Fire (Study Cases)	176
Annex I: Actions on the Tunnel	180
Annex J: Bending Moments and Axial Forces of the Tunnel from Nonlinear Thermo-mechanical Analysis of the Plate Model	182
Lebenslauf	184
Curriculum Vitae	185
List of Author's Publications	186

Symbols and Notations

Calibration of Test Results

A_{Inv}	cross-section area of Invar specimen
E_{Inv}	modulus of elasticity of Invar specimen or Invar
E_{eq}	equivalent modulus of elasticity evaluated based on displacement recordings
F	force applied on the specimen
$l_{aff,equi}$	affected length of equipment which is the sum of $l_{s,in}$ and $l_{s,out}$
$l_{Inv,spec}$	length of Invar specimen used for calibration tests
$l_{s,in}$	affected length of stamp on the top and bottom of the Invar specimen within the furnace
$l_{s,out}$	affected length of stamp on the top and bottom of furnace (outside of furnace)
$l_{0,eq}$	equivalent length of equipment
$S(\theta)$	scaling factor as a function of elevated temperature in the furnace
$\alpha_{eq}(\theta)$	equivalent free thermal expansion coefficient for all the contributing components of equipment in thermal elongation or in transient calibration tests
Δl	axial displacement
Δl_c	axial displacement of concrete cylinder specimen
Δl_{equi}	axial displacement of equipment
$\Delta l_{Inv,spec}$	axial displacement of Invar specimen
Δl_{WAT}	axial displacement recorded via WAT
Δl_W	axial displacement recorded via measurement device
$\theta_{s,out,ave}$	average temperature of affected part of stamp (outside the furnace)

Design of Reinforced Concrete Beam

A	cross-section area
A_c	cross-section area of concrete
A_s	cross-section area of reinforcement
A_l	area of layer l of concrete
$A_{s,prov}$	area of tensile steel provided
$A_{s,req}$	area of tensile steel required for design
f_{cc,θ_l}	strength of the affected fibre at temperature θ_l in the cross-section
F_{cc,θ_l}	restraint force of the affected fibre at temperature θ_l in the cross-section
$k_{c,\theta}$	strength reduction coefficient for concrete at elevated temperature
M_{Ed}	design value of the applied internal bending moment
$M_{Ed,fi}$	design value of the applied internal bending moment for fire design
M_{Rd}	design value of the moment of resistance

$M_{Rd,fi}$	design value of the moment of resistance for fire design
γ_s	partial safety factor of reinforcement at ambient temperature
$\gamma_{s,fi}$	partial safety factor of reinforcement for fire situation
ε_{cc}	compressive strain in the concrete cross-section
$\varepsilon_{c,fi}$	ultimate compressive strain in the concrete cross-section for fire design
ε_{ct}	tensile strain in the concrete cross-section
ε_{c1}	compressive strain of concrete at the peak stress according to EN 1992-1-1 for nonlinear structural analysis
ε_{c2}	strain at reaching the maximum strength according to EN 1992-1-1 for design of cross-section (Parabola-rectangle diagram)
ε_{c3}	strain at reaching the maximum strength according to EN 1992-1-1 for design of cross-section (Bi-linear stress-strain relation)
ε_{cu1}	ultimate compressive strain of concrete according to EN 1992-1-1 for nonlinear structural analysis
ε_{cu2}	ultimate compressive strain of concrete according to EN 1992-1-1 for design of cross-section (Parabola-rectangle diagram)
ε_{cu3}	ultimate compressive strain of concrete according to EN 1992-1-1 for design of cross-section (Bi-linear stress-strain relation)
ε_{sc}	compressive strain of reinforcement
ε_{st}	tensile strain of reinforcement
$\varepsilon_{st,fi}$	tensile strain of reinforcement for fire design
ε_{sty}	yield strain of tensile reinforcement
ε_{sy}	yield strain of reinforcement
$\varepsilon_{sy,fi}$	yield strain of reinforcement for fire design

Evaluation of Temperature in the Tunnel Cross-section

d	thickness of cross-section
x	orthogonal distance to the exposed boundary surface
w	width of cross-section orthogonal to heat transfer direction
α_1	coefficient of heat transfer
α_2	coefficient of cross-section
$\Delta\theta_E(t)$	nonlinear temperature difference component at time t
$\Delta\theta_M(t)$	linear temperature difference component at time t
$\Delta\theta_N(t)$	uniform temperature difference component at time t
θ	absolute temperature
θ_{exp}	exposure temperature
θ_i	initial temperature of the cross-section

θ_x temperature at distance x to the exposed side

Finite Element Method

\mathbf{B}	strain-displacement matrix
EA	extensional stiffness
\mathbf{E}_T	tangential material matrix
\mathbf{f}^{int}	matrix of internal forces
\mathbf{f}^{ext}	matrix of external forces
F	spring force
g	gravity
G	shear stiffness; also used for gravity force
\mathbf{K}_{glob}	global or system stiffness matrix
\mathbf{K}_{loc}	local element stiffness matrix
m	mass
\mathbf{O}_r	geometric boundary condition
\mathbf{O}_t	dynamic boundary condition
\mathbf{p}	vector of body forces
\mathbf{u}	vector of displacements
v	domain of system
V_{glob}	matrix of global nodal degrees of freedom
V_{loc}	matrix of local nodal degrees of freedom
W_{ext}	external work
W_{int}	internal work
W_F	internal work done by spring force F
W_G	external work done by gravity force G
W_{tot}	total potential energy
$y(x)$	displacement function
$\boldsymbol{\varepsilon}$	vector of strains
$\boldsymbol{\sigma}$	vector of stress resultants

Materials and Experiments

Superscripts

Superscripts, separated by a comma are used when relevant.

First/second

θ	reference temperature (variable or constant in the parts related to compressive strength)
θ_m	maximum temperature
θ_{max}	uniformly-distributed-maximum-desired temperature at steady-state tests

Symbols and Notations

θ_1	the first desired temperature point in heating
θ_2	the second desired temperature point in heating
σ'	load history level (stress during heating for steady-state tests)

Second/third/fourth

θ_a	ambient temperature
θ_3	the specified aimed temperature after the specimen is cooled down from θ_{max}
σ	specifies that a load has been applied during the hold time period or cooling whichever is relevant

Third/fourth/fifth

0	zero stress ($\sigma = 0$)
$\dot{\epsilon}$	strain-rate controlled test
$\dot{\sigma}$	stress-rate controlled test
d	drying (unsealed concrete)
nd	non-drying (sealed concrete)

Subscripts

co	constant temperature regime
cr	creep
cu	maximum strain
cl	strain at peak stress
el	elastic
res	residual
sh	shrinkage
th	thermal
tot	total
tr	transient temperature regime

Symbols

a	mass of aggregate
c	mass of cement
d	diameter of concrete cylinder specimen
E	modulus of elasticity at ambient temperature
$E_{c,s}$	stabilized modulus of elasticity from cyclic tests for cylinders at ambient temperature
E_{eq}	equivalent modulus of elasticity for the equipment performing calibration tests
$E^{\theta_{max}}$	modulus of elasticity for ascending branch of stress-strain relation at the elevated temperature
$E_{ci}^{\theta_{max}}$	initial modulus of elasticity for ascending branch of stress-strain relation at the elevated temperature

Symbols and Notations

$E_{res}^{\theta_{max}, \theta_a}$	residual modulus of elasticity for ascending branch of stress-strain relation for the specimen cooled down to the ambient
$E_{c,res}^{\theta_{max}, \theta_3}$	residual modulus of elasticity for ascending branch of stress-strain relation for the specimen cooled down to θ_3
$f_c^{\theta_{max}}$	compressive strength at the uniformly-distributed-maximum-desired temperature θ_{max}
$f_{c,res}^{\theta_{max}}$	residual compressive strength after cooling down from θ_{max} to ambient temperature
$f_c^{\sigma', \theta_{max}}$	compressive strength at temperature θ_{max} for a pre-loaded specimen
R	heating rate (K/min)
$t_{\theta_{max}}$	time, when θ reaches θ_{max}
t_0	time at the beginning of steady-state regime
t_l	time of not-loading (steady-state creep test)
w	mass of water
α	initial-stress ratio or pre-load level for the steady-state tests and stress or load level for the transient tests
$\dot{\epsilon}$	strain-rate for compressive tests at elevated temperatures
$\epsilon_{cl}^{\theta_{max}}$	strain at the peak stress at elevated temperatures
$\epsilon_{cu}^{\theta_{max}}$	strain at the end of the descending branch of stress-strain relation
θ_g	gas temperature
$\dot{\sigma}$	stress-rate for compressive concrete tests at elevated temperatures

Structural Analysis

M	bending moment
u	displacement
V	shear force
γ	shear strain
φ	angle of rotation

Thermal Analysis

A	normal area of wall to the direction of heat transfer
c	specific heat transfer
$\dot{E}_{gen, element}$	rate of heat generation inside the element
k	thermal conductivity
r	radius of cylinder
L	axial length of cylinder
\dot{Q}_x	rate of heat conduction in x direction
R	heating rate

Symbols and Notations

x	wall thickness
α	thermal diffusivity
α_c	convective coefficient of heat transfer
ΔT	temperature difference
ΔT_F	nonlinear temperature difference
ΔT_M	linear temperature difference
ΔT_N	constant or uniform temperature difference
ρ	density

Abbreviations

BC	boundary condition
BE	benchmark examples
CFD	computational fluid dynamics
ELE	Euler-Lagrange equation
FE	finite element
FEM	finite element method
GRG	nonlinear generalised reduced gradient solution
HSC	high-strength concrete
ISS	initial-state stress
LC	lightweight concrete
MISSET	mechanical-induced strains at elevated temperatures
NIST	National Institute of Standards and Technology
NSC	normal-strength concrete
PP	Polypropylene
PVD	principle of virtual displacement
R.H.	relative humidity
RS	remaining cylindrical pieces of specimens
SLS	serviceability limit states
SNr	specimen number
TS	thermally induced stresses
ULS	ultimate limit states

Glossary of Strain and Stress Components

The terminology used by different authors and researchers to define strain and stress components at elevated temperatures are in many cases inconsistent. Since the topic itself is complex, using different terminology might make it even more difficult to understand. Most of the used terms in this work are designated with upper and lower indices that clarify each component by explaining its state and cause.

For example in **instantaneous-stress-related strain for drying specimens**, $\varepsilon_{tot}^{\theta_{max}, \sigma', \sigma, \dot{\sigma}, d}$, the upper and lower indices represent:

- θ_{max} : uniformly-distributed-maximum-desired temperature at steady-state tests;
- σ' : pre-stress level which is applied at the beginning of the heating and held constant during the heating-up procedure;
- σ : is the stress level after the specimen is reached the maximum stabilized temperature;
- $\dot{\sigma}$: refers to stress-rate controlled tests;
- d : represents the drying specimen (not sealed);
- tot : is indicative of total strain (it can be divided into elastic and plastic strain components).

The definitions of most of main technical words for the strain and stress components are explicitly given in this section.

Compressive strength at elevated temperatures, $f_c^{\theta_{max}}$: compressive strength of concrete after the specimens are heated and reached the uniformly-distributed-maximum-desired temperature.

Compressive strength at elevated temperatures for specimen with pre-load, $f_c^{\sigma', \theta_{max}}$: compressive strength of concrete being loaded at the start of heating. This load remains constant during the heating. The compressive strength then is measured after specimen has a uniformly-distributed-maximum-desired temperature by applying load to the point of failure.

Drying shrinkage at elevated temperatures, $\varepsilon_{tr,sh}^{\theta, \theta, d}$: one of the two components (drying shrinkage and thermal strain) constituting total thermal strain of drying concrete from unrestrained transient tests and can be related to the contraction of cement paste at the temperature range of 150 to 400°C.

Elastic strain at elevated temperatures, $\varepsilon_{el}^{\theta_{max}, \sigma', \sigma, \dot{\sigma}, d}$: is the component which can be measured from the cyclic-steady-state tests. This component gives an estimation of elastic parts of stress-strain curves from steady-state tests.

Initial modulus of elasticity at elevated temperatures, $E_{ci}^{\theta_{max}}$: considering the ascending branch of stress-strain relation from the steady-state tests, the slope of the stress-strain diagram at the origin of the curve corresponding to uniformly-distributed-maximum-desired temperature (θ_{max}).

Instantaneous-stress-related strain for drying specimens, $\varepsilon_{tot}^{\theta_{max}, \sigma', \sigma, \dot{\sigma}, d}$: is a function of stress history, stress, stress rate $\dot{\sigma}$, and uniformly-distributed-maximum-desired temperature. This is the strain calculated from the measured longitudinal deformations during the steady-state tests and comprises two components; elastic and plastic strains. For the practical purposes, it is referred to as “elastic strain” according to part 8 of (RILEM, 2007).

Mechanical-induced strain at elevated temperatures, ε_m : is the sum of all mechanical-induced strain components from both transient and steady-state tests. The term “load induced thermal strain” (LITS) is also used in some literatures.

Plastic strain at elevated temperatures from stress-strain (steady-state test) relation, $\varepsilon_{pl}^{\theta_{max}, \sigma', \sigma, \dot{\sigma}, d}$: is the irreversible or plastic strain part of the stress-strain curves. Having evaluated the elastic strain from the cyclic-steady-state tests, the plastic part of stress-strain curves are distinguishable.

Relative strain at peak stress, $(\frac{\varepsilon_{cl}^{\theta_{max}}}{\varepsilon_{cl}})$: the ration of the strain at peak stress from stress-strain curves at the uniformly-distributed-maximum-desired temperature to the strain at peak stress of concrete at the ambient temperature.

Relative strength, $(\frac{f_c^{\theta_{max}}}{f_c})$: the ration of strength of concrete at the elevated temperatures measured at a uniformly-distributed-maximum-desired temperature, θ_{max} , to the strength of concrete at the ambient temperature.

Residual modulus of elasticity of ascending branch of stress-strain relation after the specimen is cooled down to ambient temperature, $E_{res}^{\theta_{max}, \theta_a}$: can be evaluated from either the elastic part of stress-strain curve for the specimen heated (not-loaded) up to θ_{max} and cooled down to θ_a and then loaded to the failure point, or from elastic modulus test for the specimen thermally treated in the same way as for stress-strain curve.

Residual modulus of elasticity of ascending branch of stress-strain relation after the specimen is cooled down to a specified temperature, $E_{res}^{\theta_{max}, \theta_3}$: can be evaluated from either the elastic part of stress-strain curve for the specimen heated (not-loaded) up to θ_{max} and cooled down to θ_3 and then loaded to the failure point, or from elastic modulus test for the specimen thermally treated in the same way as for stress-strain curve.

Residual strength after the specimen is cooled down to ambient temperature, $f_{c, res}^{\theta_{max}, \theta_a}$: specimen is heated (not-loaded) up to the θ_{max} and then cooled down to the ambient temperature. The strength of concrete is measured at the ambient temperature.

Residual strength after the specimen is cooled down to a specified temperature, $f_{c, res}^{\theta_{max}, \theta_3}$: specimen is heated (not-loaded) up to θ_{max} and then cooled down to a specified temperature, θ_3 . The strength of concrete is measured at θ_3 .

Steady-state creep for non-drying specimens, $\varepsilon_{cr(t_1-t_0)}^{\theta_{max}, \sigma, nd}$: corresponds to creep in the steady-state tests after the both temperature and stress have reached a constant level. The steady-state creep strain is dependent on the pre-load level, θ_{max} and duration. It is usually measured for several-hour heating periods. This component is called “creep strain” in some literatures.

Strain at peak stress at elevated temperatures, $\varepsilon_{cl}^{\theta_{max}}$: is the strain occurs at the maximum stress at the uniformly-distributed-maximum-desired temperature.

Thermal strain for drying specimens, $\varepsilon_{tr,th}^{\theta,0,d}$: is a function of thermal expansion coefficient and temperature. The term thermal strain in this work solely refers to the “total thermal strain for drying specimens”. Thermal strain is also called “free thermal strain” in different literatures.

Total strain at the elevated temperatures, ε_{tot} : is the sum of all strain components at elevated temperatures.

Total thermal strain of drying concrete, $\varepsilon_{tr,tot}^{\theta,0,d}$: total strain calculated by measuring the unrestrained thermal elongation of concrete specimens which composes of sum of two components; drying shrinkage and thermal strain. Since in practice both components are not easily separable, the total thermal strain of concrete is simply called “thermal strain”.

Total transient strain, $\varepsilon_{tr,tot}^{\theta,\sigma,d}$ or $\varepsilon_{tr,tot}^{\theta,\alpha,d}$: this is the strain component calculated based on the measured deformations in transient tests with different applied stresses σ or load levels α .

Transient creep, $\varepsilon_{tr,cr}^{\theta,\sigma,d}$: the irreversible time-and-stress-dependent transient strain (occurs during the first heating) when the stress level (σ) remains constant during the heating up procedure. This is the strain resulted from the subtraction of thermal strain and elastic strain (from steady-state tests) from the total transient strain. This component is also called “transient strain” and “transient thermal creep” in different literatures.

Summary

Behaviour of cut-and-cover tunnels exposed to fire can be analysed based on advanced calculation method according to EN1992-1-2 by using a realistic structural model that takes account of mechanical and thermally-induced-indirect effects acting on the structure simultaneously. In addition, EN 1992-1-2 proposes an implicit constitutive stress-strain model for concrete at elevated temperatures. This model is recommended to be used for the concrete structures under standard fire for the heating rates between 2 and 50 K/min. It is based on the mechanical and thermal strains evaluated from small-scale concrete specimens under low heating rates using steady-state and transient tests. The EN 1992-1-2's material model is implemented in different structural finite element software packages and used to perform nonlinear (physical) structural analysis for various structures exposed to fire.

Considering the cut-and-cover tunnels, in Germany, ZTV-ING fire exposure curve is adopted which has a much higher temperature-increase rate compared to standard fire curve in fire growth stage and reaches the maximum value of 1200°C in only five minutes. In addition, to decrease the risk of spalling, Polypropylene-fibres (PP-fibres) are often added to the concrete mixtures for cut-and-cover tunnels. These may result in different global structural responses in the event of tunnel fire.

In this work, different aspects of fire design (advanced calculation method) of cut-and-cover tunnels exposed to fire are investigated.

A formula is proposed to evaluate temperatures in different layers of lining of a cut-and-cover tunnel's cross-section for the affected region as a function of fire exposure curve, width normal to the heat transfer direction and thickness of cross-section. This can be implemented to evaluate temperature without performing thermal analysis and to calculate temperatures in the position of reinforcement for the practical use.

Stress analyses for a cylinder specimen under different heating rates carried out in FE software package SOFiSTiK using a volume model and a plate-layered model. This is performed to investigate the so-called structural effects that might arise in a cylinder specimen under low compressive load and high heating rate in transient tests.

To investigate, the influence of addition of PP-fibres in the concrete mixture on the thermo-mechanical behaviour of concrete, 214 cylinder specimens were tested using steady-state and transient tests. Two mixes used having 0 and 2 kg/m³ PP-fibres while the other constituents being identical. The hardened concrete should meet the requirements of 1 to 2-year-old concrete in the practice. Comparisons are made in terms of thermo-mechanical behaviour of these two at elevated temperatures for the purified strain results based on three proposed calibration methods.

Based on the test results of cylinders, an implicit constitutive material model is proposed for concrete having PP-fibres in its mixture, which is a modified form of EN 1992-1-2's material model.

Further, nonlinear (physical) thermo-mechanical analyses of cut-and-cover tunnel structure exposed to ZTV-ING fire exposure performed in SOFiSTiK. Comments are made on the extent to which the bending structural response of the lining of cut-and-cover tunnel can be influenced by changes in the constitutive material model at elevated temperatures.

Zusammenfassung

Das Verhalten von Tunneln offener Bauweise, die einem Brand ausgesetzt sind, kann auf Grundlage der allgemeinen Rechenverfahren nach der EN1992-1-2 unter Verwendung eines realistischen Tragwerksmodells analysiert werden. Dieses Modell berücksichtigt mechanische und thermisch-induzierte, indirekte Effekte, die gleichzeitig auf die Tragstruktur wirken. Darüber hinaus verweist die EN 1992-1-2 auf ein implizites konstitutives Spannungs-Dehnungsmodell für Beton bei erhöhten Temperaturen. Dieses Modell wird für die Betonkonstruktionen unter der Einheits-Temperaturzeitkurve für die Heizraten zwischen 2 und 50 K/min empfohlen. Es basiert auf den mechanischen und thermischen Dehnungen, die aus kleinen Betonproben bei niedrigen Erwärmungsraten mit stationären und instationären Versuchen ermittelt wurden. Das Materialmodell der EN 1992-1-2 ist in verschiedenen strukturellen Finite-Elemente-Softwarepaketen implementiert und dient zur Durchführung nichtlinearer (physikalischer) Strukturanalysen für verschiedene brandgefährdete Bauwerke.

Für Tunnel mit offener Bauweise wird in Deutschland die ZTV-ING-Brandbelastungskurve für den Brandfall angenommen. Diese Kurve nach der ZTV-ING weist eine wesentlich höhere Temperaturanstiegsrate auf als die Einheits-Temperaturzeitkurve und erreicht die Maximaltemperatur im Brandfall von 1200°C bereits binnen fünf Minuten. Um die Gefahr von Abplatzungen während des Brandes zu verringern, werden den Betonmischungen für Tunnel in offener Bauweise häufig Polypropylenfasern (PP-Fasern) zugesetzt. Diese können im Falle eines Tunnelbrandes zu unterschiedlichen globalen Reaktionen der Tragstruktur führen.

In dieser Arbeit werden verschiedene Aspekte der Heißbemessung (allgemeine Rechenverfahren) von Tunneln in offener Bauweise, die einem Brand ausgesetzt sind, untersucht.

Es wird im Zuge dieser Arbeit eine Formel entwickelt, um die Temperaturen in den verschiedenen Schichten innerhalb des brandbeanspruchten Querschnitts eines Tunnels in offener Bauweise zu bewerten. Die Temperaturen innerhalb des beeinflussten Bereichs lassen sich in Abhängigkeit von der Brandexpositionskurve, der Breite senkrecht zur Wärmeübertragungsrichtung und der Dicke des Querschnitts ermitteln. Dies kann angewandt werden, um die auftretenden Temperaturen in der Bewehrungslage für den praktischen Einsatz zu berechnen, ohne detaillierte thermische Analysen durchführen zu müssen.

Es werden Spannungsanalysen für eine Zylinderprobe unter verschiedenen Aufheizraten durchgeführt, die im FE-Softwarepaket SOFiSTiK unter Verwendung eines Volumenmodells und eines Plattenschichtmodells simuliert werden. Damit werden die sogenannten strukturellen Effekte untersucht, die bei einer Zylinderprobe unter geringer Druckbelastung und hoher Aufheizrate unter instationären Temperaturbedingungen auftreten können.

Um den Einfluss der zugegebenen PP-Fasern in der Betonmischung hinsichtlich des thermomechanischen Verhaltens des Betons zu untersuchen, wurden 214 Zylinderproben unter stationären und instationären Temperaturbedingungen untersucht.

Es werden zwei unterschiedliche Betonrezepturen erstellt. Eine Rezeptur enthält keine PP-Fasern, während der zweiten Rezeptur 2 kg/m³ PP-Fasern hinzugefügt werden. Alle weiteren Bestandteile der beiden Rezepturen sind identisch. Die Eigenschaften des Festbetons erfüllen dabei die Anforderungen an einen ein bis zwei Jahre alten Beton in der Baupraxis. Die Probekörper der beiden Rezepturen werden in Bezug auf ihr thermomechanisches Verhalten bei erhöhten Temperaturen miteinander verglichen. Die Bereinigung der Dehnungsergebnisse erfolgt auf der Grundlage von drei entwickelten Kalibriermethoden.

Basierend auf den Testergebnissen der untersuchten Zylinder wird ein implizites konstitutives Materialmodell für Beton mit PP-Fasern erarbeitet, welches eine modifizierte Form des Materialmodells der EN 1992-1-2 darstellt.

Darüber hinaus wurden in SOFiSTiK physikalische nichtlineare thermomechanische Analysen von Tunnelbauwerken, die einer Brandeinwirkung der ZTV-ING ausgesetzt sind, durchgeführt. Es wird untersucht, inwieweit die Beanspruchungen auf Tunnelbauwerke in offener Bauweise durch Veränderungen im konstitutiven Materialmodell bei erhöhten Temperaturen beeinflusst werden können.

Introduction

In the event of fire, the structural behaviour of cut-and-cover tunnels are affected by imposed thermal (and mechanical) effects to a high extent and this might, consequently, result in failure of the structure. This risk can be minimized by means of appropriate fire design. The latter should provide sufficient passive fire protection for the structure.

Fire design of tunnels in Europe has become more important and drawn more attention after fire incidents in Euro (1996), Tauern (1999) and Mont-Blanc (1999) tunnels. In this regard, Federal Highway Research Institute (BASt), in Germany, has financed and conducted number of research projects where the results mostly adopted in section 5 (tunnels) of the technical guideline ZTV-ING (BASt, 2015). In one of the most recent research projects, financed by BASt, on passive fire design of a 2-cell cut-and-cover tunnel, as reported in (Pouran, et al., 2014), the bending response of the structure exposed to fire were investigated for concrete having 2 kg/m³ Polypropylene-fibres (PP-fibres). The latter was performed in software package SOFiSTik using advanced method proposed by EN 1992-1-2:2004. Using advanced method (level 3), structure should be analysed by taking into account the indirect thermal effects and material strength loss of the thermally affected parts in the cross-section spontaneously. The material model used for concrete is the EN 1992-1-2's model for concrete exposed to elevated temperatures without considering the effects of any additive fibres and is designed for heating rates between 2 to 50 K/min.

Considering the cut-and-cover tunnels, in Germany, ZTV-ING fire exposure curve is adopted which has a much higher temperature-increase rate compared to standard fire curve in fire growth stage and reaches the maximum value of 1200°C in only five minutes. Corresponding, experimental fire test results for a section of tunnel were extracted from (Dehn, et al., 2013). In addition, to decrease the risk of spalling, Polypropylene-fibres (PP-fibres) are often added to the concrete mixtures for tunnels. The addition of 2 kg/m³ PP-fibres, verifiably, reduces the inner pore pressure in the concrete and decreases the risk and impact of concrete spalling (Pistol, et al., 2012). Further, (Khoury, 2000) has summarized the parameters that might affect different types of spalling. Spalling implies reduction in thickness of cross-section (decrease of concrete cover) which might expose the reinforcement directly to the fire.

Based on the results of investigation on structural response and passive fire design for 90-minutes bearing resistance of the tunnel having 2 kg/m³ PP-fibres (Pouran, et al., 2014), several questions were risen up. Some of the opened questions that are dealt with in this work are:

- Is there any simple way to evaluate the temperature fields in a cross-section of a cut-and-cover tunnel exposed to ZTV-ING for the practice use?
- What are the influences of addition of 2 kg/m³ on different mechanical properties of concrete at elevated temperatures? Should the same constitutive material model, as proposed in EN 1992-1-2, be used for concrete with 2 kg/m³ PP-fibres or should modifications be made?
- Do the potentially existing deviations in the constitutive model for concrete with PP-fibres influence the global structural analysis of a cut-and-cover? If yes, how and to what extent?

The main scopes of this work dealing with the stated questions are: a) proposing a simplified calculation method to evaluate temperature fields in cross-section of tunnel members exposed to nominal ZTV-ING fire exposure curve, b) experimental and material parts that include the investigations and experimental results to compare the mechanical properties of concrete with and without PP-fibres and construction of an implicit material model for concrete with PP-fibres as a modified form of EN 1992-1-2's model, and c) structural analysis of a cut-and-cover tunnel by using EN 1992-1-2's and

modified models in software package SOFiSTiK (2016) and investigating the effects arising from addition of PP-fibres on the structural bending response of the cut-and-cover tunnel. These areas are explained in more details in the followings:

a) Evaluation of temperature fields in a cross-section of tunnel:

In case of a cut-and-cover tunnel member exposed to ZTV-ING fire exposure curve, the first few layers of cross-section close to the exposed side are thermally affected which result in strength loss of these layers (Pouran, et al., 2014). In addition, the temperatures of steel reinforcement should not reach the critical temperature of reinforcement during fire. The latter is 300°C according to (BASt, 2015). On the other hand, to analyse the bending moments as indirect thermal effects induced by fire for statically indeterminate systems, simplified thermal actions can be assumed by considering nonlinear temperature distribution over the cross-section simplified as uniformly, $\Delta\theta_N$, and linearly changing, $\Delta\theta_M$, temperature differences.

Having temperature fields in a cross-section of a tunnel member during fire, the following questions can be correspondingly answered in the practice:

- How far and to what extent are the layers close to the exposed side thermally affected?
- Will temperature in the reinforcement exceed the critical temperature for 90-minutes fire duration (the tunnel members in the practice should be bearing resistant for 90 minutes)?
- Using a realistic assumption, what are the equivalent thermal actions (in form of $\Delta\theta_N$ and $\Delta\theta_M$) that can be used for simplified linear structural analysis?

Formulas are proposed to estimate the absolute temperature values at any point from 0 to 10 cm from the fire exposed side for member with the thickness $d \geq 60$ cm at any desired time up to 90 minutes. The proposed formulas are developed based on the results of thermal analyses performed in HYDRA (2016) for concrete elements subjected to ZTV-ING exposure curve having 60, 80, 100, 120 and 140 cm widths. The results of thermal analyses imply that the maximum distance affected by temperature is at approximately 35 cm from the exposed side. The proposed formulas are used to determine the absolute temperature values at any point from 0 to 10 cm to the exposed side as a function of distance to the fire exposed surface and time ($\theta(x, t)$). The temperature values at the layers with $10 < x \leq 35$ cm, can be simply calculated by interpolation between the estimated temperature values at $x = 10$ cm, θ_{10} , and the initial temperature, θ_i . Further, the estimation is applicable for normal-strength concrete with moisture content of 3%.

b) Experimental and material:

To write a constitutive stress-strain relationship at elevated temperatures, two types of models in general should be assumed. These are models where the stress can be evaluated from the mechanical-induced strains. These strains can be treated explicitly or implicitly in a material model. Some examples of explicit models are the models proposed by Anderberg-Thelandersson (Anderberg, 1976), Khoury-Terro (Terro, 1998) and the more recent proposed model (Schneider, et al., 2008).

In this regard, EN 1992-1-2 proposes an implicit model, where the sum of explicit mechanically induced strains are assumed as mechanical strain and the total strain is the sum of thermal strain and mechanical strain. The mechanical stress is further calculated as a function of mechanical strain, strain at peak stress and the strength of concrete at the considered elevated temperatures. Further, this model has accumulated the transient strain component (Gernay, et al., 2011). The EN 1992-1-2's model is constructed based on the results of steady and transient one-axial compression tests at elevated temperatures. The model does not take into account addition of any fibres such as PP-fibres in the concrete mix.

Considering a member of cut-and-cover tunnel, addition of PP-fibres in concrete mix influences various mechanical properties of the concrete at elevated temperatures. The influences in the one-dimensional

tests were studied by different authors: (Poon, et al., 2004), (Chang, et al., 2006), (Huismann, 2010), (Huismann, et al., 2011), (Pliya, et al., 2011), (Balazs, et al., 2012), (Huismann, et al., 2012), (Lam, et al., 2012) and (Peter, 2016).

In general, the following deficiencies, differences and contradictions exist in various experimental studies:

- The lack of sufficient data on mechanical behaviour and moisture loss of concrete specimens until the age of 200 days at ambient temperature. The 200-day strength of hardened concrete is the reference strength that should be used for a concrete member according to (RILEM, 2007);
- In many cases the strength class of concretes which are representative of concrete with and without PP-fibres are not in a comparable range;
- Too many variables or influencing parameters exist in various studies such as different heating rates, specimen sizes, concrete components, duration of holding time, moisture content at the beginning of tests, initial load levels and amount of PP-fibres content;
- There are a number of contradictory observations and reports according to different authors.

It is, therefore, almost impossible to draw solid conclusions based on the existing surveys and to construct a constitutive model based on these data for concrete with 2 kg/m^3 PP-fibres content.

In this work, thus, a test program is proposed and used to investigate the mechanical behaviour of cylinder concrete specimens with 2 kg/m^3 and without PP-fibres at elevated temperatures. The hardened concrete should meet the condition of 1 to 2-year-old concrete in the practice. Compressive strength, modulus of elasticity and moisture content were controlled and reported up to the age of 200 days at ambient temperature. Further, steady and transient tests at elevated temperatures under different initial load levels were performed and the results are explained explicitly for different mechanical components. The differences from the mechanical properties as well as strain components from the test results were investigated and identified and, correspondingly, an implicit material model is constructed for concrete having 2 kg/m^3 PP-fibres. The proposed implicit material model is based on the assumptions in EN 1992-1-2's model. Thus, two modification factors are proposed and correspondingly added to EN 1992-1-2's material model to evaluate the mechanical stresses for concrete including 2 kg/m^3 PP-fibres.

c) Structural analysis:

When members of statically indeterminate systems such as cut-and-cover tunnels are exposed to fire, the thermally affected layers close to the exposed side are intended to expand, but due to constraints, the compressive thermally stresses are induced in the cross-section. The resultants thermally induced forces in cross-section imposing a bending moment, which have to be coupled with the bending moments induced by mechanical actions. On the other hand, the mechanical properties of concrete layers, being thermally affected during the fire, are reduced for temperatures beyond 100°C . The latter is also valid for steel reinforcement exposed to elevated temperatures.

Analysing such effects should be performed using a sequentially-coupled-thermo-mechanical analysis as a scope of advanced calculation method proposed by EN 1992-1-2. Examples of such analyses for the tunnels and the influencing parameters can be found in (Pouran, et al., 2014), (Pouran, et al., 2015), (Peter, 2016) and (Pouran, et al., 2017).

Such thermo-mechanical analysis is performed by carrying out, first, thermal analyses for the members exposed to fire separately and then implementing the thermal effects into the structural model and coupling them with the existing effects induced by other mechanical actions. This has been carried out for the tunnel structure investigated in (Pouran, et al., 2014) which is exposed to fire for duration of

90 minutes. The latter is used in this work as a reference system. Using fibre-enhanced beam elements in TALPA (2016), structural analyses were performed and investigated once again for duration of 30 minutes. The effects of changes in strengths and strains at the peak stresses according to EN 1992-1-2's and proposed model on the global structural behaviour of the tunnel are compared and explained. Further, 30 minutes fire duration has been selected for this work based on the following reasons:

- Considering the global structural analysis and based on the experience from (Pouran, et al., 2014), the maximum flexural stress is implied at 30 minutes after initiation of fire for the tunnel exposed to ZTV-ING curve, already designed for serviceability and ultimate limit states at ambient temperatures. It is, therefore, expected even by using the residual strength of each layer in the model at cooling phase, being lower than its strength at elevated temperatures, the rate of decrease in the thermally induced compressive force in each layer is higher. This means the rate of flexural stiffness loss of the cross-section is much lower than the rate of decrease in the thermally induced bending moment. Therefore, considering the ultimate limit state design of the tunnel, the critical flexural state is expected to occur up to 30 minutes;
- Further, in case of performing the residual tests, it is not clear that how the cooling rate should be controlled.

The differences in strengths and strains at peak stresses between the proposed model and EN 1992-1-2's model were identified. The influences risen up from these differences on the structural bending response of the structure are correspondingly explained.

1 Fire Design

In general, fire is an incident that might occur in different places and can subject the surroundings or environment to an extraordinary condition. From the point of view of civil engineering, the probability of occurrence of such incidence in various types of structures is different. The highest number of fire attacks occurs in residential structures, mostly, due to human errors.

In order to be able to design a specified structure for a fire situation, a relevant temperature evolution on the members should be available. Having the relevant fire scenario determined, corresponding thermal actions could be estimated either using nominal fire curves (prescriptive rules) or by physically based thermal actions. According to (Moore, et al., 2007) there are four assessment methods or levels that can be assumed for fires (listed in Tab. 1). These are:

- Nominal fire exposure curves (Level 1): normative fire exposure curves adopted in EN 1991-1-2 for fire design purposes of residential structures. These give temperature values on the structural members in a compartment and have no cooling phase. For road tunnels in Germany, (BAST, 2015) proposes a normative fire curve with a cooling phase;
- Equivalent fire duration time (Level 2): Annex F of EN 1991-1-2 proposes a methodology to evaluate the equivalent duration of exposure on ISO-fire curve based on the defined parameters for a real fire in a compartment. These parameters are fire load, compartment size, the ventilation condition and properties of the compartment linings;
- Natural fire models (Level 3): simple and quick tools to calculate the gas temperatures in a compartment or localised fire. The size of openings, total area of enclosure and thermal properties of boundary of the enclosure are the main parameters. These can be utilized for the post-flashover condition by considering the uniform temperature distribution within a compartment;
- Advanced fire models (Level 4): including zone models (one-zone models and two-zone models) and computational fluid dynamics (CFD). Zone models are formed on the solution of the equations of mass and energy where one-zone models assume uniform temperature distribution in the compartment and two-zone models compose of an upper layer with time-dependent thickness and with time-dependent uniform temperature, as well as a lower layer with a time-dependent uniform temperature in the compartment. CFD models are based on the complex solution of thermodynamic and aerodynamic variables within the control zones and evolution of time-and-space-dependent temperatures.

The focus of this work is on the structural fire design of cut-and-cover tunnels. The normative fire curve for road tunnel structures in Germany, is explained in section 1.2 and assumed to be sufficiently conservative and can be considered as the relevant fire action. On the other hand, the fire design concept of EUROCODE 2 is mainly based on characteristics of a normative fire curve (ISO-fire curve) for residential structures. Therefore, it is rational to have a closer look at the nominal fire curves for compartments and road tunnel structures.

Fire Design

Table 1: Assessment methods, characteristics and applications of different fire models

Assessment method	Fire model	Type of models		Characteristics		Fire area	Guide or reference for the calculation
				Residential	Road tunnel		
Level 1	Nominal fire exposure curves	Prescriptive		Temperature analysis of structural members without cooling phase	Temperature analysis of structural members with a cooling phase	Compartment or local	Residential: EN 1991-1-2 Road tunnel: ZTV-ING, part 5, section 2
Level 2	Equivalent fire duration time	Analytical		Relates the severity of a specific real compartment fire to an equivalent duration on ISO fire. Material dependent. Not applicable for concrete and composite steel constructions		Compartment	Annex F of EN 1991-1-2
Level 3	Natural fire models			Based on specific physical parameters. Temperature analysis of structural members for the whole duration of fire		Compartment	Annex A of EN 1991-1-2
Level 4	Advanced fire models	Zone models	One-zone models	Uniform time dependent temperature distribution		Compartment	Annex D of EN 1991-1-2
			Two-zone models	Assuming an upper layer with time dependent thickness and with time dependent uniform temperature, as well as a lower layer with a time dependent uniform and lower temperature			
		Computational fluid mechanics (CFD)	Temperature evolution in a completely time dependent and space dependent way				

1.1 Compartment and Tunnel Fires

There are mainly three phases from the point of ignition to vanishing of a fire. These are pre-flashover, flashover (the state at which due to rapid spread of fire the whole compartment is involved in fire within an enclosure), and cooling phase (see Fig. 1a).

Fire growth in residential structures is mainly analysed in a compartment. Fire characteristics, for each occupancy category is different, based on the fire load intensity. This is estimated by experiments for different appropriate amount of combustible materials in the scene. The fire growth stage or pre-flashover normally takes place with a low temperature increase rate.

On the other hand, the probability of occurring of fire and exposure of infrastructures to fire action is increasing as the number of roads and population rises. For road tunnels, the lining shall be designed for the fire situation by considering the high possibility of several vehicles being involved in fire ignition and the fire rate of 100 MW (Schlüter, 2014). Temperature rises in fire growth stage, therefore, in a rapid manner.

For occupied structures and road tunnels, there have been many efforts and, correspondingly, validated experimental results to investigate the severity and characteristics of fire. The main differences influencing three fire phases are:

- The fire origin which might influence the pre-flashover and flashover phases to a great extent: in tunnel fires due to the effective heat feedback, vehicles are involved in the ignition process more intensely which affect the flashover vigorously;
- The flash-over can be assumed for tunnels to occur in a section of tunnel and be quicker due to the high heat release rate of fire (see Fig. 1b);
- Natural ventilation may influence the flashover and the post-flashover to a high extent;
- Ventilation factor for compartment fires and mechanical ventilation for tunnel fire as well as geometry and type of tunnel structures;
- The formation of the stratified smoke layer differs (Beard, et al., 2005).

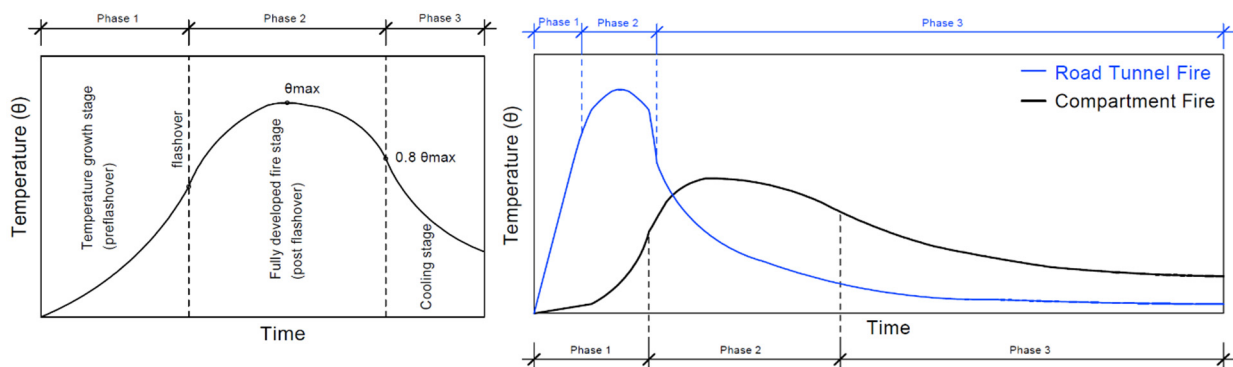


Figure 1: a. Temperature rise at different fire stages for idealized experimental fire curve (left), b. Idealized compartment and tunnel experimental fire curves (right) (Pouran, et al., 2016)

1.2 Nominal Fire Curves for Compartments and Road Tunnels

Nominal fire exposure curves are based on the fire test results by considering the physical parameters for a particular structure. There are many experimental results for compartment and road tunnel fires.

For compartments, there are three nominal fire curves adopted in EN 1991-1-2 (see Fig. 2a): standard temperature-time curve, which is the basis of most of proposed fire design methods for the main structure of residencies. External fire curve used for external members (e.g. facades). Hydrocarbon curve, where petrochemical or fuels form a considerable proportion of the overall fire load. The standard curve is

commonly used for many years to estimate the relative fire performance of construction materials. There is no cooling phase predicted for this curve. Use of tabulated data and design methods proposed in EUROCODE 2 are mostly restricted to the choice of fire curve that is similar to the standard curve. Due to this reason, the focus is mainly on standard curve in the current work, where the gas temperature is given as:

$$\theta_g = 20 + 345 \log_{10}(8t + 1) \tag{1}$$

θ_g (°C) refers to the gas temperature in the compartment and t stands for time in minutes.

For road tunnels in Germany, ZTV-ING fire exposure curve is adopted in (BASt, 2015). Fig. 2b shows ISO and ZTV-ING curves. ZTV-ING curve has a much higher temperature increase rate in fire growth and reaches the maximum value of 1200°C in only five minutes and then a constant flashover stage of 25 minutes and finally a 110-minute cooling phase.

These curves, as already stated, are based on experimental results. Figs. 2c and 2d show the test results of compartment fires for different fire load intensities extracted from (Arnault, et al., 1973) with ISO curve and experimental fire test results for a section of tunnel extracted from (Dehn, et al., 2013) along with ZTV-ING curve respectively. These figures are indicative that both ZTV-ING and ISO curves give a conservative representation of test results.

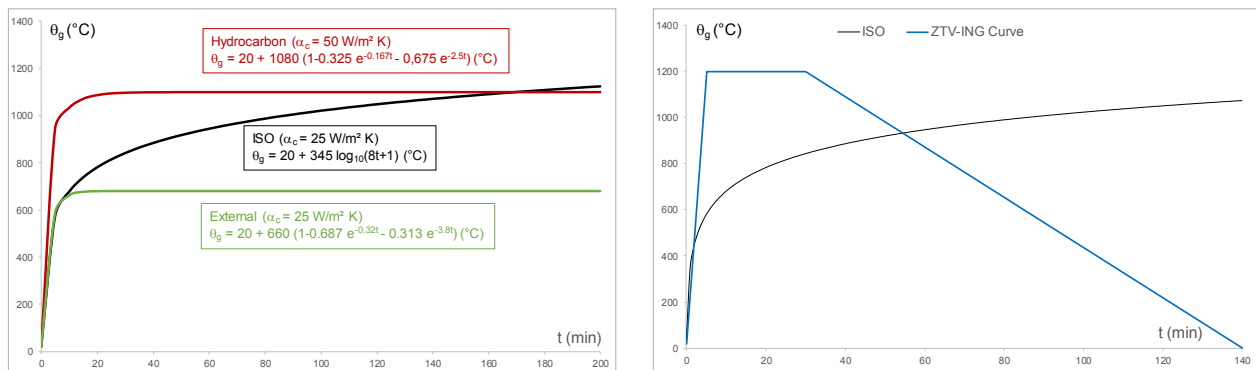


Figure 2: a. Three normative fire curves according to EN 1991-1-2 (left), b. ZTV-ING vs. ISO (right)

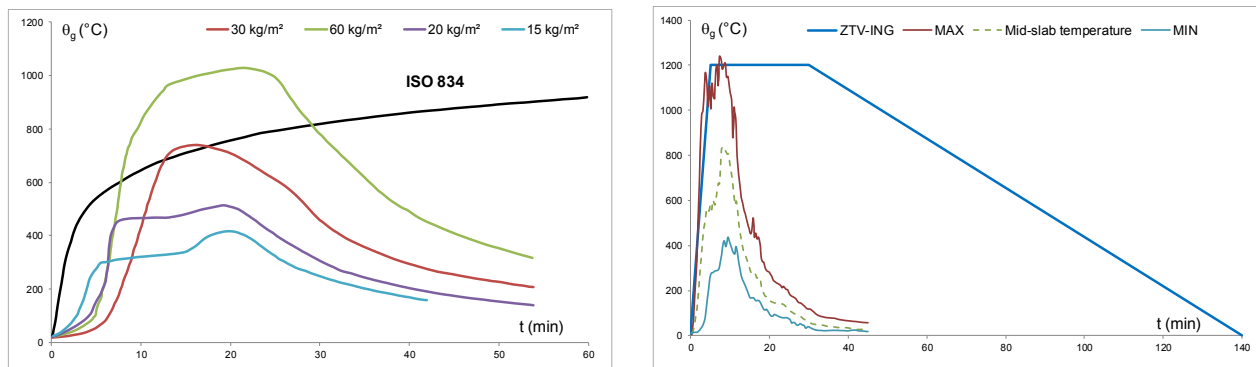


Figure 2: c. Idealized compartment curves with different fire loads from (Arnault, et al., 1973) vs ISO curve (left), d. Experimental fire curves for road tunnels from (Dehn, et al., 2013) vs. nominative fire exposure curve for tunnels (right)

1.3 Thermal Analysis of an Element of Tunnel Structure vs. Residential Structure

To compare the heating rates, thermal analyses of a tunnel member and a member in a residential structure with a thickness of 60 cm were performed for 90 minutes. 1D heat transfer is considered by making the following assumptions:

- Taking concrete as a homogeneous and isotropic material;
- Fourier’s law of heat conduction for the energy transfer in temperature gradients directions (explained in Annex A);
- The upper limit of thermal conductivity of concrete for the NSC according to EN 1992-1-2;
- Absolute temperature values as a function of time according to ZTV-ING curve on the exposed edges;
- The Newton’s law of convection with the heat convection coefficients of correspondingly $\alpha_c = 25 \text{ W/m}^2\text{K}$. The convective coefficient of heat transfer is, however, an experimental value and it is not a material constant. However, the comparison of results by the authors shows that using 25 to 50 $\text{W/m}^2\text{K}$ coefficients influence the temperature fields in the fire growth phase for the fire exposed boundary up to 10 minutes by 5%. Therefore, the effects are negligible in this range.

The comparison between heating rates within a thinnest possible wall in cut-and-cover tunnel structures in Germany (60 cm) under ZTV-ING curve has been made with the same thickness of wall under ISO curve (see Fig. 3). The maximum heating rate, R , under ZTV-ING curve is 86 K/min being three times larger than the one under ISO fire (Pouran, et al., 2017). These values decrease for the next layers towards the centre and approaches the maximum of 4 K/min at a distance of $L = 6$ and 7 cm from the exposed side.

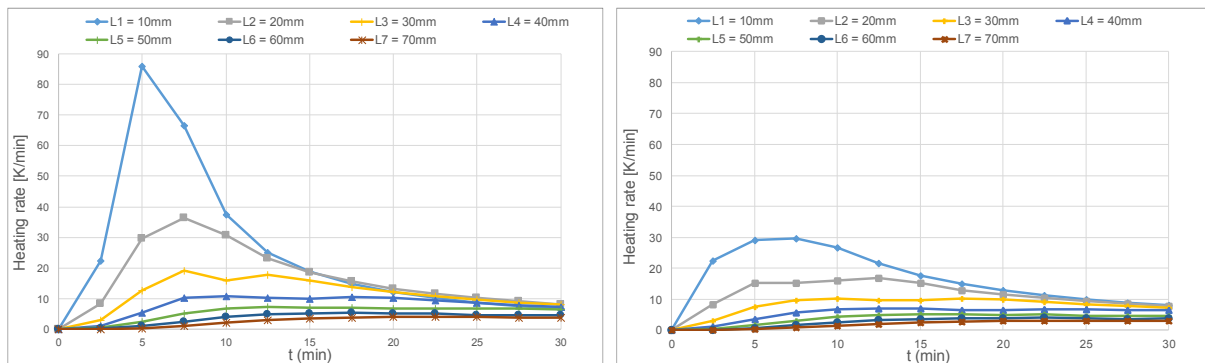


Figure 3: Heating rates within layers of a 60-cm thick concrete element exposed to ZTV-ING curve (left) and ISO curve (right)

1.4 Fire Design according to EUROCODE 2’s Concept

According to EN 1992-1-2:2004, “the general objectives of fire protection are to limit risks with respect to the individual and society, neighbouring property, and where required, environment or directly exposed property, in the case of fire”.

Further, there are three limit states (criteria) defined for fire situation according to the test results:

- **Load bearing capacity (R)** is assumed to be fulfilled when the structure does not fail mechanically for the specified duration of fire;
- **Insulation (I)** is satisfied when the temperature on the unexposed side is lower than the limit which might lead to the ignition of the combustible materials;
- **Integrity (E)** is fulfilled when the spread of flame or hot gas (separating function) should be prevented to the unexposed side and integrity of the structure should be held for the desired fire duration.

Since in case of road-tunnel fire, only load bearing criterion plays a significant role, this limit state is only discussed in the current work.

Further, by assuming nominal ISO-fire curve as thermal actions for fire design, EN 1992-1-2:2004 proposes, as shown in Fig. 4, three assessment methods:

- **Tabulated data (Level 1).** The tabulated values of minimum dimensions and axis distances for different types of members (member analysis) are given for various fire exposure periods based on test results. The minimum allowable given values are conservative. The critical temperature of steel θ_{cr} reinforcement for the load level of less or equal 70% of maximum allowable stress at normal situation is assumed to 500°C and is the limit criterion of the tests;
- **Simplified calculation models (Level 2).** By using temperature profiles of concrete members after specified duration of ISO fire with predefined given thermal boundary properties, the strength and stiffness of the cross-section are reduced. Using the zone-method, the reduced cross-section is designed for the design mechanical actions at fire situation;
- **Advanced calculation models (Level 3).** Members, part of the structure or the whole structure can be designed for fire situation by coupling the thermally induced effects with the mechanical-induced effects using nonlinear-iterative methods taking into account temperature dependent material properties. The indirect-induced-thermal effects are incorporated stepwise in the model.

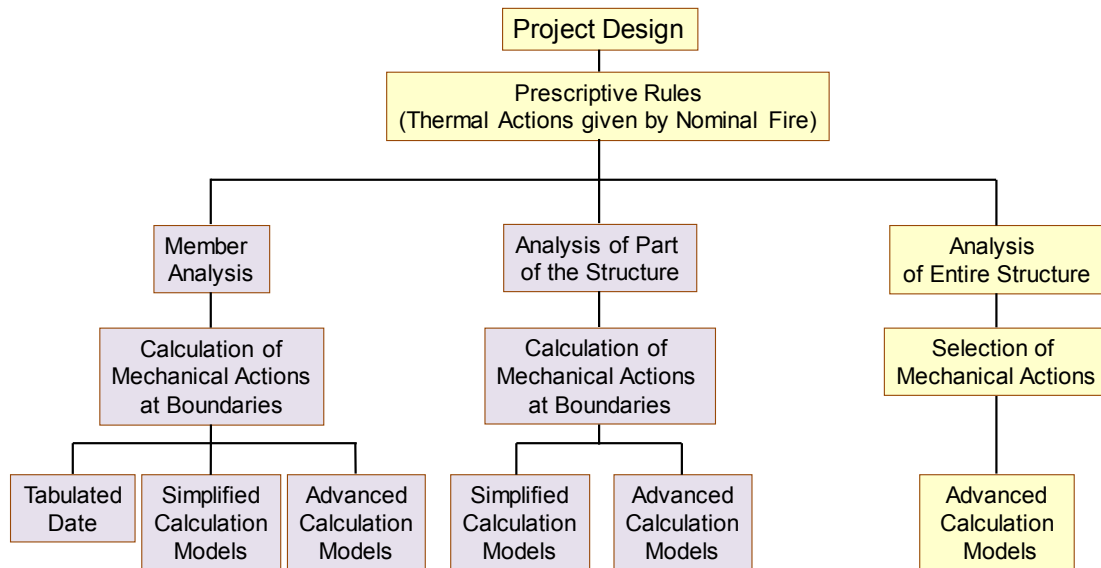


Figure 4: Fire design procedure according to EN 1992-1-2

The cut-and-cover tunnel structure selected as the basis of analysis in this work is a two-cell rectangular frame concrete structure, and therefore should be analysed and designed for fire situation by advanced calculation methods. To do this, thermally and mechanical-induced effects have to be coupled for different steps by considering the damaged cross-section properties for each time-step of analysis. Thermally induced effects are not simulated via Level 1 and Level 2 methods. The two types of thermally induced stresses, flexural stress due to temperature gradients and internal restraints and restraint stresses due to axial constraints at elevated temperatures, are for a cut-and-cover tunnel of great significance:

- Due to high rate of temperature increase in the fire growth stage, there is a high negative bending moment (considering the positive local z axis is directed inward the tunnel) expected that totally changes the behaviour of the exposed members and distribution of stresses in the member;
- Due to horizontal bedding of soils, there might also appear restraint forces in the horizontal members that cannot be taken into account by Level 1 and 2 methods.

The grade of statically indeterminacy provides much longer resistance for the whole system and failure might only occur by formation of sufficient number of plastic hinges and therefore the maximum reserve of material resistance is used parallel with stress redistribution in the analysis.

The focus of this work is, therefore, on the issues and analysis of different aspects of advanced analysis of the tunnel structure by incorporating the experimental results according to which stress-strain models should be investigated and modified.

1.5 Advanced Calculation Method

Using an advanced method proposed by EN 1992-1-2:2004 to analyse and design such structures, the following three main areas should be dealt with carefully:

- Determination of fire action for the specified project and the worst combination of actions for fire situation;
- Using realistic material model for the concrete exposed to fire action;
- Defining a thermo-mechanical model that takes account of indirect-thermally induced effects corresponding to the specified fire action and the strength reductions due to temperature rise simultaneously.

In order to be able to analyse concrete structures exposed to fire, different types and levels of advanced analyses can be categorized according to the grade of complexity and accuracy into:

- Close-to-the-reality model: development of fire is simulated via a CFD (Computational Fluid Dynamics) model by considering the fire cause and aero and atmospheric conditions. To bridge between the elevated temperatures from the transient flow and the structure, one should think of interactive-nonlinear-boundary conditions with optimized time steps. The structural analysis, then, is performed by taking into account the spontaneous loss of strength and stiffness of the cross-sections. The latter will be followed by considering the heat transferring to the surface of concrete elements by all heat transfer mechanisms, conduction, convection and radiation, transiently;
- Coupled-thermo-mechanical analysis divided into: sequentially-coupled-thermo-mechanical analysis and the fully-coupled-thermo-mechanical analysis with a simplified boundary condition and nominal fire exposure curve. Development of fire is based on the corresponding nominal fire exposure curve. In case of fully-coupled analysis the interaction between temperature fields and stresses are taken into account in the model. For sequential analysis, the heat transfer parameters at boundaries remain constant during the whole period of heat transfer analysis and the elevated temperatures from the fire exposures can be defined as prescribed temperatures acting on the exposed surface of concrete member. This process requires separate thermal analyses of concrete elements and importing the effects of elevated temperature within concrete into the mechanical model by using multi-layered strain model (Harte et al. 2000). Physical-stepwise-nonlinear analysis can now be performed by taking into account the spontaneous loss of strength and stiffness of the cross-section as well as considering the rising thermally induced stresses within the structure. This procedure is shown in Fig. 5;
- Model with an alternative temperature gradient for the nominal fire exposure curve: the transient nominal fire load can be replaced by a stationary equivalent temperature gradient acting throughout the section. The equivalent linear temperature difference acts on the tunnel cross-sections and imposes flexural stresses. The uniform temperature difference component and consequently the corresponding normal stresses can be neglected. The structural analysis is performed by considering linear material properties. This method cannot give any view of flexural strains at the elevated temperatures.

The sequential analysis is at the time the only method investigated by the author. In latter, nonlinear analysis of the structure is performed for the worst effects due to combination of mechanical actions for the fire situation. The structure is assumed, initially, subjected to the prescribed strains and thus stresses (initial-state stress or ISS) induced by the worst combination of actions. This also includes the state of material by assuming physical nonlinearity. Further, transient thermal analyses of concrete elements are performed using appropriate time intervals based on the prescribed boundary condition that is a normative fire curve. The temperature fields are read for different time intervals. Temperature fields for an appropriate number of time intervals can now be specified, stored and treated as load cases. The temperature fields in each load case is interpreted and incorporated as strains and stresses (thermally induced stresses or TS) in different layers parallel to the axis of cross-section by using multi-layered strain model (Harte, et al., 2000) in a sequential manner. This means that for instance, the initial-stress states due to the effects induced by mechanical action at the start of fire are coupled with the stresses induced by first load case describing the temperature distribution after five minutes of start of fire in the cross-section.

The coupled-thermo-mechanical stresses and the new state of cross-section is now stored as a new initial-stress state for the successive analysis step. The algorithms of sequential-coupled-thermo-mechanical analysis is illustrated in Fig. 5.

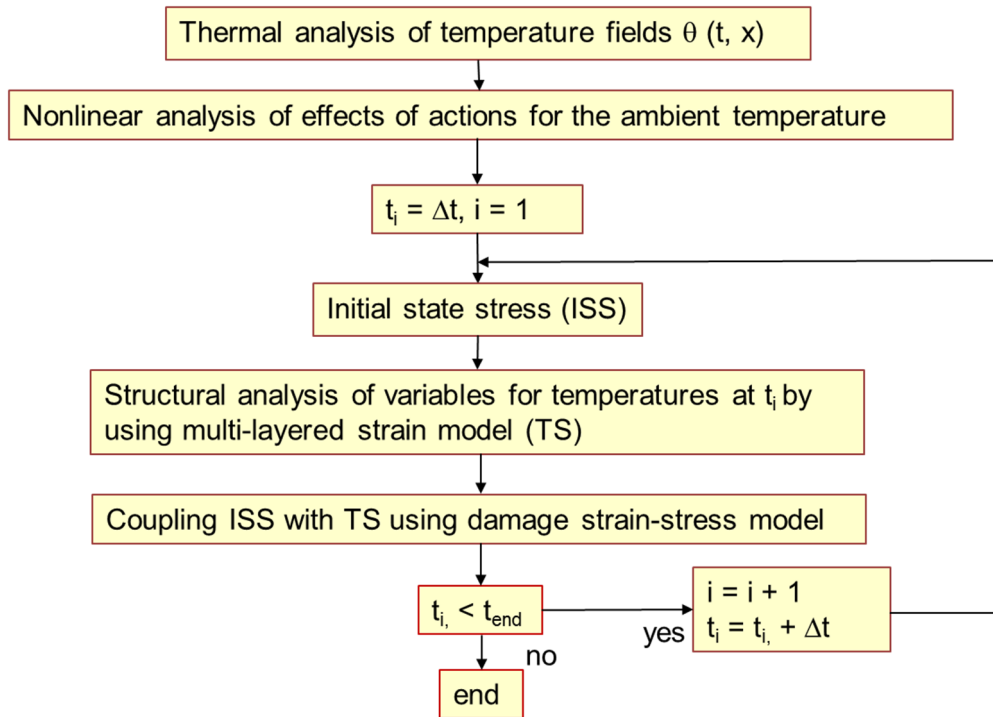


Figure 5: The procedure of sequential-thermo-mechanical analysis

2 Fire Action and Development of Temperature Fields

For the structural analysis of a cut-and-cover tunnel under ZTV-ING fire exposure, the first rational step is to understand the temperature fields and temperature differences in a cross-section of a tunnel. This can give a general view of how stress might change in the modelling of concrete under fire and enables us to control and check the outputs from the used finite element analysis at structural level.

Formulas are proposed to determine the absolute temperature values at any point from 0 to 10 cm to the exposed side over a cross-section of cut-and-cover tunnel members as a function of position and time ($\theta(x, t)$). The results of thermal analyses imply that the maximum distance affected by temperature is at approximately 35 cm from the exposed side. The temperature values at the positions $10 < x \leq 35$ cm can be simply interpolated. The latter can be used to estimate the temperature values at the position of reinforcing bars and to estimate temperatures up to 35 cm from the exposed side to find the uniform temperature difference component, $\Delta\theta_N(t)$, linear temperature difference component, $\Delta\theta_M(t)$, and nonlinear temperature difference component, $\Delta\theta_E(t)$, defined in EN 1991-1-5 (for almost stationary condition) but now time-dependent.

2.1 Temperature Difference over a Cross-section in Fire Situation and Determination of Absolute Temperature Values

In general, distinction should be made between the stationary and transient thermal condition on the boundary of a cross-section. EN 1991-1-5 proposes different temperature difference components for the case of almost stationary boundary conditions on the surface. To understand the temperature distribution in a cross-section under a 1-dimensional heat transfer induced by ZTV-ING action, two time regions should be defined:

- Initiation of fire up to 140 minutes where the transient condition governs the fire exposed boundary and structural flexural and axial strength of the member should be satisfactory;
- Post-fire condition with ambient temperature in the tunnel where the stationary condition rules the both boundaries.

The results of thermal analyses of concrete elements with variable thicknesses from 60 to 140 cm (walls and slabs thicknesses in practice) show that higher temperatures can only penetrate and influence the members under ZTV-ING up to approximately 35 cm from the exposed side.

Further, three general assumptions should be made during fire by considering different regions as reference regions for estimation of temperature difference components as a function of time:

- **Global**: considering the **whole cross-section** is subjected to the assumed temperature difference component at a specified time;
- **Quasi-local**: considering the **affected zone** (for tunnel walls and slabs approximately 35 cm from the exposed side) is subjected to the assumed temperature difference component at a specified time;
- **Local**; considering a **local-time-dependent-affected zone** close to the fire exposed side.

The temperature distributions over a tunnel cross-section at $t_1 = 30$, $t_2 = 90$, $t_3 = 140$ minutes (as arbitrary time points) and $t_4 \gg t_3$ minutes with the different assumptions are shown in Figs. 6 and 7. The combination of different assumptions are also shown for the fire situation for four cases ①, ②, ③ and ④ for temperature fields at t_1 and t_2 .

For $t < 140$ minutes, the following assumptions and combinations can be taken into account:

Global $\Delta\theta_{N,gl,t}$ and global $\Delta\theta_{M,gl,t}$: considering $\Delta\theta_N(t)$ acting at t on the whole cross-section is too conservative as the maximum affected zone includes the first 35 cm from the exposed side. Assuming that the linear temperature difference acts over the whole cross-section is also an unrealistic assumption, as this line does not approach the nonlinear temperature distributed curve for the first 90 minutes. The unrealistic high values of $\Delta\theta_{E,gl,t}$ confirms that this assumption is not appropriate for $\Delta\theta_M(t)$ values (see Fig. 6 case ①).

Quasi-local $\Delta\theta_{N,aff,t}$ and quasi-local $\Delta\theta_{M,aff,t}$: Considering $\Delta\theta_N(t)$ acting at t on the affected zone is conservative as the major amount of heat is transferred to the almost 20 cm of the wall. Considering the linear temperature difference acting over the affected zone is further a too conservative assumption as this line does not approach the nonlinear temperature distributed curve for the first 90 minutes. The unrealistic high values of $\Delta\theta_{E,aff,t}$ is indicative of the unrealistic assumption made for $\Delta\theta_M(t)$ (see Fig. 6 case ②).

Local $\Delta\theta_{N,loc,t}$ and adjusted local $\Delta\theta_{M,x_{\Delta\theta_{N,loc,t}}}$: here it is assumed that the average surface under the temperature profile is, for example at $t_1 = 30$ min, simulated by:

$$\Delta\theta_{N,loc,t_1} = \frac{1}{x_{\Delta\theta_{N,loc,t_1}}} \int_0^{x_{\Delta\theta_{N,loc,t_1}}} \theta(t, x) dx \quad (2)$$

where $x_{\Delta\theta_{N,loc,t_1}}$ is the local affected zone corresponding to $\Delta\theta_{N,loc,t_1}$. Assuming the same corresponding distance for the $\Delta\theta_M(t)$ as shown in Fig. 6 case ③, the local $\Delta\theta_M(t)$ values adjusted and applied on $x_{\Delta\theta_{N,loc,t_1}}$ underestimate the real temperature gradients overruling this region. The relatively high values of $\Delta\theta_{E,aff,t}$ is indicative of the not accurate approximation made for $\Delta\theta_M$ (see Fig. 6 case ②).

Local $\Delta\theta_{M,loc,t}$ and adjusted local $\Delta\theta_{N,x_{\Delta\theta_{M,loc,t}}}$: here it is assumed that the local reference distance corresponds to the x values, where the corresponding assumed $\Delta\theta_M(t)$ gives the best approximated values for the major part of nonlinear temperature profile (see Fig. 7 case ④). Having determined the temperature values over the cross-section at each time, the values of the local corresponding x , which is now $x_{\Delta\theta_{M,loc,t_1}}$, should be estimated. By assuming $\Delta\theta_N(t)$ corresponds to the surface under temperature profile from 0 to $x_{\Delta\theta_{M,loc,t_1}}$, the corresponding local $\Delta\theta_{N,loc,t_1}$ value is overestimated. Further, $\Delta\theta_{E,loc,t}$ values approaching zero that confirm the best possible approximation is made for $\Delta\theta_M(t)$.

Local $\Delta\theta_{M,loc,t}$ and modified global $\Delta\theta_{N,gl,mod}$: $\Delta\theta_M(t)$ acts on the x assumed in case ④ as the best approximated local region for $\Delta\theta_M(t)$. Then the best possible assumption for $\Delta\theta_N(t)$ is to consider that it acts over the whole cross-section with the knowledge from case ① that this value is too conservative and should be modified and reduced to give a realistic estimation as shown in Fig. 7 case ⑤).

And for $t \geq 140$ minutes:

Modified global $\Delta\theta_{M,gl,t,mod}$ and global $\Delta\theta_{N,gl}$: it can be assumed that $\Delta\theta_M(t)$ acts on the whole cross-section assumed in Fig. 7 case ⑥). This value should be modified to give a realistic estimation of $\Delta\theta_M(t)$ with the least deviation from the nonlinear temperature distribution at this state. Then the best possible assumption for $\Delta\theta_N(t)$ is to consider $\Delta\theta_N(t)$ acts over the whole cross-section.

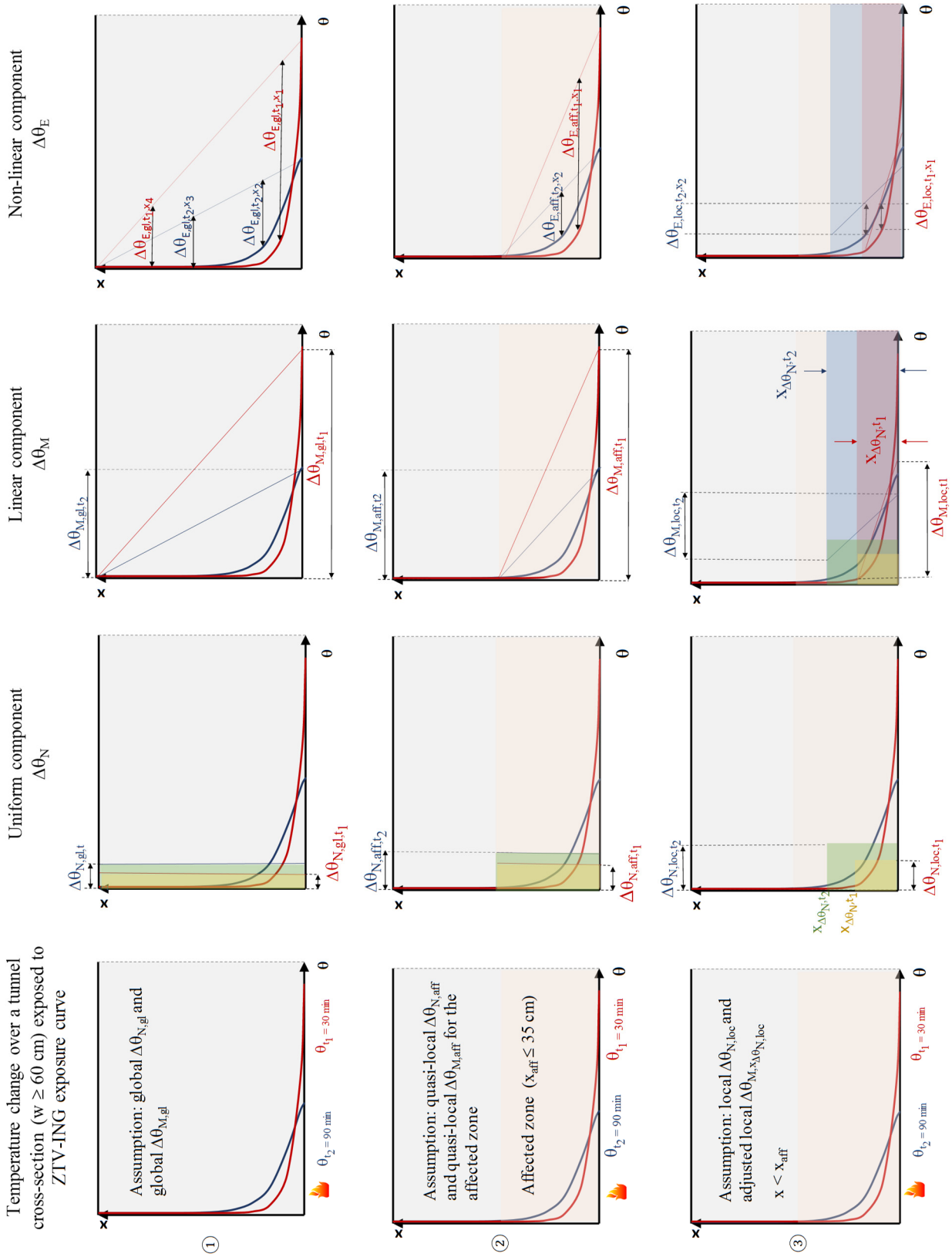


Figure 6: Different assumptions for uniform, linear and nonlinear temperature difference components for a cross-section of tunnel at $t \leq 140$ minutes

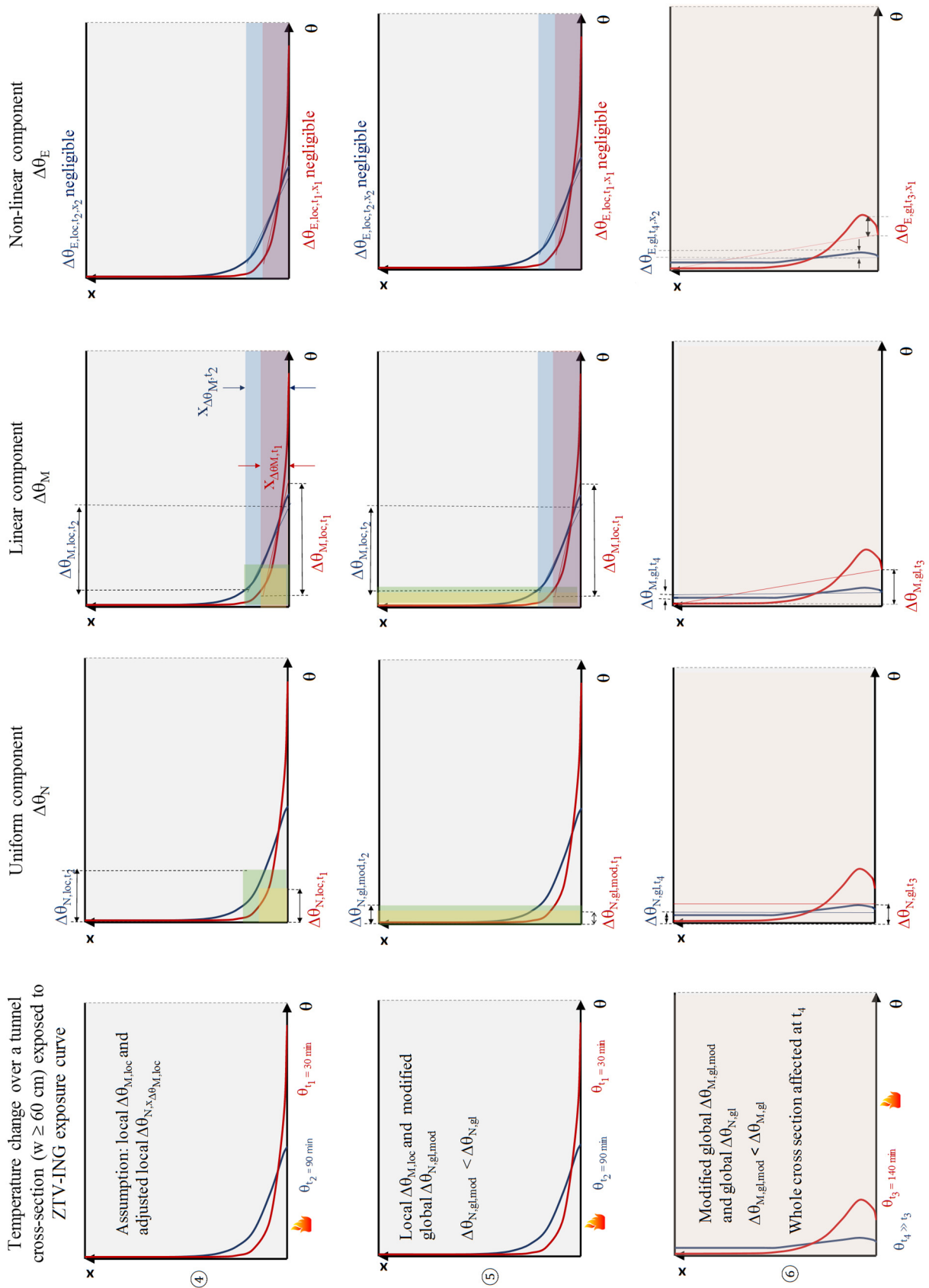


Figure 7: Different combined assumptions for uniform, linear and nonlinear temperature difference components for a cross-section of tunnel at $t \leq 140$ minutes and $t \geq 140$ minutes

In this section, a formula is proposed to estimate the absolute temperature values at any point from 0 to 10 cm from the fire exposed side for cut-and-cover tunnel cross-sections with the thicknesses $d \geq 60$ cm at any desired time up to 90 minutes (the tunnel members in the practice should be bearing resistant for 90 minutes). The temperature values at the layers with $10 < x \leq 35$ cm, can be simply calculated by interpolation between the estimated temperature values at $x = 10$ cm, θ_{10} , and the initial temperature, θ_i . It can be also assumed that for $x > 35$ cm the cross-section is unaffected and has the initial temperature. Further, the estimation is applicable for normal-strength concretes with moisture content of 3%. One-dimensional thermal analyses of concrete elements subjected to ZTV-ING exposure for the elements with 60, 80, 100, 120 and 140 cm width of orthogonal surface to the fire exposure were performed in HYDRA (2016).

The main idea is to find the absolute temperature value at any point in the heat transfer direction. The desired temperature at a specified time and position, is a function of exposure temperature, θ_{exp} , distance to the exposed side, x , and time, t , as variables:

$$\theta = f(\theta_{exp}, x, t) \quad (3)$$

The course of temperature change in the cross-section by considering once x as constant and t as variable and then t as constant and x as variable are investigated and are shown in Fig. 8. These give the main idea of how each function of temperature profile should be formed.

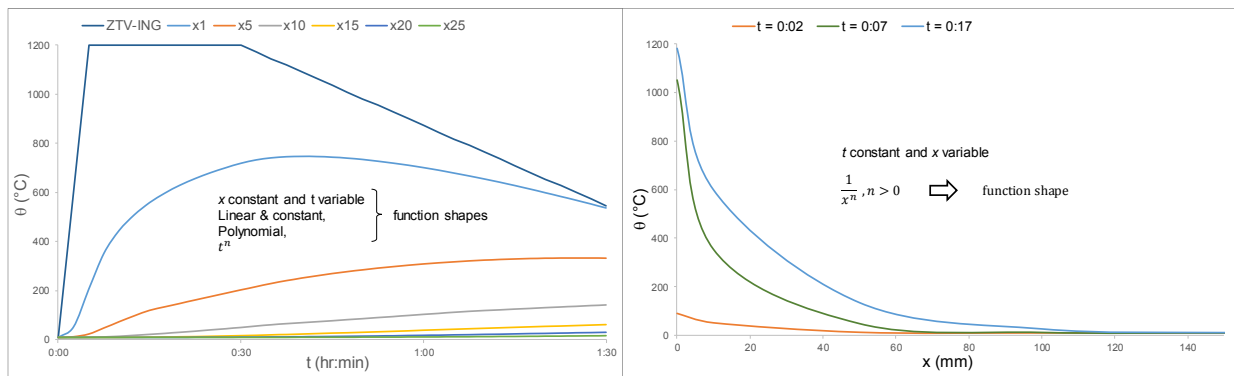


Figure 8: Course of change in temperature values in a 60-cm thick concrete cross-section exposed to ZTV-ING

Since θ_{exp} is known, the desired temperature in the cross-section can be assumed to be a factor of θ_{exp} :

$$\theta(x, t) = \alpha \theta_{exp}(t) \quad (4)$$

$$\alpha = \alpha_1 \cdot \alpha_2 \quad (5)$$

where α_1 is coefficient of heat transfer and α_2 is cross-section coefficient taking into account different width of normal surface to heat transfer direction. As a first step to specify α_1 , it is assumed that α_2 for the case of member with cross-section thickness of 60 cm and width of normal surface of 60 cm (basis width) is equal 1 (variation of α_2 will be determined in section 2.3) and, therefore, α_1 can be estimated by:

$$\frac{\theta(x, t)}{\theta_{exp}(t)} = \alpha_1 \quad (6)$$

α_1 is a function of x and t . To estimate α_1 , the ratio of temperature output values to exposure temperature, θ_x / θ_{exp} , for each layer is estimated when having t as the only variable. The latter is shown in Fig. 8 giving an overview of course of change and shape of functions for α_1 :

$$\frac{\theta(x = 0, 1, 5, 10, 15, 20 \text{ cm}, t)}{\theta_{exp}(t)} = \alpha_1 \quad (7)$$

The shape of θ_x / θ_{exp} function is for:

- $x = 0$ linear and constant (see Fig. 9);
- $x = 1$ cm , θ_x / θ_{exp} has a parabolic concave downward shape dominating almost a period of 45 minutes after fire ignition and then it turns to have exponential form with the increase of t ;
- $x = 5$ cm, the function has a parabolic concave downward shape dominating almost a period of approximately 30 minutes after fire ignition and then it turns to have exponential form with the increase of t ;
- $x = 10$ cm, θ_x / θ_{exp} has almost only an exponential form;
- $x \geq 15$ cm, the function can be assumed to have approximately a linear shape.

The investigation of course of change in θ_x / θ_{exp} gives an overview of how formulation of the general function with two variables should look like. Finding a function with many terms that can simulate the different explained shapes is almost impossible. Therefore, simplifications should be made. For:

- $x = 0$ linear and constant shapes at the boundary are only function of t and can be simply formulated;
- $1 \text{ cm} \leq x \leq 10 \text{ cm}$, a function with two independent variables is proposed which gives a good estimation for this region;
- $10 \text{ cm} < x \leq 35 \text{ cm}$, shape of θ_x / θ_{exp} function becomes almost linear and at $x = 35 \text{ cm}$ the temperature in the layer is equal θ_i . Therefore having calculated the temperature values on $x = 10 \text{ cm}$, temperature values between these two layers can be easily evaluated by linear interpolation (see Fig. 10).

Now the task is to estimate α_1 function for $x = 0, 1, 5$ and 10 cm and α_2 .

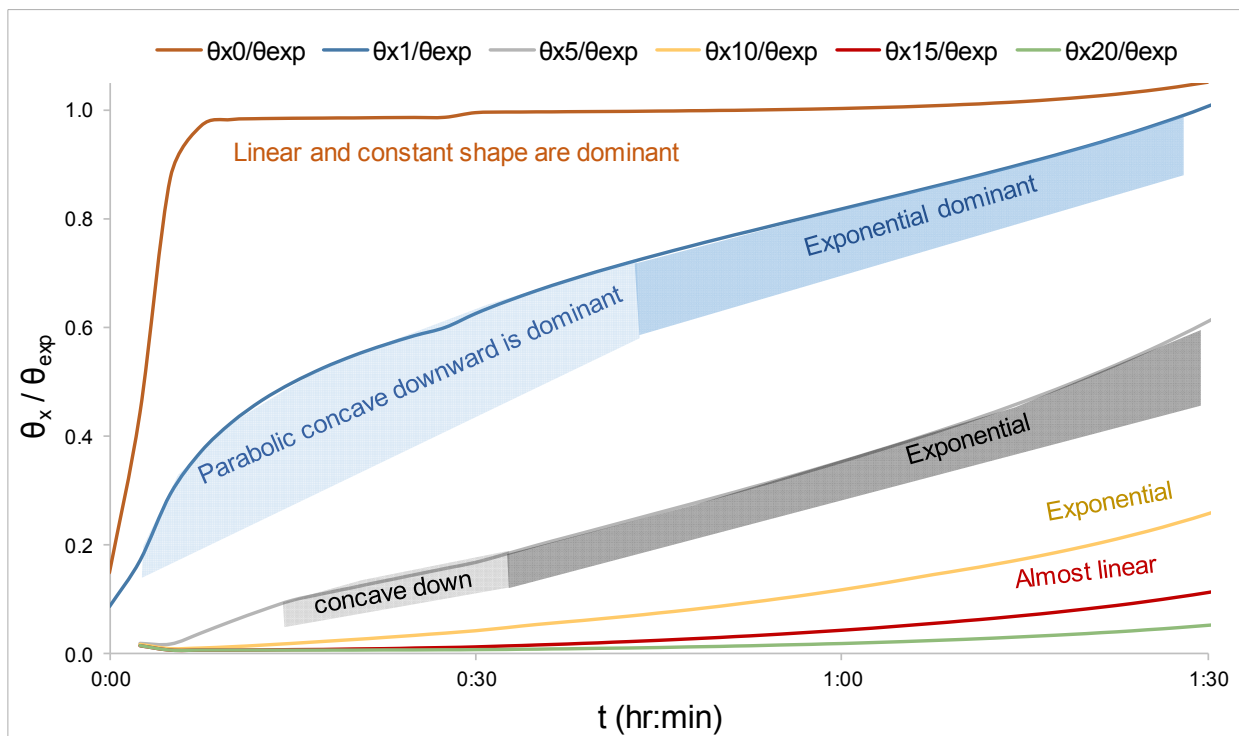


Figure 9: The ratio of temperature at layer x to fire exposure vs. time for the first 20 cm for a concrete element of 60-cm thick

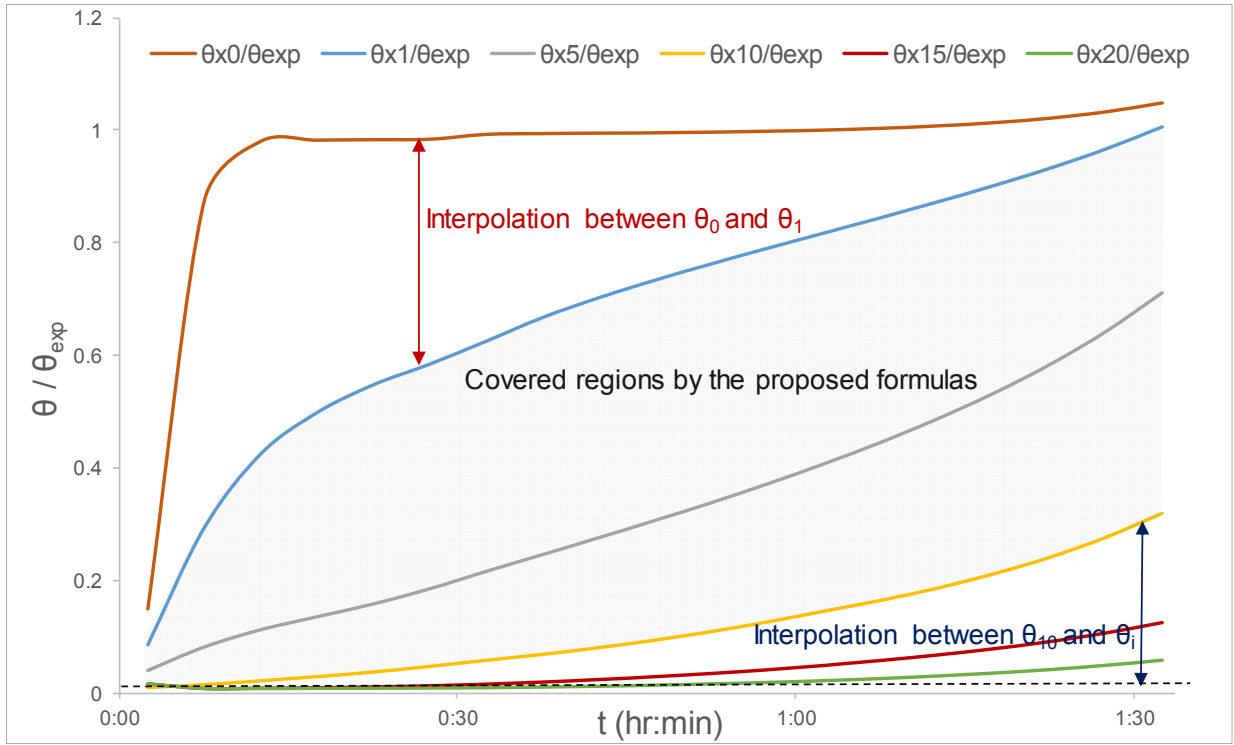


Figure 10: The covered regions to estimate α_1 by the proposed formula and regions where temperatures have to be interpolated

2.2 Determination of Functions for Heat Transfer Coefficient

The heat transfer coefficient, α_1 , from Eq. 6 should represent the course of change in θ_x / θ_{exp} for the first 10 cm of the cross-section to the exposed side. As explained in section 2.1, the estimation of α_1 for $x = 0$ is simple as temperature is only a function of t . Therefore, for $x = 0$:

$$\alpha_1 = 4.755 t \quad t \leq 0.20833 \text{ hr (12.5 min)} \quad (8)$$

$$\alpha_1 = 0.99 \quad 0.20833 < t \leq 1.5 \text{ hr} \quad (9)$$

For $1 \text{ cm} \leq x \leq 10 \text{ cm}$, α_1 has to represent a function with two independent variables matching the θ_x / θ_{exp} curves in Fig. 11 at $x = 1, 5$ and 10 cm . To define a function which represents the curve behaviour of θ_x / θ_{exp} at $x = 1$ and 5 cm , different base functions were investigated. Using the nonlinear generalised reduced gradient solution (GRG), the base functions that can estimate the form of two graphs were evaluated. The criteria are minimising the square difference values, R^2 , between the temperature values from the estimated function with $\theta(x = 1 \text{ and } 5 \text{ cm}) / \theta_{exp}$. Using this, α_1 has the primary format of:

$$\alpha_1 = A_1 t^{(mx^n)} + A_2 x \left(\frac{0}{t}\right) \quad (10)$$

where $A_1 t^{(mx^n)}$ represents more dominantly the mode of exponential increase and $\frac{A_2}{x} x \left(\frac{0}{t}\right)$ takes account of concave downward parabolic mode. The above equation is modified to gain the best approximation and the lowest difference between the estimated temperatures from the function to the curve of $\theta(x = 10 \text{ cm}) / \theta_{exp}$:

$$\alpha_1 = A_1 t^{(mx^n)} + \frac{A_2}{x} x \left(\frac{0}{t}\right) - A_3 t x \left(\frac{p}{x}\right) \quad (11)$$

where:

$$A_1 = 0.27, A_2 = 0.006, A_3 = 0.85, m = 2.4, n = 0.17, o = 0.02, p = 0.0064$$

The modification to term $\frac{A_2}{x} x^{(\frac{o}{t})}$ and initiation of $A_3 t x^{(\frac{p}{x})}$ are made to the primary anticipated function to estimate shape of curves more accurately and to enable the correct transition between curves $\theta(x = 5 \text{ cm}) / \theta_{exp}$ and $\theta(x = 10 \text{ cm}) / \theta_{exp}$. The estimated function can be written as the sum of three functions:

$$\alpha_I = f_{sum}(x, t) = f_1(x, t) + f_2(x, t) + f_3(x, t) = A_1 t^{(mx^n)} + \frac{A_2}{x} x^{(\frac{o}{t})} - A_3 t x^{(\frac{p}{x})} \quad (12)$$

Fig. 11 shows how each term in Eq. 12 takes apart in estimation of α_I for $\theta(x = 1, 5 \text{ and } 10 \text{ cm}) / \theta_{exp}$.

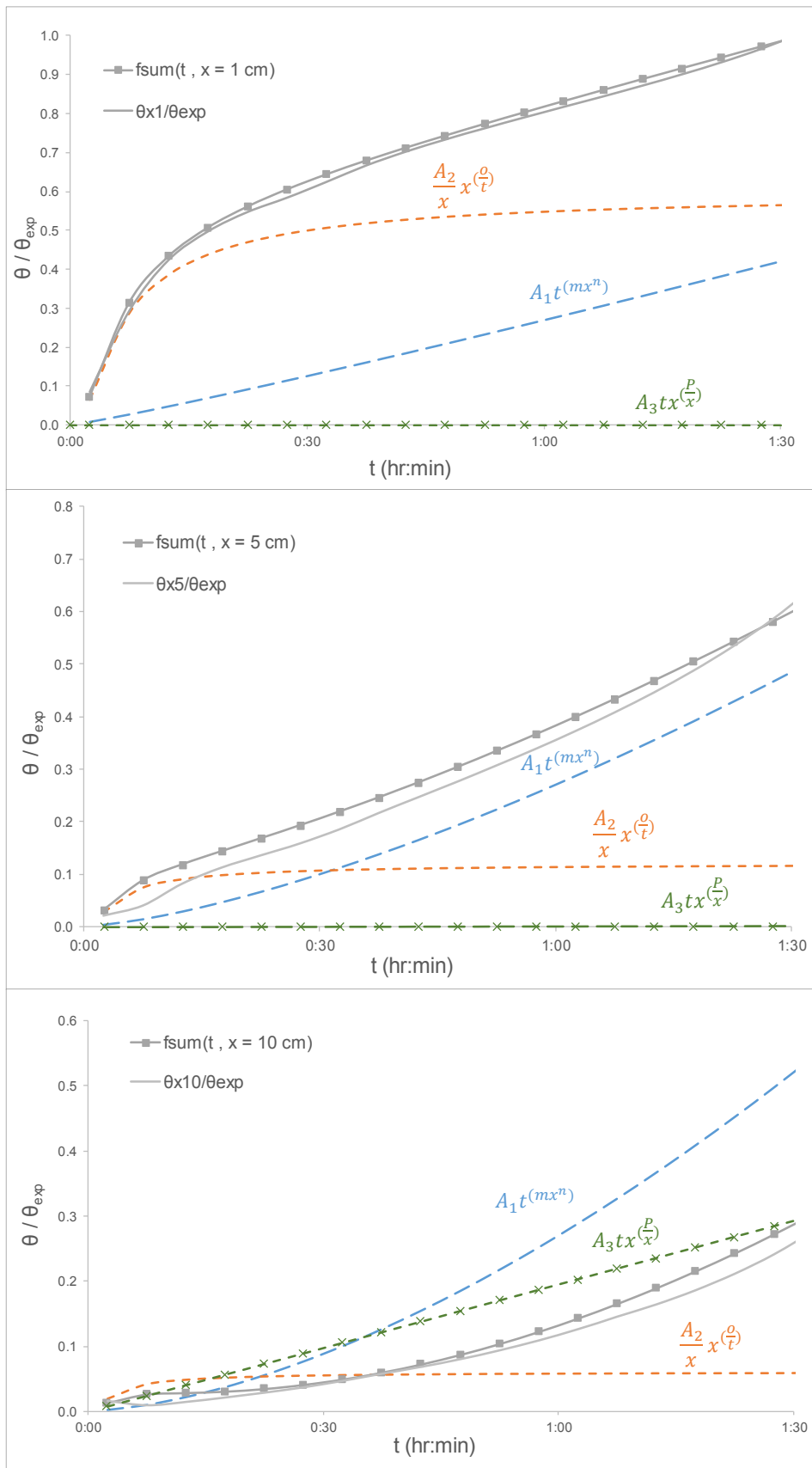


Figure 11: Proportion of each function in Eq. 12 in the main solution

2.3 Determination of Functions for Cross-section Coefficient

Having α_1 defined in the previous section, α_2 now can be determined by relating $\theta(x = 1, 5 \text{ and } 10 \text{ cm}) / \theta_{exp}$ curves of the cross-section with the width of normal surface to the heat transfer direction, $w = 60 \text{ cm}$, with the same group of curves for $w = 80, 100, 120 \text{ and } 140 \text{ cm}$. Thus, α_2 is the ratio between $\theta(w = 80, 100, 120 \text{ and } 140 \text{ cm}, x = 1, 5, 10 \text{ cm}) / \theta_{exp}$ to $\theta(w = 60 \text{ cm}, x = 1, 5, 10 \text{ cm}) / \theta_{exp}$. Since α_2 decreases from factor 1 (for $w = 60 \text{ cm}$) with the increase in w , the following solution of the nonlinear regression gives the best approximation:

$$w = 60 \text{ cm}, \alpha_2 = 1 \quad (13)$$

$$w = 80 \text{ cm}, \alpha_2 = \left(\frac{0.36}{x^{0.16}} \right) \quad (14)$$

$$w = 100 \text{ cm}, \alpha_2 = \left(\frac{0.375}{x^{0.157}} - 2x \right) \quad (15)$$

$$w = 120 \text{ cm}, \alpha_2 = \left(\frac{0.34}{x^{0.176}} - 1.9x \right) \quad (16)$$

$$w = 140 \text{ cm}, \alpha_2 = \left(\frac{0.225}{x^{0.238}} - 1.41x \right) \quad (17)$$

The estimated temperature values at $x = 1, 5 \text{ and } 10 \text{ cm}$ for different w by using α_2 are compared, as shown in Fig. 12, with temperature values from FE's temperature output. The estimated values show a very good agreement with the result from FE output. However, there is a slight increasing deviation for the first 30 minutes with the increase of w between the estimated values at $x = 1 \text{ cm}$ layer ($f_{sum}(t, x = 1 \text{ cm})$) and the outputs from FE ($\theta_{x1} / \theta_{exp}$). Since the estimated temperature values are higher, the estimation in this region gives a slightly conservative result.

2.4 Evaluation of Temperature Values in Tunnel Members

Having α_1 and α_2 estimated in the previous sections, the general expression may be reformulated and written as:

$$\theta(x, t) = \alpha_1 \alpha_2 \theta_{exp}(t) \quad (18)$$

where

$$\theta_{exp}(t) = 14400 t \quad \text{for} \quad 0 \leq t \leq 0.08\bar{3} \text{ hr} \quad (19)$$

$$\theta_{exp}(t) = 1200^\circ\text{C} \quad \text{for} \quad 0.08\bar{3} < t \leq 0.5 \text{ hr} \quad (20)$$

$$\theta_{exp}(t) = 1200 - 654.545 (t - 0.5) \quad \text{for} \quad 0.5 < t \leq 1.5 \text{ hr} \quad (21)$$

2.5 Summary

In first part of this chapter (section 2.1), six assumptions to extract temperature difference components $\Delta\theta_N$ and $\Delta\theta_M$ from a nonlinear temperature distribution for a member of tunnel exposed to ZTV-ING curve were explained. These components can be used as equivalent simplified thermal actions for linear elastic design to estimate stresses and bending states of a tunnel structure for fire situation.

Further, in sections 2.2 to 2.4, formulas were developed to estimate the absolute temperature values at any point from 0 to 10 cm from the fire exposed side for cut-and-cover tunnel cross-sections with the thicknesses $d \geq 60 \text{ cm}$ at any desired time up to 90 minutes. Fire action is the known ZTV-ING exposure curve θ_{exp} . The temperature values at the layers with $10 < x \leq 35 \text{ cm}$, can be simply calculated by interpolation between

the estimated temperature values at $x = 10$ cm, θ_{10} , and the initial temperature, θ_i . In addition, it can be also assumed that for $x > 35$ cm the cross-section is unaffected and has the initial temperature. Further, the estimation is applicable for normal-strength concretes with moisture content of 3%. The formulas are based on results of one-dimensional thermal analyses for the elements with 60, 80, 100, 120 and 140 cm widths of orthogonal surface to the fire exposure side.

A general formulation for estimating temperature at a distance x from the exposed side can be written as:

$$\theta(x, t) = \alpha_1 \alpha_2 \theta_{exp}(t) \quad (18)$$

The heat transfer coefficient α_1 is a function of x and t :

$$\alpha_1 = 0.27 t^{(2.4 x^{0.17})} + \frac{0.006}{x} x^{(\frac{0.02}{t})} - 0.85 t x^{(0.0064)} \quad (12)$$

The cross-section coefficient α_2 is only function of x and can be written for different cross-section widths:

$$w = 60 \text{ cm}, \alpha_2 = 1 \quad (13)$$

$$w = 80 \text{ cm}, \alpha_2 = \left(\frac{0.36}{x^{0.16}} \right) \quad (14)$$

$$w = 100 \text{ cm}, \alpha_2 = \left(\frac{0.375}{x^{0.157}} - 2x \right) \quad (15)$$

$$w = 120 \text{ cm}, \alpha_2 = \left(\frac{0.34}{x^{0.176}} - 1.9x \right) \quad (16)$$

$$w = 140 \text{ cm}, \alpha_2 = \left(\frac{0.225}{x^{0.238}} - 1.41x \right) \quad (17)$$

$\theta_{exp}(t)$ is the gas temperature of ZTV-ING fire exposure curve and can be expressed as:

$$\theta_{exp}(t) = 14400 t \quad \text{for} \quad 0 \leq t \leq 0.08\bar{3} \text{ hr} \quad (19)$$

$$\theta_{exp}(t) = 1200^\circ\text{C} \quad \text{for} \quad 0.08\bar{3} < t \leq 0.5 \text{ hr} \quad (20)$$

$$\theta_{exp}(t) = 1200 - 654.545 (t - 0.5) \quad \text{for} \quad 0.5 < t \leq 1.5 \text{ hr} \quad (21)$$

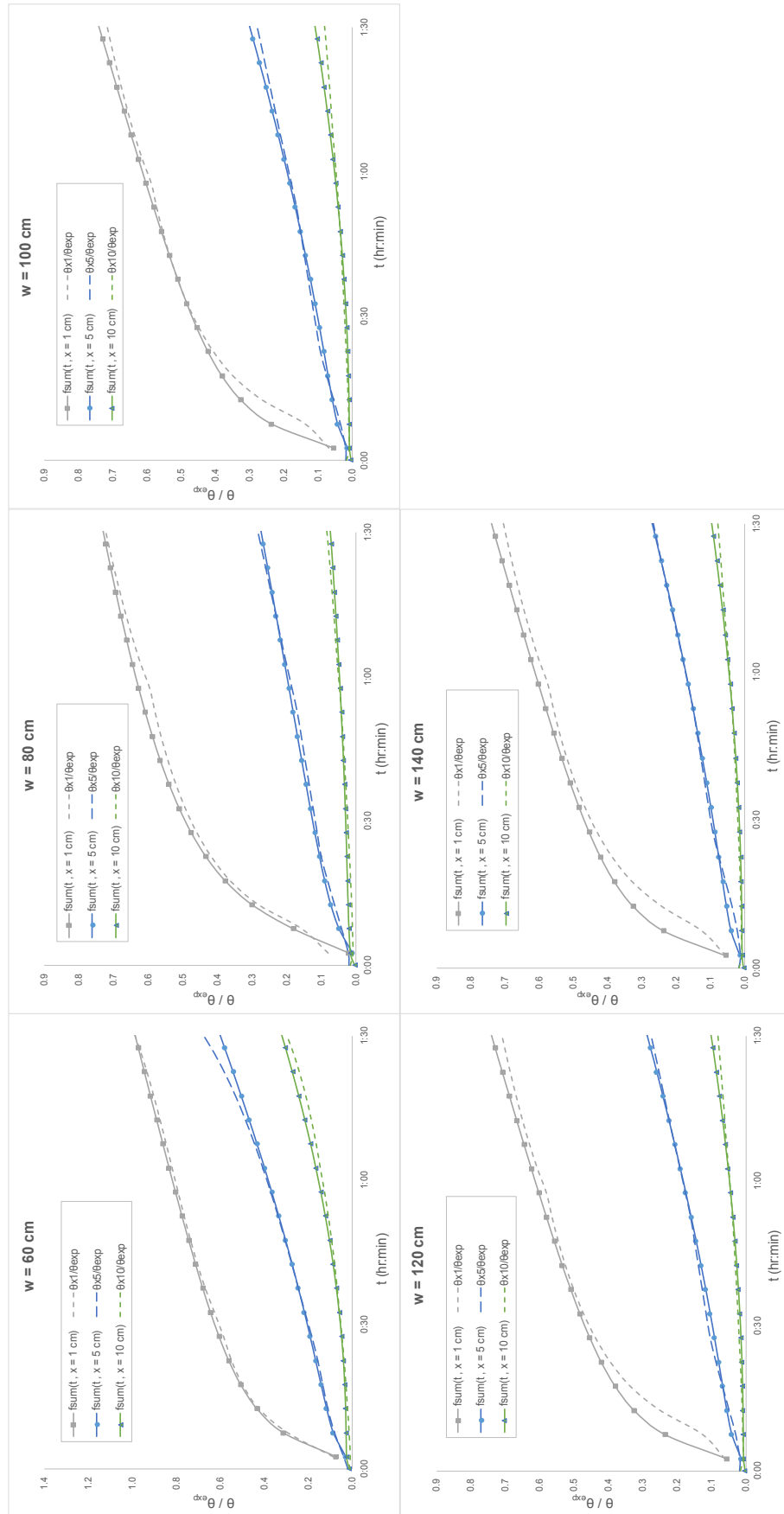


Figure 12: Comparison of each layer's temperature factors with the results of thermal analysis for elements with different width normal to the heat transfer direction

3 Concrete Material Model at Elevated Temperatures

Material behaviour of concrete at elevated temperature is to a very high extent parameter sensitive and understanding its complexity needs sufficient knowledge in the various microscopic areas such as:

- Water migration / pressure during the temperature rise within concrete, which plays an important role for the steady-state tests up to a constant stabilized temperature of 450°C where the concrete is almost dried out and for transient tests during the heating procedure. This further is the cause of spalling phenomena;
- Material chemical transformation which normally occurs at high temperatures for concrete components;
- Comprehension of the phenomenon of transient creep;
- Understanding the questions why and how different test parameters affect strain components and compressive strength of concrete at elevated temperatures.

A good knowledge of the mentioned parameters may result in a realistic estimation of constitutive stress-strain relationship of concrete under fire. This is, normally, carried out by using an **explicit** or **implicit** material model.

3.1 Explicit and Implicit Models

To write a constitutive stress-strain relationship at elevated temperatures, two types of models in general should be assumed. These are models where the stress can be evaluated from the mechanical-induced strains at high temperatures. These strains can be treated explicitly or implicitly in a material model.

a) Explicit models, in which instantaneous-stress-related strain for drying specimens, transient-creep strain, steady-state creep for non-drying specimens, and thermal strain are represented individually. The older models proposed by Anderberg-Thelandersson (Anderberg, 1976), Khoury-Terro (Terro, 1998) and the more recent proposed model (Schneider, et al., 2008) are some examples of explicit models (Bamonte, et al., 2010).

The basic assumption in the mentioned models is that the different strain components from steady and transient tests should be taken into account and superposed (all the strain components are explained in Glossary of this work). As a result, the total strain in concrete is the sum of the following four components (Bamonte, et al., 2010):

$$\varepsilon_{tot} = \varepsilon_{tr,th}^{\theta,0,d} + \varepsilon_{tot}^{\theta_{max},\sigma',\sigma,\dot{\sigma},d} + (\varepsilon_{cr(t_1-t_0)}^{\theta_{max},\sigma,nd}) + \varepsilon_{tr,cr}^{\theta,\sigma,d} \quad (22)$$

- **Thermal strain**, $\varepsilon_{tr,th}^{\theta,0,d}$, is total strain considered by measuring the unrestrained (free) thermal elongation of concrete specimens;
- **Instantaneous-stress-related strain for drying specimens**, $\varepsilon_{tot}^{\theta_{max},\sigma',\sigma,\dot{\sigma},d}$, with σ' as load history level (stress during heating for steady-state tests), σ stress or stress level after reaching a uniformly-distributed-maximum-desired temperature in the specimen, $\dot{\sigma}$ stress-rate controlled test and d referring to drying specimen;
- **Transient creep**, $\varepsilon_{tr,cr}^{\theta,\sigma,d}$, the irreversible time-and-stress-dependent transient strain (σ remains constant during the heating) evaluated from the transient tests;

- **Steady-state creep for non-drying specimens**, $\varepsilon_{cr(t_1-t_0)}^{\theta_{max},\sigma,nd}$, is the strain component where σ remains constant after reaching uniformly-distributed-maximum-desired temperature in the specimen.

The instantaneous-stress-related strain $\varepsilon_{tot}^{\theta_{max},\sigma',\sigma,\dot{\sigma},d}$ composes of two components:

$$\varepsilon_{tot}^{\theta_{max},\sigma',\sigma,\dot{\sigma},d} = \varepsilon_{el}^{\theta_{max},\sigma',\sigma,\dot{\sigma},d} + \varepsilon_{pl}^{\theta_{max},\sigma',\sigma,\dot{\sigma},d} \quad (23)$$

where $\varepsilon_{el}^{\theta_{max},\sigma',\sigma,\dot{\sigma},d}$ is the elastic strain and $\varepsilon_{pl}^{\theta_{max},\sigma',\sigma,\dot{\sigma},d}$ stands for plastic strain.

Further, the total transient strain $\varepsilon_{tot,tr,th}^{\theta,0,d}$ for a drying concrete under no stress normally consists of two components:

$$\varepsilon_{tot,tr,th}^{\theta,0,d} = \varepsilon_{tr,th}^{\theta,0,d} + \varepsilon_{tr,sh}^{\theta,0,d} \quad (24)$$

where $\varepsilon_{tot,tr,th}^{\theta,0,d}$ is the total thermal strain of drying concrete. $\varepsilon_{tr,th}^{\theta,0,d}$ and $\varepsilon_{tr,sh}^{\theta,0,d}$ are thermal and shrinkage strains respectively which are commonly not separable.

In practice, the term thermal strain is used for total thermal strain of concrete. The total strain can be assumed by all its subcomponents as:

$$\varepsilon_{tot} = \varepsilon_{tr,th}^{\theta,0,d} + \varepsilon_{tr,sh}^{\theta,0,d} + \varepsilon_{el}^{\theta_{max},\sigma',\sigma,\dot{\sigma},d} + \varepsilon_{pl}^{\theta_{max},\sigma',\sigma,\dot{\sigma},d} + \varepsilon_{tr,cr}^{\theta,\sigma,d} + \varepsilon_{cr(t_1-t_0)}^{\theta_{max},\sigma,nd} \quad (25)$$

b) Implicit models, which accumulate (lump) all the strain components except for thermal strain into a single component which is called mechanical strain, ε_m . EN 1992-1-2:2004's fire design method belongs to this group.

The EN 1992-1-2's model is simple and relatively reliable under ISO fire condition. The transient creep is considered implicitly in the model and treated as reversible (at a given temperature) as the elastic modulus is considered equal to the initial slope of the constitutive curve in terms of (ε_m ; σ) rather than ($\varepsilon_{tot}^{\theta_{max},\sigma',\sigma,\dot{\sigma},d}$; σ). The implicit EN 1992-1-2's model has shown a good accuracy in different occasions but the structural behaviour during cooling is not as accurate as heating phase due to its inherent limitations according to (Gernay, et al., 2010) and (Gernay, et al., 2011).

$$\varepsilon_{tot} = \varepsilon_{tot,tr,th}^{\theta,0,d} + \varepsilon_m \quad (26)$$

$$\varepsilon_m = \varepsilon_{el}^{\theta_{max},\sigma',\sigma,\dot{\sigma},d} + \varepsilon_{pl}^{\theta_{max},\sigma',\sigma,\dot{\sigma},d} + \varepsilon_{tr,cr}^{\theta,\sigma,d} + (\varepsilon_{cr(t_1-t_0)}^{\theta_{max},\sigma,nd}) \quad (27)$$

EN 1992-1-2 stress strain model can be interpreted as:

$$\frac{\sigma}{f_c^{\theta_{max}}} = \frac{3\varepsilon_m^{implicit}}{\varepsilon_{c1}^{\theta_{max}} \left(2 + \left(\frac{\varepsilon_m^{implicit}}{\varepsilon_{c1}^{\theta_{max}}} \right)^3 \right)} \quad (28)$$

where $\varepsilon_{c1}^{\theta_{max}}$ is strain at peak stress at uniformly-distributed-maximum-desired temperature, θ_{max} , and ε_m accumulates the transient creep component. Further, EN 1992-1-2 proposes:

$$\frac{E_{EC2}^{implicit}(\theta)}{f_c^{\theta_{max}}} = \frac{3}{2\varepsilon_{c1,EC2}^{\theta_{max}}} \quad (29)$$

$f_c^{\theta_{max}}$ is the compressive strength at θ_{max} .

3.2 Strains and Modulus of Elasticity from Steady-state Tests

To understand both implicit and explicit concrete material models at elevated temperatures, different strain components from steady-state tests are explained in this chapter. Different strain components from steady-tests, explained previously, are explained here explicitly.

3.2.1 Instantaneous-stress-related Strain

The instantaneous-stress-related strain $\varepsilon_{tot}^{\theta_{max}, \sigma', \sigma, \dot{\sigma}, d}$ is a function of stress history, stress, and temperature. The shape of stress-strain curve is characterized by the value of peak-stress strain $\varepsilon_{c1}^{\theta_{max}}$ and the initial value of modulus of elasticity $E_{ci}^{\theta_{max}}$ (Youssef, et al., 2007).

Strain at Peak Stress at Elevated Temperatures

There are a number of models for both cases of concrete with and without initial stress (σ') applied during heating. Distinguish should be made between two types of models:

- Implicit models like EN 1992-1-2's model having the transient strain incorporated in the stress-strain model;
- Explicit models do not include transient strain in the stress-strain diagram. Most of models are proposed to calculate the strain at peak stress, $\varepsilon_{c1}^{\theta_{max}}$, are only function of temperature (or function of both strain at peak stress at the ambient temperature, ε_{c1} , and temperature, θ). Some of these models are:

Lie's model (Lie, 1992):

$$\varepsilon_{c1}^{\theta_{max}} = 0.0025 + (6.0 \cdot \theta + 0.04 \cdot \theta^2) \times 10^{-6} \quad (30)$$

Khennane and Baker's model (Khennane, et al., 1993). For the concrete without initial stress during heating:

$$\varepsilon_{c1}^{\theta_{max}} = 0.003 \quad \text{for } 20 \leq \theta \leq 200^\circ\text{C} \quad (31)$$

$$\varepsilon_{c1}^{\theta_{max}} = 0.00001156 \cdot \theta + 0.000686 \leq 0.0082 \quad \text{for } \theta \geq 200^\circ\text{C} \quad (32)$$

Anderberg and Thelandersson's model (Anderberg, et al., 1976):

$$\varepsilon_{c1}^{\theta_{max}} = 0.00000167 \cdot \theta + 0.002666 \geq 0.003 \quad \text{for } \theta \leq 800^\circ\text{C} \quad (33)$$

Bazant and Chern's model (Bazant, et al., 1987):

$$\varepsilon_{c1}^{\theta_{max}} = 0.0000064 \cdot \theta + 0.00216 \quad \text{for } 0 \leq \theta \leq 600^\circ\text{C} \quad (34)$$

$$\varepsilon_{c1}^{\theta_{max}} = 0.000015 \cdot \theta - 0.003 \quad \text{for } 600 \leq \theta \leq 650^\circ\text{C} \quad (35)$$

For the concrete with initial stress, (Khennane, et al., 1993) has also proposed a model based on test results of (Anderberg, et al., 1976) which might give a lower boundary for the $\varepsilon_{c1}^{\theta_{max}}$ values.

The EN 1992-1-2's stress-strain model composes of increasing strain values at peak stresses, $\varepsilon_{cl}^{\theta_{max}}$, up to 600°C (see Fig. 13). Beyond this temperature, $\varepsilon_{cl}^{\theta_{max}}$ remains constant ($\varepsilon_{cl}^{\theta_{max}} = 0.025$). The strain values at peak stresses from different test results and models are illustrated in Fig. 14. Lie's model is in a good agreement with the EN 1992-1-2's model (lumped model including transient strain). Khennane and Baker, and Bazant and Cherns' models evaluate the strains at peak stresses for their test results as shown in Fig. 14. There is a large difference between the values of $\varepsilon_{cl}^{\theta_{max}}$ from EN 1992-1-2's and Lies' models compared with the test results and other models. This is due to the existence of transient strain accumulated in the EN 1992-1-2's model. The maximum transient creep value which might occur at stress level of $\alpha = 0.5$ at about 600°C being approximately is equal to 0.01 that justifies the differences between the stress-strain values in Fig. 14. Further, the elastic strain values are relatively small compared to transient strains.

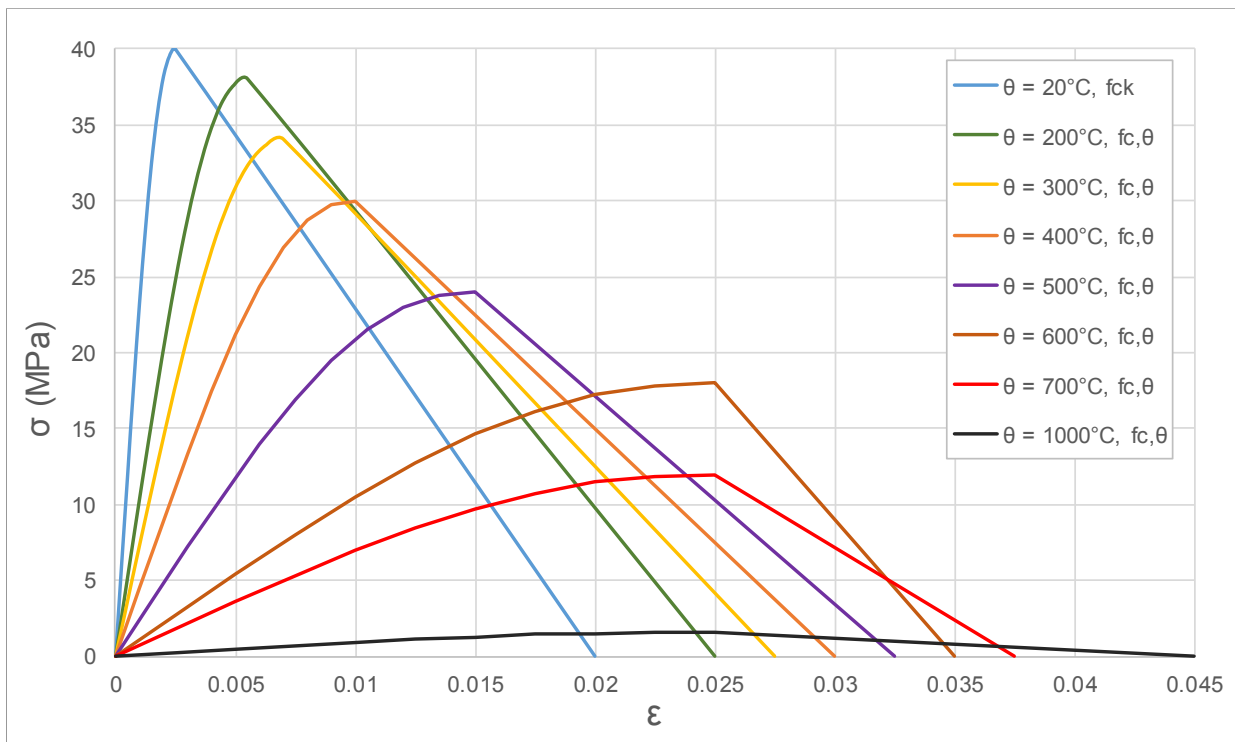


Figure 13: Stress-strain diagrams of concrete at elevated temperatures according to EN 1992-1-2 including the transient creep component within the model

Initial Modulus of Elasticity at Elevated Temperatures

The modulus of elasticity is influenced by the same factors that affect its compressive strength (Youssef, et al., 2007). Most of proposed models to calculate $E_{ci}^{\theta_{max}}$ are function of initial modulus of elasticity at ambient temperature (E_{ci}) and θ_{max} .

The minimum number of tests needed for estimating modulus of elasticity $E^{\theta_{max}}$ or $E_{res}^{\theta_{max}}$ is equal or more than two for each of combination of test parameters. These should be carried out under cyclic tests with $E^{\theta_{max}}$ evaluated at the third cycle (RILEM, 2007).

Further, Khennane and Baker's model for concrete not-pre-loaded (Khennane, et al., 1993) is expressed as:

$$E_{ci}^{\theta_{max}} = (-0.001282 \cdot \theta_{max} + 1.025641) E_{ci} \quad \text{for } 20 \leq \theta_{max} \leq 800^{\circ}\text{C} \quad (36)$$

And for pre-loaded concrete as:

$$E_{ci}^{\theta_{max}} = (-0.000634 \cdot \theta_{max} + 1.012673) \cdot E_{ci} \quad \text{for } 20 \leq \theta_{max} \leq 525^{\circ}\text{C} \quad (37)$$

$$E_{ci}^{\theta_{max}} = (-0.002036 \cdot \theta_{max} + 1.749091) \cdot E_{ci} \quad \text{for } 525 \leq \theta_{max} \leq 800^{\circ}\text{C} \quad (38)$$

By comparing the ratios of $E_{ci}^{\theta_{max}} / E_{ci}$ from the proposed models with the corresponding values from EN 1992-1-2's model, as shown in Fig. 15, it is clear that the estimation of initial modulus of elasticity is according to EN 1992-1-2's model less than these models. This is due to the fact that in the proposed stress-strain curves of EN 1992-1-2, transient creep component is accumulated.

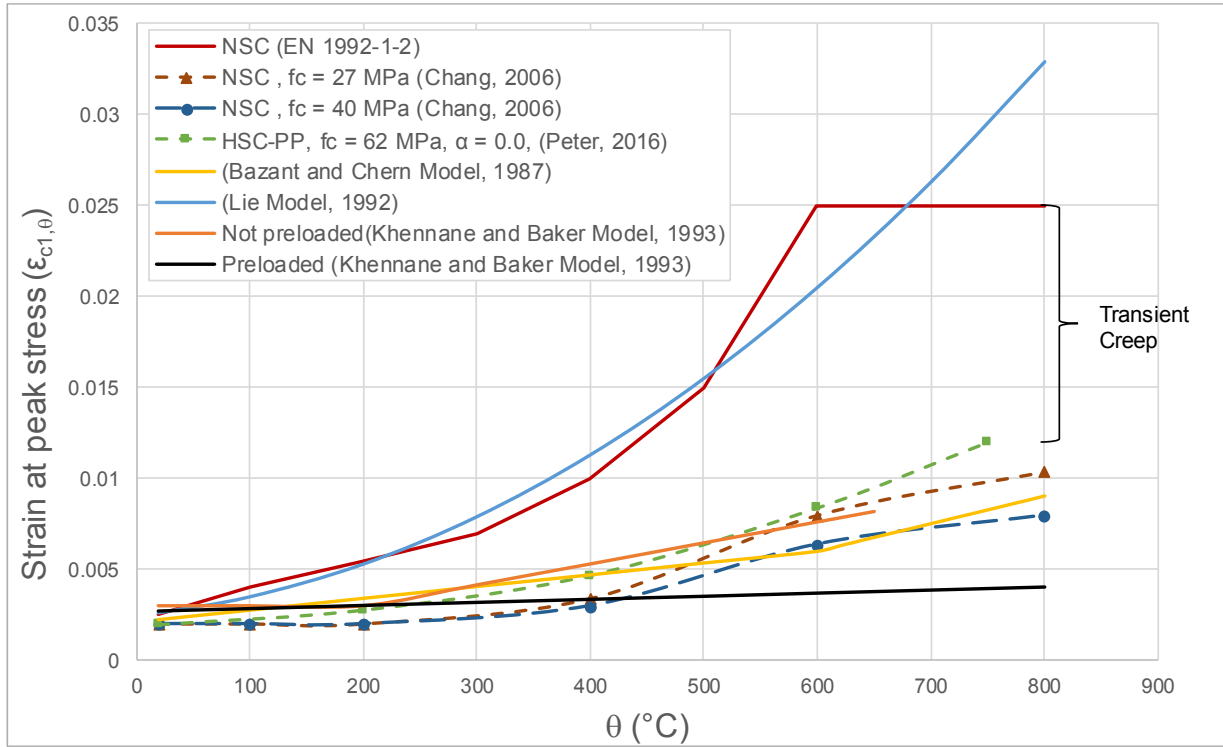


Figure 14: Strain values at peak stress for different models and test results

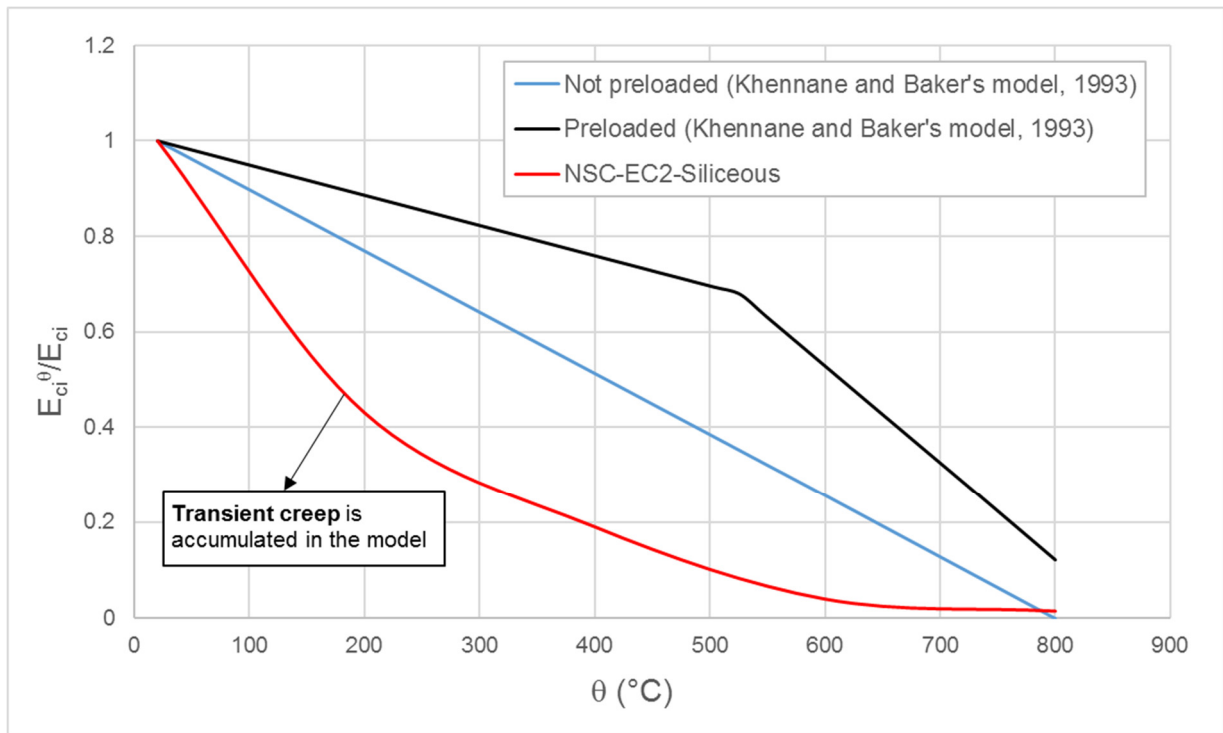


Figure 15: Relative initial modulus of elasticity at elevated temperatures due to different models

3.2.2 Steady-state Creep

Steady-state creep corresponds to creep in the steady-state tests after the both temperature and stress have reached a constant level. The steady-state creep strain $\varepsilon_{cr(t_1-t_0)}^{\theta_{max}, \sigma, nd}$ (here explained only as an example for non-drying specimen not-stressed during heating) occurs between t_0 and t_1 and corresponds to the creep induced after the whole cross-section has reached a uniformly-distributed-maximum-desired temperature, θ_{max} , under a constant load. After temperatures reached θ_{max} on the concrete specimen at $t_{\theta_{max}}$, θ_{max} is kept constant for a duration of less than 30 minutes up to t_0 . A constant level of loading then is applied at t_0 and being held for a long duration of time up to t_1 (for hours or days).

Creep of concrete at the uniform developed elevated temperatures is normally tested over a maximum period of 5 hours and is much larger than the concrete creep under ambient temperature. (Anderberg, et al., 1976) have developed a creep strain formula at elevated temperatures based on strain hardening principle as a function of stress level, time and ultimate stress at the elevated temperature:

$$\varepsilon_{cr(t_1-t_0)}^{\theta_{max}, \sigma, nd} = \beta_o \frac{\sigma}{\sigma_U^{(\theta)}} \left(\frac{t}{t_1}\right)^p e^{k_1(\theta-20)} \quad (39)$$

where $\beta_o = -0.53 \cdot 10^{-3}$, σ is stress, $\sigma_U^{(\theta)}$ ultimate stress at current temperature, t stands for time, $t_1 = 3$ hrs, $p = 0.5$, $k_1 = 3.04 \cdot 10^{-3} \text{ }^\circ\text{C}^{-1}$ and θ is temperature.

The values of creep strains at elevated temperatures based on Eq. 39 are plotted in Fig. 16 for $\theta = 400, 600$ and 800°C under stress levels $\alpha = 0.1, 0.3$ and 0.5 for duration of three hours. For the latter, siliceous concrete reduction factors for C30/37 based on EN 1992-1-2 are considered. The results show that the creep strain of concrete for temperatures up to 400°C remains, comparably, small for all load levels up to three hours. The steady-state creep does not represent behaviour of concrete in the fire situation. In case of fire situation, each layer of concrete cross-section is under load change. Further, temperature in reality does not reach a constant level over the cross-section of concrete and fire normally does not occur for a long duration of time.

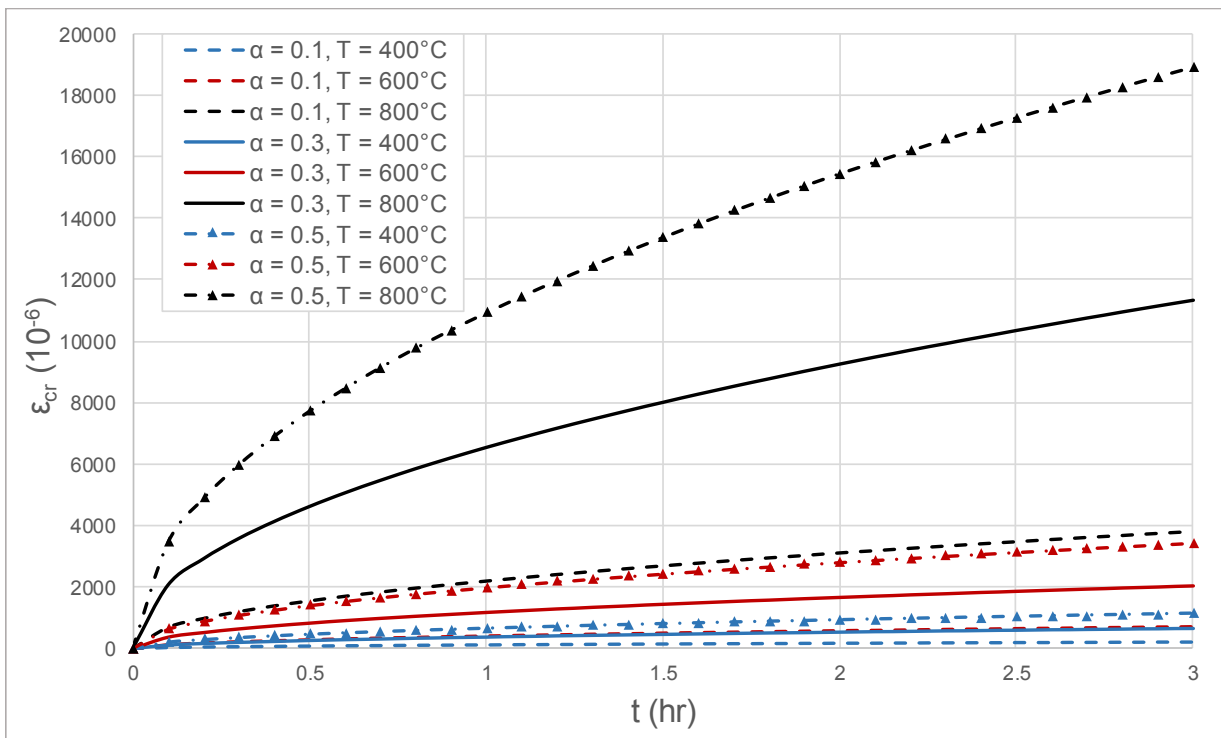


Figure 16: Creep strain at different constant temperatures and load levels based on Eq. 39

3.3 Strains from Transient Tests

3.3.1 Transient-creep Strain for Drying Specimen

Transient-creep strain $\varepsilon_{tr,cr}^{\theta,\sigma,d}$ is in most of existing models function of stress at rising temperature, strength of concrete at ambient temperature, thermal strain and temperature. There are number of surveys comparing the result of transient-creep strains for load levels approximately $\alpha = 0.1, 0.3$ and 0.5 . The higher the stress level, the higher the compressive strain (more clearly after 400°C). The magnitude of this component is a function of heating rate, concrete mix and the stress level. Transient creep can be formulated as:

$$\varepsilon_{tr,cr}^{\theta,\sigma,d} = \varepsilon_{tr,tot}^{\theta,\sigma,d} - \varepsilon_{tr,tot}^{\theta,0,d} - \varepsilon_{tot}^{\theta,max,\sigma',\sigma,\dot{\sigma},d} \quad (40)$$

Transient creep is a unique phenomenon of concrete and beyond 100°C is independent of time and is a function of temperature. Transient creep is much higher regardless of type of cement or aggregate than the elastic strain for the specimen with 20% stress level (Khoury, 2000). Further, heating rates between 0.5 and 5 K/min have small influence on the results of small-sized specimens with diameter less than 75-80 mm. Transient creep is also observed to increase with the heating rate more pronounced at higher load levels (Khoury, et al., 1985). In this regard, (Anderberg, et al., 1976) propose a formula for transient creep of concrete at elevated temperatures which has a linear relation with the ratio of applied stress σ to the concrete strength at ambient temperature σ_{u0} and is also function of temperature:

$$\varepsilon_{tr,cr}^{\theta,\sigma,d} = \frac{\sigma}{\sigma_{u0}} \cdot g(\theta) \quad (41)$$

where $g(\theta)$ is a function of temperature. Further, he inspected that $g(\theta)$ can be approximated proportional to ε_{th} data for temperatures up to 550°C :

$$\varepsilon_{tr,cr}^{\theta,\sigma,d} = k_{tr} \frac{\sigma}{\sigma_{u0}} \cdot \varepsilon_{tr,tot}^{\theta,0,d} \quad (42)$$

k_{tr} is a dimensionless constant. For his tests $k_{tr} = 2.35$ gives a good approximation up to 550°C .

The estimation of transient creep is of great importance as it gives a good impression of magnitude of each strain component in the model. Fig. 17 shows the values of thermal strains (based on EN 1992-1-2) and transient strains for different stress levels (based on Eq. 42) for C30/37 siliceous concrete. It is to be noted that the absolute value of transient creep increases with the increase of load level. Further, the elastic strain usually has a low contribution to the total strain. Therefore, the sum of transient creep and thermal strain might also give a first impression of total strain:

$$\varepsilon_{tr,cr}^{\theta,\sigma,d} + \varepsilon_{tr,tot}^{\theta,0,d} = \varepsilon_{tr,tot}^{\theta,\sigma,d} - \varepsilon_{tot}^{\theta,max,\sigma',\sigma,\dot{\sigma},d} \quad (43)$$

The values of $\varepsilon_{tr,cr}^{\theta,\sigma,d} + \varepsilon_{tr,tot}^{\theta,0,d}$ are illustrated in Fig. 18. These graphs give a rough estimation of subtraction of instantaneous-stress-related strain from total transient strain. The estimation of elastic strains at elevated temperatures is covered in section 3.4.3 for temperatures up to 600°C that lay between 0.2 and 0.3%. This is generally very small proportion of total transient strain. The latter suggests that elastic strain is a very minor part of the transient creep and total transient strain.

3.3.2 Mechanical-induced Strain at Elevated Temperatures

This is the sum of all mechanical-induced strain components from both transient and steady-state tests. The main contribution to the mechanical-induced strain at the elevated temperature (MISSET) is made by transient creep and drying creep and to a lesser extent by elastic strain.

$$MISSET = \varepsilon_m = \varepsilon_{tr,cr}^{\theta,\sigma,d} + \varepsilon_{tot}^{\theta_{max},\sigma',\sigma,\dot{\sigma},d} \quad (44)$$

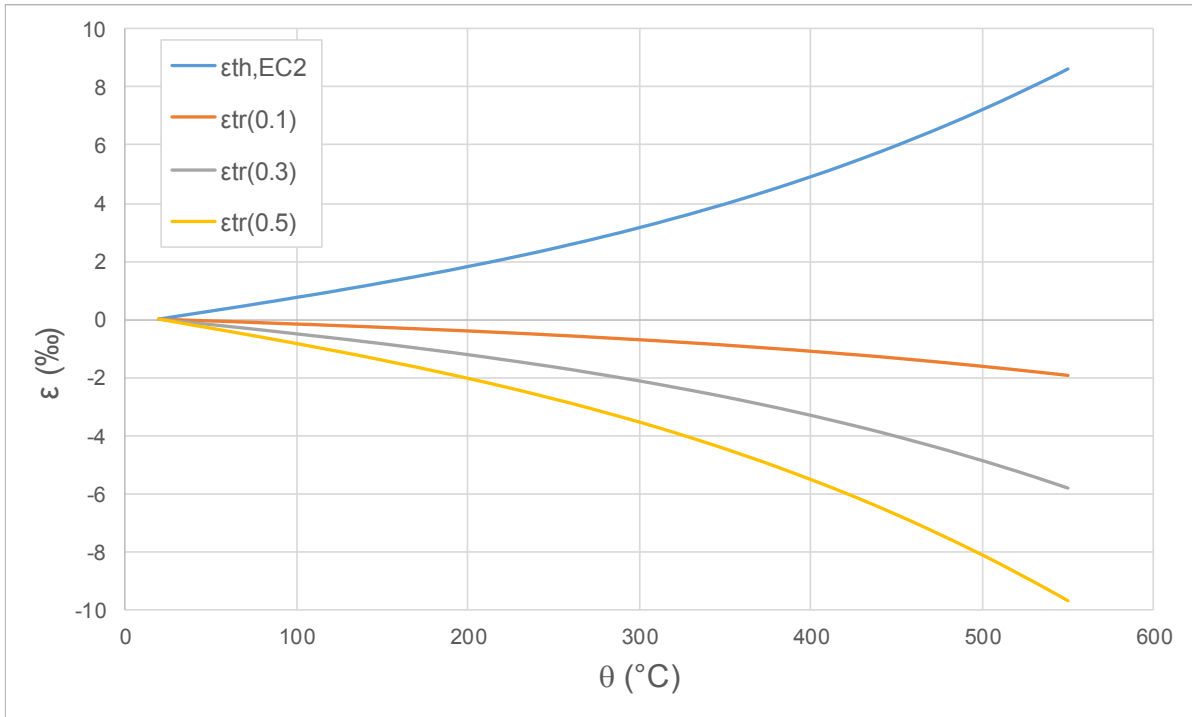


Figure 17: Estimation of transient creep based on Eq. 42 and $k = 2.35$ and thermal strain for siliceous concrete proposed in EN 1992-1-2 up to 550°C

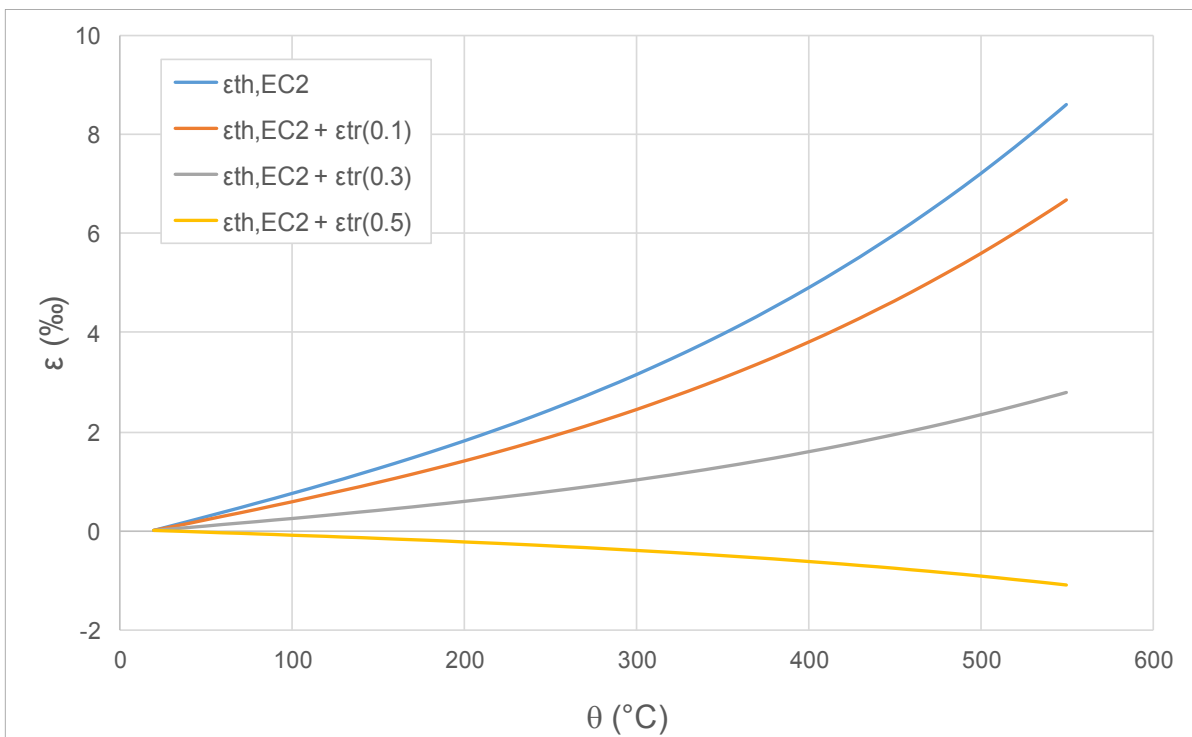


Figure 18: Estimation of transient creep + thermal strain for siliceous concrete

3.4 Strain Components and Influential Parameters

3.4.1 Thermal Strain

Thermal strain is a function of both temperature and time. It includes both shrinkage and thermal expansion caused by development of cracking. Thermal strain tests for $\alpha = 0$ are normally performed with a small pre-load of less than 1 MPa. The thermal strain is mainly affected by type of aggregates, moisture content and heating rate.

Influence of Aggregate Type

A great volume of concrete composes of aggregates (65-70%). Thermal strains vary considerably with respect to the thermal expansion of aggregates used in the mix. Figs. 19 and 20 show the thermal strains of concrete with different types of aggregates. It is to be noted that the large elongation of the concrete with gravel is caused by the expansive break-up of these aggregates that occurs above 350°C, whereas this is for the limestone (chemical change, breakdown around 650°C), basalt concrete above 550°C. The latter is partially caused by inversion of α - β of quartz (siliceous aggregates) being at 573°C. The lightweight concrete does not contain quartz. Further, Fig. 21 illustrates the thermal strain of moist and dried concrete with strain of basalt aggregates. It is to be noted that the basalt aggregate is shown as a lower boundary and the moist basalt concrete as the upper boundary. The differences between curves are due to thermal drying properties of specimens.

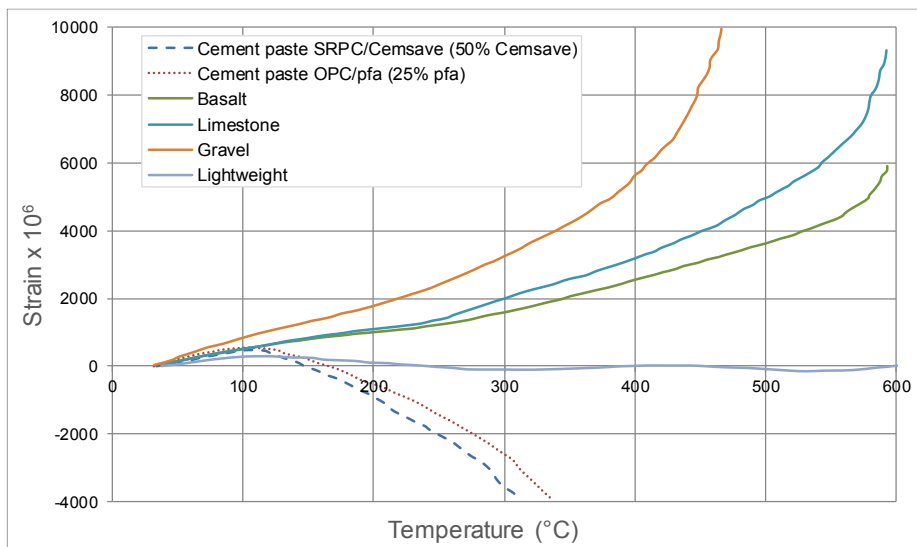


Figure 19: Thermal strain of five concrete groups with different aggregates and two cement pastes measured during heating from the initially moist condition at 1 K/min (digitalized and extracted from (Khoury, et al., 1985))

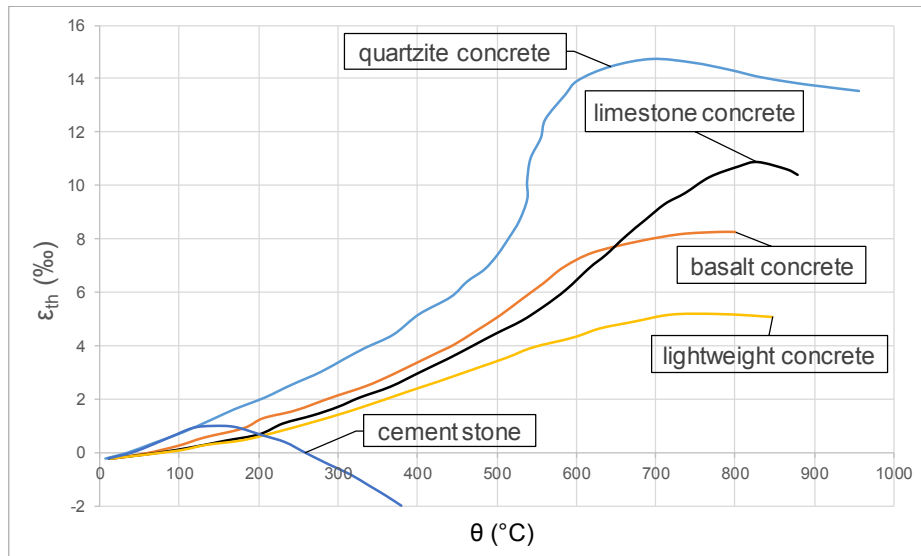


Figure 20: Thermal strain of concrete with different aggregate types (digitalized and extracted from (Schneider, 1988))

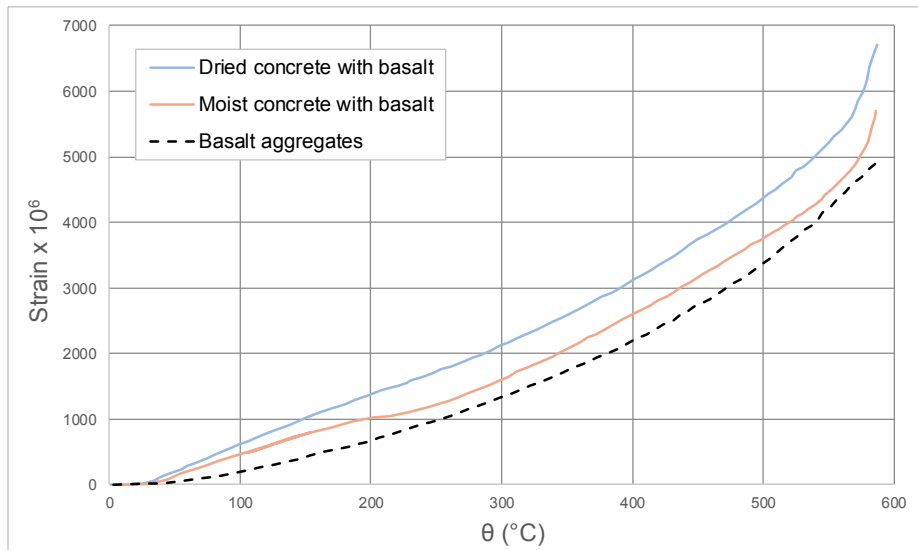


Figure 21: Thermal strain measured during first heating of basalt and concrete with basalt aggregates (digitalized and extracted from (Khoury, et al., 1985))

Influence of Moisture Content

Thermal strain of concrete is not only a nonlinear function of temperature but it is also dependent on the moisture content of specimen. Decrease in the amount of thermal strain for the moist concrete specimen (100% R.H. as cast) compared to both air-dry (65% R.H.) and oven-dry (105°C) specimens for temperatures between 150 and 220°C can be attributed to drying shrinkage in the moist concrete (see Fig. 22). For temperatures up to about 150°C, the maximum thermal strain is occurred by the air-dry specimens compared to both oven-dry and moist specimens. The difference between thermal strains of oven-dried and moist specimens above 150°C is owned to drying shrinkage. The thermal strain, can be considered as being independent of the moisture content as studied in (Khoury, et al., 1985) above 250°C under low heating rates (0.2 and 1 K/min). This is because concrete has been exposed for a longer time to the heating and therefore the whole specimen is almost dried out at this temperature.

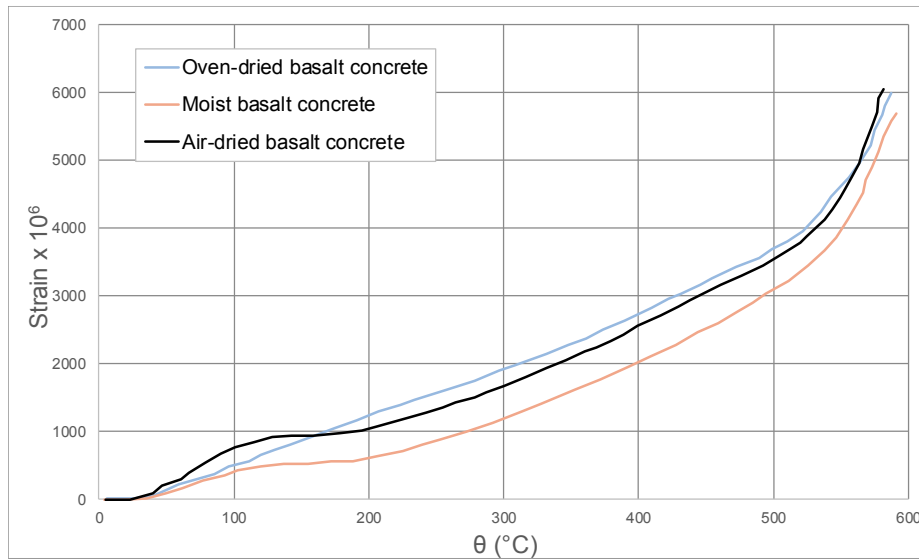


Figure 22: Influence of moisture content on the thermal strain of basalt concrete under heating rate $R = 0.2 \text{ K/min}$ (digitalized and extracted from (Khoury, et al., 1985))

Influence of Heating Rate

Heating rate has generally two effects on the thermal strain of concrete specimens at elevated temperatures:

- It might cause thermal incompatibilities or structural effects caused by temperature gradients. This can be minimized to a great extent by choosing a sufficient small diameter of specimens;
- Using lower heating rates, a concrete specimen is longer exposed to heating to reach a desired temperature compared to higher rates. This leads to higher rate of moisture loss for the low heating rates and thus a higher value of drying shrinkage.

For the very low heating rates of 0.2 to 1 K/min, one can define a temperature region up to which the difference between thermal strains of concrete specimens with two heating rates are time dependent. This limit is up to 200°C. For temperatures between 200°C and 500°C, the difference between thermal strains are almost constant and not influenced by heating rate (see Fig. 23). The reduction in thermal expansion of slowly heated specimen from 400°C and 500°C might be due to the disassociation of larger amount of Ca(OH)_2 in the concrete mixture that contributed to thermal shrinkage.

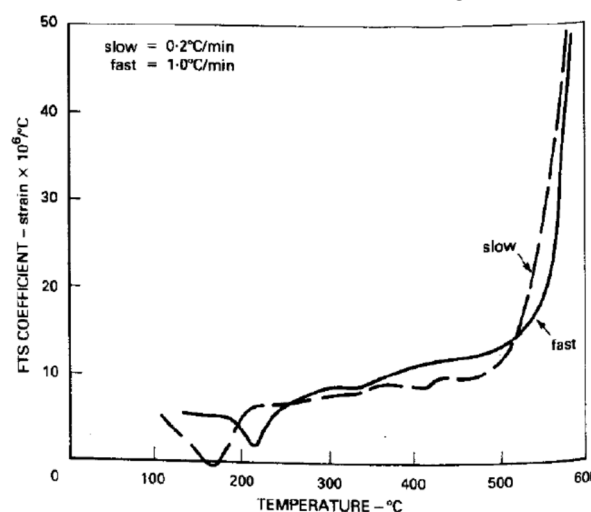


Figure 23: Influence of heating rate on the thermal strain coefficient of initially moist basalt concrete (Khoury, et al., 1985)

3.4.2 Mechanical-induced Strain at Elevated Temperatures

Influence of Type of Concrete and Initial Moisture Content

(Khoury, et al., 1985) used different aggregates (with the same aggregate content by volume), cement blends and applied load levels and despite the initial strength, the curves of mechanical-induced strains at elevated temperatures (MISSET) were almost the same except for gravel up to 450°C (see Figs. 24 and 25). This suggests that the thermal incompatibilities were not significant and the type of aggregates did not influence the MISSET. The cement type did not affect the result and it indicates that the MISSET originated in a common gel, below 450°C. These results suggest that the capacity of different types of concrete with the same strength to relax thermal stresses and structural effects were similar and high.

The increase in the slope of MISSET above 450°C can be related to the phase changes and reactions and dehydration of cement blends. The disassociation of Ca(OH)_2 may also contribute to MISSET at temperatures above 400°C.

In contrast to thermal strain, MISSET is not affected by the initial moisture content (65% air-dry or 100% R.H.) conditions.

3.4.3 Elastic Strain

There is a slight change in the amount of elastic strains measured by (Khoury, et al., 1985) for three concrete specimens (two concretes with basalt and one with limestone shown in Fig. 26) under $\alpha = 0.2$ load level (5.6 N/mm²) and tested at various temperatures. Thus, the changes in transient creep cannot be linked to changes in elastic strains.

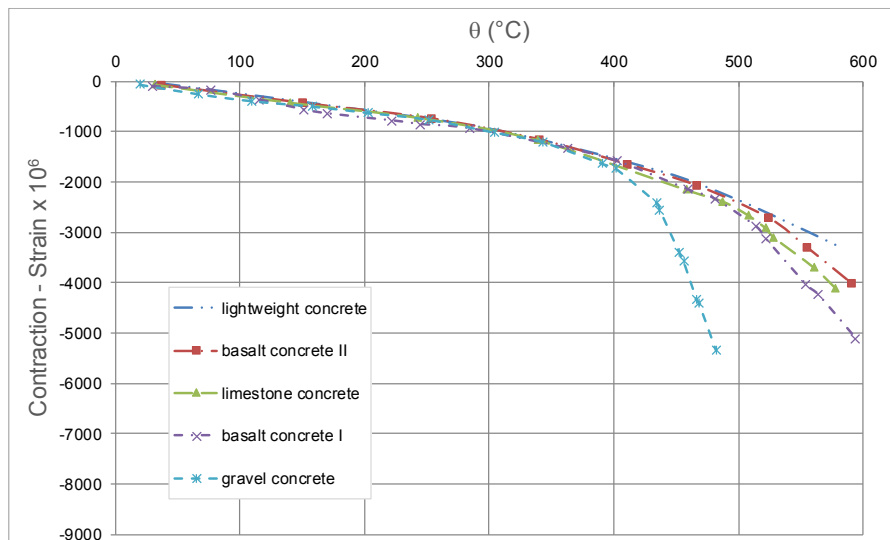


Figure 24: MISET of different air-dried concrete specimens under load level $\alpha = 0.1$ and heating rate $R = 1$ K/min (digitalized and extracted from (Khoury, et al., 1985))

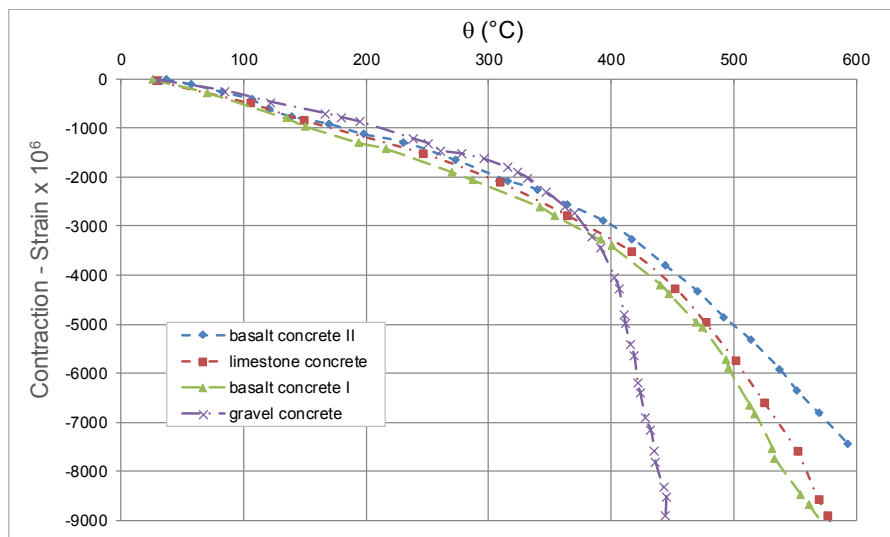


Figure 25: MISET of different air-dried concrete specimens under load level $\alpha = 0.2$ and heating rate $R = 0.2$ K/min (digitalized and extracted from (Khoury, et al., 1985))

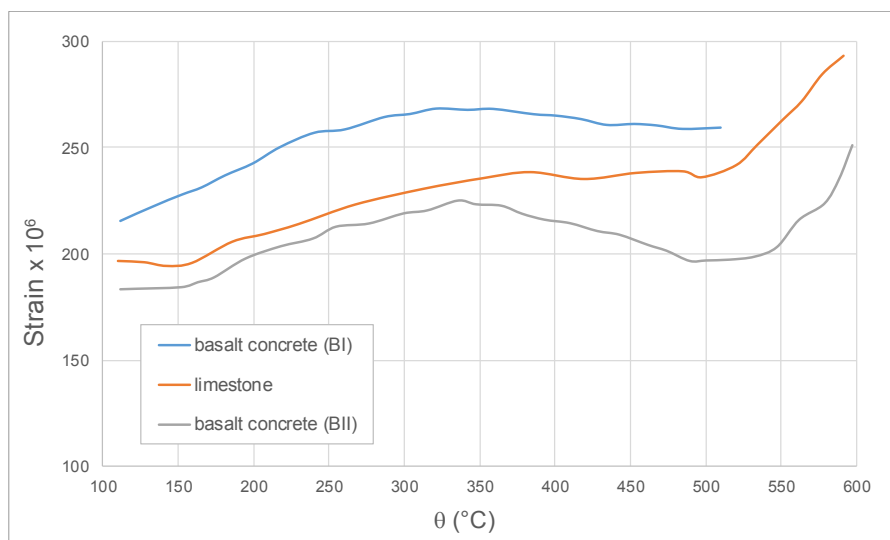


Figure 26: Elastic strains of concrete with three types of aggregates tested at various temperatures (digitalized and extracted from (Khoury, et al., 1985))

4 Compressive Strength and Residual Strength of Concrete

Compressive strength of concrete at the uniformly-distributed-maximum-desired temperature, θ_{max} , as well as compressive residual strength, $f_c^{\theta_{max}}$ and $f_{c,res}^{\theta_{max}}$, may be evaluated from specimens pre-loaded or not-pre-loaded during the heating.

4.1 Compressive Strength

Various results of tests on concrete properties of high-strength concrete (HSC) and normal-strength concrete (NSC) at elevated temperatures have indicated considerable difference in their behaviour. The main two differences are in:

- The relative strength loss within the temperature range of 100 to 400°C;
- The occurrence of spalling phenomena in a similar temperature range (Lam, et al., 2012).

(Li, et al., 2011) gathered 198 results of not-pre-loaded hot compressive strength tests and evaluated their average values as well as 607 results of not-pre-loaded residual compressive strength tests for different specimens (cube, prism and cylinder) for $f_c \leq 60$ MPa with different types of mix and aggregates including carbonate, calcareous, limestone, siliceous, granite and flint (see Fig. 27). The curve of average test results gathered by (Li, et al., 2011) shows higher values of relative compressive strength for all the values compared to EN 1992-1-2's curve for C55 and C60. For the case of HSC for C70 and C80, there is a higher reduction of concrete strength for temperatures up to 400°C.

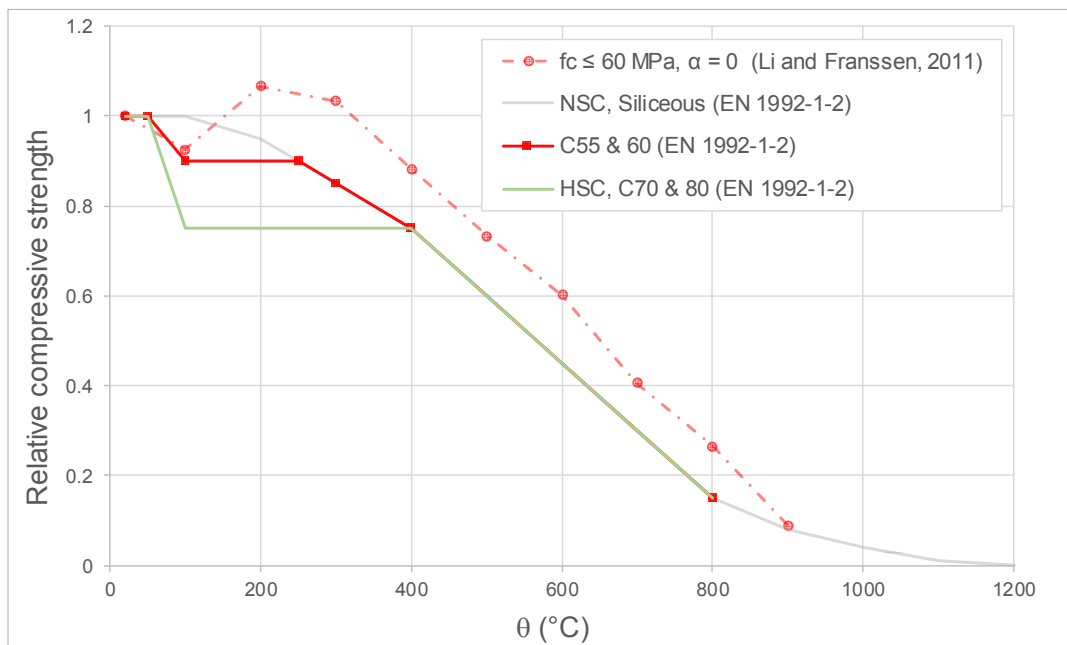


Figure 27: Relative compressive strength test results with proposed HSC and NSC curves acc. to EN 1992-1-2

4.2 Parameters Affecting the Compressive Strength

4.2.1 Effects of Load Level during Heating-up Stage on High and Normal-strength Concrete

There are many test results for concrete with siliceous and carbonate aggregates with and without initial stress during heating. The higher the level of applied initial compressive stress on the concrete specimen during heating, the lower the thermal effects and higher the compressive strength (Youssef, et al., 2007).

The beneficial effect of applied load $\alpha = 0.1$ or 0.3 during heating exposure temperatures of 250°C or 450°C are presented in (Naus, 2006) (referred to (Schneider, 1982)). The choice of load level considered prior to (and during) heating-up process for HSC cylinder specimens is dependent on the member in practice (Huisman, 2010). According to the latter author, the pre-load levels of $\alpha = 0.2$ and 0.4 correspond to the utilization factor (or load factor) of 50 and 100% of the design value of compressive strength of HSC given in EN 1992-1-1. In this regard, (Phan, 2002) compared at-the-time-existed provisions of codes for HSC and NSC with respect to pre-load level for cylinder specimens corresponding to the service load they carry in reality. Finland's RakMK B4 (RakMK B4, 1993) prescribes different design rules for HSC and NSC and designated HSC from K70 to K100 (70-100 MPa). The RakMK B4 also prescribes different design rules for pre-loaded concrete (with $0.3f_{23^{\circ}\text{C}}$) and for concrete which is not loaded during heating.

Pre-loaded-compressive-strength tests' data for cylinder specimens from different authors are listed in Tab. 2 and compared with different codes by (Phan, 2002) as shown in Fig. 28.

Table 2: Summary of data on pre-loaded tests at elevated temperature carried out by various studies (extracted from (Phan, 2002))

Test methods and programs	Specimen (mm)	$f_{23^{\circ}\text{C}}$	w/c	Silica Fume (% by mass)	Pre-stress % of ambient strength	Heating rate ($^{\circ}\text{C}/\text{min}$)
NIST Mixture I (Phan and Carino, 2001)	100 x 200	98	0.22	10	40	5
NIST Mixture II (Phan and Carino, 2001)	100 x 200	88	0.33	10	40	5
NIST Mixture III (Phan and Carino, 2001)	100 x 200	75	0.33	0	40	5
NIST Mixture IV (Phan and Carino, 2001)	100 x 200	50	0.57	0	40	5
(Castillo & Durrani, 1990)	51 x 102	89	0.33	0	40	7 to 8
(Khoury, et al., 1999)	60 x 180	85	0.32	0	20	2
(Abrams, 1971)	75 x 150	45	Unknown	0	40	Unknown

Comparison of the results of the latter (see Figure 28) indicates that EN 1992-1-2 strength-reduction factors for calcareous aggregate concrete are not conservative to estimate the compressive strength of HSC below 450°C . Above this temperature, the strength loss given by EN 1992-1-2 is more consistent with strength loss of NSC and HSC data. The estimation of strength by EN 1992-1-2 is more significant when spalling occurs for HSC specimens at temperatures less than 450°C . The RakMK B4's provision (RakMK B4, 1993) for HSC's strength at elevated temperatures with $\alpha = 0-0.3$ is shown in Figure 28 with a thick dark line with open circle and is not conservative at temperatures below 150°C .

Further, (Schneider, 1988) expressed that sustained stresses during the heating period influence the shape of strength-temperature relationship significantly. However, load levels (during heating-up phase) $\alpha > 0.2$ have a small influence on the ultimate strength of concrete at elevated temperatures. The latter author compared in (Schneider, et al., 2008) the effects of different pre-load levels for $\alpha = 0.0, 0.1$ and 0.3 (see

Fig. 29) according to (Schneider, et al., 1977) as well as $\alpha = 0, 0.2, 0.4, 0.6$ (see Fig. 30) according to (Shi, et al., 2002) and concluded that there is no significant effect on the strength of concrete specimens tested with pre-load level $\alpha \geq 0.4$. In addition, (Castillo, et al., 1990) considered a pre-load level of $\alpha = 0.4$ as a corresponding level to simulate the service loads on concrete structures and concluded that the not-loaded compressive concrete tests at elevated temperatures have no practical applications.

Further, in series of tests for pre-load levels of $\alpha = 0.2, 0.4$ and 0.6 according to (Guo, et al., 2011), as shown in Fig. 31, the relative compressive strength of concrete (relative to strength for not-loaded at elevated temperatures) increases with the pre-stress or pre-load level.

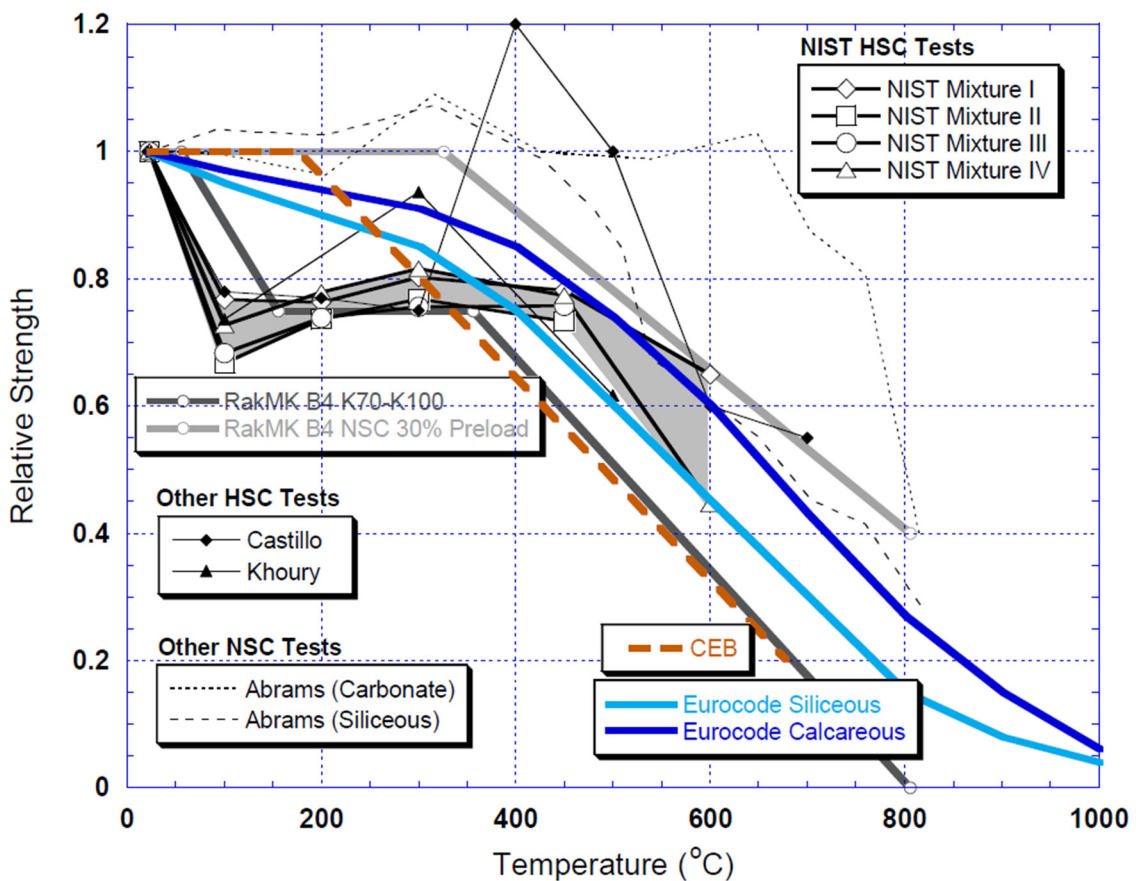
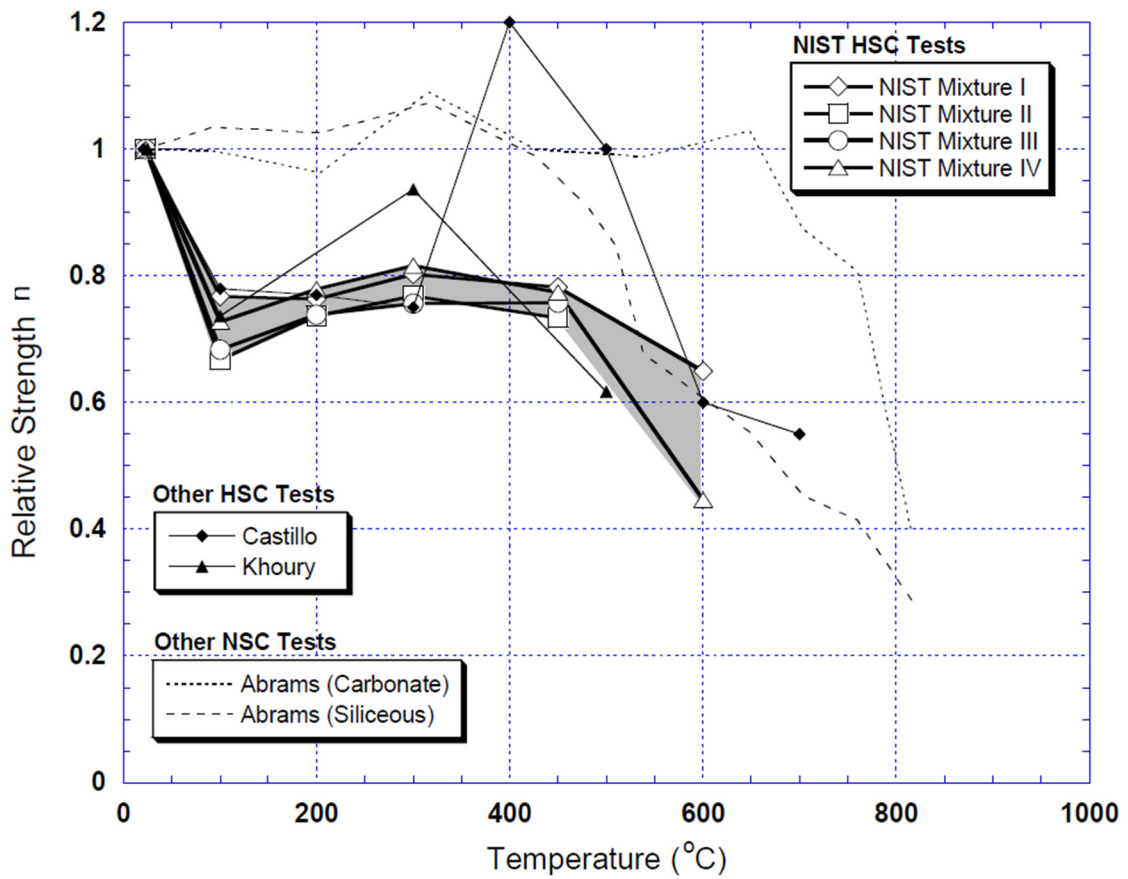


Figure 28: Comparison of pre-loaded test results with various codes (Phan, 2002)

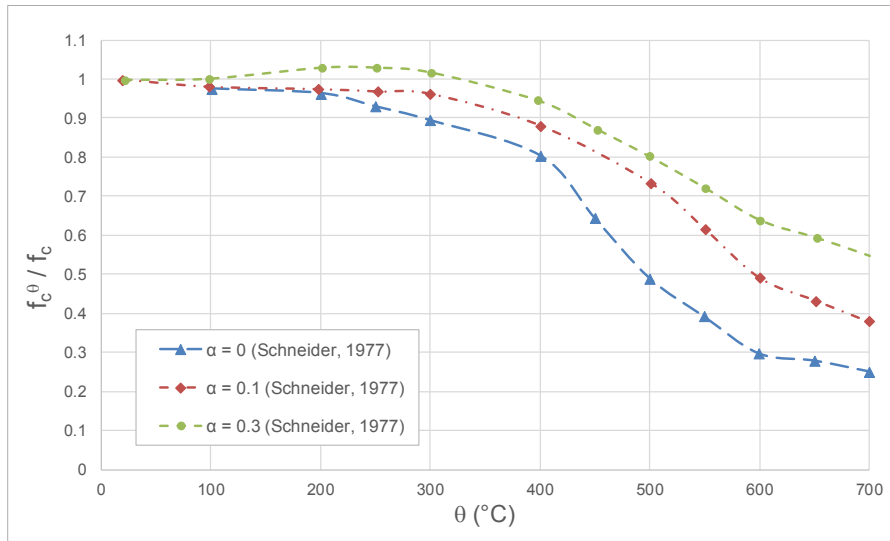


Figure 29: Relative compressive strength of siliceous concrete with different pre-load levels, α , during heating up - according to (Schneider, et al., 1977) (digitalized and extracted from (Schneider, et al., 2008))

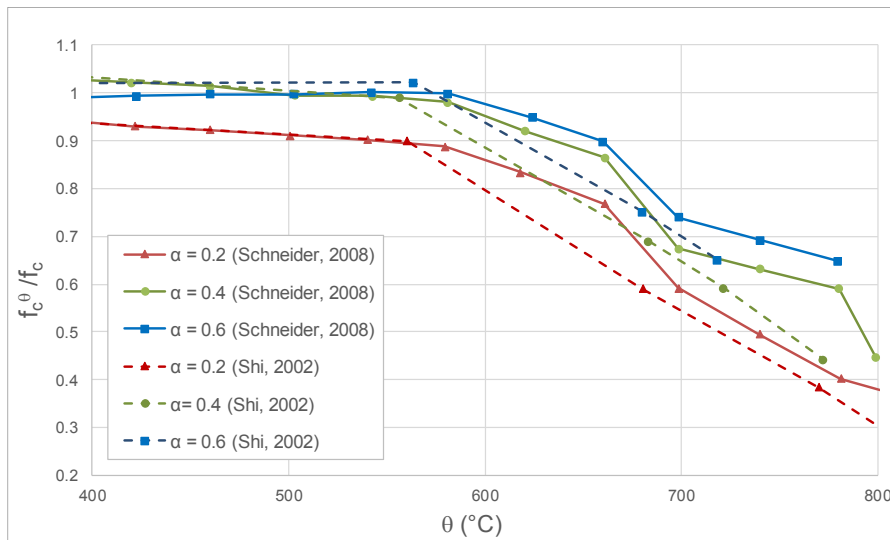


Figure 30: Comparison of concrete cube relative strength for different stress-temperature history and different pre-load levels

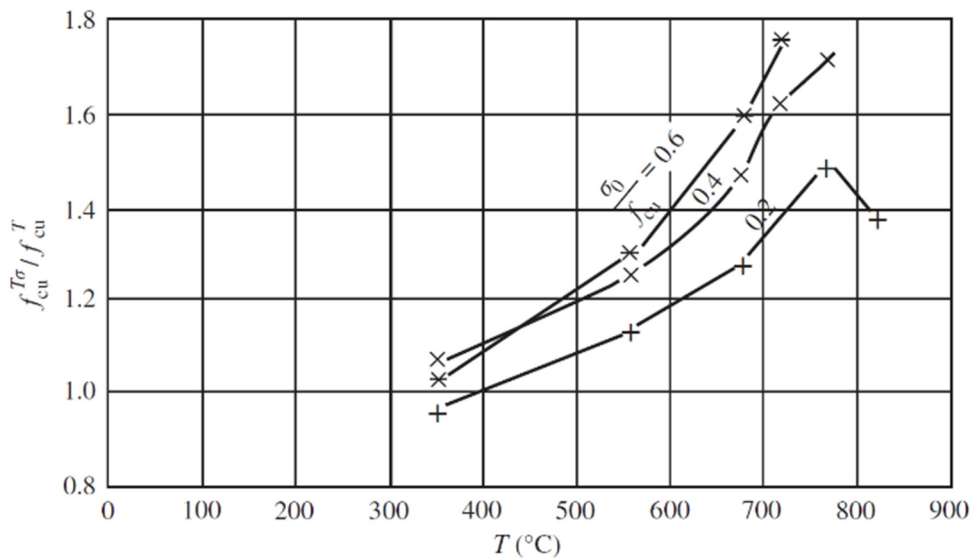


Figure 31: Relative compressive strength for pre-loaded concrete (Guo, et al., 2011)

High-strength Concrete Supplementary Rules and Fire Design RakMK B4

RakMK B4 (RakMK B4, 1993) distinguishes between the compressive strength of NSC, lightweight concrete (LC) and HSC based on pre-load levels applied in the tests at elevated temperatures. HSCs have strength class of 70 to 100 MPa (K70-K100) according to this code. It further specifies an upper limit for silica content being 6% of mass of cement. It also makes a distinction between the concrete strength of specimens with $\alpha = 0$ and 0.3 during the heating phase. This is shown in Fig. 32 where for the HSC a lower limit has been introduced (line ③) for specimens with load level $0 \leq \alpha \leq 0.3$ during the heating phase. Comparing this line with line 1b, which corresponds to concrete compressive strength of NSC under $\alpha = 0.3$ stress, there is much higher concrete-strength loss in HSCs compared to the loaded NSC specimens.

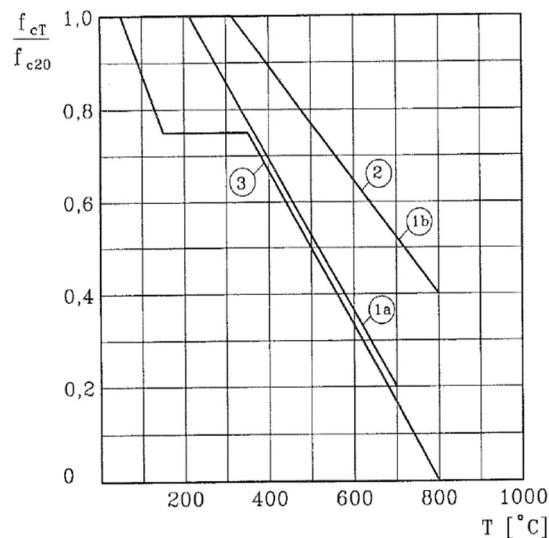


Figure 32: Different concrete strength reduction factors for lightweight, normal-and high-strength concretes (RakMK B4, 1993),

- 1a) conventional concrete with load level 0,
 1b) conventional concrete with 30% load level,
 2) light concrete with load level 0-30%,
 3) high-strength concrete (70-100 MPa) with pre-load level 0-30%.

4.2.2 Heating Rate and Other Parameters

For the heating rates < 10 K/min, by having the temperature gradients in the specimen limited, heating rate has a negligible influence on the result (Schneider, 1988).

Other parameters affecting the compressive strength of concrete at elevated temperatures are:

- Loading rate;
- Original strength and water-cement ratio;
- Aggregate-cement ratio;
- Different types of aggregates;
- Type of cement;
- Maximum size of aggregates (Schneider, 1988).

4.3 Spalling of High-strength Concrete (HSC)

Spalling is a violent or non-violent breaking off in layers or pieces of concrete from the surface of a structural element when exposed to high and rapid rising of temperatures as experienced in fire with different heating rates. There are four types of spalling: aggregate, explosive, surface and corner/sloughing off spalling. Different features, causes and parameters affecting these types are extracted from (Khoury, 2000) and modified with respect to cylinder specimen's requirements and listed in Tab. 3.

Table 3: Different types of spalling in high-strength concrete (summarized based (Khoury, 2000))

Type of spalling	Time range of occurrence in fire (min)	Nature of spalling	Main parameters influencing each spalling type
Aggregate	7-30	Splitting	Heating rate, aggregate thermal expansion, aggregate size, aggregate thermal diffusivity, moisture content
Explosive	7-30	Violent	Heating rate, aggregate size, shear strength of concrete, heating profile, aggregate size, moisture content, section size
Surface	7-30	Violent	Heating rate, moisture content, permeability, tensile strength
Corner	30-90	Non-violent	Maximum temperature, aggregate thermal expansion, tensile strength

4.3.1 Mechanisms of Explosive Spalling

The mechanisms that explain explosive spalling phenomena can be divided into three groups:

- Pore pressure spalling;
- Thermal stress spalling;
- Combined pore pressure and thermal stresses.

The main causes and parameters influencing each mechanism are listed in Tab. 4.

The dense microstructure of HSC causes delay in the moisture transport and consequently increases the internal vapour pressure. The vapour pressure along with thermomechanical stresses may result in explosive spalling.

Table 4: Mechanisms of explosive spalling, features and measurements against spalling (summarized based (Khoury, 2000))

Mechanism of Spalling	Main parameters influencing	Grade of dominancy	Relevance to tests	Measurements might reduce the spalling occurrence
Pore pressure	Permeability of the concrete, the initial water saturation level, heating rate	More dominant than thermal stress mechanism	For small not-loaded specimens acts alone	Aggregate: low thermal expansion and small size, low heating rates (from literature survey heating rates > 2 for cylinder specimens may increase the potential of spalling.
Thermal stress	Heating rate, external loading acts singly or on combination, section size, type of concrete, moisture content	Minor		
Combined pore pressure and thermal stress	Heating rate, external loading act singly or on combination, section size, type of concrete, moisture content		Activated by larger specimens and or loaded specimens	Cement replacement: use of silica fume should be preferably avoided (Hertz, 1984). Water/cement: should not be too low

4.3.2 Influence of Heating Rate on Spalling during Tests

In Tabs. B1-B5 in Annex B, a large number of test results of cylinder specimens according to different authors are gathered. In these tables, the spalling phenomena that have been observed or reported are listed. It can be concluded that heating rates greater than 2 K/min may increase the potential of spalling for the HSC to a high extent. This is more critical for the specimens loaded under the heating-up phase. Observations in Tabs. B4 and B5, summarizing the results of (Huisman, 2010) and (Huisman, et al., 2012), are indicative that even for the specimens with $R < 1$ K/min and $\alpha > 0.1$ all the tests were failed due to explosive spalling.

Further, the recommended values of heating rates and temperature-recording intervals for cylinder specimens with 60 mm diameter are extracted from (RILEM, 2007) and listed in Tab. 5 corresponding to each type of test at elevated temperatures. The recommended heating rate for transient tests is 2 K/min. For steady-state tests, the corresponding heating rate, R , value is 4 K/min. This heating rate might result in (most probably) explosive spalling for HSC when the specimens are loaded during the heating-up phase. The latter has occurred in the majority of pre-loaded compressive tests due to (Phan, et al., 2001) as given in Tab. B3.

Table 5: Recommendations of RILEM on heating rates and temperature measurements intervals for cylinder specimens with diameter of 60 mm (RILEM, 2007)

	Stress-strain	Compressive strength	Modulus of elasticity	Thermal strain	Transient creep
Heating rate R (°C/min)	4	For $d = 75$ mm, $R \leq 2$ For $d = 50$ mm, $R \leq 4$	4	2	2
Temperature recording intervals (min)	2	Appropriate to the heating rate	2	1	1

Use of high heating rate increases the temperature gradients between the exposed surface and centre of specimens. Further, the influences of the heating rates of 1 and 15 K/min have been investigated by (Huisman, 2010) for HSC with Polypropylene fibres (PP-fibres) on the compressive strength and modulus of elasticity (for $\alpha = 0.0$ and 0.2). The results show a small deviation for both heating rates on the compressive strength. For the modulus of elasticity and ultimate strains, the differences were slightly larger. Even for the heating rate of 1 K/min, all the tests of (Huisman, et al., 2012) (for HSC without PP-fibres with $\alpha > 0.2$) explosively spalled (about 325°C).

The high value of heating rate, results in thermal incompatibilities or as called by (Khoury, et al., 1985) structural effects that might influence the strain results. Due to excessive temporary tensile stresses at the centre of specimens, the results of transient strain tests might be not accurate especially for the specimens with $\alpha < 0.2$ during the heating up procedure. This should be investigated by using correct thermal diffusivities for the specimens with PP-fibres. Then, the upper boundary of heating rate can be estimated for the concrete with PP-fibres.

4.4 Residual Compressive Strength

EN 1994-1-2 proposes two types of residual compressive strengths that can be adopted using natural fires with a descending heating branch for use in advanced calculation models:

- Residual compressive strength after concrete is heated to θ_{max} and then cooled down to ambient temperature θ_a , $f_{c,res}^{\theta_{max},\theta_a}$ (designated as $f_{c,\theta,20}$ in figures);
- Residual compressive strength for concrete heated to θ_{max} temperature and subsequent cooling to a specified temperature θ_3 , $f_{c,res}^{\theta_{max},\theta_3}$, where $\theta_3 < \theta_{max}$ (designated as f_{c,θ,θ_3} in figures).

$f_{c,res}^{\theta_{max},\theta_a}$ according to Annex C of EN 1994-1-2, can be evaluated:

$$f_{c,res}^{\theta_{max},\theta_a} = \phi f_c \tag{45}$$

whereas $\phi = 1,0$ to $0,9 \cdot k_{c,\theta_{max}}$ for $\theta < 300^\circ\text{C}$ and $\phi = 0,9 \cdot k_{c,\theta_{max}}$ $\theta \geq 300^\circ\text{C}$.

Further, $f_{c,res}^{\theta_{max},\theta_3}$ corresponds to the concrete strength when the concrete is heated to θ_{max} and then cooled down to a specified lower temperature of θ_3 . The heating and cooling procedures and designation of different parameters are shown in Fig. 33. The proposed relationship to calculate $f_{c,res}^{\theta_{max},\theta_3}$ is a function of strength of concrete at θ_{max} ($f_c^{\theta_{max}}$), $f_{c,res}^{\theta_{max},\theta_a}$, θ_{max} and θ_3 . The relative compressive strength values of $f_{c,res}^{\theta_{max},\theta_3}$ (see Fig. 34) are much lower than $f_c^{\theta_{max}}$ and $f_{c,res}^{\theta_{max},\theta_a}$. As shown in Fig. 34, the compressive strength of concrete at θ_{max} within the concrete according to EN 1992-1-2 is slightly higher than the compressive strength measured after the specimens are heated and then cooled down to ambient temperature proposed by EN 1994-1-2. This is more significant for temperatures between 150 to 600°C. The increase in the strength loss rate above 200°C is mainly due to the continuous dehydration of hydrated cement paste from 105 to 850°C and crystalline transformation from α -quartz to β -quartz occurs between 500 and 650°C (Chang, et al., 2006).

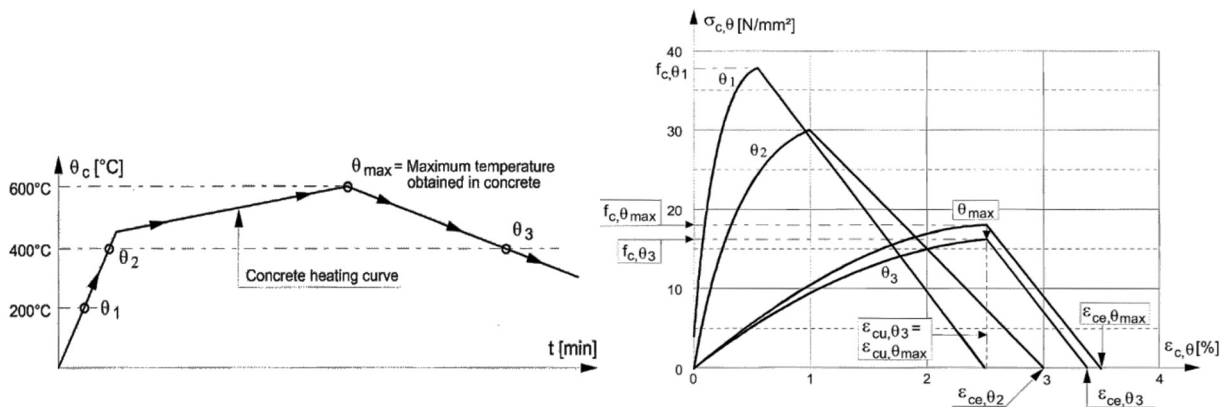


Figure 33: Stress-strain relationships of the concrete strength class C40/50 according to Annex C of EN 1994-1-2

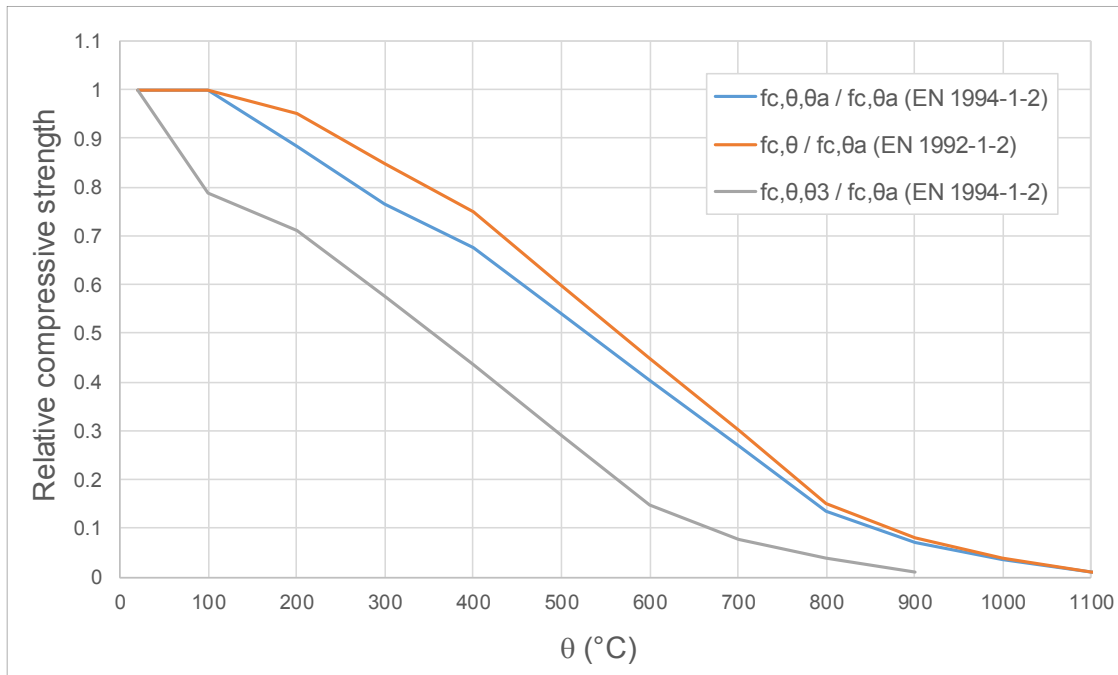


Figure 34: Relative compressive strengths at θ_{max} acc. to EN 1992-1-2, relative strength values after cooled down to θ_a and to θ_3 according to EN 1994-1-2

4.4.1 Residual Compressive Strength after Cooled Down to Ambient Temperature

Fig. 35 shows the stress-strain diagrams for compressive strength at θ_{max} , $f_c^{\theta_{max}}$, according to EN 1992-1-2 and for concrete when heated to θ_{max} and then cooled down to ambient temperature, $f_{c,res}^{\theta_{max},\theta_a}$, according to EN 1994-1-2 for concrete with $f_c = 40$ MPa. Peak compressive stresses deviate as mentioned earlier for the temperature range between 150 to 600°C more considerably.

EN 1992-1-2 takes into account that the compressive strength of concrete is not reversible after cooling. Since the strength recovery of concrete after cooling is favourable, neglecting this effect for evaluation of long-term load bearing may lead to more conservative results and they will be on the safe side. (Li, et al., 2011) narrowed down different test results to compare the average values of 288 calcareous and 32 siliceous specimens with $f_c \leq 60$ MPa as shown in Fig. 36. It is to be noted that in temperature range of 600°C to 1000°C, the residual strength of concrete is slightly larger than the hot compressive strength of concrete at these temperatures. From 0 to 400°C there is no large difference between the proposed values for hot strength and test results for residual strength. The lower amount of residual strength compared to compressive hot strength is positioned between 400 to 600°C. In the same work, it was also shown from the gathered data that the concrete residual compressive strength reduction of concrete with siliceous aggregates, similarly to EN 1992-1-2 hot compressive strength, is higher than mixes including calcareous aggregates (Li, et al., 2011).

It can be assumed that EN 1992-1-2's compressive strength curves are extracted so that all the proposed reduction values are higher than the worst probable compressive strength values at elevated temperatures for $\alpha = 0$. Further, comparing the results gathered by (Li, et al., 2011) for the relative compressive strength measured after the specimen cooled down to ambient temperature with the proposed values due to EN 1994-1-2 shows that EN 1994-1-2's values are on the safe side for temperature range higher than 200°C. The compressive strength test results of (Yang, et al., 2009) on cylindrical specimens after 7, 30, 90, 180 days after being heated indicate that there is generally a slight increase in the residual compressive strength with age of specimens (see Fig. 37).

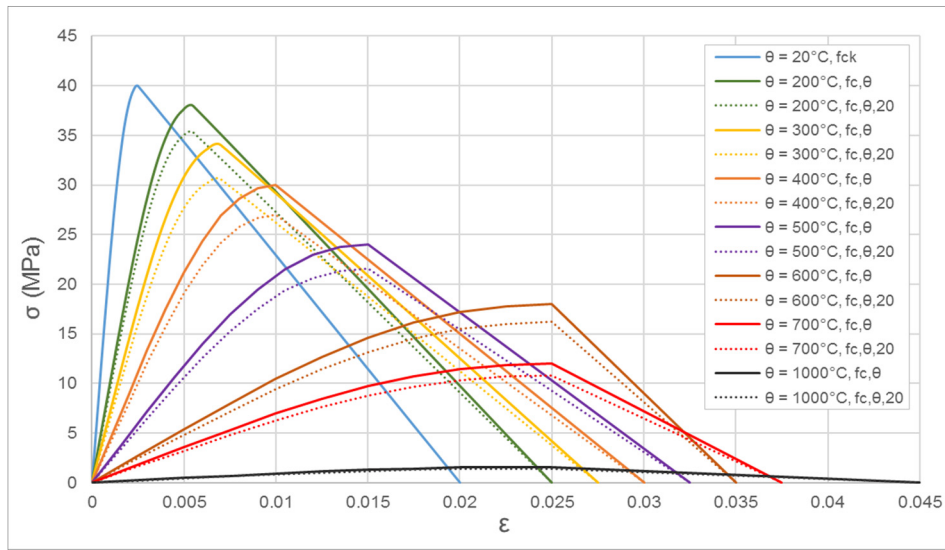


Figure 35: Comparison of stress-strain diagrams according to EN 1992-1-2 with residual stress-strain diagrams according to EN 1994-1-2 for a concrete with 40 MPa compressive strength

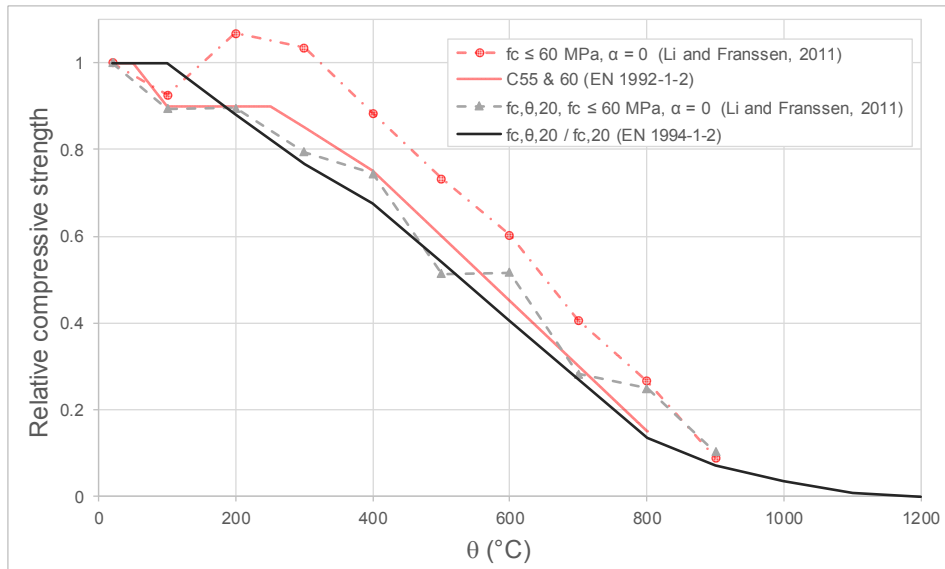


Figure 36: Comparison of test results for residual relative compressive strength after cooled down to ambient temperature according to test results and EN 1994-1-2 with relative compressive strength at θ_{max} acc. to tests and EN 1992-1-2

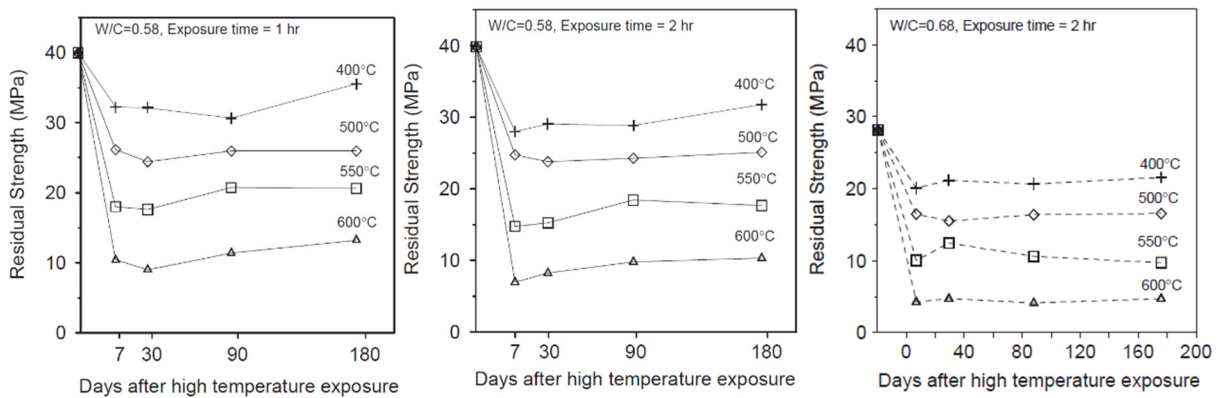


Figure 37: Residual compressive strength values with respect to the age of concrete specimens after exposure (Yang, et al., 2009)

4.4.2 Residual Compressive Strength after Cooled Down to a Specified Temperature

EN 1994-1-2 proposes concrete stress-strain relationships adopted according to natural fires with a decreasing heating branch for use in advanced calculation models. Stress-strain curves, as shown in Fig. 38, for concrete heated to θ_{max} and cooled down to θ_3 and then loaded are compared with the concrete heated to θ_{max} and cooled down to θ_a and then loaded. The compressive strengths at θ_3 are considerably smaller than the values at θ_a .

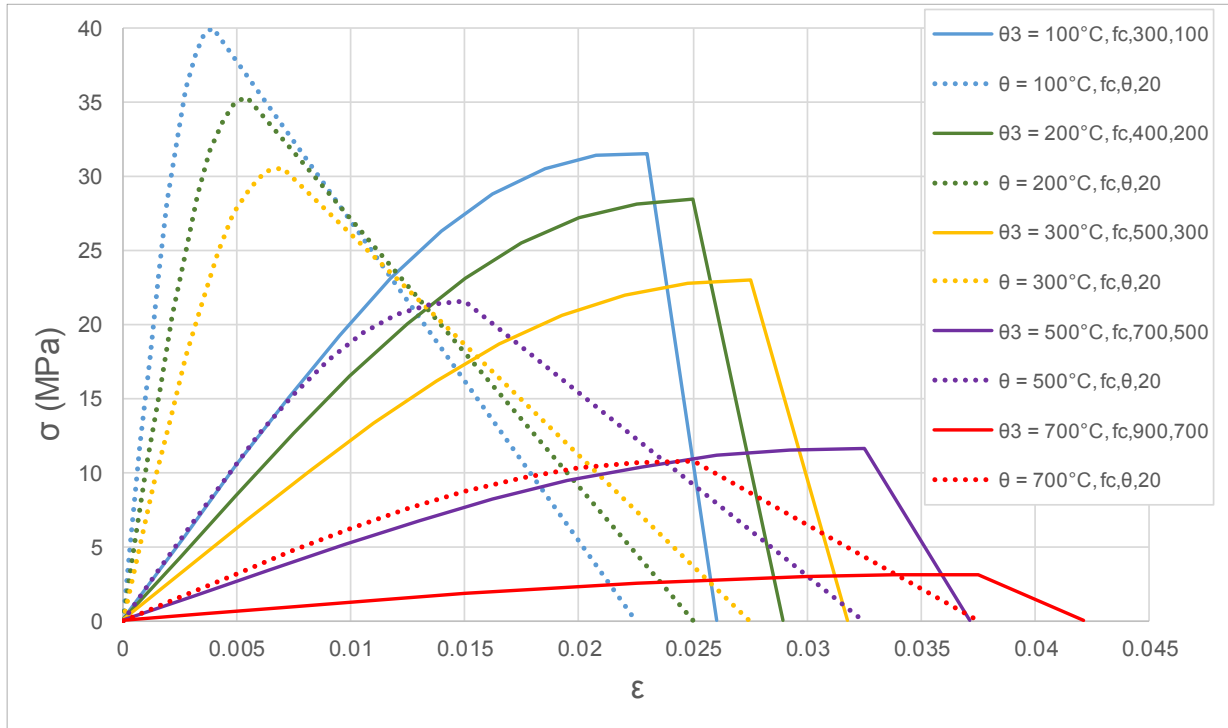


Figure 38: Stress-strain curves for residual compressive strength of specimens after cooled down to ambient temperature θ_a and for the specimens cooled down to θ_3

5 Influence of Polypropylene Fibres on Material Properties of Concrete Exposed to Elevated Temperatures

By addition of PP-fibres, the permeability of concrete increases at elevated temperatures. This causes quicker escape of water and as a result decrease of pore pressure. This might be caused due to micro-cracking. However, these cracks may be due to vapour pressure or different thermal dilation of concrete constituents. It might also be due to volume dilation of melting PP-fibres.

5.1 Thermal Strain

PP-fibres within concrete accelerate moisture transport in temperature range between 200 and 250°C leading to drying shrinkage in opposite direction of thermal strain. At higher temperatures, thermal strain of HSC with PP-fibres in the mix (HSC-PP) is significantly lower than the concrete without PP-fibres. The results of thermal cylinder strain tests for HSC-PP with 2 kg/m³ and without PP-fibres keeping all the other constituents equal for not-dried and pre-dried samples under $R = 1$ K/min has been shown in the Fig. 39 from (Huismann, et al., 2012).

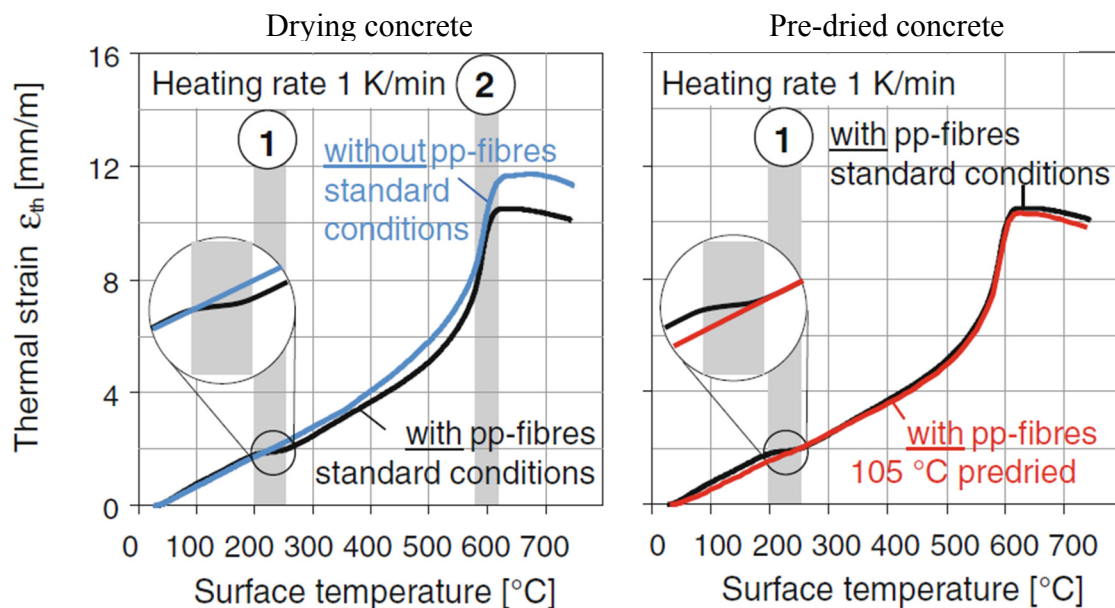


Figure 39: Thermal strain for HSC with and without PP-fibres for drying concrete (left) and pre-dried concrete (right) (Huismann, et al., 2012).

At temperatures higher than 250°C, thermal strain of HSC-PP is significantly lower than HSC. In temperature range of 200 to 270°C, the rate of weight loss of concrete with PP-fibres is faster than the concrete without PP-fibres being due to accelerated evaporation that causes drying shrinkage acting opposite to free thermal expansion. Difference between thermal strains of two concrete types are much higher at temperature above 600°C when the quartz transformation of the aggregates at 573°C has occurred. The fibres turn into vapour at 341°C but the fibre beds are still there and act as defects in internal damage progress that aids the nucleation and increase of micro-cracking. Around 600°C, HSC-PP possess stronger internal damage progress than HSC. The results of microscopic analysis at 600°C shows that HSC exhibits larger crack widths (up to 30 μ m) whereas for HSC-PP, this was less than 10 μ m and well distributed.

Similar results reported in (Huismann, 2010) for HSC-PP heated up to 400°C. From these observations, it can be hypothesized that the well distribution of micro-cracks have reduced the thermal elongation of HSC-PP (Huismann, et al., 2011).

Fig. 39 shows there is generally no large difference in the global points of view for concrete with and without PP-fibres, having all other concrete constituents equal. It is also to be noted that decrease of thermal strain for concrete with PP-fibres compared to the one without PP-fibres started at the temperature around 250°C which can be related to higher drying shrinkage of concrete specimens with PP-fibres that act opposite to the thermal expansion.

The test results of (Peter, 2016) as shown in Fig. 40 are indicative of the fact that concrete with PP-fibres has generally lower thermal strain compared to the concrete without PP-fibres.

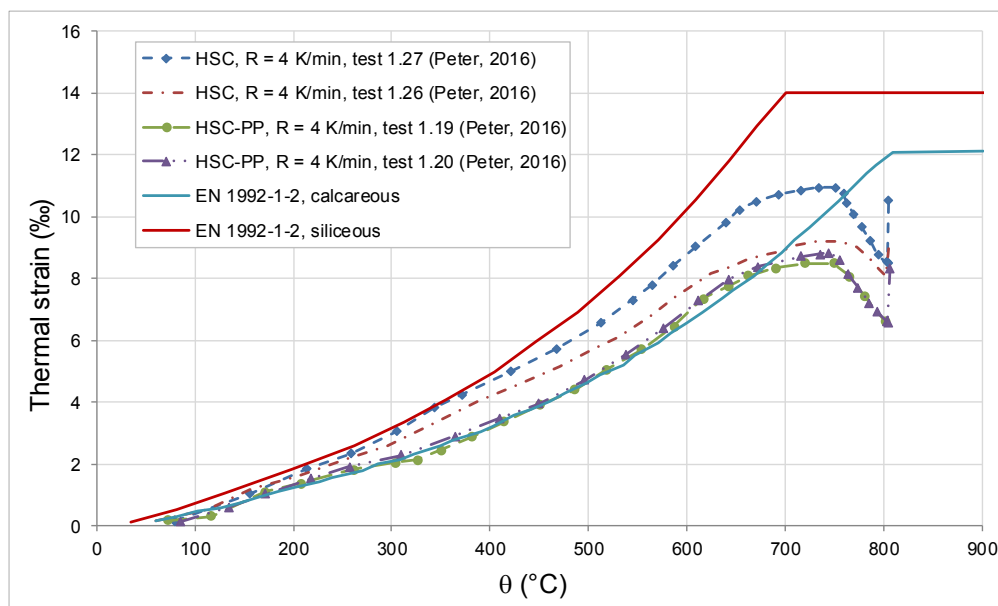


Figure 40: Thermal strain test results vs. EN 1992-1-2 (digitalized and extracted from (Peter, 2016))

5.2 Mechanical-induced Strain at Elevated Temperatures

One of the main differences of HSC and NSC is the larger proportion of the mechanical-induced strain component during the first heating. This is attributed to the higher content of binder agent in the cement paste. Up to 250°C there is practically no influence rising from the addition of PP-fibres on mechanical strain of HSC, however, this is not the case for temperature above 250°C. PP-fibres act like defects in the concrete and by micro-cracking releases the stresses as well as internal pore pressures. It is, therefore, assumed that micro-cracking contributing in the deformation and is the main reason for increasing mechanical strain of the HSC-PP as shown in Fig. 41.

5.3 Modulus of Elasticity

(Pliya, et al., 2011) studied the modulus of elasticity after the specimens are cooled down by assuming three loading-unloading cycles until reaching 30% of strength for the cylinder specimens with PP-fibres. The results are shown in Fig. 42. A comparison is also made between the residual elastic modulus of HSC-PP and HSC. Correspondingly, reduction values for concrete with PP-fibres are slightly higher at 150 and 450°C than those without PP. Generally, there was no large deviation between different specimens with different fibre contents. It is to be noted that the reduction in $E^{\theta_{max}}$ according to EN 1992-1-2 for specimens

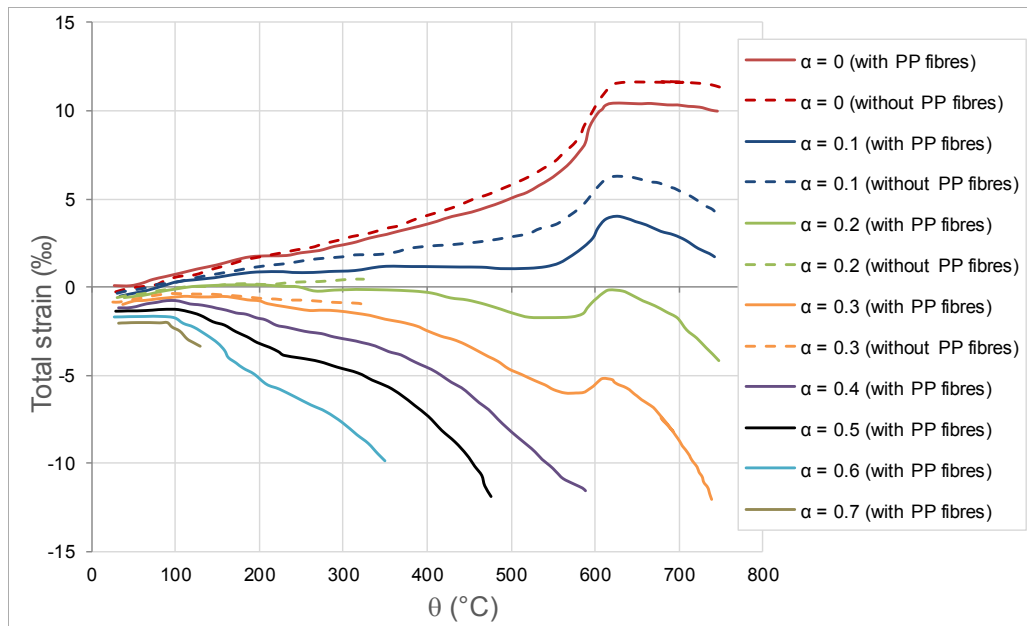


Figure 41: Mechanical strain for HSC with and without PP-fibres with heating rate $R = 1 \text{ K/min}$ (digitalized and extracted from (Huismann, et al., 2012))

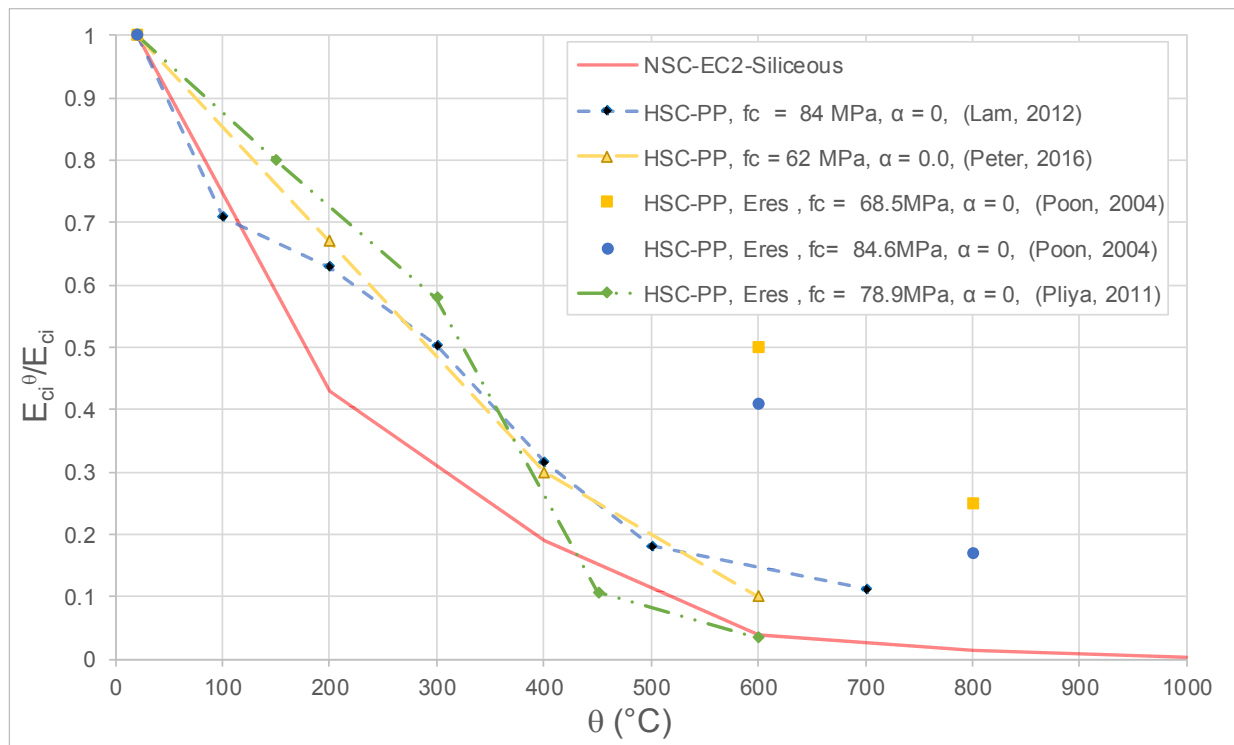


Figure 42: Comparison of relative moduli of elasticity after heating (for cooled down specimens) with modulus of elasticity according to EN 1992-1-2

with θ_{max} are from implicit model. Further (Chang, et al., 2006) have taken the secant modulus at 40% of the peak stress as for unheated concretes for comparative purposes. They stated that the ratio of reduction in modulus of elasticity is much higher than the reduction in compressive strength. Further, the compressive stress-strain relationships to EN 1994-1-2 has the same non-dimensional curves for heating and cooling. Thus, the reduction in the elastic modulus is also the same as the secant modulus at the peak point. Due to (Chang, et al., 2006), the original strength of concrete has no considerable influence on the values of $E^{\theta_{max}}$ at elevated temperatures. Further, the results of different HSC-PP tests are plotted in Fig. 42. Two series of these test results with the lowest values are shown in Fig. 43 along with the Khennane and Baker's model

(Khennane, et al., 1993). The results show that the relative elastic strain values for these two series are less than the proposed model. It should be beard in mind that the strain values at the peak stresses as shown in section 3.2.1 are underestimated by (Khennane, et al., 1993) compared to different test results. For comparison, the relative value of modulus of elasticity for C40/50 has been taken into account by considering secant modulus at 40% of peak stress. Fig. 44 shows the value of relative modulus of elasticity corresponding to the proposed stress-strain curve for ascending branch due to EN 1992-1-2, $E^{\theta_{max}}$, and the values of residual compressive strengths, $E_{res}^{\theta_{max},\theta_a}$ and $E_{res}^{\theta_{max},\theta_3}$ (designated in figures as $E_{\theta,2\theta}$ and $E_{\theta,03}$), based on EN 1994-1-2 values. It is to be noted that there is slightly higher increase in reduction rate of $E_{res}^{\theta_{max},\theta_a}$ compared to $E^{\theta_{max}}$. This is due to the fact that the transient strain, which is accumulated in EN 1992-1-2's stress-strain curves, considered to be reversible for $E_{res}^{\theta_{max},\theta_a}$. On the other hand, the curve of $E_{res}^{\theta_{max},\theta_3} / E$ has very sharp slope that demonstrates a very high value of stiffness loss.

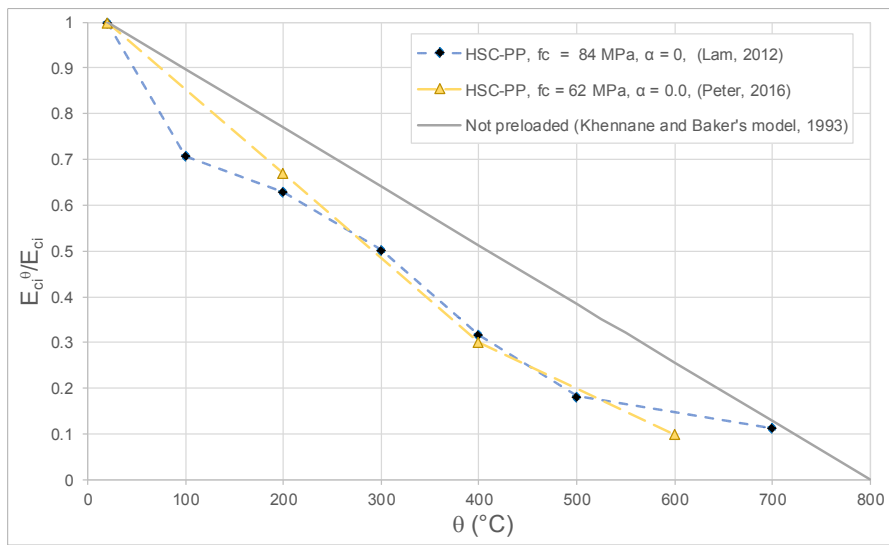


Figure 43: Comparison of relative initial moduli of elasticity of tests for HSC-PP and the proposed model by (Khennane, et al., 1993)

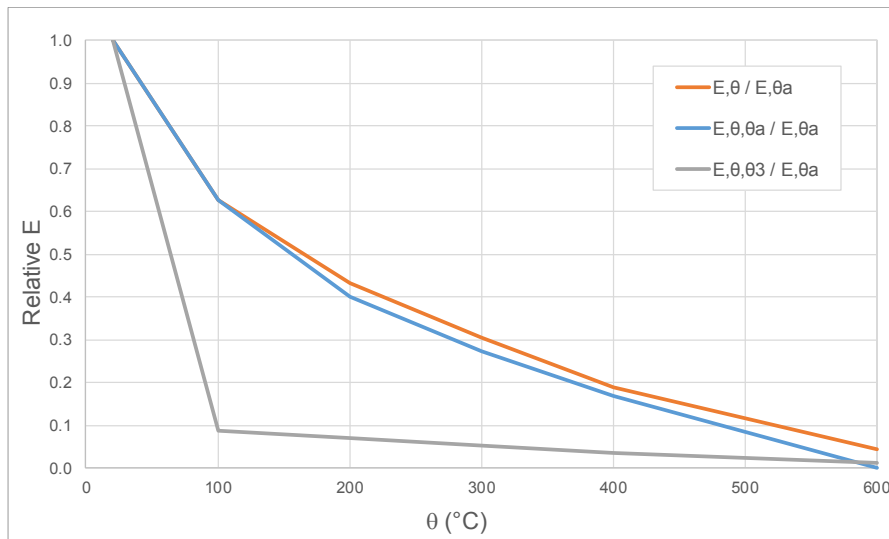


Figure 44: Comparison of relative modulus of elasticity corresponding to stress-strain at elevated temperatures acc. to EN 1992-1-2 and the residual relative moduli of elasticity due to EN 1994-1-2

5.4 Relative Porosity

Porosity increases with the increase of temperature. This can be related to the water and the cracking induced by departure of water and cracking generated by different amount of thermal expansion of the cement paste, aggregates and fibres. The porosity increases more rapidly for HSC-PP (2 kg/m³) than for HSC as temperature increases, as shown in Fig. 45. This is due to the melted PP-fibres leading to more porous material (Pliya, et al., 2011).

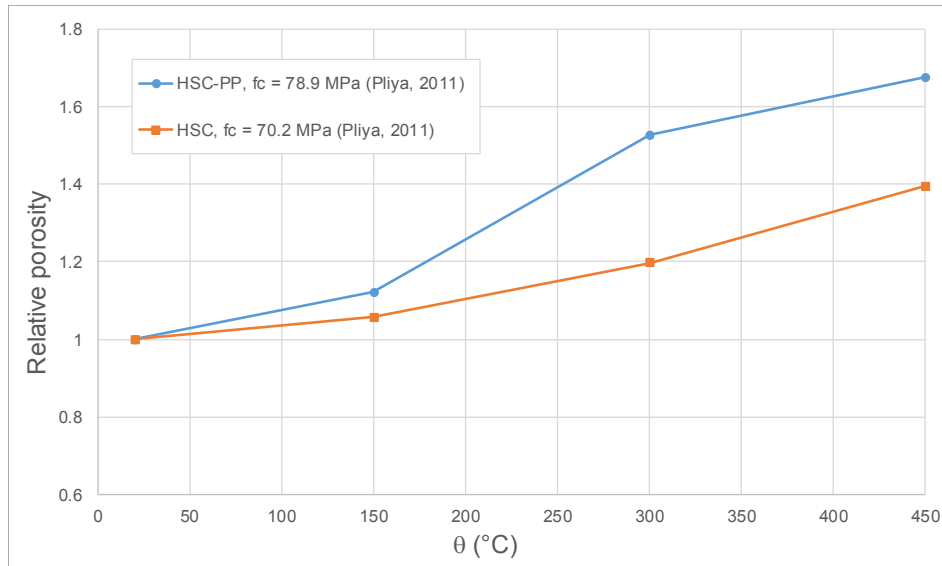


Figure 45: Relative porosity for HSC and HSC-PP (extracted from (Pliya, et al., 2011))

5.5 Mass Loss

Addition of PP-fibres influences the mass loss of concrete at higher temperatures to a low extent. This can be concluded from Fig. 46.

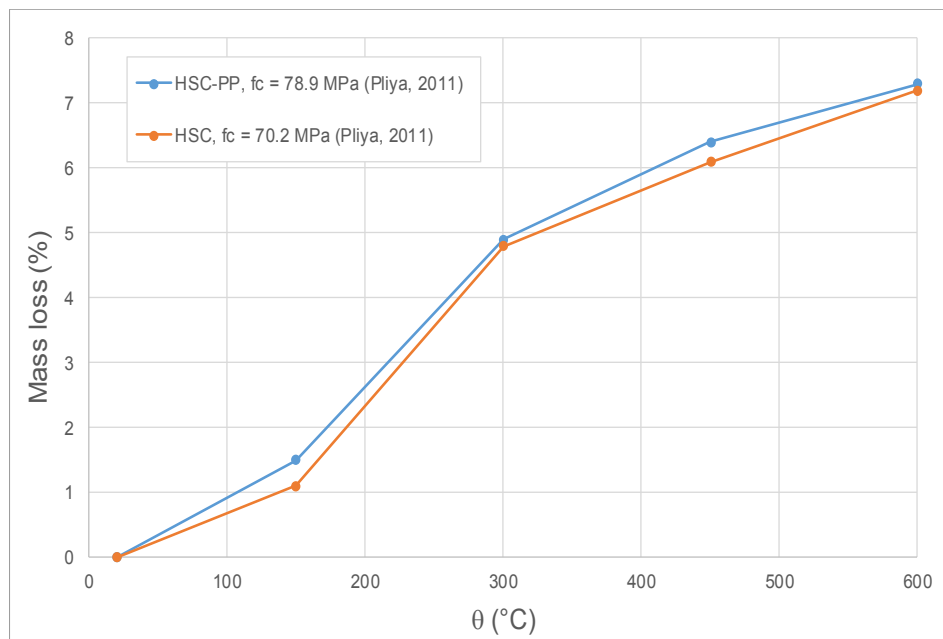


Figure 46: Mass loss of HSC and HSC-PP (extracted from (Pliya, et al., 2011))

5.6 Compressive Strength

HSC with PP-fibres loses a great amount of strength at low temperatures and recovers some part of it after 100°C up to 400°C. Within this range, it has a small increase in the strength that might be due to the stiffening of the cement gel, increase of forces between different particles of gel and/or the removal of absorbed water. The relative decrease in strength at 500°C is probably due to the increase of micro-cracks and dehydration of cement gel. HSC with PP-fibres is particularly more porous at higher temperature due to evaporation of PP-fibres and dehydration of cement gel.

Regarding the relative compressive strength of high-strength concrete, EN 1992-1-2 (chapter 6) introduces three classes of concrete and correspondingly three sets of relative compressive strengths: the recommended classes are Class 1 for concrete C55/67 and C60/75, Class 2 for concrete C70/85 and C80/95 and Class 3 for concrete C90/105. There is no further explanation if these are extracted from the results of pre-loaded or not-pre-loaded tests. To compare the results of relative compressive strength for HSC-PP with HSC according to EN 1992-1-2, test results of HSC-PP should be compared to the relevant HSC classes. Thus, as shown in Fig. 47, test results of HSC-PP due to (Peter, 2016) and (Lam, et al., 2012), for not-pre-loaded tests, with average compressive strengths of 62 and 84 MPa respectively should be compared with Class 1 and 2 concrete according to EN 1992-1-2. Comparing both sets of results with HSC, relative compressive strengths according to (Lam, et al., 2012) are considerably lower than EN 1992-1-2 values for temperatures up to 200°C. In case of comparing the relative strength results according to (Peter, 2016) to Class 1, test results are generally lower than the values proposed by EN 1992-1-2 and for temperatures up to 400°C this is more significant.

Further, (Balazs, et al., 2012) have conducted series of compressive strength tests for HSC-PP and different other combinations on cubes of 150 mm. The results for specimens with PP-fibres (1 kg/m³) for $f_c = 63.6$ MPa have been plotted in Fig. 47. The compressive strength of their specimens are lower compared with EN 1992-1-2 curves for C55 and 60 up to 300°C.

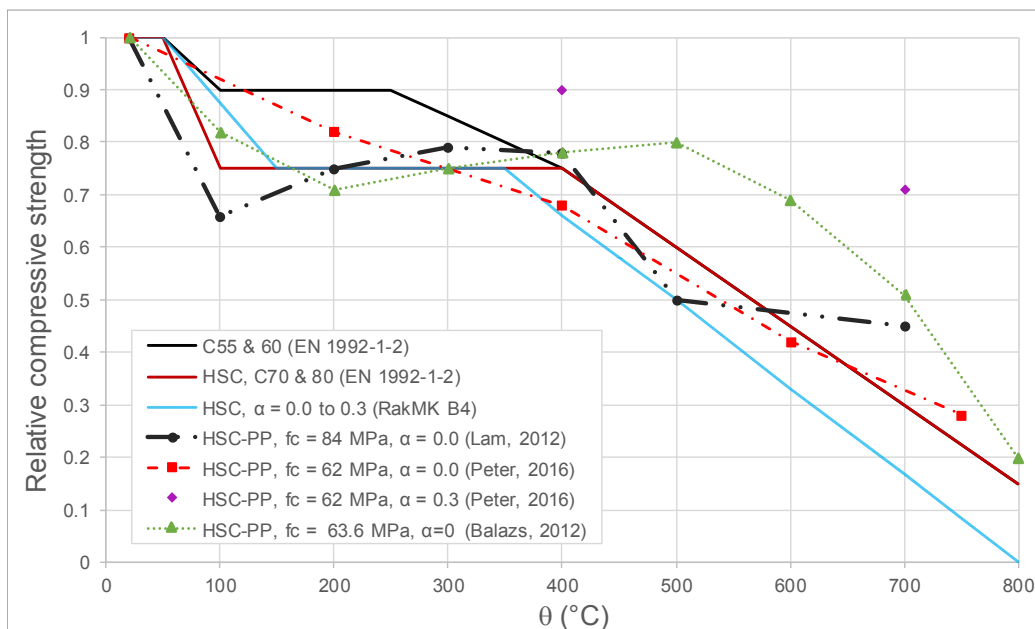


Figure 47: Comparison of HSC-PP relative compressive strength test results with HSC according to EN 1992-1-2 and RakMK B4

5.7 Residual Compressive Strength

(Poon, et al., 2004) compared the results of relative residual compressive strength of HSC cylinder specimens ($f_c > 68$ MPa, 100 x 200 mm) for PP-fibres amount of 0, 1 and 2 kg/m³ as well as for specimens with 2 kg/m³ and 78 kg/m³ steel fibres for 600 and 800°C under a heating rate of 2.5 K/min. They have not observed any beneficial influence of inclusion of PP-fibres on the residual mechanical properties.

Further, the result of a study carried out by (Horiguchi, et al., 2004) show that there is a high strength reduction for HSC with PP-fibres ($f_c = 89.8$ MPa) compared to the $f_{c,res}^{\theta_{max}}$ for $f_c \leq 60$ MPa. PP-fibres melt at around 170°C and provide escape way for moisture but it reduces the fracture toughness when the specimen is heated. They proposed using a hybrid fibre reinforcement with both PP and steel fibres to improve the strength as well as fracture characteristics after heating. In addition, (Peter, 2016) conducted one test for HSC with PP-fibres ($f_c = 62.6$ MPa) with $\alpha = 0$ after cooling from θ_{max} of 600°C. As shown in Fig. 48, the reported value is considerably lower than the results of $f_{c,res}^{\theta_{max}}$ for $f_c \leq 60$ MPa. In this regard, (Behnood, et al., 2009) carried out cylinder residual concrete strength tests for HSC with cylinders (100 x 200 mm) used different proportions of PP-fibres and compared the results with HSCs'. They concluded that the addition of PP-fibres cannot significantly influence the relative residual compressive strength at 100°C. At 200, 300, and 600°C, the relative residual concrete strength of mixture with PP-fibres were higher than the ones without PP-fibres. Further, existence of 2 kg/m³ amount of PP resulted in the maximum residual concrete strength of mixture for concrete with PP-fibres. The increase in strength at 200°C is due to increase in surface forces between gel particles as the moisture content is removed. At 300°C, PP-fibres are already melted and higher proportion of vapour pressure can extend the interconnected network of micro-cracks and change them into macro-cracks and consequently result in sharp strength drop. Further, during the heating region the aggregates expand and cement gel contracts. This different behaviour of concrete components can also result in stress concentration and influence the result of residual concrete strength. Melting of PP-fibres before 300°C results in more escape routes that reduces the amount of pore pressure. Disappearance of PP-fibres may also result in thermal incompatibilities between aggregates and paste due to provision of more free space and act as thermal shock absorber. After 600°C, there is a sharp decrease in the residual concrete strength. At the temperature range of 450-550°C calcium hydroxide is decomposed and generates lime and water. Strength gain after cooling can be attributed to rehydration of the gel, hydration of unhydrated cement grains and the carbonation of calcium oxide. The strength loss is due to rehydration of lime accompanied by 44% increase in volume. The residual concrete compressive strength of specimens with PP-fibres due to (Behnood, et al., 2009) and (Horiguchi, et al., 2004) as shown in Fig. 48 are lower than the compressive strength reduction factors for HSC according to EN 1994-1-2.

Further, (Pliya, et al., 2011) studied the residual compressive strength of concrete cylinders (160 x 320 mm) without PP and with PP (1 and 2 kg/m³) and combined PP-and steel fibres under 1 K/min. They concluded that both relative residual compressive strength and modulus of elasticity of concrete with PP-fibres have been reduced much higher than the ones without PP-fibres for HSC-PP ($f_c = 78.9$ MPa) and HSC ($f_c = 70.2$ MPa). They added that the addition of steel fibres can improve the residual compressive strength of concrete and delay the time of occurrence of spalling. Further from their literature survey the addition of PP-fibres may result in more porous material after the melting of PP-fibres and consequently reduce the residual compressive strength. This contradicted some other authors' observations. In another study, (Poon, et al., 2004) compared the results of relative residual compressive strength of HSC cylinder specimens ($f_c > 68$ MPa, 100 x 200 mm) for PP values (0, 1 and 2 kg/m³) and for a specimen with 2 kg/m³ and steel fibres at 600 and 800°C with the heating rate of 2.5 K/min. They have not observed any beneficial influence of addition of PP-fibres on the residual concrete strength of specimens. The value of strains at peak stresses for cylinder specimens after the heating exposure up to 600°C and 800°C with

$f_c = 69.1, 86.1$ and 82.8 MPa have reported to be about 0.81% and 1.0 for both specimens with and without PP-fibres respectively. However, in the diagrams, the maximum strain values at the peak stresses have been shown to be lower for concrete with PP-fibres compared to those without PP-fibres. The addition of 1% steel fibres has increased the maximum strain at the peak stress and elastic modulus compared to the specimens only with PP-fibres.

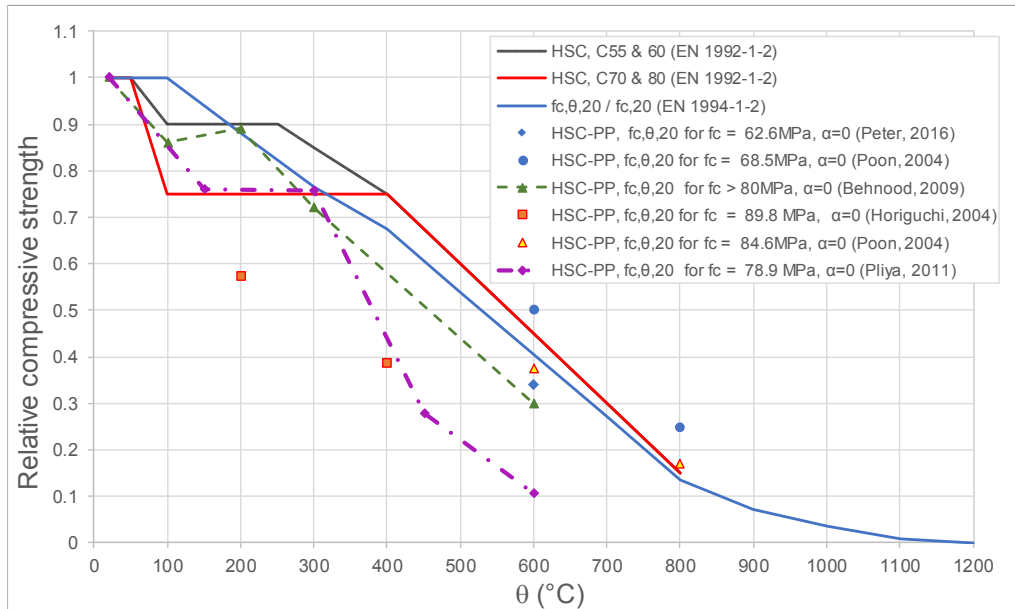


Figure 48: Comparison of test results of relative residual compressive strength for concrete with and without PP-fibers

5.8 Strain at Peak Stress

Comparing the relative strain at peak stress values of NSC from EN 1992-1-2 and the results for HSC-PP from two sets of tests carried out by (Peter, 2016) and (Lam, et al., 2012) show that the rate of increase in the relative strain at peak stress values is for HSC-PP almost less than half of the values for NSC given by EN 1992-1-2 (accumulated transient creep).

Further, (Chang, et al., 2006) carried out 108 tests on siliceous concrete cylinders without PP-fibres (150 x 300 mm) for $f_c = 27$ and 40 MPa under heating rates between 1 and 4.5 K/min. Based on the results, the relative value of strain at peak stress increases with rising temperature. Further, results of different tests show that the strain at peak stress is almost equal to ambient temperature for temperature values below 200°C. The values of relative strain at peak stress according to EN 1992-1-2 for normal concrete strength and the test results according to different authors are plotted in Fig. 49.

5.9 Stress-strain Curves

The comparison of stress-strain curves of (Poon, et al., 2004) at elevated temperatures for specimens with 1 and 2 kg/m³ and without PP-fibres show that the stress-strain curves of PP-fibres have slightly steeper descending path with the exception of curves for $\theta_{max} = 800^\circ\text{C}$ (see Fig. 50). Stress-strain curve of HSC-PP for $\theta_{max} = 800^\circ\text{C}$ has a smaller strain at peak stress value compared to HSC. The addition of 1% steel fibres to concrete with PP-fibres has reduced the slope of descending branch to a very high extent. The combined use of PP and steel fibres showed little benefits compared with adding only steel fibres to the mixture. The stress-strain curves at ambient temperature and elevated temperatures for HSC with PP-fibres according to (Peter, 2016) ($f_c = 62$ MPa, $\theta_{max} = 600$ and 750°C and $R = 25$ K/min) and according to (Poon, et al., 2004)

for $f_c = 69.1$ MPa, $\theta_{max} = 600$ and 800°C are compared and shown in Fig. 51. The strain at peak stress values for the elevated temperatures show a good agreement for $\theta_{max} = 600^\circ\text{C}$ whereas for $\theta_{max} = 800^\circ\text{C}$, the strain at peak stress values according to (Peter, 2016) are almost 25% higher ($\epsilon_{cl}^{\theta_{max}} = 0.0125$) compared to (Poon, et al., 2004).

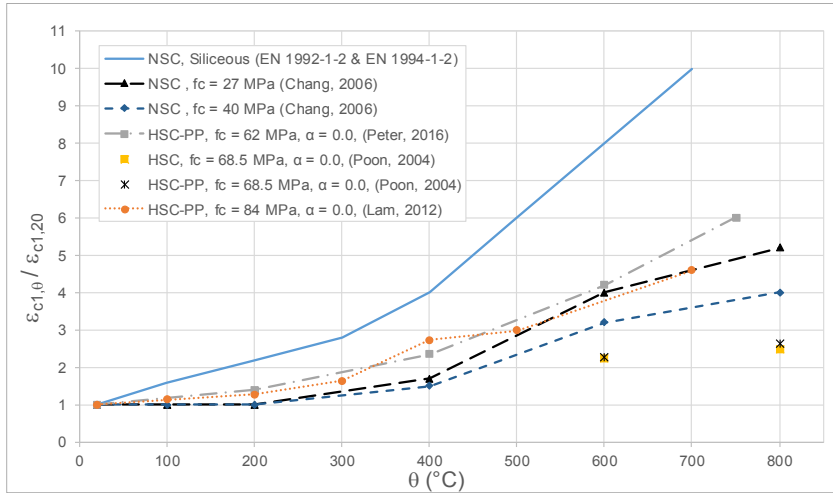


Figure 49: Comparison of relative strains at peak stresses from test results of NSC and HSC with EN 1992-1-2 and 1994-1-2

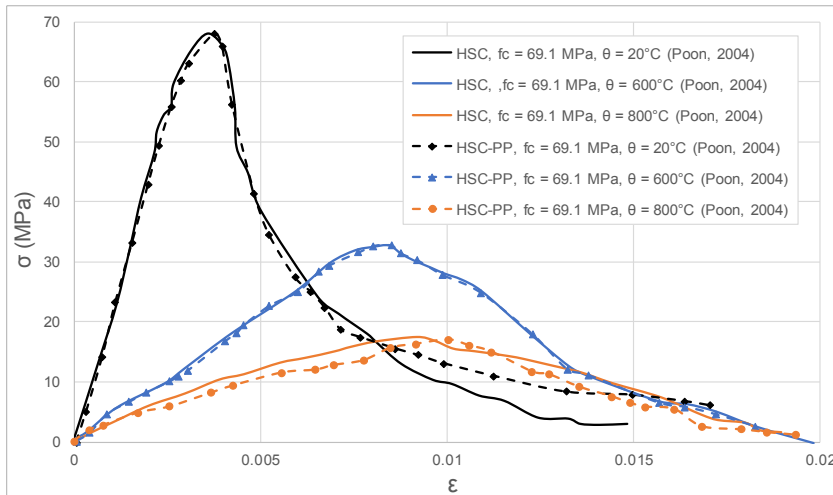


Figure 50: Stress-strain curves for HSC and HSC-PP

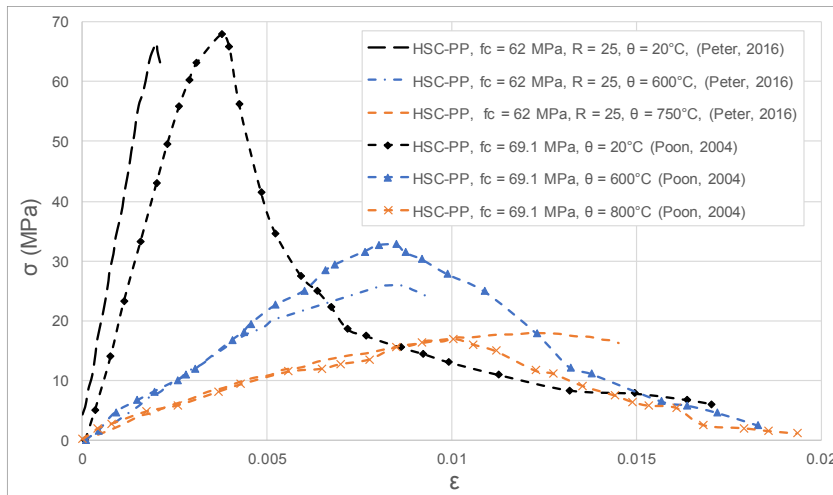


Figure 51: Stress-strain curves from test results for HSC-PP

6 Tests and Mixture Characteristics

6.1 Design Mix

The hardened concrete with the used design mix should simulate a practice-relevant concrete of a member of a cut-and-cover tunnel structure according to (BAST, 2015) with and without PP-fibres in its mixture (2 kg/m³ PP-fibres as suggested by ZTV-ING section 5). The hardened concrete should meet the condition of 1 to 2-year-old concrete in the practice. At this age, concrete is more hardened than 28 days. It is also expected that the concrete loses considerable amount of its moisture content. Two base mixtures proposed for concrete with and without PP-fibres are given in Tab. 6. The only difference between two mixes except PP-fibres is amount of admixture.

Table 6: Calculated design mix for concrete with and without PP-fibres

Description of the reference mix	Concrete without PP-fibres	Concrete with PP-fibres
Aggregate	Siliceous aggregates	Siliceous aggregates
w / c	0.49	0.49
Concrete grade	C30/37	C30/37
Cement content [kg/m ³]	365	365
Fly Ash [kg/m ³]	--	--
Water [kg/m ³]	178.85	178.85
Polypropylene fibres [kg/m ³]	0	2
Concrete admixture		
Superplasticizer		
Glenium 51 [%-cement]	0.63	1.1-1.6
Aggregates [kg/m ³]	1824.28	1824.28
Quarz-sand (0-0.25 mm)	3%	3%
0/2 mm	60.2%	60.2%
2/8 mm	36.8 %	36.8 %
8/16 mm	---	---

6.2 Properties of Specimens

In terms of geometrical shape, there are three specimen types used in the tests that are cylinders, cubes and prisms. The geometries of each type are illustrated in Fig. 52.

- **Cylinder specimens** are foreseen to investigate the mechanical behaviour at the ambient temperature and thermo-mechanical behaviour at the elevated temperatures relative to their ambient temperature by doing stationary and transient tests;
- **Immersed cube specimens** are used to estimate the concrete compressive strength at ambient temperature after 28 days;

- **Prisms** are used for temperature measurements. Since installation and fixing the thermo-wires and sensors within the cylinder specimens are very difficult and might produce more inaccuracies, number of prisms with comparable geometries to the cylinder specimens were formed to simulate temperature distribution in the cylinder specimens.

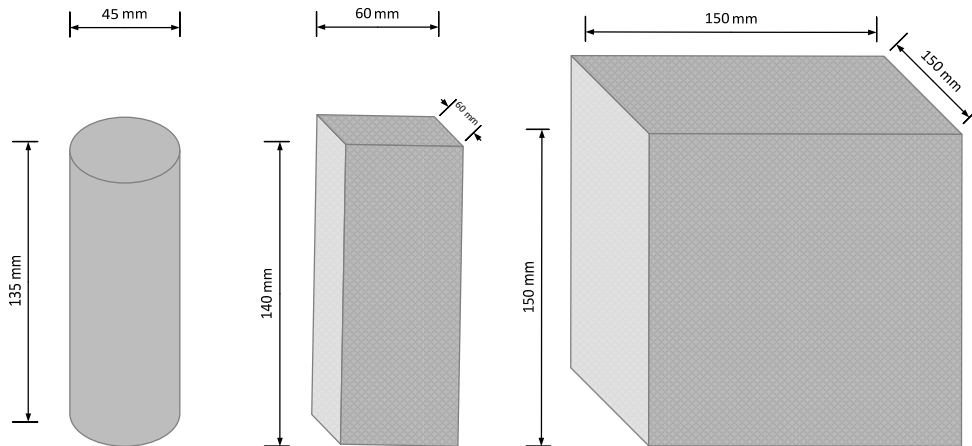


Figure 52: Geometries and dimensions of concrete specimens

Prisms with identical sizes of 14 x 6 x 6 cm were generally used to measure temperatures. To be able to measure temperatures in the prisms, two 2-mm-thick copper rods were installed and fixed in the prismatic wooden moulds. As shown in Figs. 53 and 54, two configurations are assumed for the position of tip of thermo-wires, configuration 1 (c1) having a row of measuring points on the surface (1 mm to 3 mm from the surface) and at the distance of 1.5 cm from the surface, configuration 2 (c2) having a row of measuring points on the surface and 3 cm away from the surface (see Fig. 55).

6.3 Batches

In order to estimate the number of batches needed for the tests, different considerations should be taken into account based on the specification and the main aims. According to (RILEM TC 129-MHT, 1998), the specimens should be at least 90 days old. All batches are mixed with the same machine. Therefore, the volume needed for each batch is limited to the capacity of the machine. Four batches are totally mixed from which three having PP-fibres (batch 1, 2 and 3) and one does not contain PP-fibres (batch 4).

6.4 Curing

To be able to simulate the moisture content of 1 to 2-year-old concrete with and without PP-fibres in practice, the procedure of moisture loss is accelerated for the specimens in the early age of concrete. To approximate the amount of free water that exist in the cylinder specimens when drying-out tests are performed for the first and second batches. Different types of curing are performed for each specimen type. The storage in the moulds are performed according to DIN EN 12390-3.

Cubes

Cube specimens are used to measure the 28-day-old strength of immersed specimen for each batch.

Cylinders

For the cylinder specimens, generally, three types of curing were considered:

- Stored in water up to 28th day. This is performed for comparison of compressive strength with normative cube strengths;

Tests and Mixture Characteristics

- First cured in water for 10-13 days (various for each batch) and then stored exposed to indoor air;
- First cured in water for 10-13 days and then moved to a ventilated oven and kept under 30 and 40°C for 2 and 4 days.



Figure 53: Wooden moulds with two fixed copper rods and fixed thermal wires at different measurement points



Figure 54: Prisms with thermo-wires. Casted out (left), hardened (right)

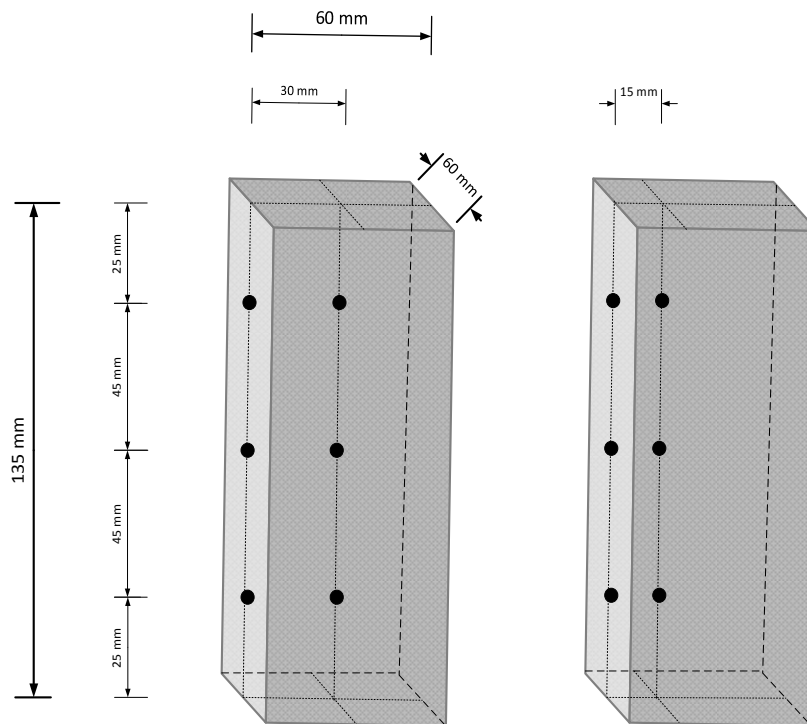


Figure 55: Configuration of measuring points in the prisms

Prisms

First cured in water for 10 days and in the successive step for 5 days in an oven in 30 to 40°C and then stored in an indoor air condition.

6.4.1 Mass and Moisture Content of Oven-dried Specimens

Drying out is performed according to DIN EN 12390-7 for two cylinder specimens from batch 1 and also 2 cylinder specimens from batch 2. Further, for batches 2 and 3, small remained cylindrical pieces (designated with RS) about $\frac{1}{4}$ to $\frac{1}{3}$ of the cylinder specimens are dried out in the oven. Mass of the specimens weighed at 4th and 28th (from the water storage) and at 32nd, 33rd and 34th days after they are moved to the ventilated oven (4, 5 and 6 days in oven dried) are listed in Tab. 7. In addition, the moisture content, in gr, percentage of mass loss relative to the saturated specimens are given in this table.

6.4.2 Accelerated Curing and Moisture Content of Cylinder Specimens

To evaluate the amount of moisture loss, two types of curing are used for the first batch:

- Wet curing and air exposed: specimens kept in water for 13 days and then stored in air (abbreviated as 13WA-B1, where 13W refers to first 13 days cured in water, the letter A corresponds to the successive air storage condition and B1 stands for batch 1)
- Wet curing, oven drying and air exposed: specimens kept 13 days in water and then moved to ventilated oven and heated at 40°C. The percent of mass loss relative to the mass of the saturated specimens at 13th day are evaluated by weighing the specimens in 24-hr intervals. The percentage of mass loss after 48 hours has reached almost an average of 3% (3% corresponds approximately to the long term moisture loss of concrete in the practice). The specimens were therefore moved and stored in air. This is abbreviated as 13W2O(40)A-B1 where 2O(40) refers to successive 2-day curing in the oven at 40°C after 13 days cured in water. The amount of average mass loss due to unnatural curing for batch 1 (for 28 days) and for all the four batches (for 200 days) are illustrated in Fig. 56 and Fig. 57 respectively.

For all batches, it was tried to keep the mass loss (M.-%) of cylinder specimens lower than 3% after drying in the oven. The plot of mass loss of each batch relative to the saturated specimens are given in Annex C. Table 8 summarizes the considered curing conditions for each batch.

6.4.3 Curing and Moisture Content of Prisms

Prisms were first stored for 10 days in water and then for 5 days in an oven in 30 to 40°C (up to the moisture loss of approximately 2.5 % of mass). Then they were stored in an indoor air condition.

Tests and Mixture Characteristics

Table 7: Mass loss and moisture content of the cylinders and small-remained cylinder pieces, dried out under 105°C

Mass loss and moisture content								
Batch	Specimen	M at 4 days (gr)	M at 28 days (gr)	M at 32 days (gr)	M at 33 days (gr)	M at 34 days (gr)	Moisture content [M.-%]	Moisture content (gr)
I	1	--	529.3	--	--	498.7	5.78	30.59
	2	--	518.8	--	--	483.2	6.86	35.59
	Average	--	524.05	--	--	490.9	6.32	33.15
II	1	529.2	529.2	499.8	--	--	5.56	--
	2	533	519	504.3	--	--	5.38	--
	Average	531.3	524.1	502.05	--	--	5.47	29.25
	RS1	119.1	114.8	111.6	--	--	6.30	--
	RS2	123.7	119.6	116.5	--	--	5.82	--
	RS3	125	121	118	--	--	5.60	--
	Average	122.6	118.47	115.37	--	--	5.91	7.23
III	RS1	140.7	141.5	--	132.7	--	5.69	--
	RS2	259.2	260.8	--	244.5	--	5.67	--
	RS3	249.1	250.3	--	234.8	--	5.74	--
	RS4	247.8	248.9	--	233.6	--	5.69	--
	RS5	214	215.1	--	201.7	--	5.75	--
	Average	222.16	223.32	--	209.46	--	5.71	12.7

Table 8: Curing condition of each batch

Designation of batch	Duration of water curing (days)	Duration of oven curing (days)	Temperature in oven (°C)
1	13	2	40
1	13	0	---
2	10	4	30
3	11	4	30
4	11	4	30

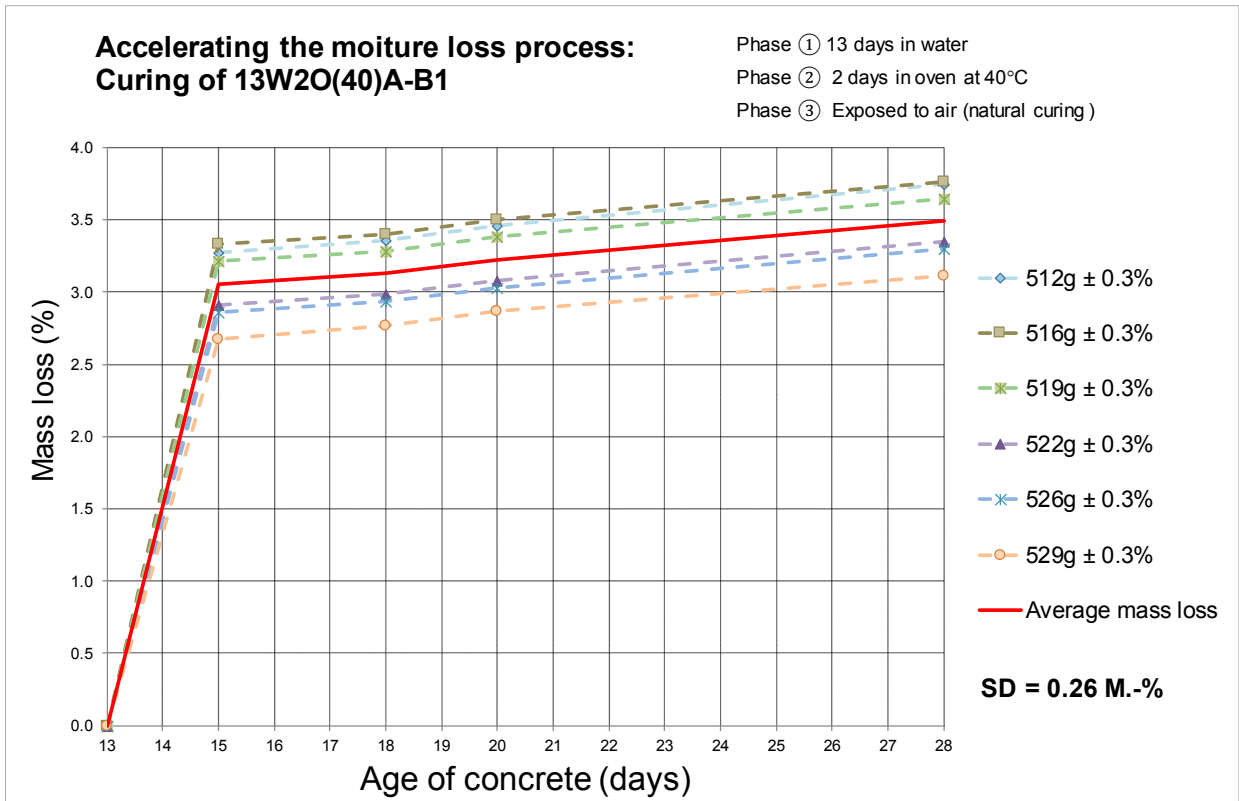


Figure 56: Mass loss of WOA specimens of batch 1 relative to the 13-day-old-saturated concrete specimens

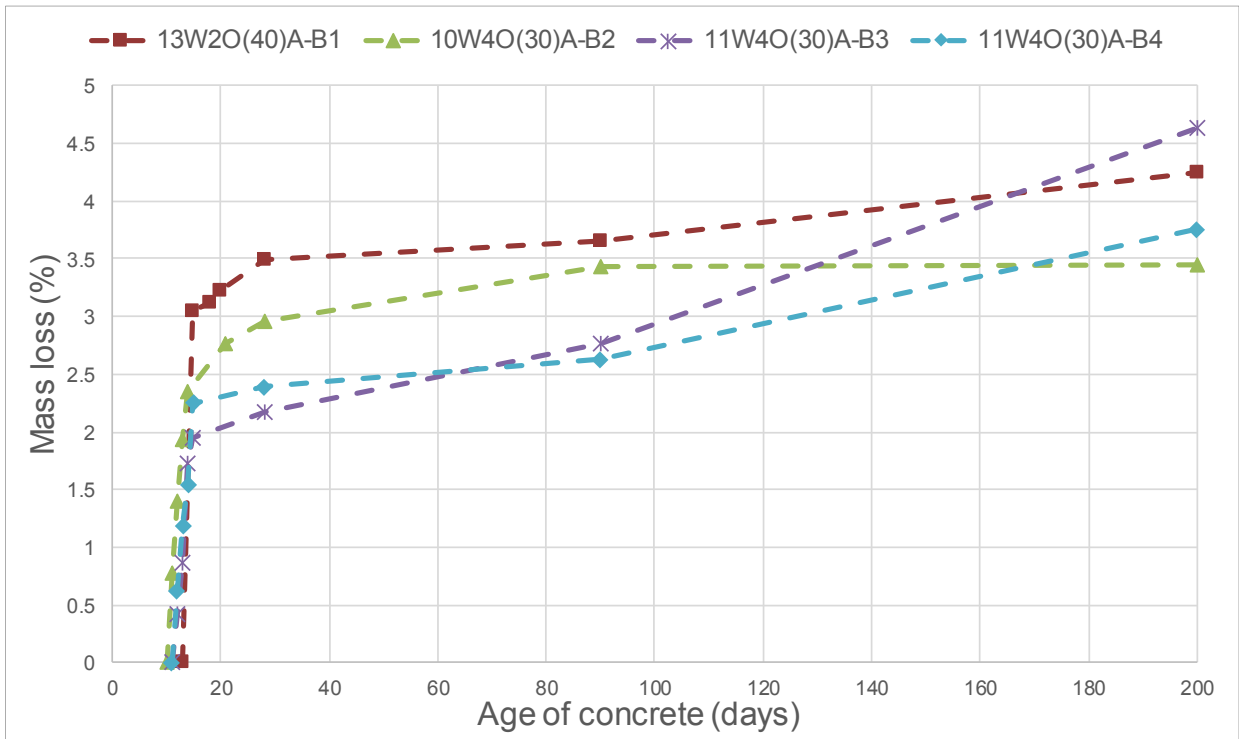


Figure 57: Mass loss of all four batches during 200 days

7 Compression Tests at Ambient Temperatures and Thermal Considerations

To have a good understanding of stress-strain behaviour and generally material model at elevated temperatures, the first step should be analysing the concrete mechanical properties of all four batches and comparing them with the existing proposed properties according to EN 1992-1-1 at ambient temperature. It should be noted, the stress-strain curves according to EN 1992-1-1 are proposed for the concrete with the specified normative size of specimens.

Tests performed in the laboratory at ambient temperatures are divided into the following tests:

Cylinders

- Stress-strain tests after 28, 90 and 200 days, whereas due to use of CEM I 52.5 N, it is assumed that the growth of concrete compressive strength after 60 days is negligible;
- Elastic modulus tests after 28, 90 and 200 days.

Cubes

- Strength tests for 28-day-water-immersed specimens.

7.1 Compressive Strength and Stress-strain Tests

In order to do compressive stress-strain tests and to measure the deformations to the point of failure, a testing machine of type UMP with the maximum applicable force of 250 kN has been used. The loading speed is chosen 0.6 MPa/s which corresponds to the proposed rates in DIN EN 12390-3 (0.6 ± 0.2 MPa/s).

To evaluate strains and correspondingly stress-strain diagrams to the point of failure, a deformation measuring device of type WAT is used. The testing machine is fixed on the concrete cylinder specimen with a pre-load of 1-2 kN. The accuracy of the used measuring device is ± 10 nanometres.

7.1.1 Compressive Strength Results

Measured 28-day cube and cylinder compressive strength values for different batches are listed in Tab. 9.

Table 9: Average values of compressive strength for 28-day-old cubes and cylinders

Designation of batch	CEM 52.5 N (older cement = O, just opened packet = N)	Measured average $f_{cm,cube}$ (MPa)	Measured average $f_{cm,cyl}$ (MPa)	Amount of PP-fibres (kg/m ³)
B1	O	42.75	20.5	2
B2	O	---	26.0	2
B3	N	48.71	40.0	2
B4	N	47.56	41.0	0

Further, the average 200-day compressive strength of cylinder specimens (10-13 days laid in water and 2-4 in the oven and then exposed to indoor air) are listed in Tab. 10 and compared with 28-day cylinder strength for specimens laid 4 weeks in water. Besides the designations of batches, new designations were defined, as illustrated in Tab. 10, based on strength class and if there is PP-fibres in the considered batch: batches 1 and 2 designated with C30-PP, batch 3 with C50-PP and batch 4 with C50. It should be also noted that due to the process of curing in the oven, the hydration process is accelerated and it might influence the 28-day concrete compressive strength of cylinders. Further, the concrete strength of all batches within age of 200 days are plotted in Fig. 58.

Table 10: Average values of compressive strength for 28-and 200-day-old concrete for cylinder specimens

Designation of batch	CEM 52.5 N (older cement: O, just opened packet: N)	28 days		200 days	Designation based on concrete grade and PP-fibres content
		Duration of water curing (days)	$f_{cm,cyl,28}$ (MPa)	$f_{cm,cyl,200}$ (MPa)	
B1	O	13	20.5	30.0	C30-PP
B2	O	10	26.0	35.6	
B3	N	11	40.0	52.9	C50-PP
B4	N	11	41.0	52.0	C50

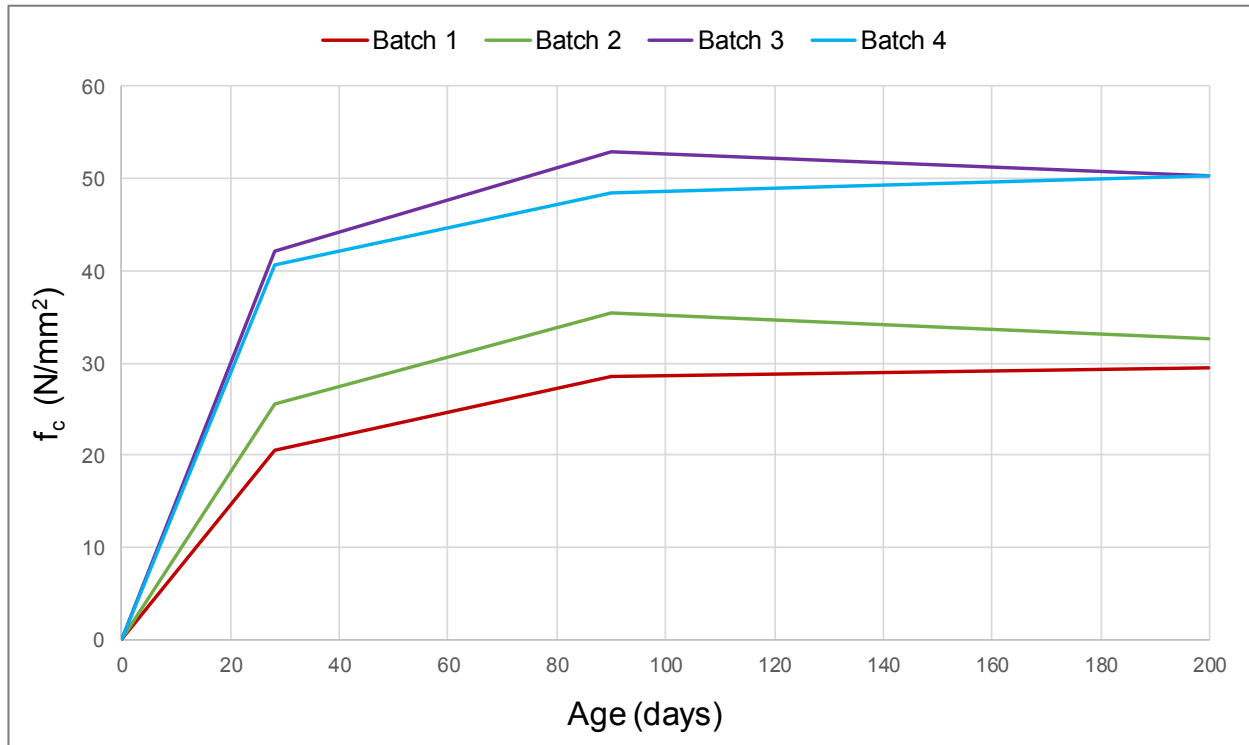


Figure 58: Concrete strength of four batches during 200 days

7.1.2 Stress-strain Results

Stress-strain models for nonlinear structural analysis and cross-section design in EN 1992-1-1 consider strains at peak stress ϵ_{c1} and ϵ_{c2} of 0.002 and 0.0022 and an ultimate strain of 0.0035. The value of strain at peak stress, ϵ_{c1} , from the tests for the first two batches have been observed to be considerably higher than normative values whereas for batches 3 and 4 the corresponding values are slightly larger than the EN 1992-1-1's normative values. EN 1992-1-2 also gives ϵ_{c1} values that are slightly higher than EN 1992-1-1's values. These are given in Tab. 11. Further, stress-strain curves of cylinder specimens at ambient temperatures for all four batches are illustrated in Annex D.

Table 11: Strain at peak stress according to EN 1992-1-1 and tests

Age	Designation of batches	ϵ_{c1} according to EN 1992-1-1	ϵ_{c1} according to EN 1992-1-2	ϵ_{c1} from tests
90 days	B1	0.0020	0.0025	0.0031
	B2	0.0021		0.0035
	B3	0.0023		0.0025
	B4			0.0028

7.2 Modulus of Elasticity Tests

To evaluate the modulus of elasticity, DIN EN 12390-13 suggests to use the secant modulus. It gives further detailed information on how to conduct cyclic tests to evaluate the modulus of elasticity (see Fig. 59). The secant modulus evaluated from the stress-strain curve tests and estimated from modulus of elasticity tests showed a good agreement to the normative values.

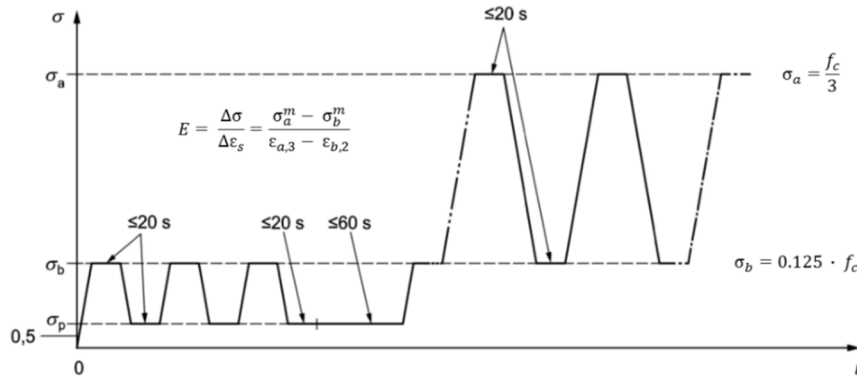


Figure 59: Modulus of elasticity test procedure

For the sake of comparison, beside the deformation-measuring device of type WAT (see Fig. 60a), a measuring device of type DD1 is also used for some modulus of elasticity tests (see Fig. 60b). The accuracy is similarly ± 10 nanometres.

The corresponding values of stabilized moduli of elasticity, $E_{c,s}$, for 90-day-old specimens are listed and compared with secant moduli of elasticity, E_{cm} , from EN 1992-1-1 for all batches in Tab. 12. The results show a good agreement with EN 1992-1-1's values. Further, the moduli of elasticity of all batches within 200 days are plotted in Fig. 61.

Table 12: Moduli of elasticity according to the test results and EN 1992-1-1

Age of concrete (days)	Designation of batches	E_{cm} from EN 1992-1-1 (GPa)	$f_{cm,cyl}$ (MPa)	$E_{c,0}$ (GPa)	$E_{c,s}$ (GPa)	$E_{c,s} / E_{cm}$
90	B1	30	30.0	22.0	27.1	0.9
	B2	31	35.6	26.6	30.8	0.99
	B3	35	52.9	29.8	33.9	0.96
	B4	35	52.0	27.1	32.5	0.93



Figure 60a: Configuration of type WAT deformation measuring device

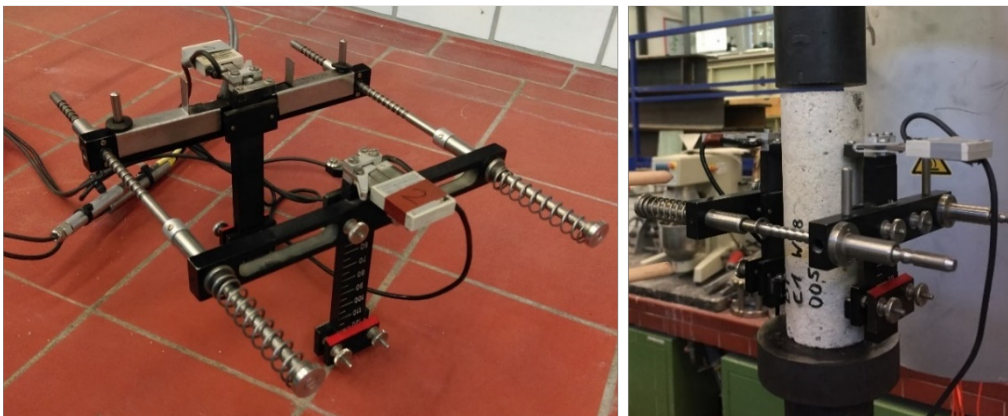


Figure 60b: Deformation measuring device of type DD1

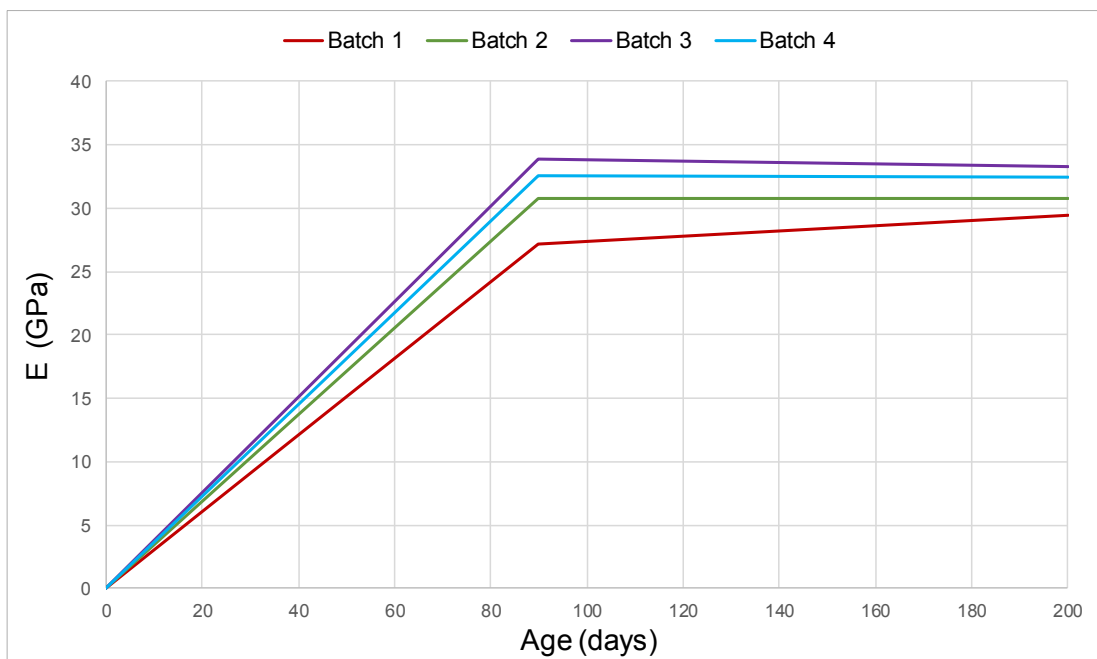


Figure 61: Modulus of elasticity of all batches for duration of 200 days

8 Calibration of Test Results at Elevated Temperatures

8.1 General

For the tests, a clamshell-furnace with a length of 34 cm has been used. The available used electro mechanical testing device with a maximum applicable load of 250 kN has a displacement measuring device which is installed on the side support of the equipment. There was no other measuring device available for the existing small clamshell-furnace that could be used or installed on the specimen. The displacement measurement includes a fraction of total displacement of the traverse. Therefore, values of displacements should be modified and corrected. In this regard, (Peter, 2016) has conducted calibration tests with the same machine using a 46.5-cm clamshell-furnace on a nickel-iron alloy metal specimen or so called Invar that generally possess a low thermal expansion. Figure 62 shows the test set-up of (Peter, 2016) using an Invar specimen and clamshell-furnace parallel with the test set-up of used in this study for calibration tests.

These tests are performed to estimate the amount of error induced via equipment or energy saved in the testing equipment at the elevated temperatures.

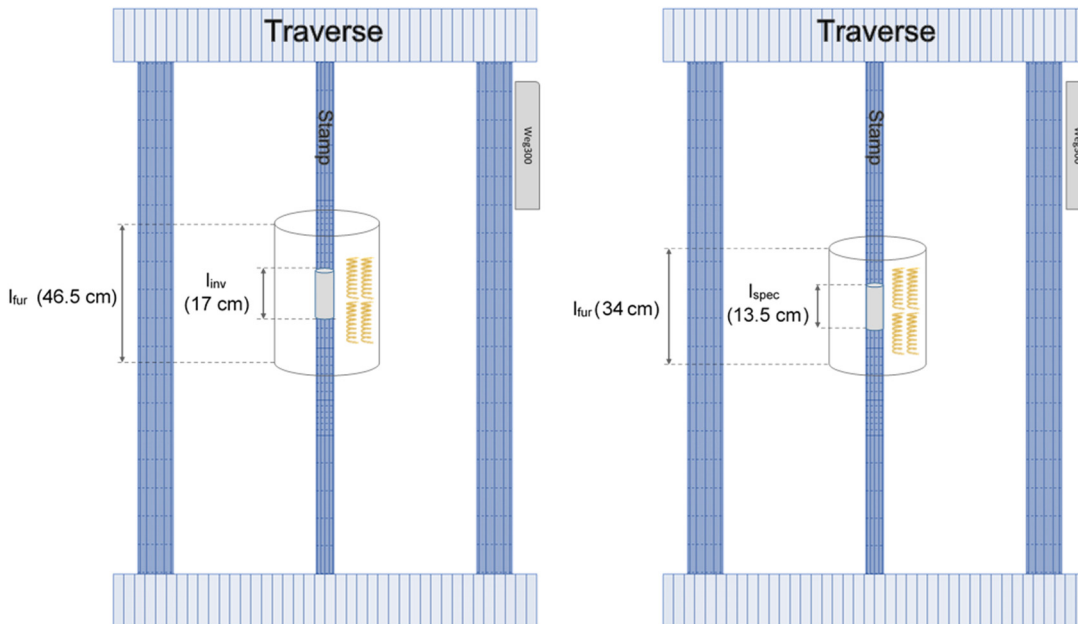


Figure 62: Calibration test set-up according to (Peter, 2016) (left), the used set-up in this study (right)

It is assumed by (Peter, 2016) that the Invar specimen has low thermal expansion and has the same material properties as the pressing stamp at the elevated temperatures. Therefore, the amount of error induced via equipment at the elevated temperatures can be estimated using a simplified method. Three types of tests are performed by (Peter, 2016) and the results are used partially for the sake of comparison in this study. He performed tests on an Invar cylinder specimen having a diameter of 6 cm and length of 17 cm under an applied heating rate of $R = 4$ K/min as follows:

- Transient test to estimate the error induced via equipment for the unconstrained condition (thermal strain) to 800°C;
- Transient test by applying a constant load level to 800°C ($\alpha = 0.1$);
- Steady tests under an applied load of 120 kN for 200, 400 and 600°C.

8.2 Scaling Factor for Free Thermal Elongation Based on Proposed Method

The total free elongation for the performed tests and conducted by (Peter, 2016) on an Invar specimen under the heating-up procedure are shown in Fig. 63.

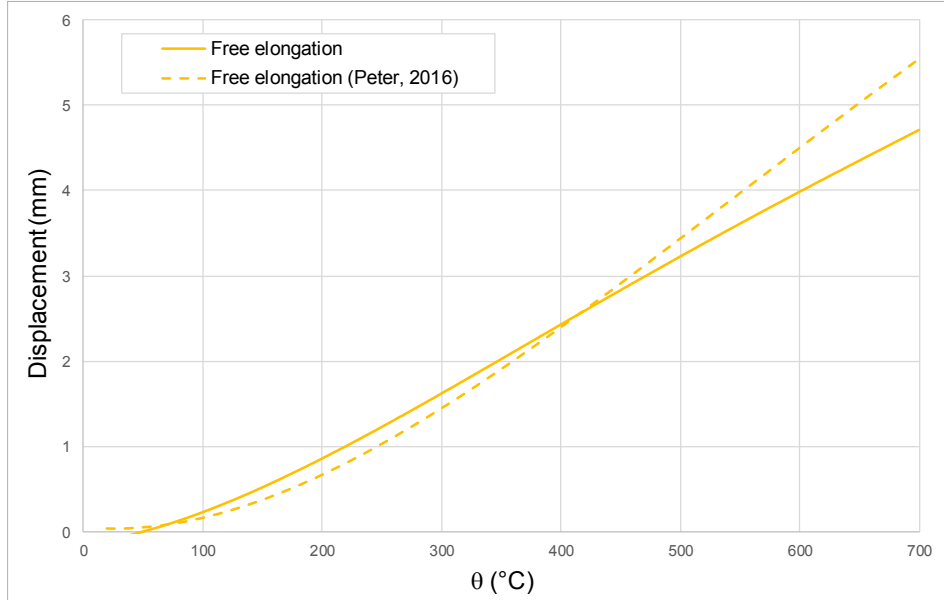


Figure 63: Free elongation for tests with Invar specimen performed by (Peter, 2016) and from the tests

Since the thermal material properties of compressing stamp and the Invar specimen used in these series of tests are not particularly specified, the following method is proposed to estimate the amount of error induced via equipment and correspondingly estimating the scaling factor.

The following components are explicitly assumed on the equipment to take apart in the free total displacement (see Fig. 64):

Affected length of stamp by elevated temperatures:

- $l_{s,in}$: is the affected length of stamp on the top and bottom of the Invar specimen within the furnace. It is assumed that due to relatively high thermal conduction of stamp and low heating rate used for the tests, there is a uniformly distributed temperature ruling the stamp cross-section during the heating-up;

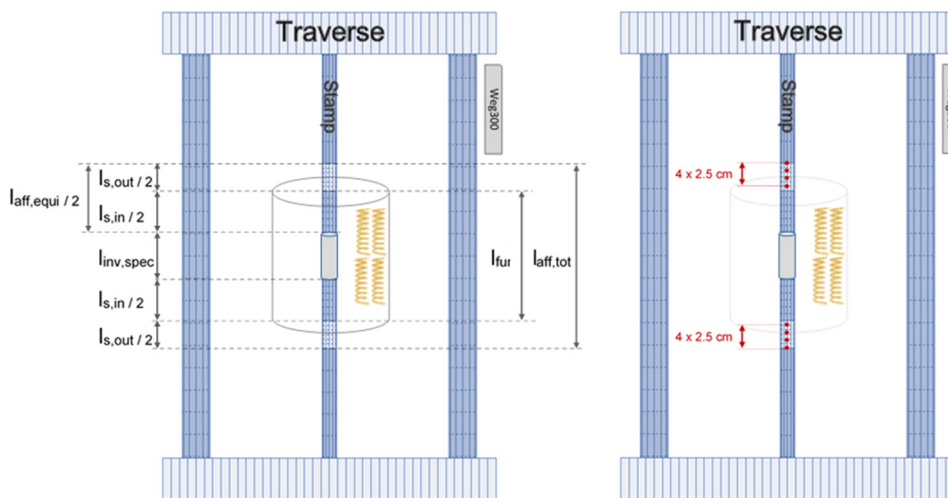


Figure 64: Different regions in total free elongation of the test with Invar specimen

- $l_{s,out}$: is the affected length of stamp on the top and bottom of furnace (outside of furnace). It is assumed that approximately 10 cm above and 10 cm below the furnace is affected by the elevated temperatures;
- $l_{aff,equi}$: the affected length of equipment is the sum of $l_{s,in}$ and $l_{s,out}$.

Invar specimen exposed to the elevated temperatures:

- $l_{inv,spec}$: the Invar specimen used for the test with a length of 20 cm.

It can be now considered that there are corresponding free elongations for each region. Elongations are temperature-dependent and the sum of different components give the free displacement as:

$$\Delta l_{s,in}(\theta) + \Delta l_{s,out}(\theta) + \Delta l_{inv,spec}(\theta) + \Delta l_{equi}(\theta) = \Delta l_w(\theta) \quad (46)$$

$$\alpha_{s,in}(\theta) \Delta \theta_{s,in} l + \alpha_{s,out}(\theta) \Delta \theta_{s,out,ave} l + \alpha_{inv,spec}(\theta) \Delta \theta_{inv,spec} l + \Delta l_{equi}(\theta) = \Delta l_w(\theta) \quad (47)$$

where $\Delta l_{equi}(\theta)$ is the error induced via equipment as a function of temperature and $\theta_{s,out,ave}$ refers to the average temperature on affected part outside the stamp. The temperatures were measured on the stamps on different points with 2.5-cm intervals along the stamp for two tests with the same heating rates as used in the Invar test. Further, the average temperature $\theta_{s,out,ave}$ is determined as a function of temperature inside the furnace by:

$$\frac{\theta_{s,out,ave}}{\theta_{in}} = f(\theta_{in}) \quad (48)$$

The main issue in solving Eq. 47 is that free thermal expansion coefficients have not been available. Therefore, using nonlinear regression method, the function of thermal expansion coefficient is determined for all components so that for each temperature input:

$$\Delta l_w(\theta) - (\alpha_{eq}(\theta) \Delta \theta_{s,in} l + \alpha_{eq}(\theta) \Delta \theta_{s,out,ave} l + \alpha_{eq}(\theta) \Delta \theta_{inv,spec} l) = \Delta l_{equi}(\theta) = 0 \quad (49)$$

where $\alpha_{eq}(\theta)$ is the equivalent free thermal expansion coefficient for all the components. Having the error induced via equipment equal zero, the total elongation is only dependent on the thermally elongated parts. This means on the other hand, the elongation of the three components with $\alpha_{eq}(\theta)$ accumulates the error induced via equipment.

The proportion of elongation due to two affected components of stamps in the furnace and outside of furnace now can be assumed as the amount of error induced via equipment as a function of temperature:

$$\alpha_{eq}(\theta) \Delta \theta_{s,in} l + \alpha_{eq}(\theta) \Delta \theta_{s,out,ave} l = \Delta l_{aff,equi}(\theta) \quad (50)$$

The scaling factor then can be related to the total displacement and is again function of temperature:

$$\frac{\Delta l_{aff,equi}(\theta)}{\Delta l_{w,inv}(\theta)} = S(\theta) \quad (51)$$

The real free elongation of concrete cylinder specimen then can be expressed as:

$$\Delta l_c(\theta) = \Delta l_{w,c}(\theta) - S(\theta) \cdot \Delta l_{w,inv}(\theta) \quad (52)$$

where $\Delta l_c(\theta)$ refers to thermal elongation of concrete specimen at elevated temperature θ (index c stands for concrete).

8.3 Different Assumptions to Evaluate Scaling Factors

(Peter, 2016) has assumed by performing such calibration tests, a scaling factor can be evaluated according to the followings:

$$\Delta l_c(\theta) = \Delta l_{w,c}(\theta) - S \cdot \Delta l_{w,Inv}(\theta) \quad (53)$$

$$S = I - \frac{l_{spec}}{l_{0,eq}} \quad (54)$$

where:

at $\theta =$ ambient temperature, $l_{0,eq} = l_{fur}$ (see Fig. 64)

$$S = I - \frac{l_{spec}}{l_{fur}} \quad (55)$$

and at $\theta = 700^\circ\text{C}$

$$l_{0,eq,\theta=700^\circ\text{C}} = \frac{\Delta l_{Inv,test}}{\alpha_{Inv,ave} \cdot \Delta \theta} \quad (56)$$

$$S = I - \frac{l_{spec}}{l_{0,eq,\theta=700^\circ\text{C}}} \quad (57)$$

It is assumed that thermal coefficient expansion of the Invar specimen and stamps are invariable at higher temperatures and $\alpha_{Inv,ave}$ is assumed to be an average value of thermal coefficient expansion for these two. The scaling factors for different temperature values are then interpolated between ambient temperature and 700°C . Further, an average thermal expansion coefficient of $\alpha_{Inv,ave} = 10.7 \cdot 10^{-6} \text{ K}^{-1}$ is assumed that does not correspond to any existing nickel-iron alloy metal known.

Since assuming an average thermal expansion coefficient in this method is the most important consideration and assumption to estimate the equivalent affected length at elevated temperatures, $l_{0,eq,\theta}$, and correspondingly scaling factor S , for the sake of comparison, 4 assumptions are additionally made and discussed regarding this parameter:

Assumption 1 used in (Peter, 2016) by taking into account $\alpha_{Inv,ave}$

Since there is no information on percentage of nickel-iron alloy or generally the material properties of both Invar and stamps used in this study, it is assumed that Invar36 as the most common used Invar was meant in his study. (Peter, 2016) assumed that the both stamps and Invar specimen have the same material properties as Invar36, and the thermal expansion coefficient of these two do not change with temperature increase. Thus an average coefficient of thermal expansion is assumed for the final temperature of 700°C for both materials. Since α_{Inv36} at 700°C is more than 10 times larger than this coefficient at the ambient temperature, considering an average thermal expansion coefficient to estimate the equivalent affected length of specimen at the elevated temperatures is not an accurate assumption.

Assumption 2:

It is assumed that both stamps and the Invar specimen have the similar material properties and have an average equivalent coefficient of thermal expansion at the elevated temperatures, $\alpha_{eq,ave}$.

$$l_{0,eq,\theta=700^\circ\text{C}} = \frac{\Delta l_{Inv,test}}{\alpha_{eq,ave} \cdot \Delta \theta} \quad (58)$$

$$S = I - \frac{l_{spec}}{l_{0,eq}(\alpha_{eq,ave})} \quad (59)$$

Assumption 3:

It is assumed that both stamps and the Invar specimen have the same material properties as Invar36 and the equivalent length can be estimated for example at 700°C by taking into account of $\alpha_{Invar36, \theta=700^\circ C}$:

$$l_{0,eq,\theta=700^\circ C} = \frac{\Delta l_{Invar, test}}{\alpha_{Invar36, \theta=700^\circ C} \cdot \Delta \theta} \quad (60)$$

$$S = I - \frac{l_{spec}}{l_{0,eq}(\alpha_{Invar36})} \quad (61)$$

Assumption 4:

It is assumed that both stamps and the Invar specimen have an equivalent thermal expansion α_{eq} and the equivalent length can be estimated at the point of 700°C by taking into account of $\alpha_{eq, \theta=700^\circ C}$:

$$l_{0,eq,\theta=700^\circ C} = \frac{\Delta l_{Invar, test}}{\alpha_{eq, \theta=700^\circ C} \cdot \Delta \theta} \quad (62)$$

$$S = I - \frac{l_{spec}}{l_{0,eq}(\alpha_{eq, \theta})} \quad (63)$$

In Tab. 13, the lower and upper values of S factors in the beginning and at 700°C according to the different assumptions are listed. S factors for temperatures between initial and final points are linearly interpolated.

Table 13: Equivalent affected length and scaling factors based on different assumptions

Assumption	Temperature (°C)	Equivalent affected length $l_{0,eq}$ (mm)	$\Delta l_{W, Invar, test}$ (mm)	$\alpha_{Invar36, \theta=700^\circ C}$ (K ⁻¹)·10 ⁻⁶	$\alpha_{eq, \theta=700^\circ C}$ (K ⁻¹)·10 ⁻⁶	$\alpha_{Invar36, ave}$ (K ⁻¹)·10 ⁻⁶	$\alpha_{eq, ave}$ (K ⁻¹)·10 ⁻⁶	Scaling factor S
	20	340	0					0.603
1	700	990	4.71	---	---	7	---	0.864
2		433		---	---	---	16	0.688
3		700		12.4	---	---	---	0.760
4		382		---	18.4	---	---	0.647

S factors for the four assumptions are compared with the S factor proposed in the pervious section in Fig. 65. The purified thermal strain values for test 137 using scaling factors due to four different assumptions and the explained proposed method in the previous section are shown in Fig. 66. The red and dark blue lines show the purified thermal strains based on the simplified assumption that the both stamps and Invar specimen have the same thermal expansion coefficient as Invar36 (assumptions 1 and 3). The implausible results of assumptions 1 and 3 are due to the overestimation of scaling factors estimated based on these assumptions.

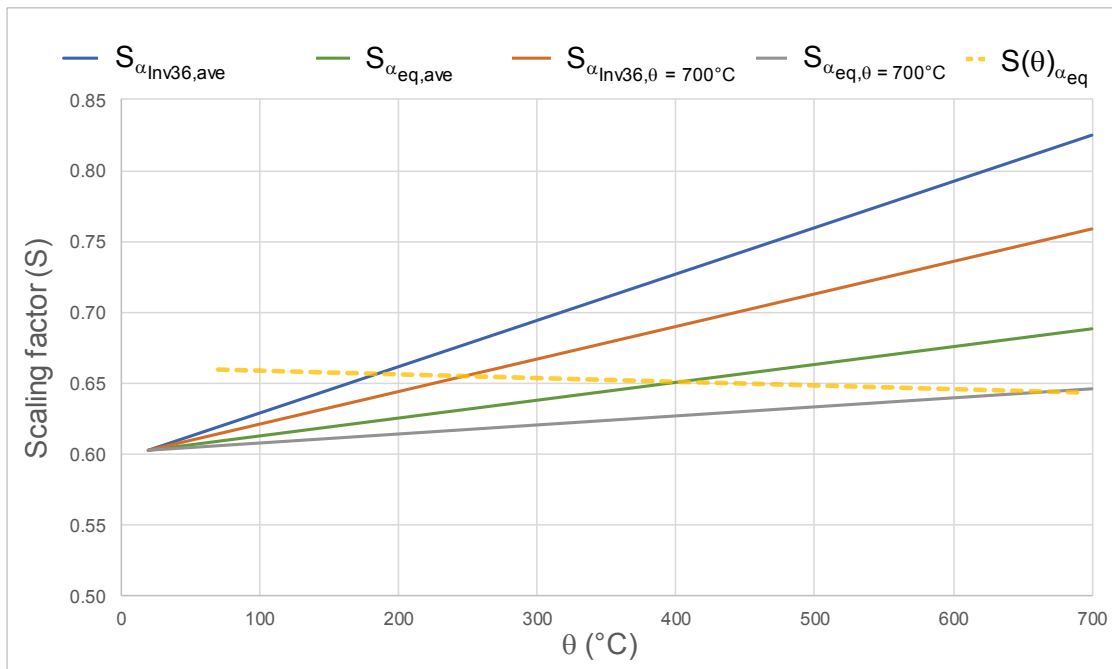


Figure 65: Scaling factors to estimate thermal strain of concrete due to different assumptions

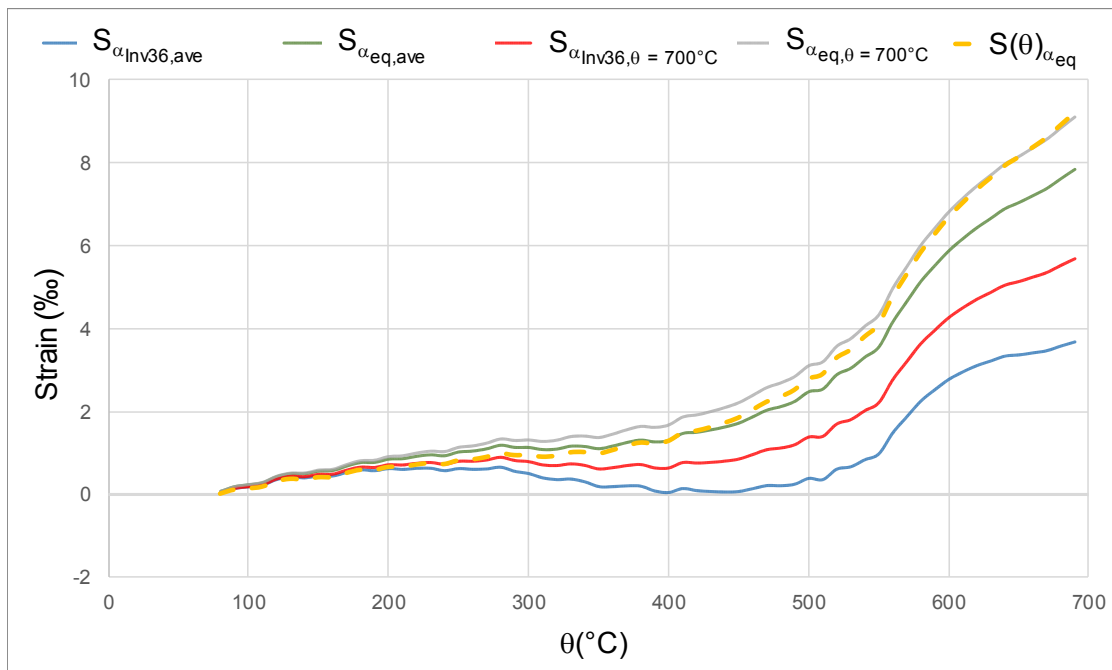


Figure 66: Purified thermal strains by considering different scale factors for test 193

8.4 Compressive Steady-state Tests at Elevated Temperatures

In this section, first the simplified calibration method considered by (Peter, 2016) is discussed and then the two proposed methods by author. (Peter, 2016) , as explained, conducted steady tests with a pre-load of 120 kN on an Invar specimen. In the latter, it is assumed that the following components are known:

F : force applied on the specimen = 120 kN

A_{Inv} : area of Invar specimen

E_{Invar} : modulus of elasticity of Invar specimen = 143 GPa at 20°C

Then using the displacement results of calibration tests the equivalent length of equipment at the ambient temperature can be estimated by:

$$\frac{F}{A_{Inv}} = \frac{\Delta l_{test,Inv}}{l_{eq}} \cdot E_{Inv} \quad (64)$$

Therefore, having the total displacement, $\Delta l_{test,Inv}$, the equivalent modulus of elasticity of the Invar specimen and stamps can be estimated at higher temperatures. The estimated values are given in Tab. 14.

Table 14: Displacements measured and $E_{eq,Inv}$ measured for calibration tests with Invar specimen according to (Peter, 2016)

θ (°C)	20	200	400	600
Δl_{Inv} under an applied load of 120 kN (mm)	0.65	0.66	0.67	0.69
$E_{eq,Inv}$ (GPa)	143.00	140.83	138.73	134.71

The axial deformation of concrete specimen can be therefore estimated as:

$$\Delta l_c = \Delta l_w - \Delta l_{equi} \quad (65)$$

where:

$$\Delta l_{equi} = \frac{F \cdot l_{eq}}{A_{Inv} \cdot E_{eq,Inv}} \quad (66)$$

The results of stress-strain tests on Invar36 specimens at different constant elevated temperatures performed by (Li, et al., 2017) show the elastic moduli change at the elevated temperatures (see Fig. 67). Further, the results of displacement recorded according to (Peter, 2016)’s calibration test show that error induced via equipment based on the deformation of stamps is almost at the elevated temperatures identical to the ambient temperature. Change in the deformation at different temperatures under a constant applied load of 120 kN in the calibration test is in order of 0.01-0.04 mm (see Tab. 14) from ambient temperature to 600°C which is compared to the deformation of cylinder concrete specimens at elevated temperatures and total deformation of the stamp negligible. Further, as given in Tab. 15, the minimum yield strength of Invar36 at

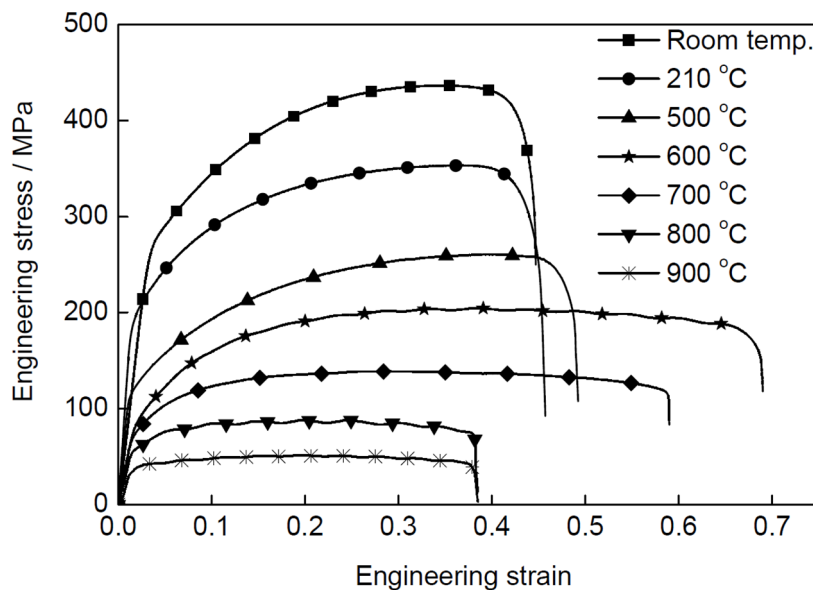


Figure 67: Stress-strain curves of Invar36 at elevated temperatures according to (Li, et al., 2017)

temperatures 800°C is 56 MPa that is far larger than the applied stresses at 800°C on the concrete specimens in this study.

Table 15: Strength of Invar36 at elevated temperatures (Li, et al., 2017)

θ (°C)	Yield strength (MPa)	Ultimate tensile (MPa)
Room temperature	292	447
210	185	352
500	113	267
600	81	203
700	71	138
800	56	88

The simplified method used in (Peter, 2016) inherits the following assumptions and considerations. These are investigated in the next section:

- Equivalent modulus of elasticity is assumed to be equal to 143 GPa at ambient temperature. 143 GPa may refer to Invar36 material properties in the reality but is not representative of equivalent E_{eq} which is;
- Modulus of elasticity of equipment is assumed to be constant for different force intervals at ambient temperature.

8.4.1 Equivalent Modulus of Elasticity for Calibration Tests at Ambient Temperature

Considering both Invar specimen and stamps have similar mechanical properties, the error in measuring displacements is much larger in the lower force levels. The strain-force result of the calibration tests on the Invar specimen at ambient temperature with the maximum force level of 100 kN is shown in Fig. 68. Different force intervals of $F_0 = 0-8$ kN ($\alpha = 0-0.1$), 8-24 kN ($\alpha = 0.1-0.3$), 24-48 kN ($\alpha = 0.3-0.6$) and 48-100 kN are investigated. In this case, the displacement of Invar specimen is measured via WAT external displacement measuring device parallel to total recorded displacement. The total length of stamp and Invar

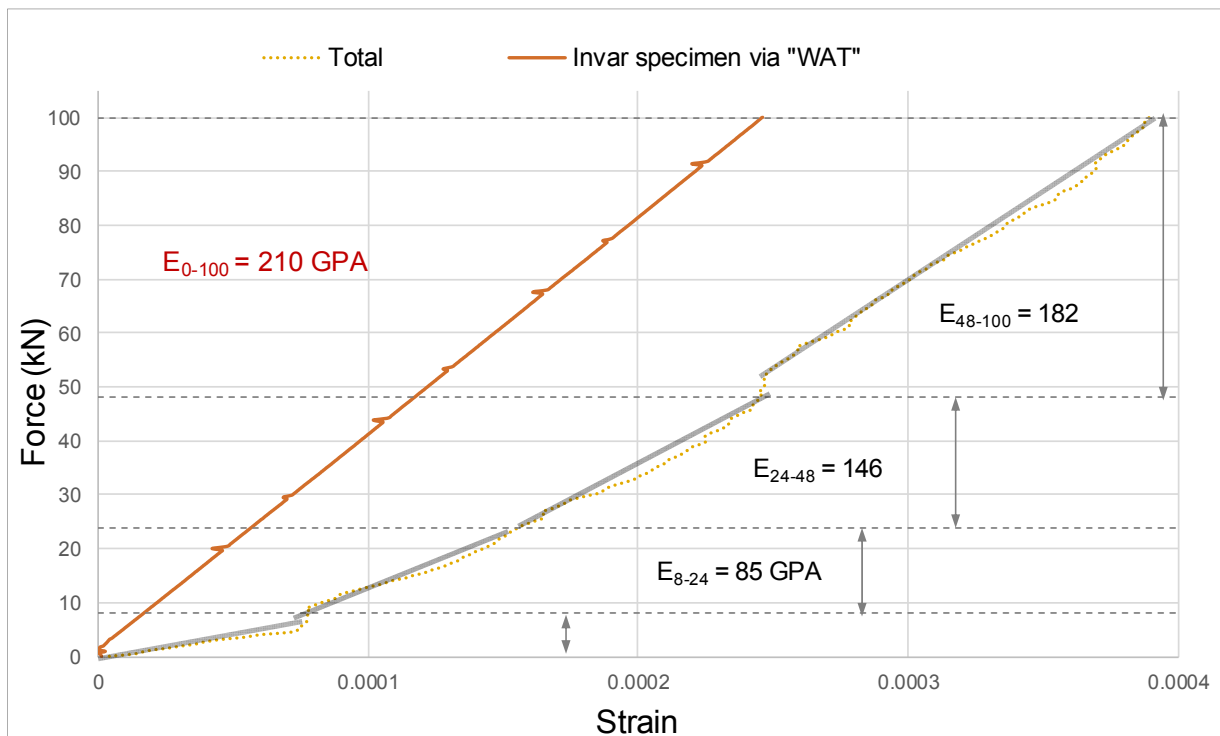


Figure 68: Moduli of elasticity for calibration tests with Invar specimen at ambient temperature

specimen are $l_0 = 950$ mm. The modulus of elasticity calculated by WAT on Invar specimen can be assumed to have a good accuracy and remain constant for all force intervals and is equal to 210 GPa. On the other hand, the equivalent modulus of elasticity calculated for the both stamps and Invar specimen measurements shows that for the lower force levels the equivalent modulus of elasticity is much lower compared to the real values as the displacements and correspondingly strains are highly overestimated in these levels. The average equivalent modulus of elasticity, $E_{eq,ave}$, for the force range 0-100 kN can be then taken as 110 GPa. It can be noted from Fig. 68 that for the load level 0-8 kN and 8-24 kN the equivalent modulus of elasticity, 30 GPa and 85 GPa respectively, are much lower compared to the real modulus of elasticity of equipment. Equivalent modulus of elasticity evaluated based on measurements are very low up to 8 kN (or to 10 kN) and low for the force interval up to 8-24 kN. Thus, using an average equivalent modulus of elasticity at the ambient temperature may result in overestimation of axial deformation of concrete specimens in the low force levels. Further, the displacements recorded at the maximum applied load and the corresponding equivalent moduli of elasticity are listed in Tab. 16.

Table 16: Equivalent moduli of elasticity for different force intervals

θ (°C)	20			
F (kN)	0-8	8-24	24-48	48-100
$\Delta l_{Inv,test}$ at max force (mm)	0.07	0.15	0.23	0.37
$E_{eq,cyc}$ (GPa)	30	85	146	182
$E_{eq,ave}$ (GPa)	57.5		---	
	87			---
	110			

8.4.2 Equivalent Modulus of Elasticity of Steady-state Tests at Elevated Temperatures Based on 1st Proposed Method

Three different steady tests performed with heating condition identical to the tests on the concrete specimens ($R = 5$ and 10 K/min) under loading of 0-100 kN at 700°C . Equivalent modulus of elasticity for different force intervals are plotted in Fig. 69. In addition, the results of the tests with $R = 10$ K/min are listed in Tab. 17. Using an equivalent average modulus of elasticity for 0-100 kN, the lower and upper boundaries are 66 and 78 GPa (with an average of 72 GPa) that compared to the ambient temperature gives a reduction factor of 0.6 and 0.71 respectively.

The average equivalent modulus of elasticity for 0-100 kN of other temperatures can be further linearly interpolated between average equivalent modulus of elasticity at 700°C (72 GPa) and average equivalent modulus of elasticity at ambient temperature being equal 110 GPa, see Tab.18.

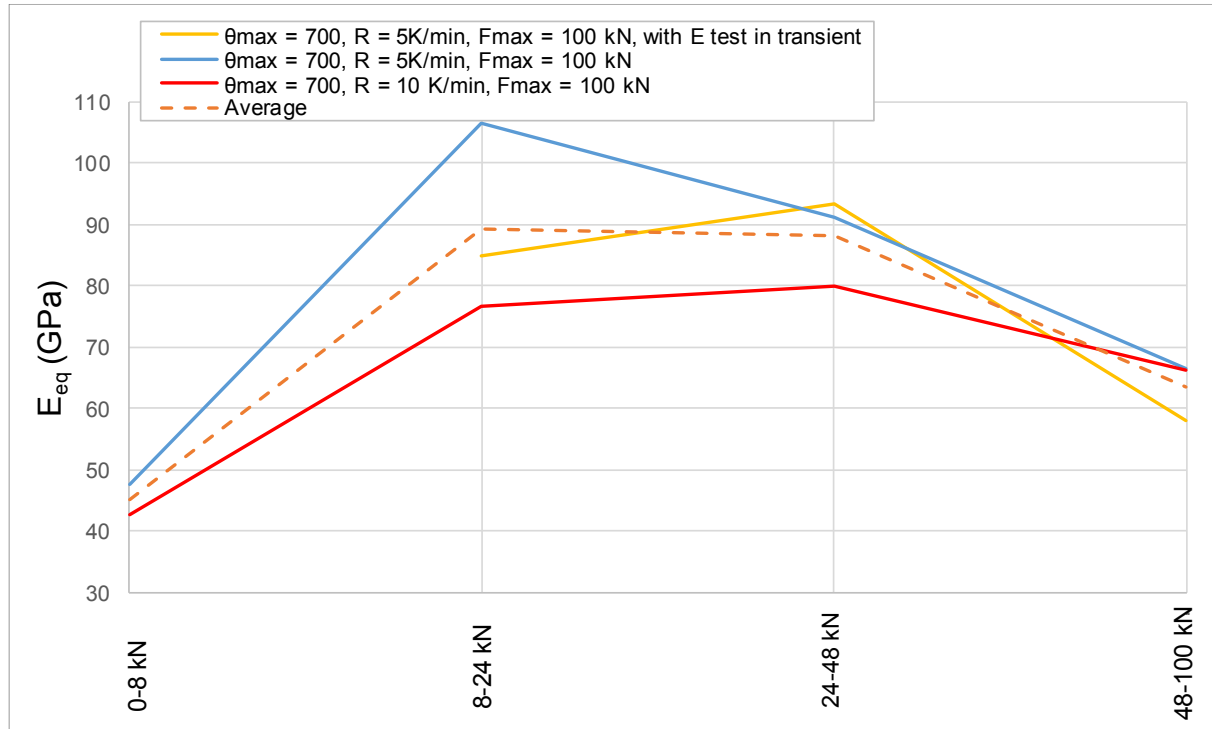


Figure 69: Equivalent moduli of elasticity for the steady calibration tests at different force intervals

Table 17: Equivalent moduli of elasticity for different force intervals and average equivalent modulus of elasticity

From the steady Invar test (0-100 kN)				
θ_{max} (°C)	700			
F (kN)	0-8	8-24	24-48	48-100
$\Delta l_{Inv, test}$ at max force (mm)	0.09	0.19	0.35	0.72
E_{eq} (GPa)	41	76	80	66
$E_{eq, ave, tot}$ (GPa)	66			

Table 18: Average equivalent moduli of elasticity for each temperature level from steady tests

θ_{max} (°C)	20	100	200	300	400	500	600	700
$E_{eq, ave, tot}$ (GPa)	110.0	105.5	99.9	94.4	88.8	83.1	77.6	72.0

Having now the forces and correspondingly the stresses in the equipment as well as average equivalent modulus of elasticity at different temperatures, the corresponding equivalent strain induced via equipment can be estimated in advance:

$$\frac{F}{A_{equi}} = \sigma_{equi} \quad (67)$$

$$\frac{\sigma_{equi}}{E_{eq, ave}} = \epsilon_{eq} = \frac{\Delta l_{eq}}{l_{0, eq}} \quad (68)$$

where $l_{0, eq}$ is the equivalent length of equipment that is for the tests carried out equal 750 mm.

Therefore, at each step the corresponding displacement of the concrete specimen can be expressed as:

$$\Delta l_c(\theta) = \Delta l_{w,c}(\theta) - \Delta l_{eq}(\theta) \quad (69)$$

The equivalent displacement of equipment at different temperatures are plotted in Fig. 70.

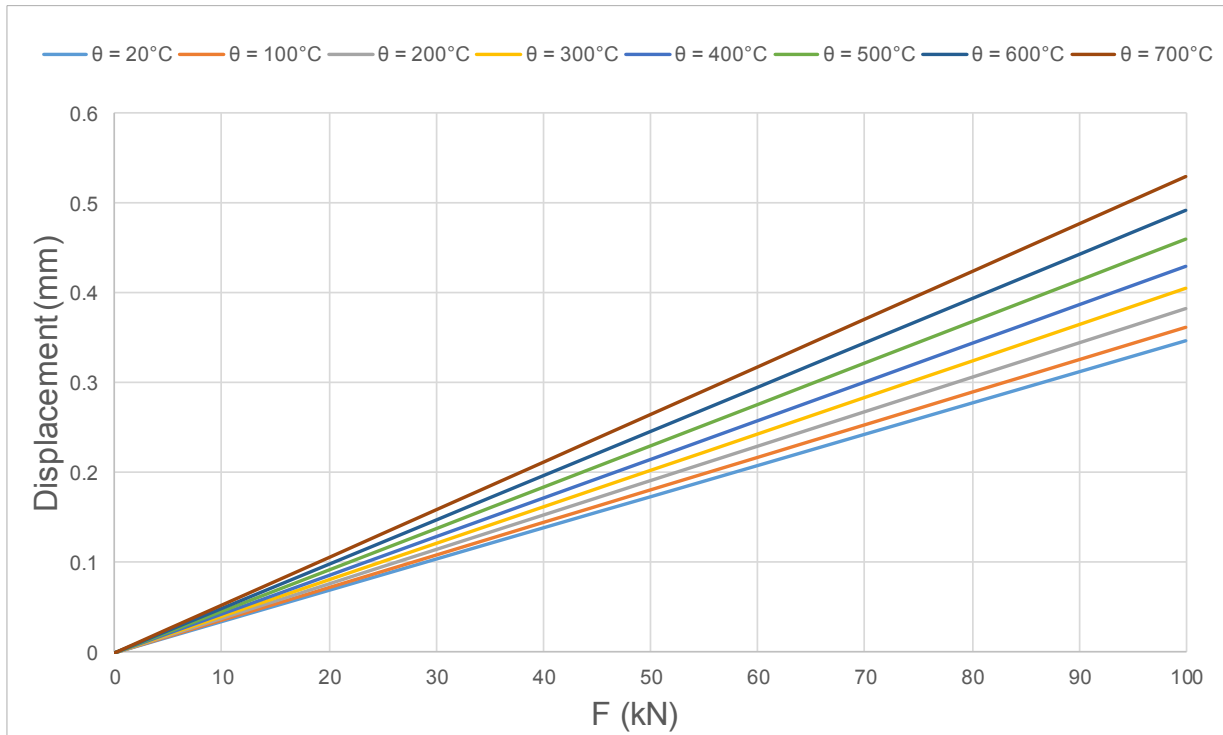


Figure 70: Displacement of equipment (error induced within equipment + deformation of the stamp)

8.4.3 Calibration of Steady-state Tests Based on 2nd Proposed Method

In this section, the mechanism of finding the error induced via equipment is independent of the Invar calibration tests and is based on energy principle.

The magnitude of the compressive force applied on the concrete specimen via stamp and the force applied on the traverse are almost exact and available during the tests. This is shown in Fig. 71. On the other hand, the magnitude of recorded Δl_w are available at each step. It can, therefore, be assumed that for the concrete cylinder specimens:

$$\Delta l_w = \Delta l_c + \Delta l_{equi} \quad (70)$$

where Δl_{equi} is the error induced via equipment and accumulates the displacement of the stamp:

$$\Delta l_{equi} = \Delta l_{st} + \Delta l_{equi,r} \quad (71)$$

where Δl_{st} is the axial deformation of stamps and $\Delta l_{equi,r}$ refers to the rest of error induced via equipment.

Further, for the concrete cylinder specimens at the ambient temperatures, an external displacement measuring-device of type WAT has been installed on the surface of concrete specimens. Therefore, the values of deformation directly on the surface of specimen as well as the value of displacement recorded are available during the tests on the concrete (see Fig. 72). Thus, for different values of applying forces, the error induced via equipment or corresponding to the energy saved in the equipment can be determined. The error induced via equipment is expressed as:

$$\Delta l_{equi} = \Delta l_{w,c} - \Delta l_{WAT,c} \quad (72)$$

Comparison of the results of different tests showed that the magnitude of Δl_{equi} can be approximated to a sufficient extent as a function of applied load F . Therefore, the coefficient $\alpha(F)$ can be estimated as follow:

$$\frac{\Delta l_{equi}}{F} = \alpha(F) \quad (73)$$

Having estimated $\alpha(F)$, it is possible, to evaluate the amount of Δl_{equi} at the ambient temperature by having the magnitude of the applied forces. The used $\alpha(F)$ coefficient is plotted in Figs. 73 and 74. It should be noted, at the initial point of application of force, approximately from 0-5 kN, the stiffness of equipment is observed to be much lower. Therefore, a linear $\alpha(F)$ is assumed to give a sufficient accuracy for the force levels larger than 5 kN for the tests. It generally gives a better approximation for all tests with applied load larger than 10 kN.

Stress-strain curves for a steady test at maximum uniformly distributed temperature of 700°C purified according to the both proposed methods are plotted in Fig. 75.

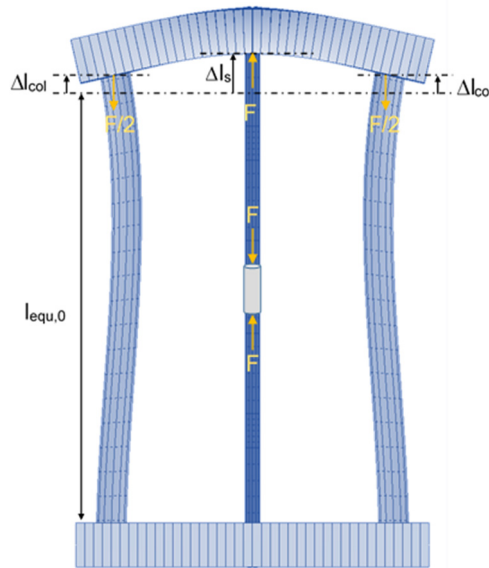


Figure 71: Force and displacement mechanisms of the 250 kN compressive equipment. The displacements are illustrated based on enlarging factor of 750

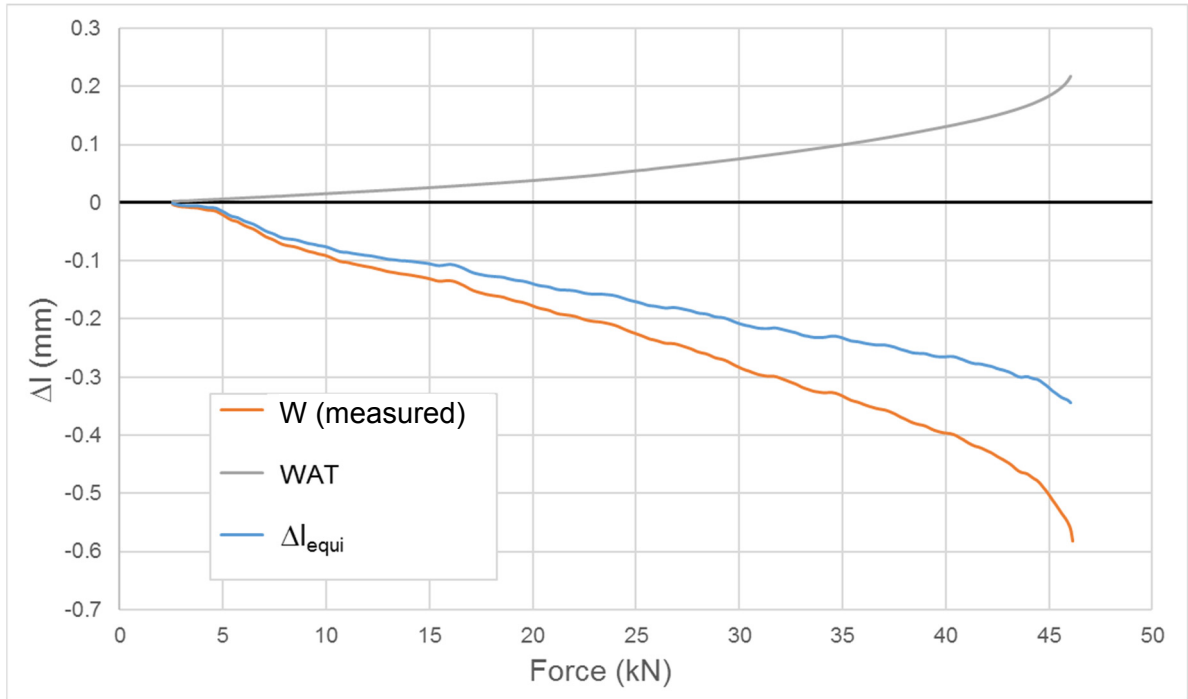


Figure 72: Measured displacements for test 10 (force-rate controlled) at ambient temperatures via two measurement devices

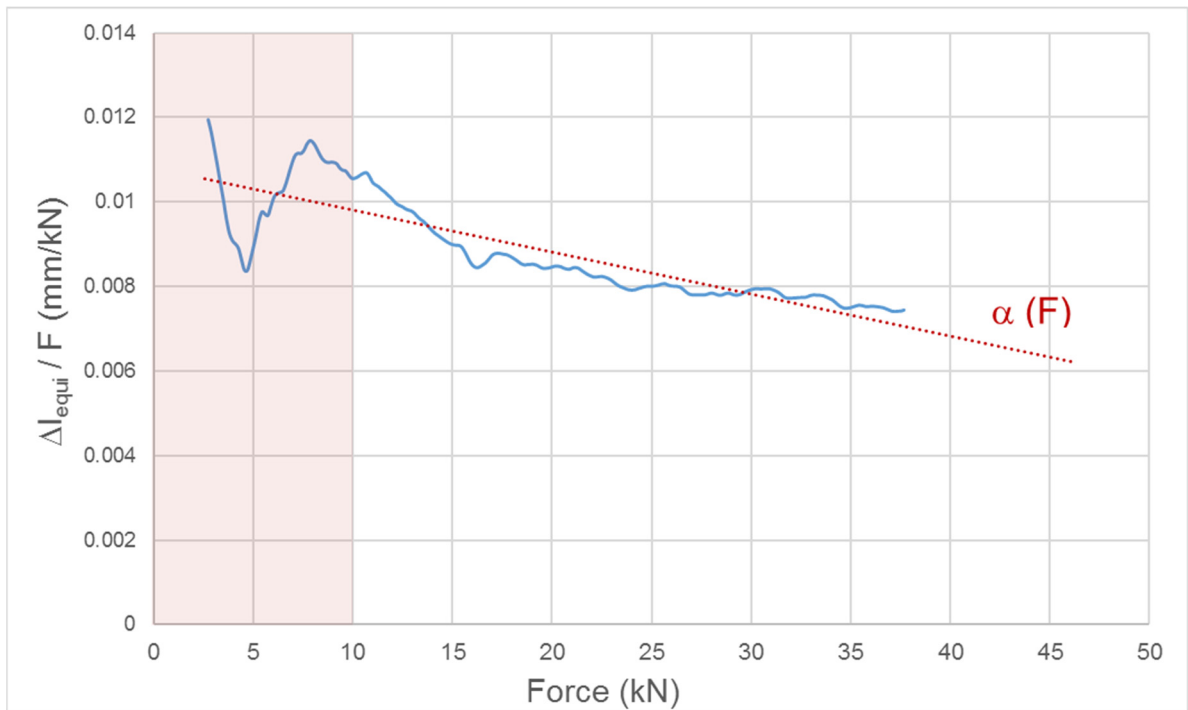


Figure 73: The used function for α from the results of test 10

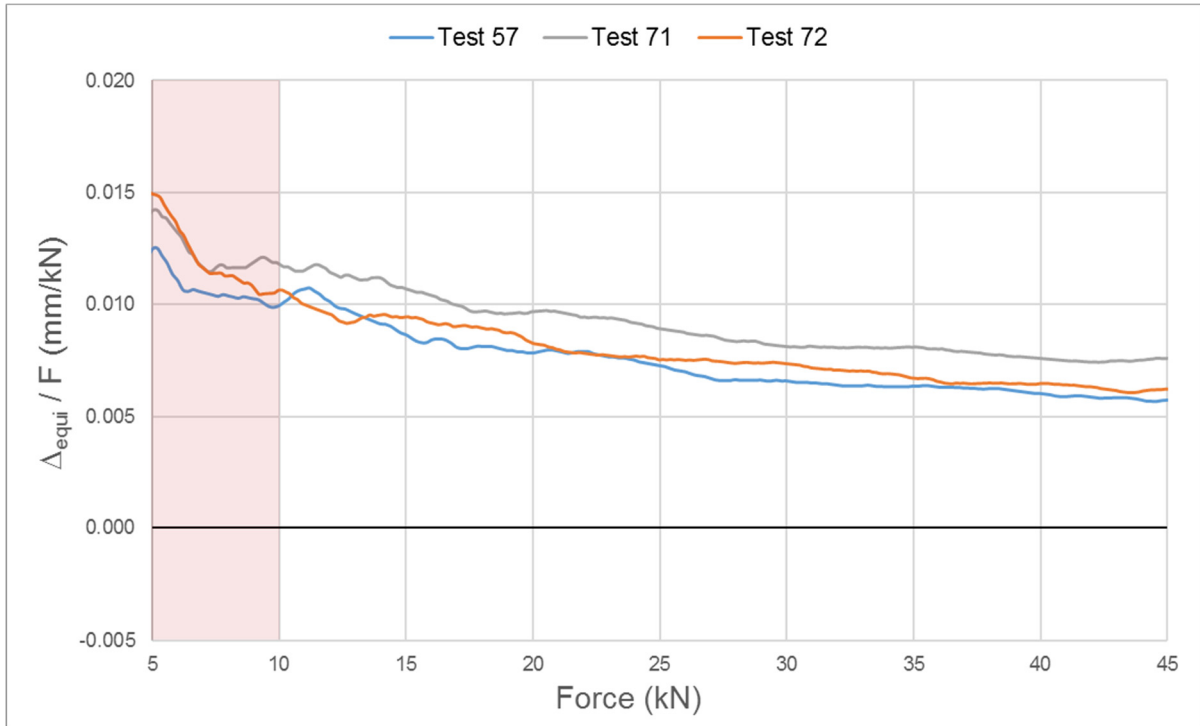


Figure 74: The ratio of displacement of equipment to the applied force for different test results

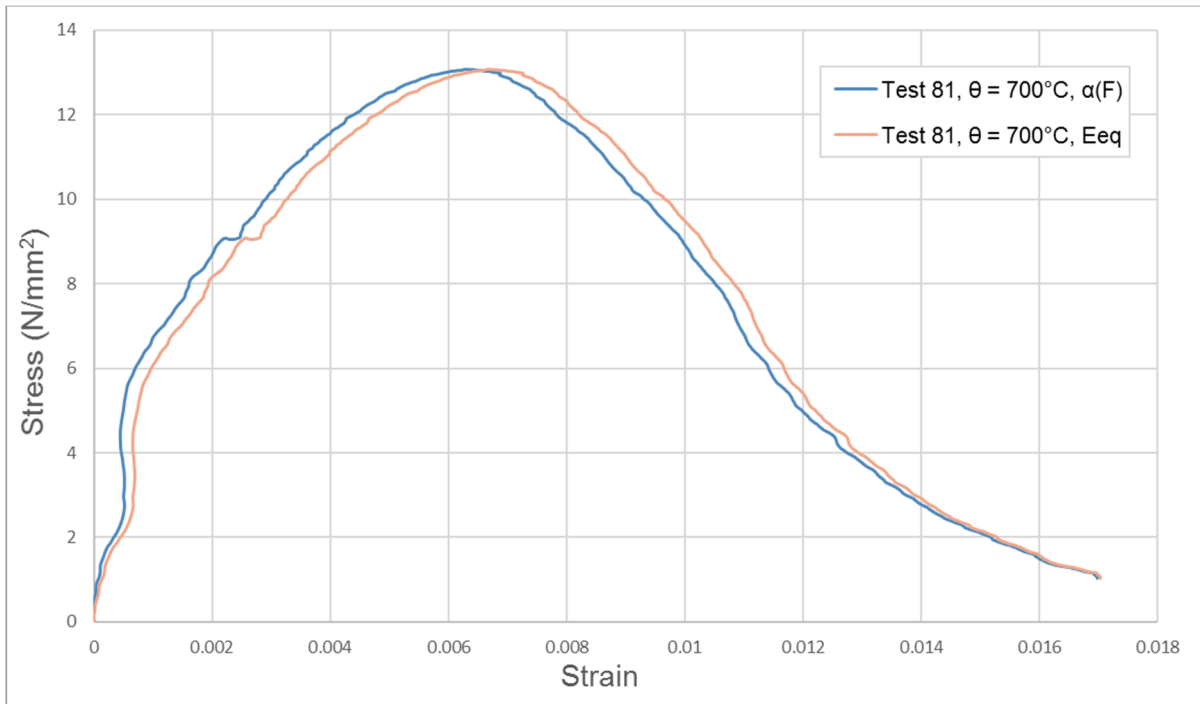


Figure 75: Purified stress-strain curves for a steady test at maximum temperature of 700°C based on two proposed methods

8.5 Calibration of Transient Tests with a Specified Constant Applied Load Level Based on 1st Proposed Method

Transient tests were performed on an Invar specimen under different load levels corresponding to the applied load levels on batches 3 and 4 for $\alpha = 0, 0.1, 0.3$ and 0.6 . The total measured displacements are plotted in Fig. 76.

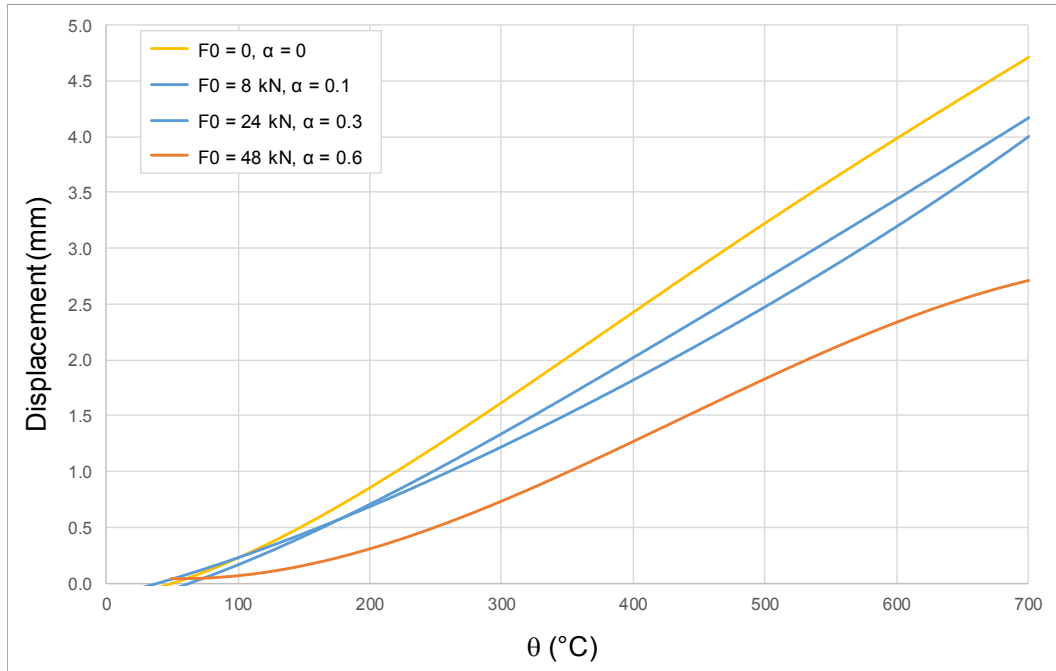


Figure 76: Thermal elongation for the transient calibration tests under different load levels

As explained in section 8.4.2 and in Fig. 69, the equivalent modulus of elasticity corresponding to the measured values varies for different force intervals.

Further, Fig. 77 illustrates the measured displacements during a calibration test at ambient temperature up to maximum force of 100 kN. In this figure, the rate of displacement growth is higher at the lower forces compared to the higher force levels.

Initially, three cyclic compressive tests are conducted on an Invar specimen at ambient temperature to have an estimation of equivalent modulus of elasticity. These tests are performed for the force intervals of 0-8, 8-24, 24-48, 48-100 and 0-100 kN. It has been observed that at the ambient temperature the displacement results and therefore the equivalent modulus of elasticity changes for identical force cycles (see Tab. 16).

Further, transient tests performed on the Invar specimen up to 700°C with the cyclic loading and unloading for the stated load intervals applied at 200, 400, 600 and 700°C. The equivalent modulus of elasticity is for different force cycles at different temperatures as plotted in Fig. 78. This shows, the higher the force level, the less the error, and E_{eq} approaches the real modulus of elasticity of equipment. For each cycle, an average equivalent modulus of elasticity has been assumed for temperatures between 20 and 700°C and listed in Tab. 19.

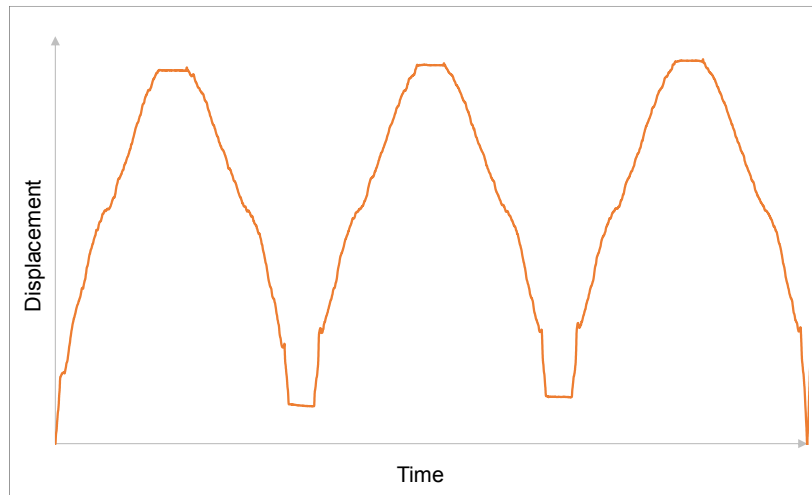


Figure 77: Displacement recorded for the calibration test at ambient temperature

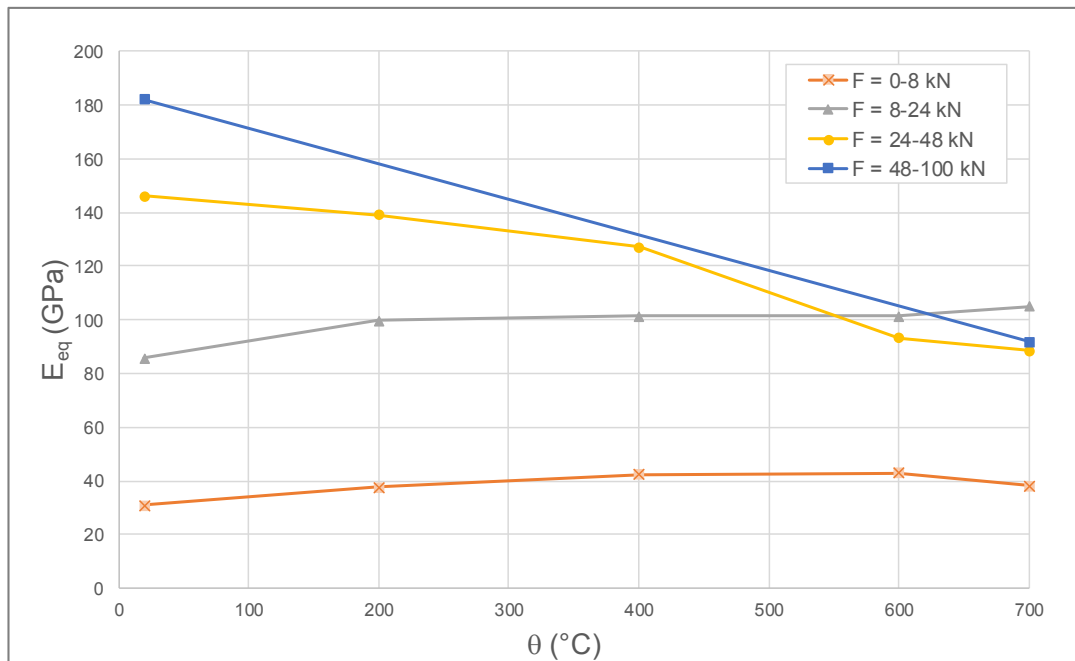


Figure 78: Equivalent moduli of elasticity for 250 machine in transient stage under different load levels

Table 19: Average equivalent moduli of elasticity from the transient calibration tests

	From transient Invar test with cyclic tests up to 48 kN			From 0-100 kN test
θ (°C)	20-700			
F (kN)	0-8	8-24	24-48	48-100
$E_{eq,ave,cyc}$ (GPa)	38	99	119	137
$E_{eq,ave,tot}$ (GPa)	98			

Further, the displacement results of the calibration transient test with a constant applied load of 48 kN with the numerically estimated free elongation of Invar36 are illustrated in Fig. 79.

Having all the tests performed, the scaling factors for each displacement's curve now can be estimated based on α_{eq} method for different transient calibration tests. α_{eq} curves and scaling factors estimated for the tests are illustrated in Figs. 80 and 81 for the used load levels respectively.

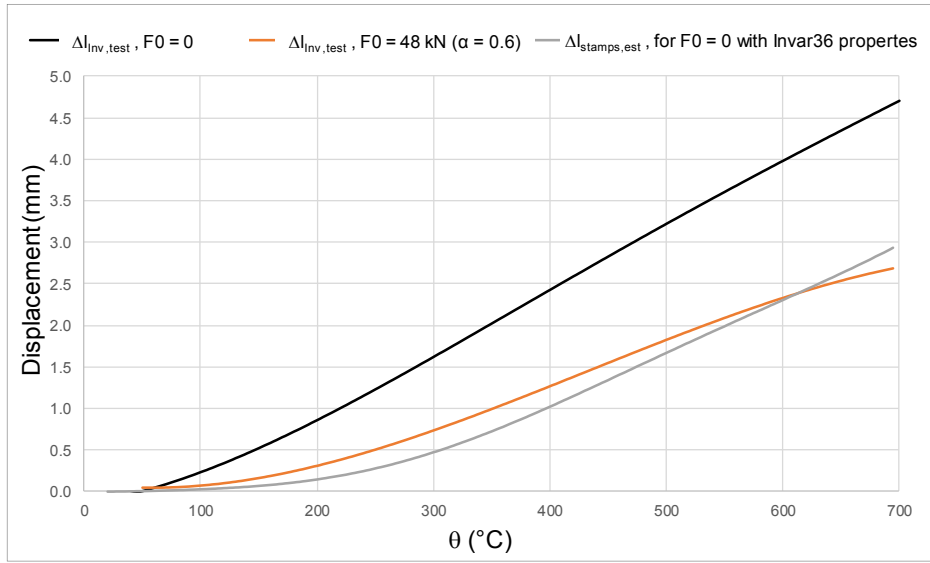


Figure 79: Elongation measured via calibration tests and estimated free elongation of stamps by considering Invar36 thermal expansion coefficients

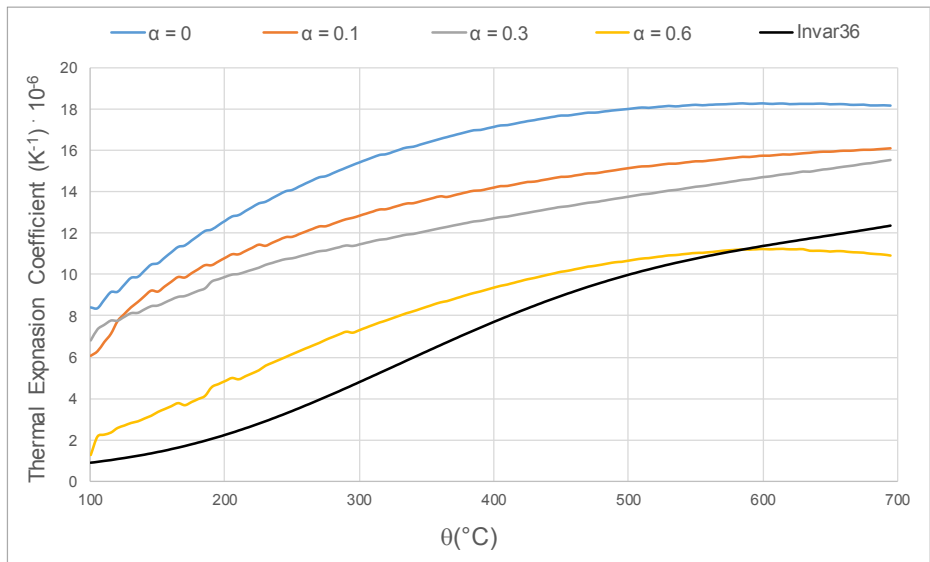


Figure 80: Equivalent thermal expansion coefficient for different calibration tests with various load levels ($\alpha = 0, 0.1, 0.3$ and 0.6)

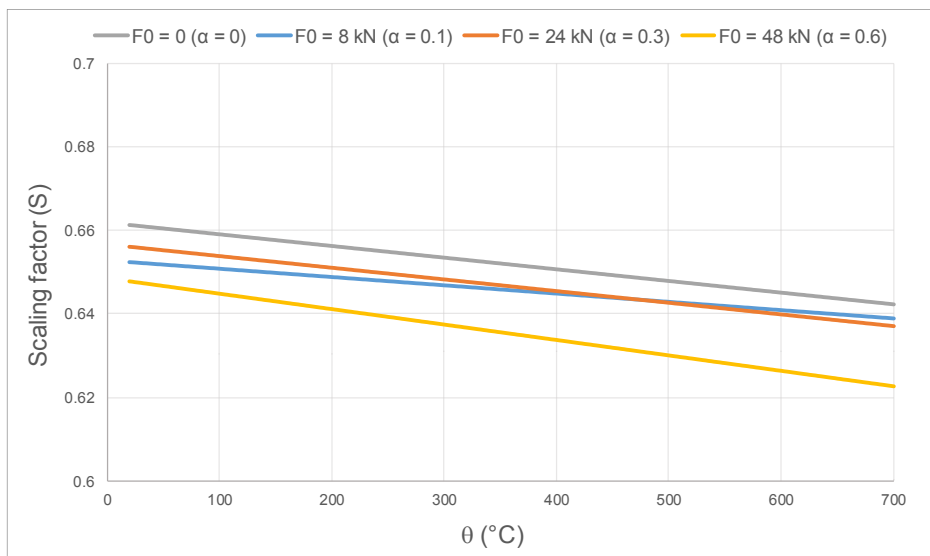


Figure 81: Scaling factors for the transient calibration tests under different load levels

9 Tests at Elevated Temperatures

9.1 Test Program

Generally, all the compressive steady and transient tests at elevated temperatures are performed on cylinder specimens. These are listed in Annex E. The desired heating rate of $R = 5$ K/min on the surface of concrete specimens has been considered as the main used heating rate. Due to the small diameter of cylinders, the heating rate of 5 K/min is assumed to cause no special thermal effects induced by changing temperatures over the cylinder cross-section. Further, heating rate of 10 K/min is used for the small number of tests at transient stage. Force-rate and displacement-rate controlled tests are carried out to achieve stress-rate of $\dot{\sigma} = 0.5 \pm 0.1$ MPa/s and strain-rate of $\dot{\epsilon} = 0.1 \pm 0.05$ %/s according to (RILEM, 2007).

Using the force-controlled test, it is possible to reach a desired constant stress-rate as the applied loads on the specimens are available and accurate. On the other hand, using the displacement-controlled tests the following issues should be dealt with:

- The displacement-rate is set on the machine is the displacement-rate that will correspond to measurements not the axial deformation of the concrete specimen;
- The stiffness of the 250 kN machine for the lower force levels (0-10 kN) is considerably lower than the higher load levels.

Therefore, the higher the strength of concrete specimen, higher is the force applied to reach a specified constant displacement-rate. Thus, the displacement-rate inputs to reach a similar desired strain-rates as given in (RILEM, 2007), are the function of concrete strength and temperature.

Different displacement-rates applied for the steady tests of batches 1 and 2 to investigate and optimize the displacement-rate inputs for batches 3 and 4. Further, to gain a better estimation of descending branch of stress-strain curves, the second displacement-rate is set on the machine applied to the specimens from approximately 70 to 80% of the corresponding strength level of the concrete specimen. A graph of strain-rate vs. force for test 136 from batch 3 with two displacement-rate inputs on the machine is plotted in Fig. 82. Schematics of different steady and transient tests performed for this study are given for both loaded and not-loaded specimens during the heating-up procedure in Fig. 83.

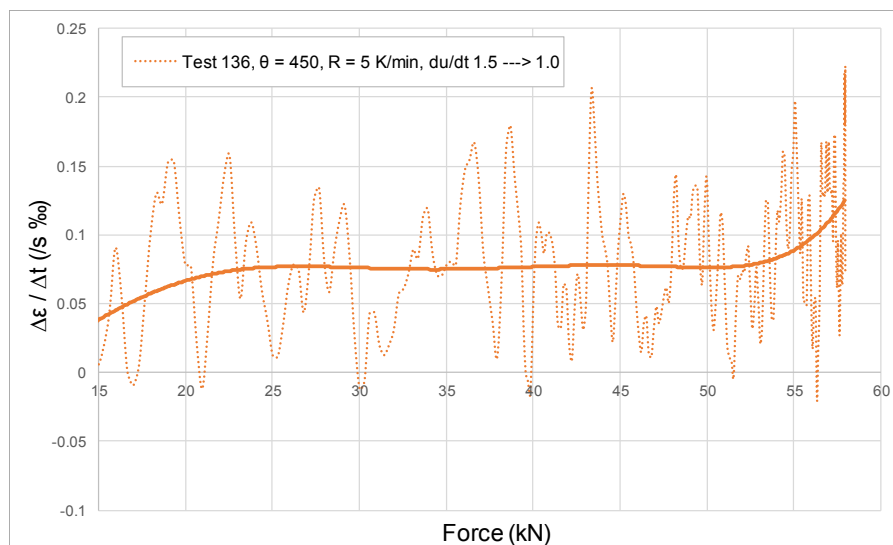
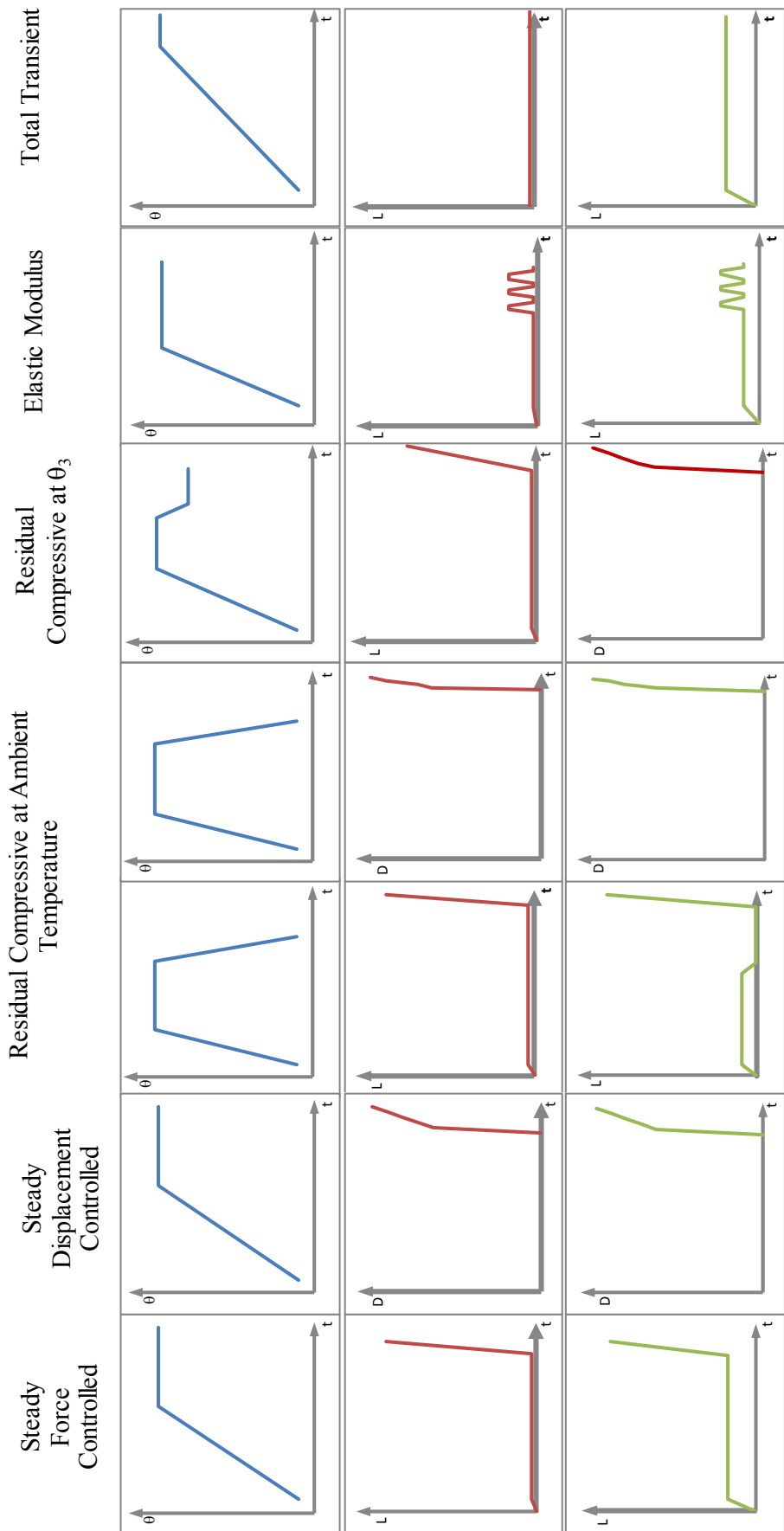


Figure 82: Strain-rate vs. force for test 136 at uniformly distributed temperature of 450°C



Load variation for not stressed specimen during the heating-up procedure
 Load variation for stressed specimen during the heating-up procedure

Figure 83: Schematics of load and temperature configurations of steady and transient tests

9.2 Temperature Measurements

Generally, temperatures were measured only for the prisms with a comparable size (slightly larger) with respect to the cylinder specimens. As shown in Fig. 84, two sets of configurations for temperature measuring points were predicted and numbered. The measuring points can be divided into three rows (A, B and C) with a distance to the shortest sides of concrete. Row:

- A lays near the surface of concrete under approximately 2.5 mm concrete cover;
- B has a distance of almost 15 mm from the width;
- C lays in the middle of prism with a distance of 30 mm.

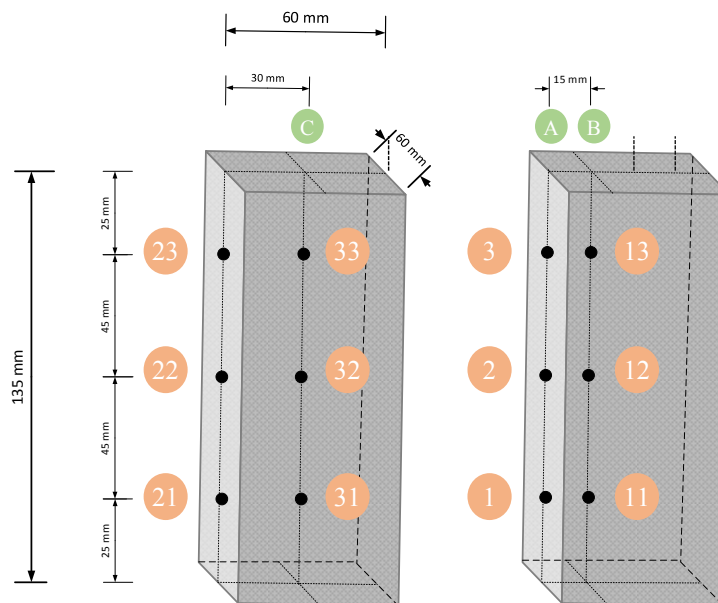


Figure 84: Configuration of measuring points in the prisms

Temperatures were measured in a tempering oven (Vötsch, type VAW 60/60) for temperatures up to 600°C via a 4-measuring-channel thermo-logger (VOLCRAFT K 204 data logger). The temperatures are then recorded and read in a software called Se309. The configuration is shown in Fig. 85. For the measurements, due to the available 4 channels of thermo-logger, three measuring points were recorded within the concrete (for each specimen) and an extra thermal wire is located on the outer surface of concrete.

A heating rate of 5 K/min has been aimed to be applied on the surface of the prisms. This theoretical heating rate, could not be applied in the reality as each oven showed error in producing the desired input heating rate. Further, in Fig. 86, the temperature on the surface of the concrete is designated with “on” and plotted with a continuous line for the specimen number 101. In Annex F, all the temperature measurements are given.

The differences in the temperature fields in each prism might be due to the following reasons:

- Different moisture contents of the prisms;
- Different temperature loads on the surface of each prism produced by furnace;
- Error due to changing instable position of measuring points.

The temperature values recorded via measuring points 21 and 1 for the specimens 104 and 108 respectively with the results from SOFiSTiK based on EN 1992-1-2 temperature dependent material properties are shown in Fig. 87. Generally, with respect to the global structural analysis of reinforced concrete cut-and-cover tunnel members exposed to fire, the difference between the measured temperature values for the prisms with PP-fibres and the results of SOFiSTiK for the concrete without PP-fibres are negligible.



Figure 85: Temperature measurement in tempering oven (Vötsch, type VAW 60/60) for temperatures up to 600°C via a 4-measuring-channel thermo-logger (VOLCRAFT K 204 data logger)

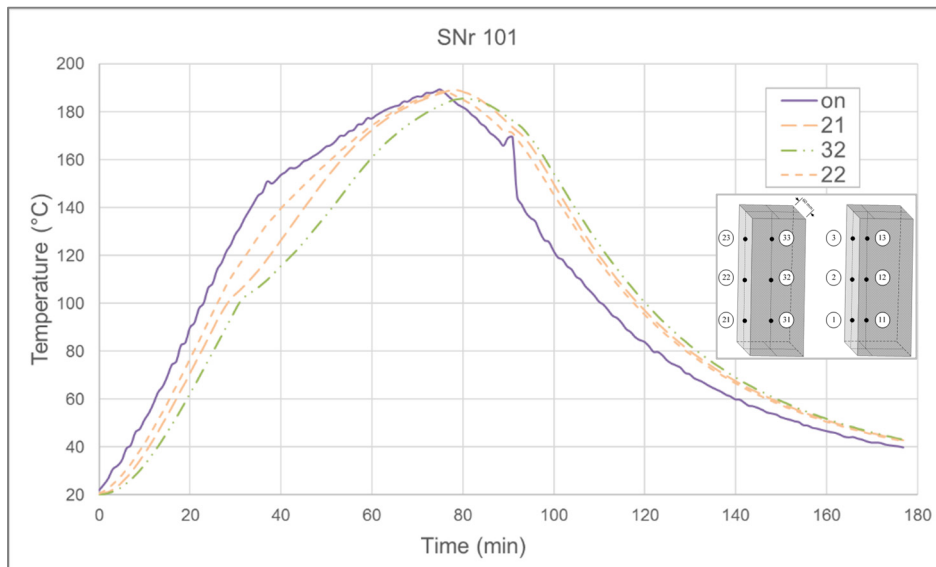


Figure 86: Temperature values at different points of a prism (SNr 101) under heating-up to a desired temperature of 200°C and cooling phase up to 40°C

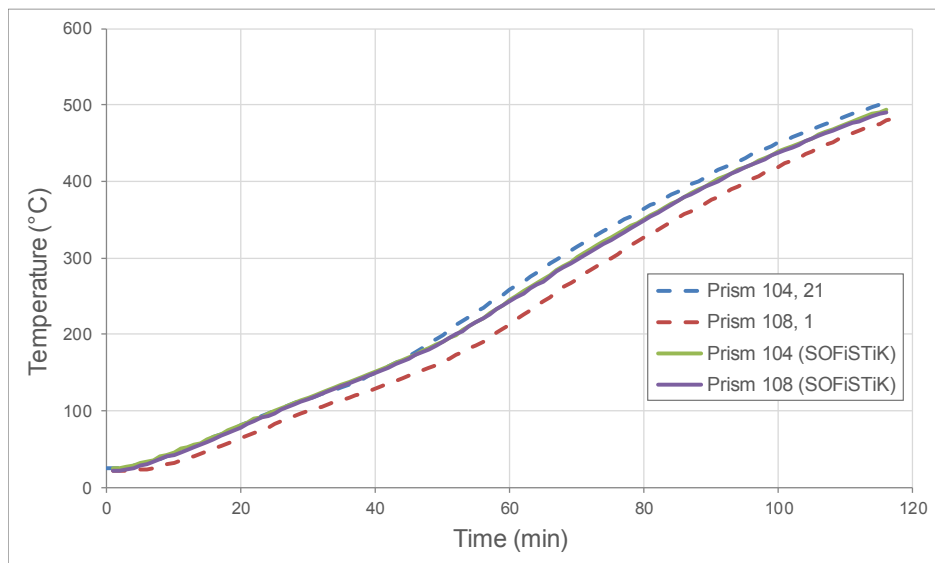


Figure 87: Comparison of temperature measurements with the results from SOFiSTiK

9.3 Heating Rate and Thermal Incompatibilities

To find the uniform temperature distribution in the cylinder concrete specimens under compressive load during heating, (RILEM TC 129-MHT, 1998) limits the use of heating rates dependent on the radius of cylinder to $R \leq 4$ K/min. The high value of heating rates results in thermal incompatibilities or as called by (Khoury, et al., 1985) structural effects that might influence the strain results. Due to temporary tensile stresses at the centre of specimens, the results of transient strain tests might be not accurate especially for the specimens with a load factor $\alpha < 0.2$ ($0.2f_c$) during the heating up procedure. In Annex G, the results of investigation on thermally induced stresses in concrete specimens under different heating rates are explained. Due to small diameters of the used cylinder specimens, it can be assumed that the desired selected heating rate of 5 K/min does not influence the experimental results considerably.

9.4 Relative Compressive Strength

Compressive strength tests have been performed on cylinder specimens generally under aimed heating rate of 5 K/min. To measure the temperature outside the circumference of cylinders, thermal-resistant wires are located in the furnace and temperatures are measured throughout the tests. The compressive strength tests are done in a small clamshell-furnace. The adjusted temperatures and heating rates are given for C30-PP in Tab. 20.

Table 20: Properties and input data for temperature adjustments

Concrete designation	Desired maximum temperature (°C)	Desired heating rate (K/min)	Adjusted maximum temperature (K/min)	Adjusted heating rate on the machine (K/min)
C30-PP	200	5	350	6.5
	450	5	600	7.5
	700	5	1050	8
	900	5	1050	10

The estimated relative compressive strength values for cylinder specimens for C30-PP are given in Tab. 21.

Table 21: Relative compressive strength for C30-PP and according to EN 1992-1-2

Concrete designation	Temperature (°C)	$f_c^{\theta_{max}} / f_{cm,200}$		$f_c^{\theta_{max}} / f_{ck}$
		$f_c^{\theta_{max}}$ (N/mm ²)	Tests	
C30-PP	200	26.44	0.81	0.95
	450	24.77	0.76	0.67
	700	13.08	0.40	0.30
	900	5.05	0.15	0.08

All steady compressive strength tests for the four batches performed on the specimens with different load levels and with or without modulus of elasticity tests are listed in Tabs. 22 and 23.

The relative compressive strengths at elevated temperatures are evaluated by taking into account the concrete strength at ambient temperature at the age of 200 days. Strength reduction factors for all four batches are plotted in Fig. 88 with the corresponding given factors in EN 1992-1-2 for normal-strength

Tests at Elevated Temperatures

concrete for concrete with siliceous aggregates. The largest deviations rise at 200°C where the reduction factors according to the tests is to a high extent smaller than EN 1992-1-2 values which on the other hand means the code values do not lay on the safe side. For other temperatures, EN 1992-1-2 values remain almost consistently on the safe side. Comparing the relative strength of the tests, generally, the highest relative strength reduction has occurred for C50 compared to other batches with an exception at 700°C where the reduction of strength of C50 is slightly less than C50-PP. Looking at the graphs of relative strength reduction of all batches at 200°C, they all lay compared to EN 1992-1-2 on the unsafe side. Further, comparing the test results of C50-PP and C50 at 200°C, the addition of PP-fibres has increased the strength of concrete more clearly.

Table 22: List of compressive strength tests for batches 1 and 2

Batch Nr.	Test Nr.	R (K/min)	θ_{max} (°C)	α	Force rate (kN/s)	Displacement rate (mm/min)	E-test	Comments or explanations
1	15	5	450	0	0.75			
	16	5	700	0	0.75			
	17	5	200	0	0.75			Implausible records
	18	5	450	0	0.75			
	19	5	200	0	0.75			
	20	5	900	0	0.83			
	21	5	900	0	0.83			
	22	5	700	0	0.83			
	23	5	450	0	0.83		✓	
	24	5	450	0	0.83		✓	
	25	5	450	0		1.0 → 0.4		
	26	5	200	0		1.0 → 1.0		
	29	5	450	0	0.83	1.2 → 0.8	✓	
	30	5	200	0		1.0 → 1.0		
	31	5	450	0		1.2 → 1.2		
	32	5	200	0	0.83			
	33	5	700	0		1.4 → 1.4		
	34	5	200	0		1.0 → 1.8	✓	
35	5	900	0		1.8 → 1.8			
36	5	900	0	0.83	2.2 → 2.8	✓		
37	5	700	0	0.83	1.6 → 1.8	✓		
2	67	5	200	0.1	0.75			Without displacement-force records.
	68	5	700	0.1	0.75			
	69	5	900	0.1	0.75			
	70	5	450	0.1	0.75			
	78	5	200	0		1.0 → 1.0		
	79	5	200	0		1.0 → 0.5		
	80	5	450	0	0.83	1.2 → 0.6	✓	
	81	5	700	0	0.83	1.6 → 0.8	✓	
	82	5	700	0.1		2.0 → 1.0		
	83	5	450	0.1		1.2 → 0.6		
	84	5	700	0.3		2.0 → 1.0		
	85	5	450	0.5		1.6 → 1.8		
	93	5	900	0.1		2.2 → 1.1		
	95	10	900	0.1		2.2 → 1.1		
097	10	900	0	0.83	2.2 → 1.0	✓		

Tests at Elevated Temperatures

Table 23: List of compressive strength tests for batches 3 and 4

Batch Nr.	Test Nr.	R (K/min)	θ_{max} (°C)	α	Force rate (kN/s)	Displacement rate (mm/min)	E-test	Comments or explanations
3	130	5	200	0	0.83	1.0 → 0.5	✓	
	131	5	900	0	0.83	1.8 → 1.0	✓	
	132	5	200	0	0.83	1.6 → 1.0	✓	
	133	10	900	0	0.83	1.5 → 1.0	✓	
	136	5	450	0	0.83	1.5 → 1.0	✓	
	137	5	700	0	0.83	1.5 → 1.0	✓	
	138	5	450	0	0.83	1.0 → 1.0	✓	
	139	10	700	0	0.83	1.5 → 1.0	✓	
	158	10	700	0.1		1.3 → 1.0		
	159	10	700	0.1		1.3 → 1.0		
	162	5	700	0.5		1.0 → 1.0		
	163	5	700	0.3		1.3 → 1.0		
	165	5	450	0.3		0.9 → 0.9		
	166	5	450	0.1		1.0 → 1.0		
	167	5	450	0.5		0.7 → 0.7		
4	184	5	450	0	0.83	1.0 → 1.0	✓	
	188	5	200	0	0.83	0.8 → 0.8	✓	
	192	5	900	0	0.83	1.6 → 1.0	✓	
	193	5	700	0	0.83	1.5 → 1.0	✓	
	194	10	700	0	0.83	1.5 → 1.0	✓	
	195	5	700	0.1		1.3 → 1.0		
	197	5	700	0.3		1.3 → 1.0		Sudden automatic jump from 24 kN to 47.4 kN caused an unexpected failure.
	198	5	700	0.5		1.0 → 1.0		
	200	10	700	0.3		1.3 → 1.0		
	201	5	450	0.3		1.0 → 1.0		

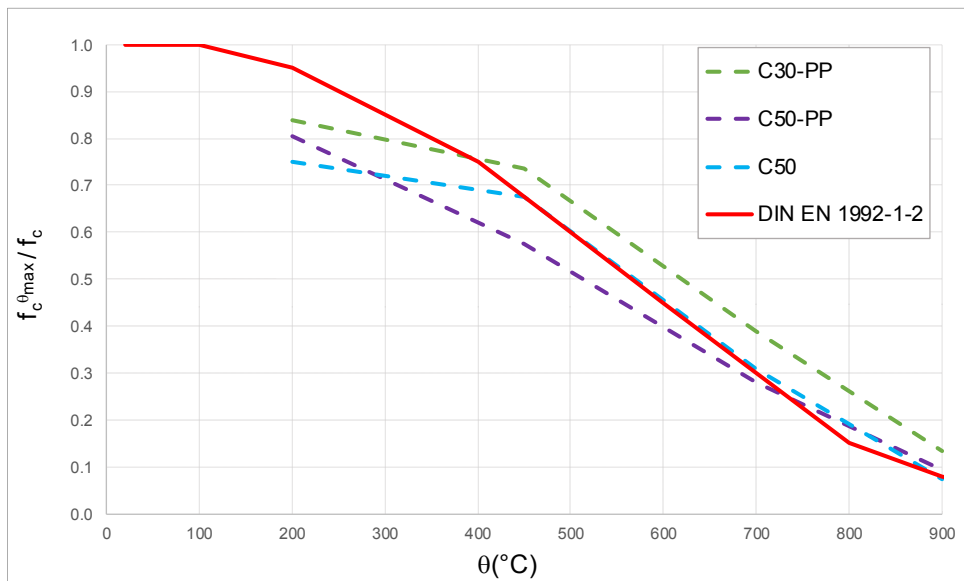


Figure 88: Relative concrete compressive strengths of concrete with and without PP-fibres vs. EN 1992-1-2

9.5 Relative Compressive Strength of Pre-loaded Tests

The relative strength reduction of concrete with and without PP-fibres for the tests with pre-load levels $\alpha = 0, 0.1$ and 0.3 are plotted in Figs. 89, 90 and 91 respectively. The tests with $\alpha = 0.5$ for C50-PP and C50 failed at about 540°C .

Generally, the trends of reduction strength factors for all three batches for $\alpha = 0, 0.1$ and 0.3 show that the higher the pre-load level, the higher is the relative strength of concrete at the corresponding elevated temperatures. On the other hand, 540°C for the test with $\alpha = 0.5$, can be assumed as the critical temperature for this load level.

In addition, the strength reduction factors of concrete with and without PP-fibres for $\alpha = 0.1$ and 0.3 are compared in Figs. 92 and 93 respectively. In general, it can be concluded from the results, the lower the strength of concrete, the higher is the relative strength at the elevated temperatures for the pre-loaded specimens. Comparison of the results from C50-PP and C50, the relative strength of C50 is higher than C50-PP for both pre-load levels. Thus, the addition of PP-fibres slightly decreased the relative strength of concrete under pre-load levels of $\alpha = 0.1$ and 0.3 .

9.6 Stress-strain Curves from Tests

In this section, the relative ratio of the stress at uniformly distributed maximum temperature, $\sigma^{\theta_{ma}}$, to concrete strength f_c are plotted versus strains for concrete with and without PP-fibres (see Fig. 94). It should be noted, that these curves should not be compared with stress-strain curves from EN 1992-1-2. It is observed that the failure of concrete specimen for C50-PP at 200°C has been brittle.

Further, the corresponding curves for C50-PP and C50, which have similar strength at ambient temperature, are plotted in Fig. 95. It can be seen that the relative stress-strength values for temperatures above 200°C are smaller for C50-PP compared with C50. These are for 900°C almost the same.

9.7 Explicit Modulus of Elasticity from Cyclic Tests

The reduction factors of modulus of elasticity for the four batches are plotted in Fig. 96. Again, these values should not be compared with modulus of elasticity from EN 1992-1-2's model. This is due to the fact that EN 1992-1-2's model is an implicit model and its stress-strain curves have accumulated the transient creep component and correspondingly E-moduli are extracted from these curves. Here, moduli of elasticity are evaluated and plotted from the cyclic-tests' records at the elevated temperatures. Further, C50 gives the lowest boundary limit with an exception at 700°C . Relative modulus of elasticity of C50 at 450°C is considerably lower than the corresponding values for C50-PP.

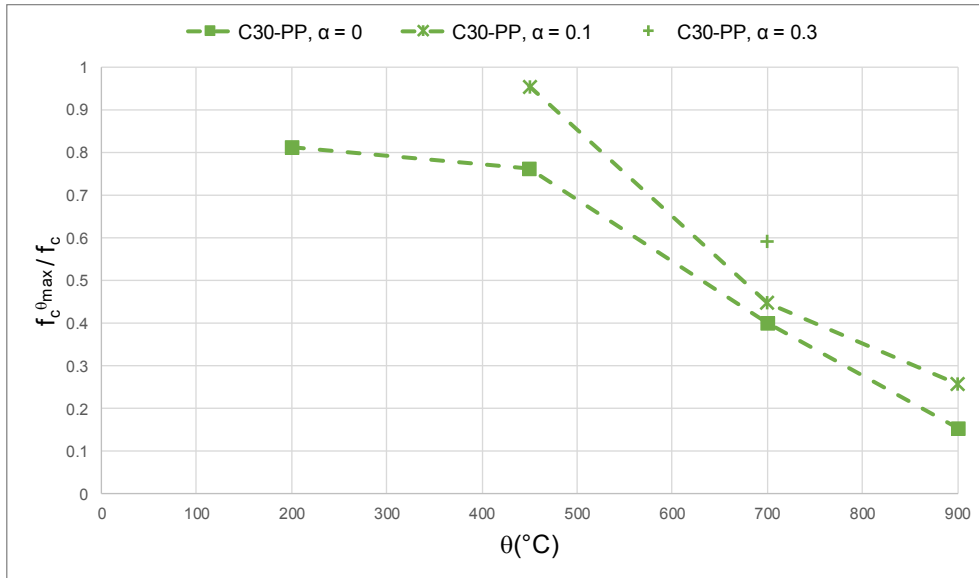


Figure 89: Relative strength of the tests for C30-PP with various pre-load levels

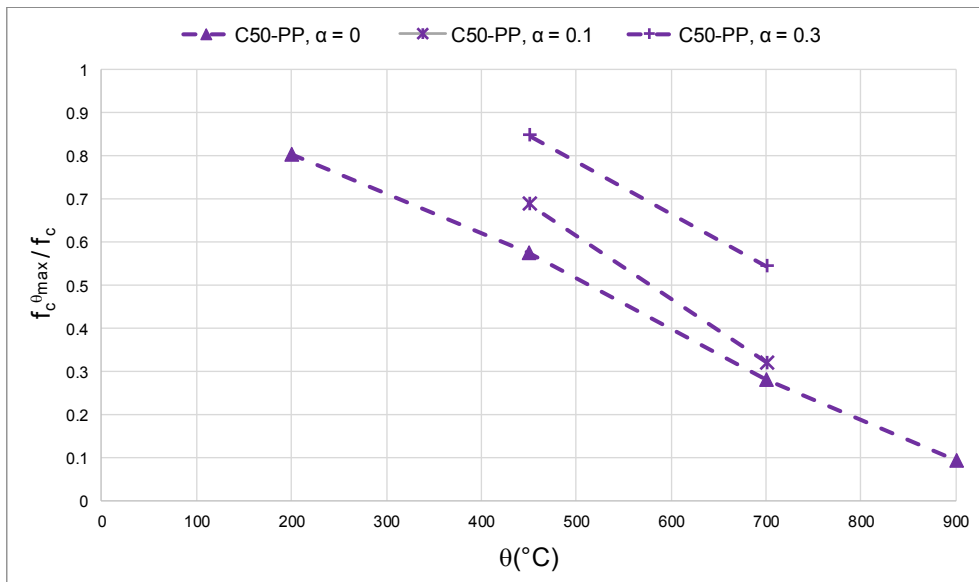


Figure 90: Relative strength of the tests for C50-PP with various pre-load levels

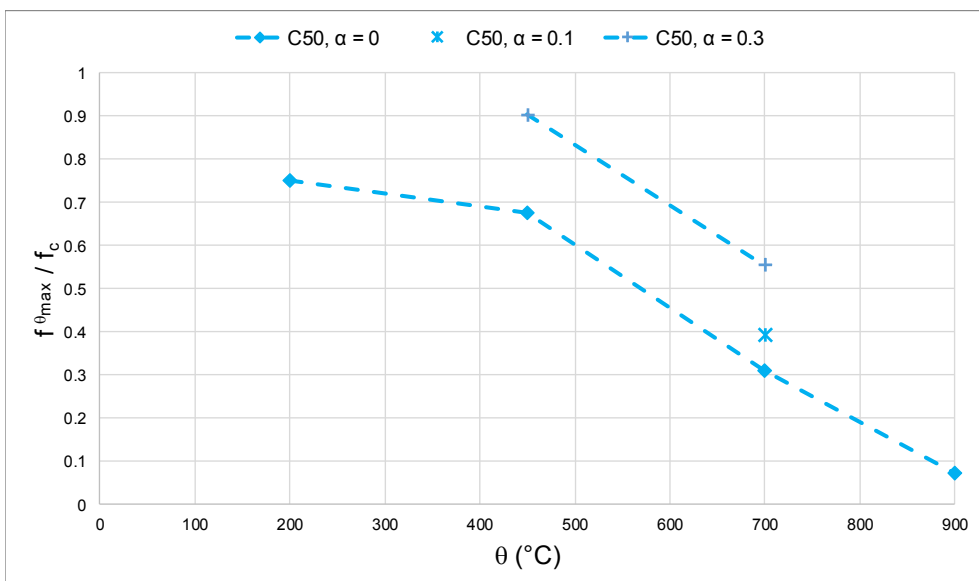


Figure 91: Relative strength of the tests for C50 with various pre-load levels

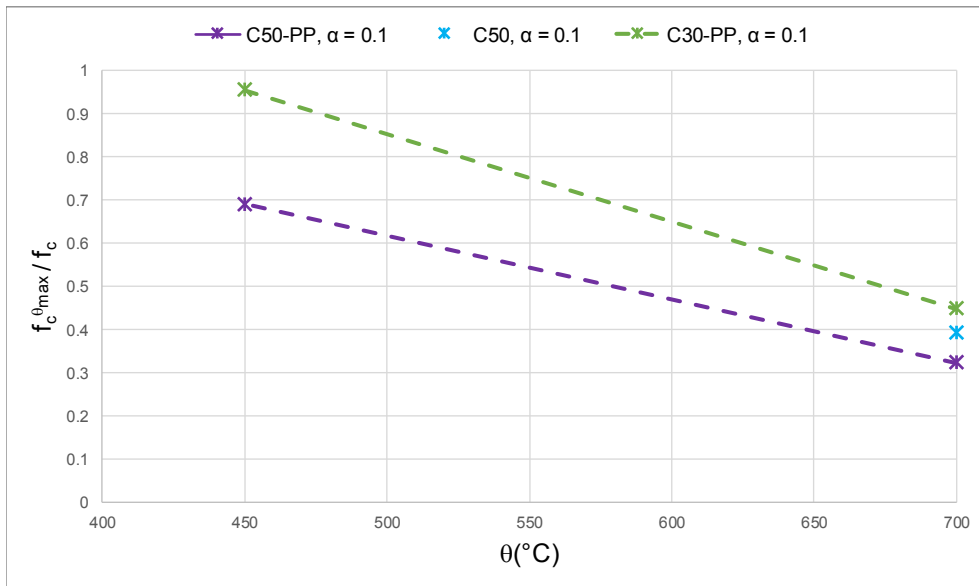


Figure 92: Relative strengths of C30-PP, C50-PP and C50 under pre-load level of $\alpha = 0.1$

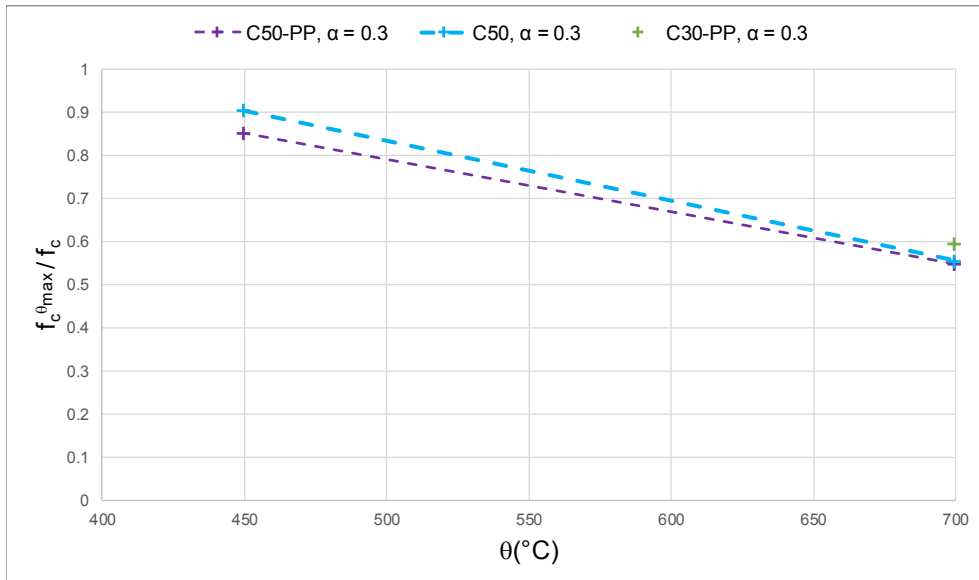


Figure 93: Relative strengths of C30-PP, C50-PP and C50 under pre-load level of $\alpha = 0.3$

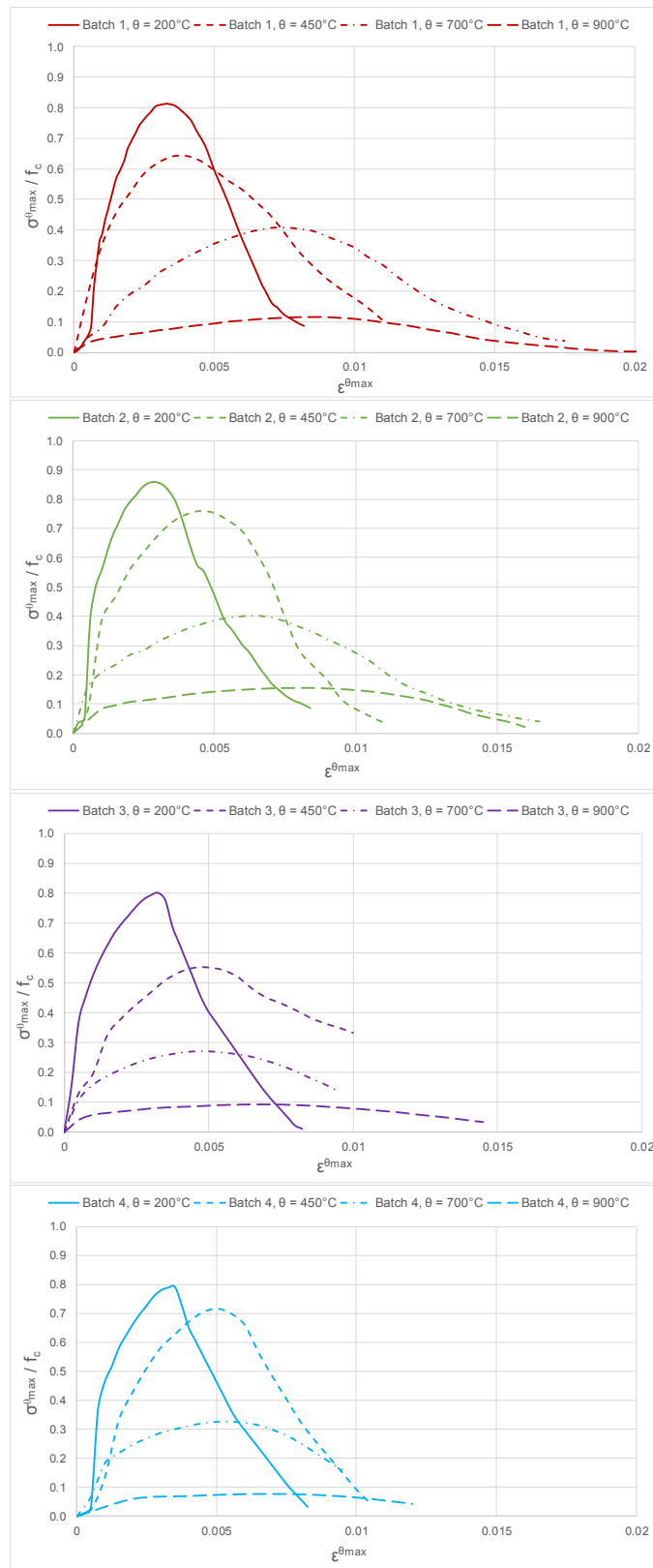


Figure 94: Relative ratio of stress at uniformly distributed maximum temperature, $\sigma^{\theta_{max}}$, to concrete strength, f_c , versus strain for all batches

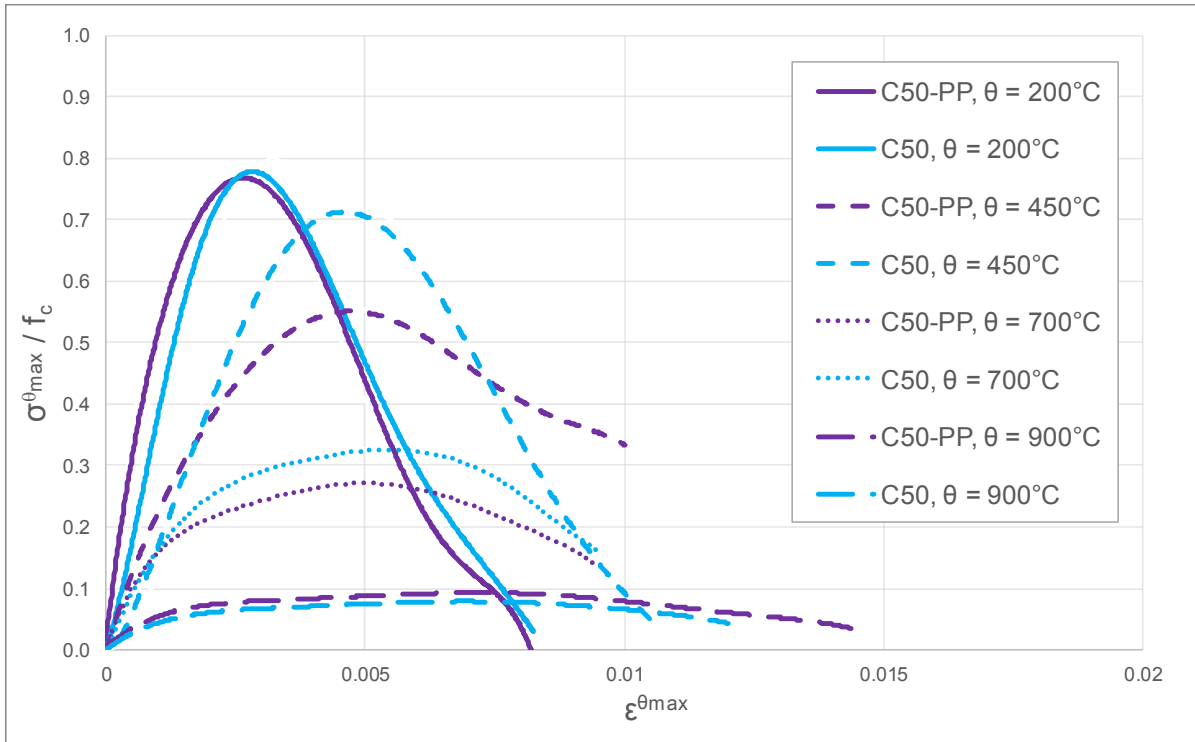


Figure 95: Relative ratio of stress at uniformly distributed maximum temperature, $\sigma^{\theta_{max}}$, to concrete strength, f_c , versus strain for C50-PP and C50

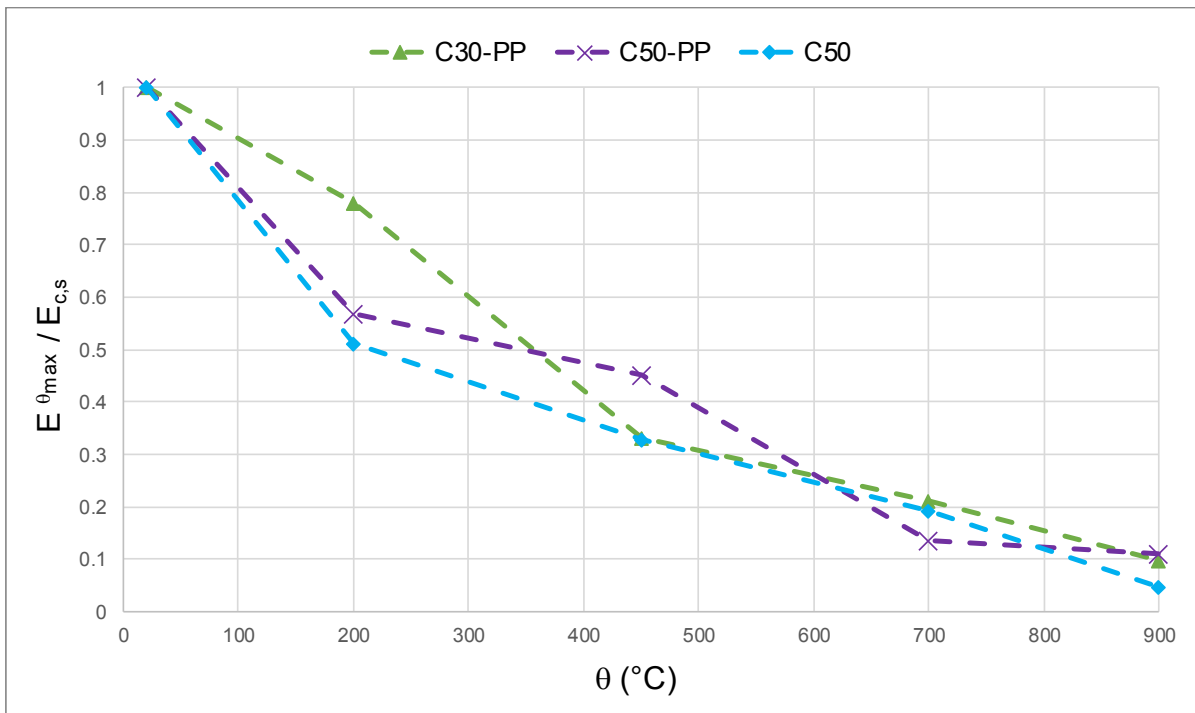


Figure 96: Relative moduli of elasticity at elevated temperatures for concrete with and without PP-fibres

9.8 Residual Compressive Strength after the Specimen Is Cooled Down to Ambient Temperature

To gain the results of residual compressive strength at the ambient temperature, a tempering oven (Vötsch type VAW 60/60) is used for the desired maximum temperatures up to 450°C. The maximum constant reachable temperature in the Vötsch oven is equal to 650°C. For the tests with maximum temperature of 700°C and 900°C, the small clamshell-furnace has been used.

List of residual compressive strength tests is given in Tab. 24.

Table 24: List of the residual compressive strength tests for the four batches

Batch Nr.	Test Nr.	θ_{max} (°C)	α
1	27	450	0
	28	450	0
2	58	200	0
	59	200	0
	61	450	0
	62	450	0
	63	650	0
	64	650	0
	65	900	0.1
	66	900	0.1
	76	450	0
	77	450	0
3	123	900	0.1
	126	200	0
	127	450	0
	128	450	0
	129	650	0
4	179	200	0
	180	650	0
	181	450	0
	182	450	0
	183	700→500	0
	185	900	0
	186	900	0
	187	200	0

The results of residual strength reduction factors for C30-PP, C50-PP and C50 are illustrated with EN 1994-1-2 values in Fig. 97. It is clear that the residual concrete strength of C50 is almost consistently higher than the C30-PP and C50-PP. On the other hand, at 200°C, residual concrete strength of C30-PP and C50-PP are considerably lower than C50 and have the lowest relative values.

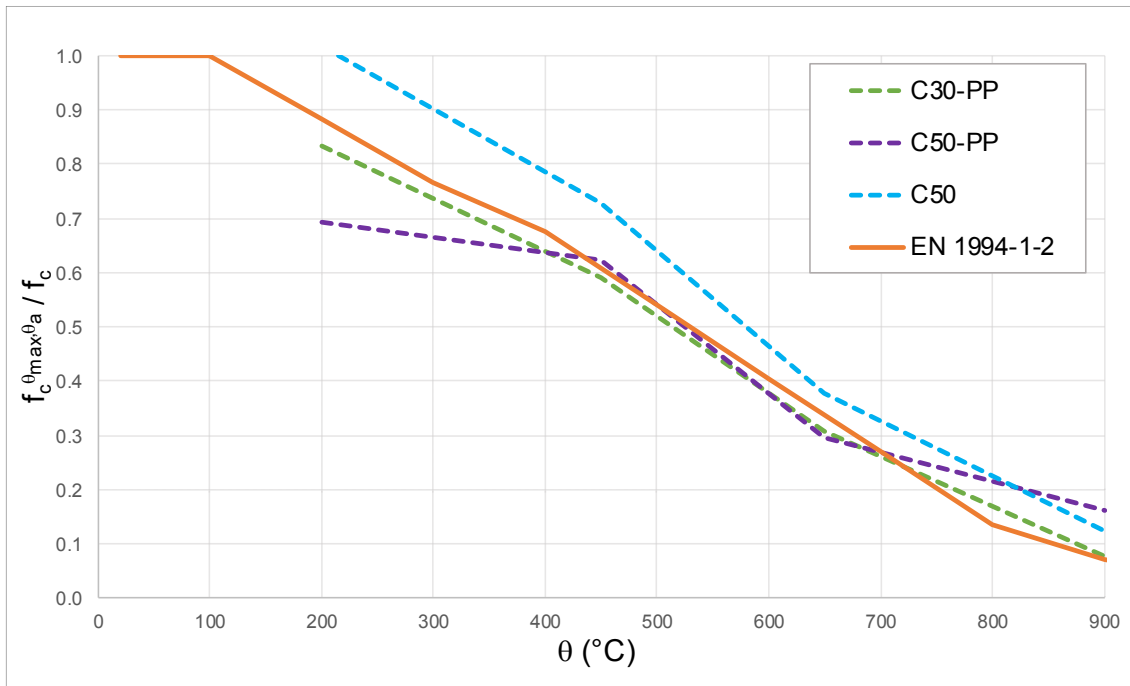


Figure 97: Residual strength reduction factors according to tests and EN 1994-1-2

9.9 Residual Compressive Strength after Specimen Is Cooled Down to a Specified Temperature

Series of residual compressive strength tests are performed for batches 2 and 3 (C30-PP and C50-PP) where the specimens heated to uniformly-distributed-maximum-desired temperatures of $\theta_{max} = 200, 450, 700$ and 900°C and then cooled down to uniformly distributed temperatures of $\theta_3 = 100, 200, 450$ and 700°C respectively and then subjected to compressive forces up to failure. Test numbers and configurations are given in Tab. 25. The relative residual reduction strength factors for C30-PP and C50-PP are illustrated in Figs. 98 and 99. It can be observed that residual reduction factors of the specimens cooled down to θ_3 is almost identical to the reduction strength factors of specimens at θ_{max} corresponding to each test for $\theta_{max} > 200^\circ\text{C}$.

Table 25: List of residual compressive strength tests after specimens cooled down to specified temperatures θ_3

Batch Nr.	Test Nr.	R (K/min)	α	θ_{max} (°C)	$f_c^{\theta_{max}}$ (MPa)	θ_3 (°C)	$f_c^{\theta_{max}, \theta_3}$ (MPa)	Displacement rate (mm/min)	E-test
2	86	5	0	700	13.08	450	14.39	1.6 → 0.8	
	89	5	0	700	13.08	450	15.87	1.6 → 0.8	
	90	5	0	200	26.43	100	29.78	1.0 → 0.5	
	91	5	0	900	5.05	700	4.76	2.2 → 1.0	
	92	10	0	900	5.05	700	5.22	2.2 → 1.0	
	94	5	0	450	24.77	200	24.57	2.0 → 1.0	
	96	5	0	450	24.77	200	23.41	1.0 → 0.5	
3	160	5	0	450	29.00	200	33.35	1.0 → 1.0	✓
	161	5	0	700	14.18	450	12.08	1.5 → 1.0	✓
4	199	5	0	450	29.00	200	40.04	1.0 → 1.0	✓

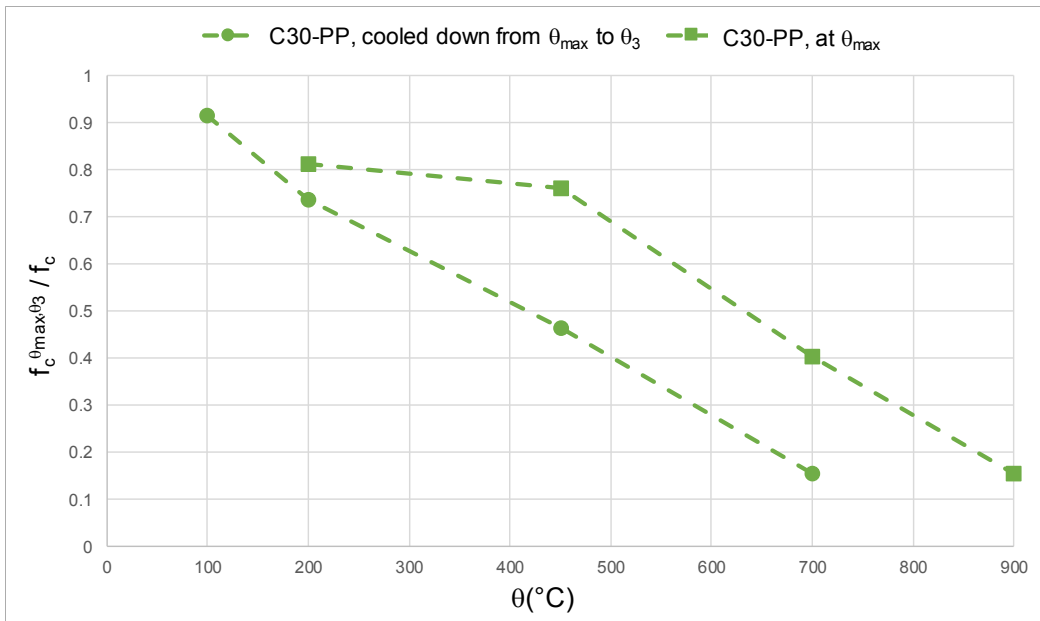


Figure 98: Residual reduction strength factors for C30-PP heated to θ_{max} and then cooled down to θ_3

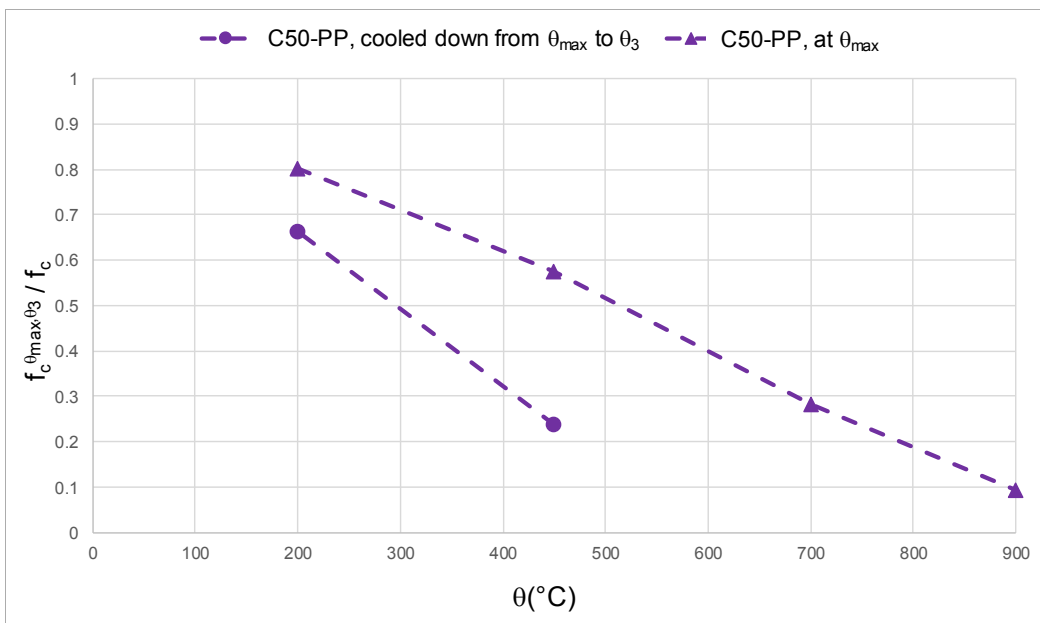


Figure 99: Residual reduction strength factors for C50-PP heated to θ_{max} and then cooled down to θ_3

9.10 Thermal Strains

Free thermal elongation of concrete specimens under a heating rate of $R = 5$ K/min are measured and correspondingly the thermal strains for all four batches are plotted in Fig. 100. In this figure, the upper boundary of thermal strains $\varepsilon_{tr,th}^{\theta,0,d}$ of all batches are illustrated with continuous line and the lower boundary with dotted line. Thermal strain of concrete specimens clearly decreases with the increase in compressive strength of concrete.

Comparing batches 3 (C50-PP) and 4 (C50), thermal strains $\varepsilon_{tr,th}^{\theta,0,d}$ of C50 are higher than C50-PP. For the temperature range between 200 and 270°C, PP-fibres within concrete accelerates moisture transport that results in an accelerated drying shrinkage in opposite direction of thermal strain. Difference between thermal

strains of C50-PP and C50 are much higher at temperature approximately above 580°C when the quartz transformation of the aggregates at 573°C has occurred.

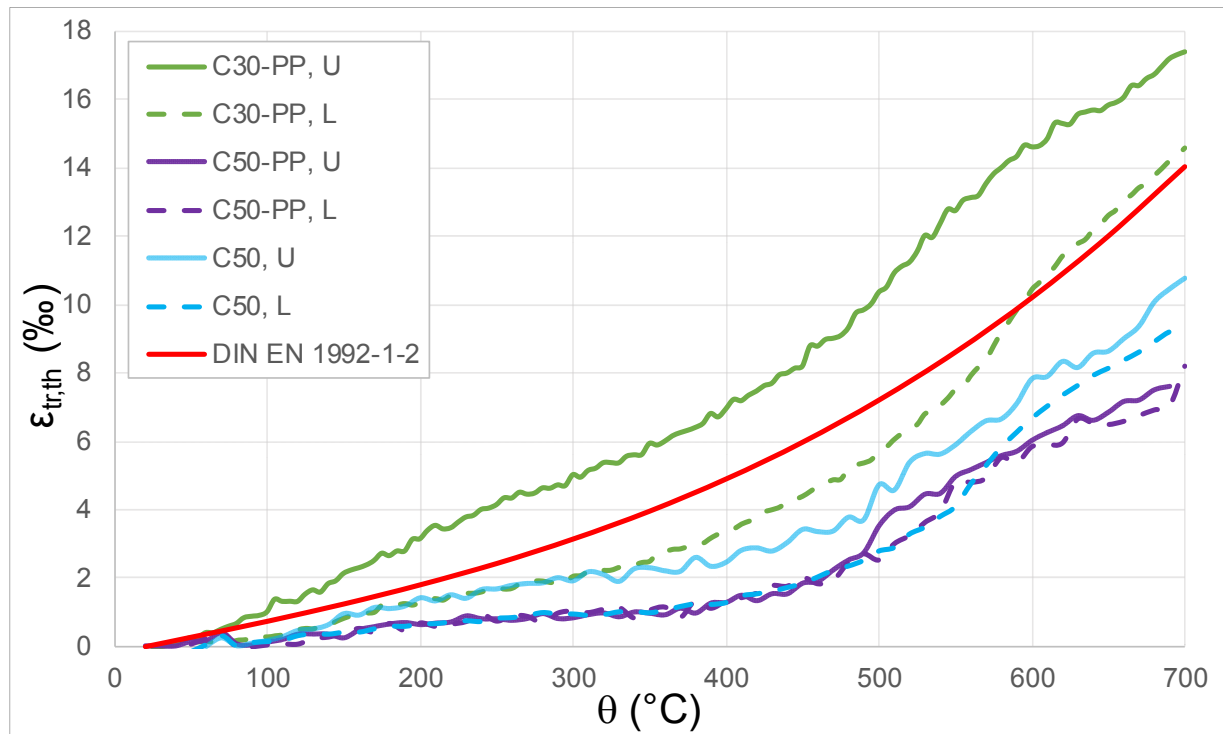


Figure 100: Upper (U) and lower (L) limits of thermal strains $\varepsilon_{tr,th}^{\theta,0,d}$ for concrete with and without PP-fibres

9.11 Total Transient Strains with Different Load Levels

Transient tests with various load levels $\alpha = 0, 0.1, 0.3$ and 0.5 are performed. The results of total transient strains $\varepsilon_{tr,tot}^{\theta,\sigma,d}$ are plotted for C50-PP and C50 in Figs. 101 and 102 respectively. Further, total transient strains of the both batches are plotted in Fig. 103. It can be noted that at load level $\alpha = 0.3$, the compressive strain level almost remains constant for temperatures up to 600°C for C50-PP. On the other hand, for C50 under the same load level, thermal axial elongation of concrete specimen has ruled the compressive forces within the concrete. Deviation between the strain-curves from both batches increases from approximately 200°C. This is due to the fact that the PP-fibres melt and provide escape paths for moisture content and at the same time making more porous structure in the concrete at this range. For the load level $\alpha = 0.5$, specimens failed at temperature range of 450-490°C. On the other hand, under load level $\alpha = 0.3$, none of the specimens failed up to 700°C. It can be noted that up to approximately 200°C, there is practically no influence arising from the addition of PP-fibres on the strain results from transient tests. For temperatures above 250 or 270°C, PP-fibres act like defects in the concrete and by micro-cracking releases the stresses. Micro-cracking contributes in the deformation and this might be the main reason for increasing mechanical strain of specimens with PP-fibres.

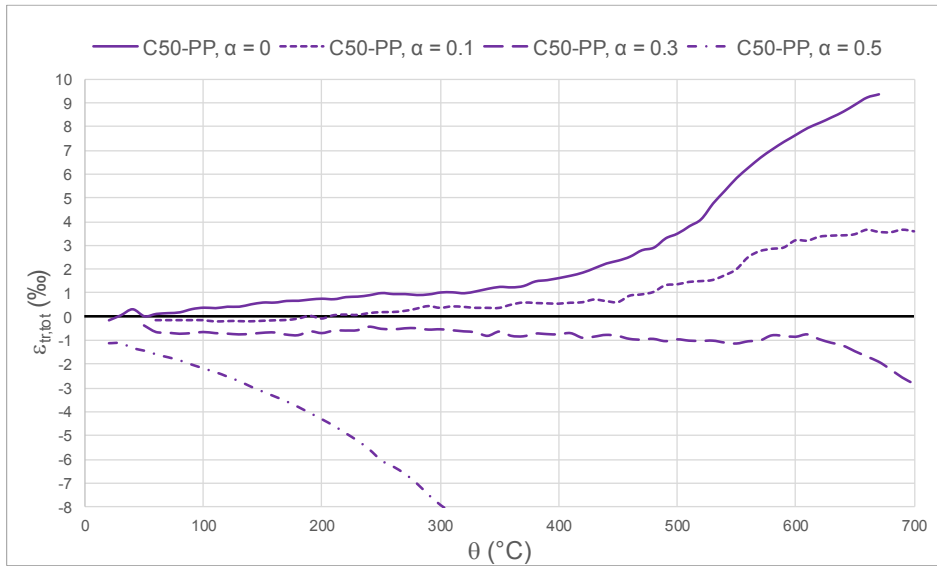


Figure 101: Total transient strains of C50-PP under different load levels

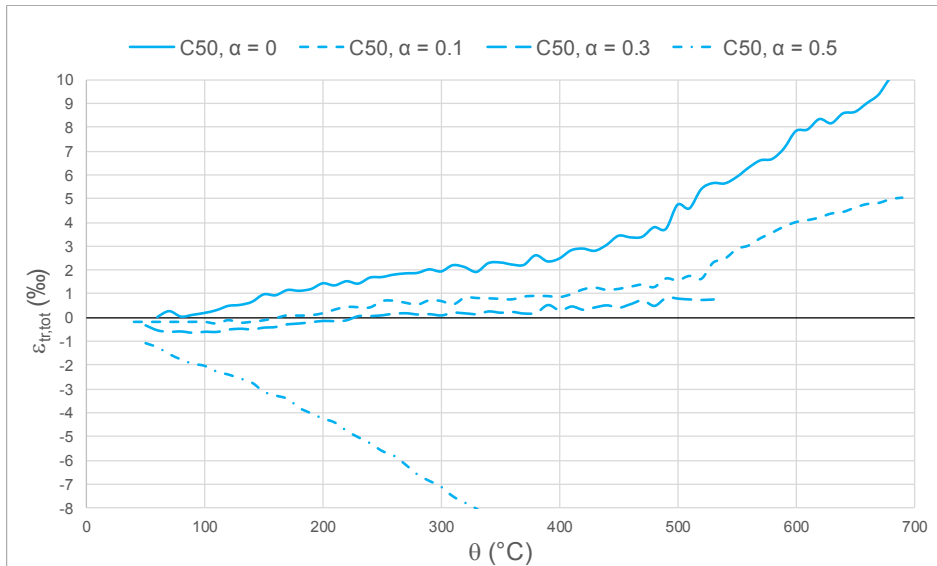


Figure 102: Total transient strains of C50 under different load levels

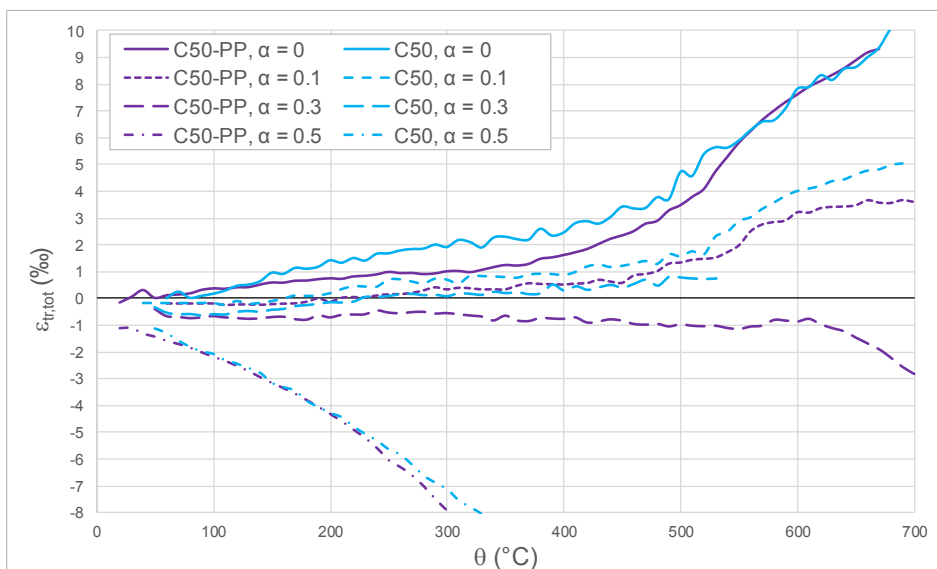


Figure 103: Total transient strains of C50-PP and C50 under different load levels

9.12 Strains and Relative Strains at Peak Stress Values for Specimens with Different Load Levels

In this section, strain values at the point of maximum stress, extracted from stress-strain curves, for C50-PP and C50 are considered (see Figs. 104 and 105) for load levels $\alpha = 0, 0.1$ and 0.3 . The absolute strain values for $\alpha = 0$ at the maximum stress for C50-PP are slightly lower for almost all the temperatures except for 450°C compared to C50 (Fig. 104). On the other hand, relative strain at peak stress values, $\varepsilon_{cI}^{\theta_{max}}$, in Fig. 105 show that for both batches these are almost identical with an exception of 450°C for $\alpha = 0$. In addition, $\varepsilon_{cI}^{\theta_{max}}$ values according to the performed tests are plotted in parallel with $\varepsilon_{cI}^{\theta_{max}}$ according to EN 1992-1-2 (implicit model) in Fig. 106. The normative curve accumulates transient creep component and is, thus, highly larger.

The $\varepsilon_{cI}^{\theta_{max}}$ as well as relative $\varepsilon_{cI}^{\theta_{max}}$ for pre-loaded tests with $\alpha = 0.1$ and 0.3 are evaluated by setting displacements at the beginning of the loading equal zero. The compressive peak and relative $\varepsilon_{cI}^{\theta_{max}}$ for the both pre-load levels are considerably higher for concrete without PP-fibres at 450 and 700°C compared to concrete with PP-fibres.

9.13 Strains at Peak Stress Values for Specimens Cooled Down to Specified Temperatures

For the specimens subjected to θ_{max} and then cooled down to θ_3 , the $\varepsilon_{cI}^{\theta_3}$ values are plotted in Figs. 107 and 108 for C30-PP and C50-PP along with the $\varepsilon_{cI}^{\theta_{max}}$ values from the stress-strain curves at θ_{max} for each batch respectively. The $\varepsilon_{cI}^{\theta_3}$ values at $\theta_3 = 200^\circ\text{C}$ are considerably higher compared to the $\varepsilon_{cI}^{\theta_{max}}$ at $\theta_{max} = 200^\circ\text{C}$. This difference becomes smaller for temperature equal to 450°C for C30-PP, whereas for C50-PP the $\varepsilon_{cI}^{\theta_{max}}$ and $\varepsilon_{cI}^{\theta_3}$ at θ_3 and $\theta_{max} = 450^\circ\text{C}$ are almost identical. This might be due to the higher thermal elongation of the cooled down specimens that further leaves more room within the specimen.

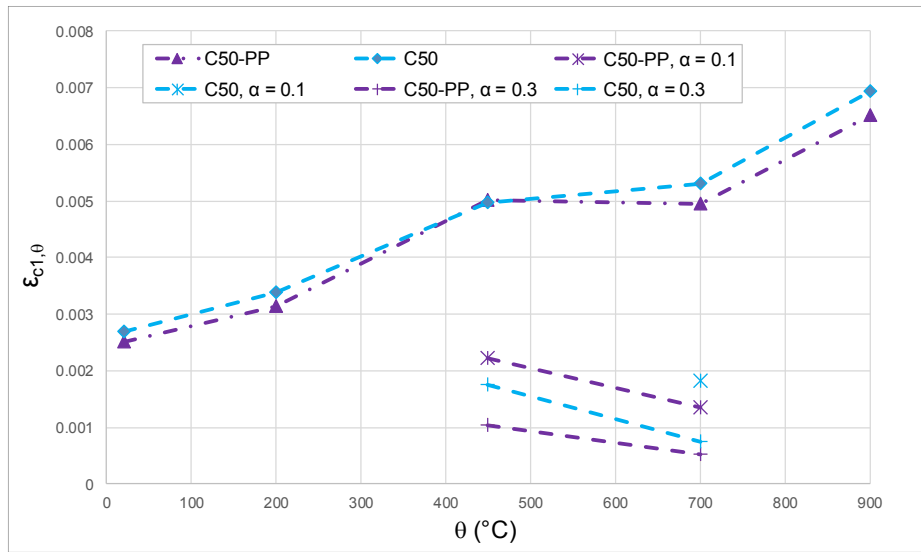


Figure 104: Strains at peak stress values for C50-PP and C50

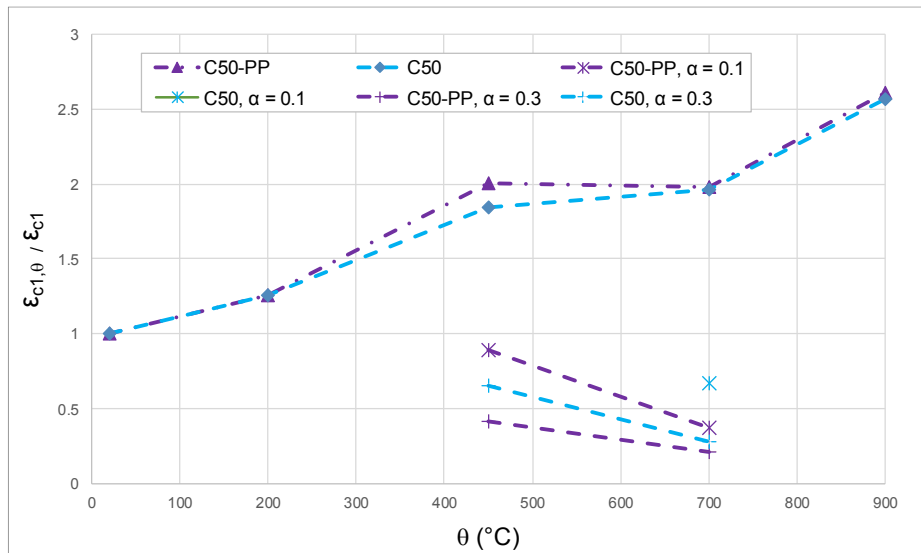


Figure 105: Relative strains at peak stress values for C50-PP and C50

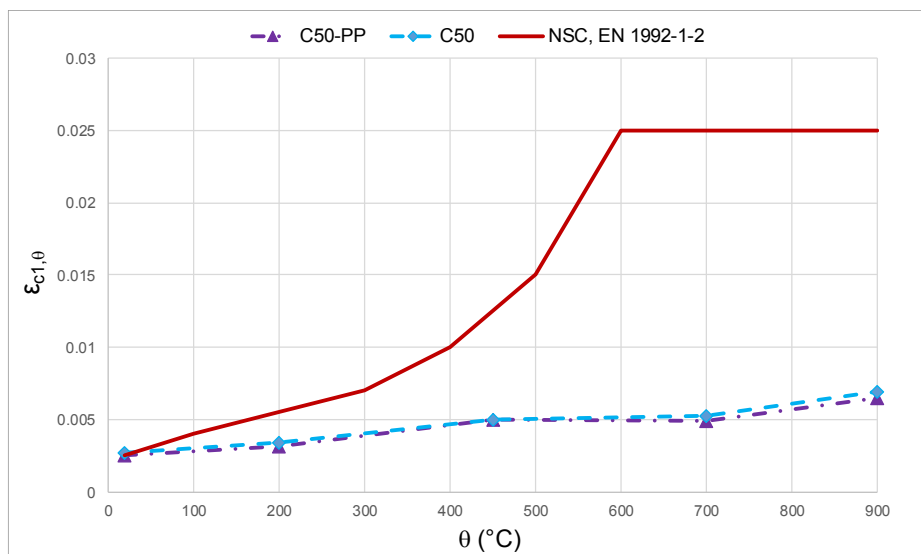


Figure 106: Strains at peak stress values from tests vs. the values from EN 1992-1-2 (implicit model)

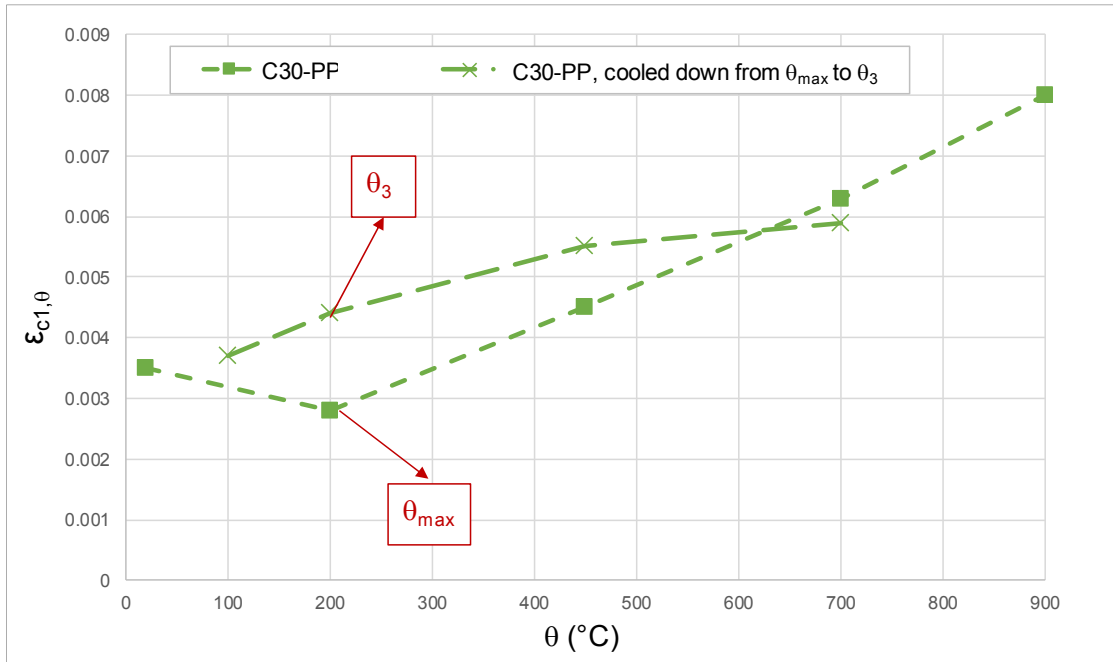


Figure 107: Comparison of strains at peak stress values for not-preloaded specimens ($\alpha = 0$) cooled down to specified temperature, θ_3 , with compressive tests at θ_{max} for C30-PP

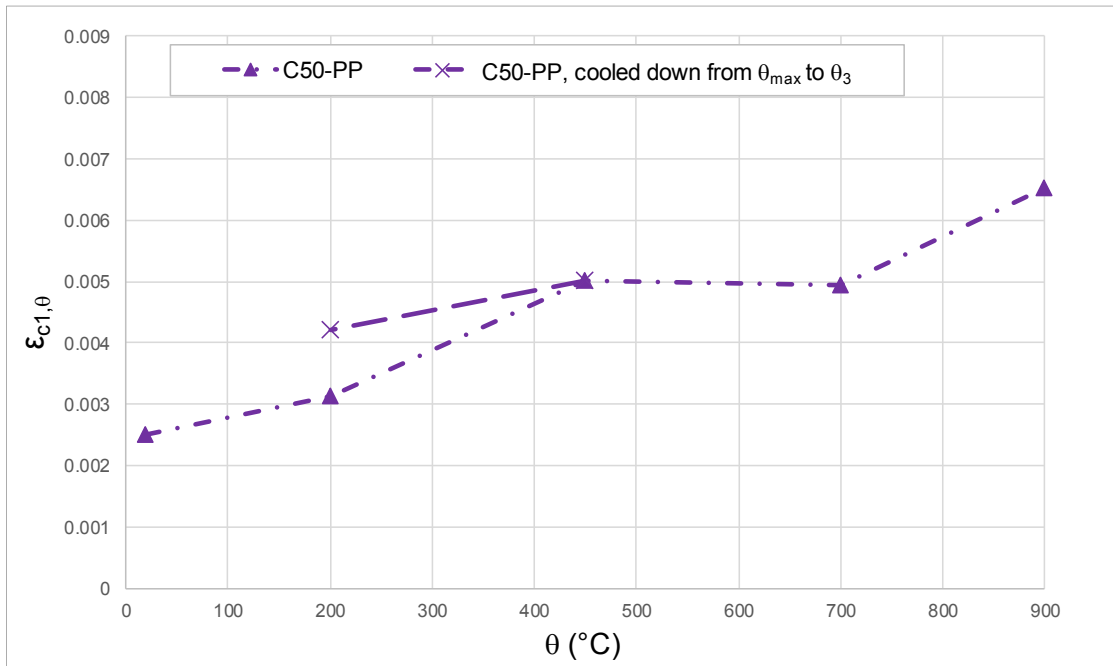


Figure 108: Comparison of strains at peak stress values for not-preloaded ($\alpha = 0$) specimens cooled down to specified temperature, θ_3 , with compressive tests at θ_{max} for C50-PP

9.14 Proposing a Constitutive Implicit Model for Concrete with Polypropylene Fibres

In this section, steady and transient results are used to construct an implicit constitutive model for concrete with PP-fibres based on the results of batch 3.

9.14.1 Strain at Maximum Stress for an Implicit Model

Using results of transient tests, transient creep values are evaluated for C50-PP and C50. These values are added to strains at peak stresses, as shown in Fig. 109, by assuming the upper boundaries of load levels equal $\alpha = 0.3$ and 0.5 . In addition, EN 1992-1-2 strain at peak stress values for implicit EN 1992-1-2's material model are illustrated in this figure. The upper boundary of $\alpha = 0.5$ should be assumed as relevant when the temperatures are to a sufficient extent below the failure temperatures of the transient tests (450-490°C). Comparing the results of tests under $\alpha = 0.3$, with EN 1992-1-2's values, the evaluated "strain at peak stress + transient creep" ($\varepsilon_{cl}^{\theta_{max}}$) values are considerably smaller than EN 1992-1-2 values. It is not known for the author under which load level was taken into account for the normative EN 1992-1-2 tests have been performed. Further, there are not any tests done by the author under $\alpha = 0.4$ to find the critical design temperature for this level.

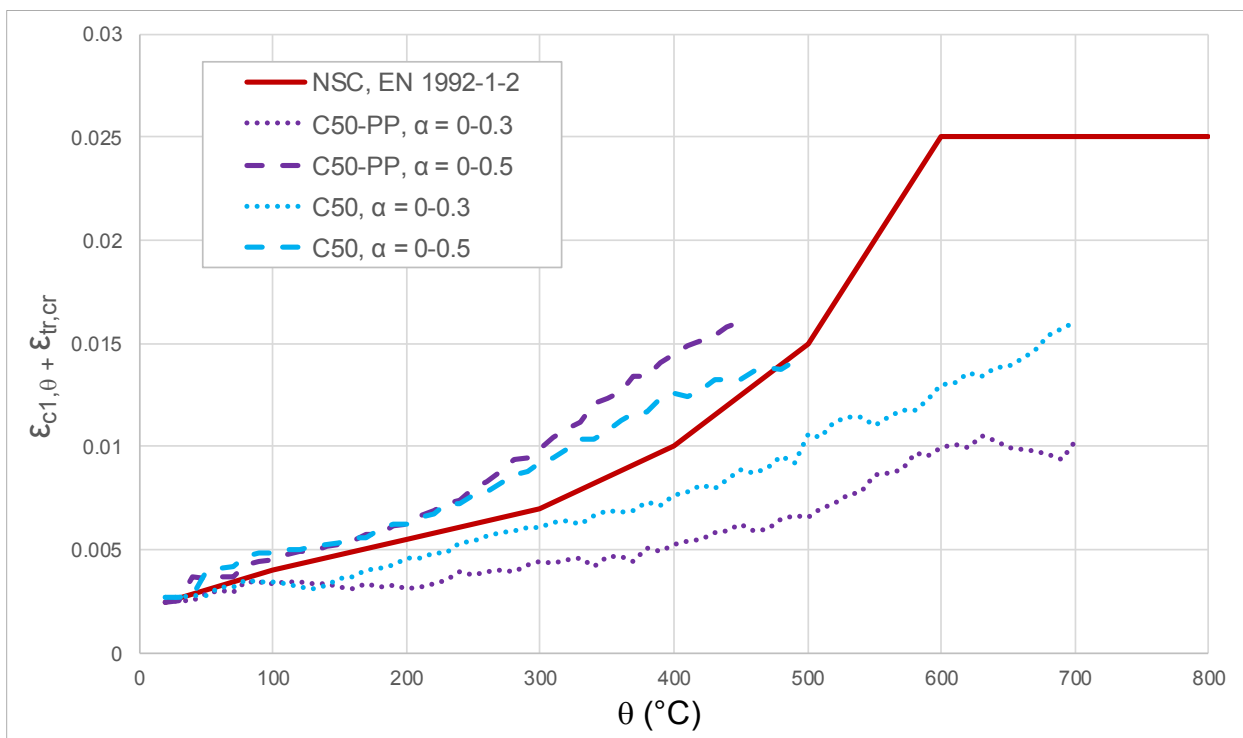


Figure 109: Strains at peak stress values due to tests and EN 1992-1-2

9.14.2 Stress-strain

EN 1992-1-2 proposes implicit stress-strain curves for different temperatures based on the strain at peak stress values, $\varepsilon_{cl}^{\theta_{max}}$, that accumulate the transient creep component. To compare the stress-strain curves with EN 1992-1-2, implicit stress-strain curves for the test results of C50-PP are constructed in this section.

To include the transient creep into the model, first it should be specified what is the realistic assumption for the upper load level, α , at the transient tests. As explained in the previous section, the upper limits of $\alpha = 0.3$ and 0.5 are assumed for the test results. For the tests with $\alpha = 0.5$, the failure temperature of transient tests occurred at 450-490°C. On the other hand, for $\alpha = 0.3$, specimens did not fail under the transient heating

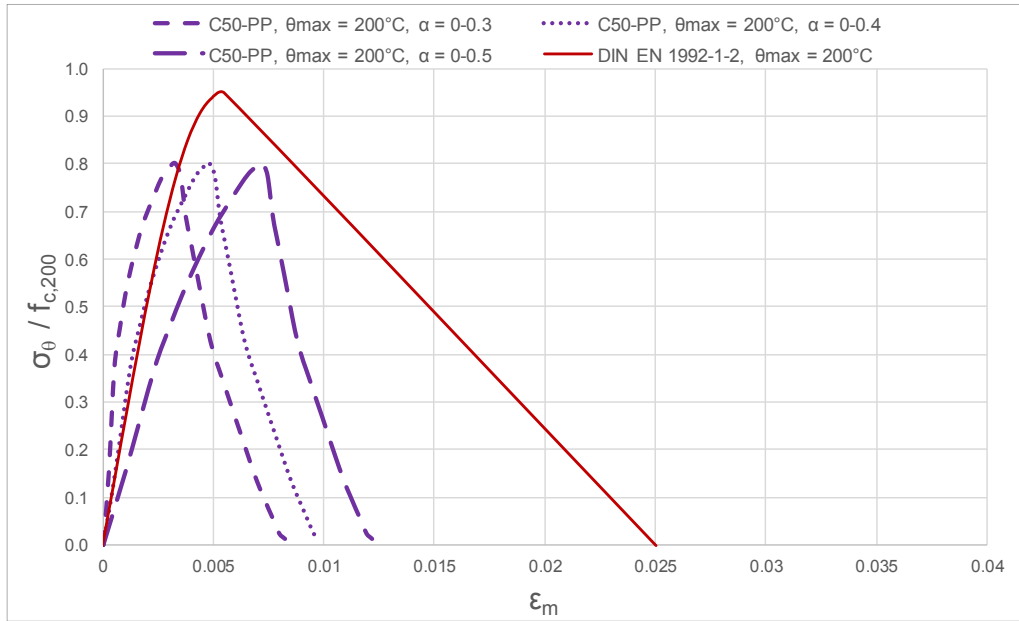


Figure 110: Implicit stress-strain curves at $\theta_{max} = 200^\circ\text{C}$ accumulating transient creep with different upper boundaries for C50-PP vs. EN 1992-1-2's stress-strain curve

to 700°C . It can be, therefore, assumed that $\alpha = 0.5$ might be an acceptable upper boundary assumption to evaluate transient creep when the temperatures are to a sufficient extent below 450°C .

Implicit stress-strain curves for C50-PP are plotted in Figs. 110, 111 (at 200°C) and Fig. 112 (at 450°C) respectively. The stress-strain curves are due to the upper and lower load level boundaries of 0.5 and 0.3 respectively. Further, the transient creep values for $\alpha = 0.4$ are predicted by taking the average strain values for $\alpha = 0.3$ and 0.5 at different points. Comparing the $\varepsilon_{cl}^{\theta_{max}}$ values of tests with EN 1992-1-2 curves for 200 and 450°C , it can be seen that for the predicted results with $\alpha = 0.4$, the estimated values and EN 1992-1-2's values are in a good agreement. Further, the slope of descending branch of the normative curve is close to the tests for 450°C . In addition, it should be noted that brittle failure occurred at 200°C . For the latter, EN 1992-1-2 considers a ductile failure with the ultimate strain values almost twice as large as tests.

EN 1992-1-2's model considers a constant $\varepsilon_{cl}^{\theta_{max}}$ value of 0.025 for NSC above 600°C . For a temperature of 700°C , the stress-strain results from tests with $\alpha = 0.3$ are plotted with EN 1992-1-2 in Fig. 113. The descending branch of both curves have a similar slope. It can be further observed that the $\varepsilon_{cl}^{\theta_{max}}$ of EN 1992-1-2 at 700°C is highly larger than $\varepsilon_{cl}^{\theta_{max}}$ values of the tests. Further, the transient creep values for $\alpha = 0.4$ at 700°C for C50-PP are predicted. It is done by using an upper $\varepsilon_{cl}^{\theta_{max}}$ limits of 0.025 subtracted by the average transient creep differences for load level $\alpha = 0.3$ at 700°C and $\alpha = 0.5$ at 450°C as follows:

$$\varepsilon_{tr,cr}^{700, \alpha = 0.4} = 0.025 - \text{average} \left[\left\{ \varepsilon_{tr,cr}^{700, \alpha = 0.3} (\text{batch 3}) - \varepsilon_{tr,cr}^{700, \alpha = 0.3} (\text{batch 4}) \right\} \text{ and } \left\{ \varepsilon_{tr,cr}^{450, \alpha = 0.5} (\text{batch 3}) - \varepsilon_{tr,cr}^{450, \alpha = 0.5} (\text{batch 4}) \right\} \right] \quad (74)$$

The predicted curve of $\varepsilon_{cl}^{\theta_{max}}$ for $\alpha = 0.4$ (at $\theta_{max} = 700^\circ\text{C}$) is illustrated in Fig. 113. The predicted $\varepsilon_{cl}^{\theta_{max}}$ values of this curve for C50-PP are, similarly to 200 and 450°C , lower than the strain at peak stress values proposed by EN 1992-1-2 model. The slope of descending branches are for EN 1992-1-2, tests and predicted values for $\alpha = 0.4$ similar.

Three modifications should be therefore implemented into the EN 1992-1-2 model to assume the influence of addition of PP-fibres by:

- Decreasing the allowable peak stress value (higher reduction of strength);
- Reducing the allowable strain at peak stress values;
- Modifying the ultimate strain values at the end of descending branch.

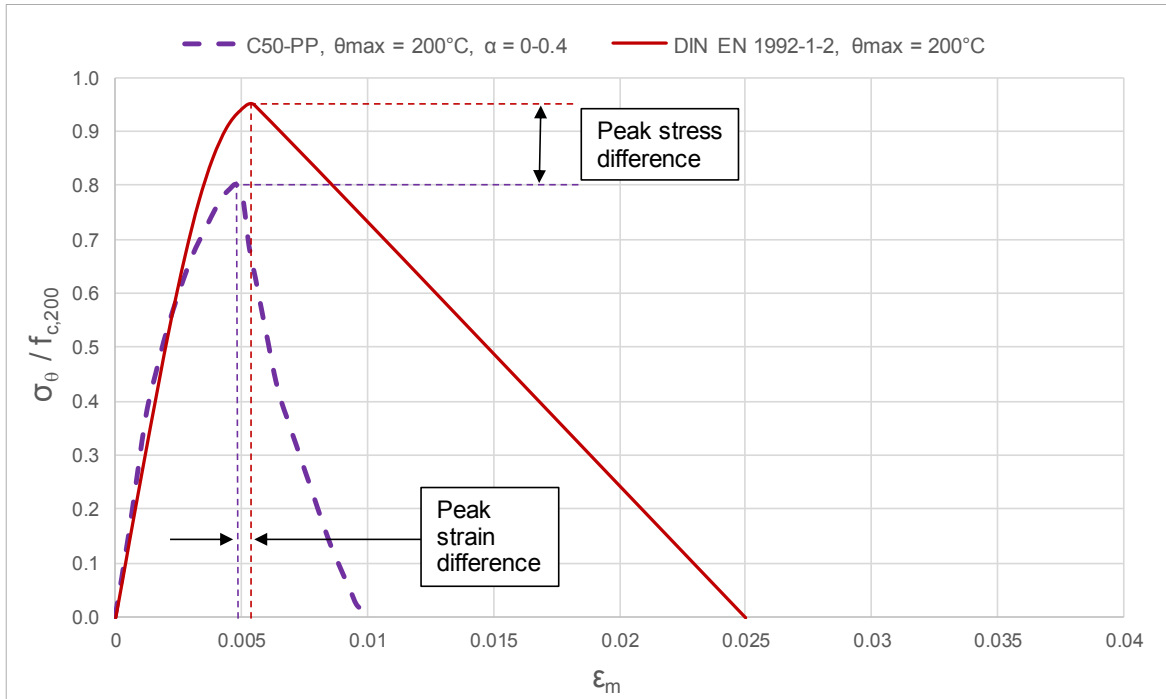


Figure 111: Implicit stress-strain curves for C50-PP vs. EN 1992-1-2's stress-strain curve at $\theta_{max} = 200^{\circ}\text{C}$ for $\alpha = 0.4$

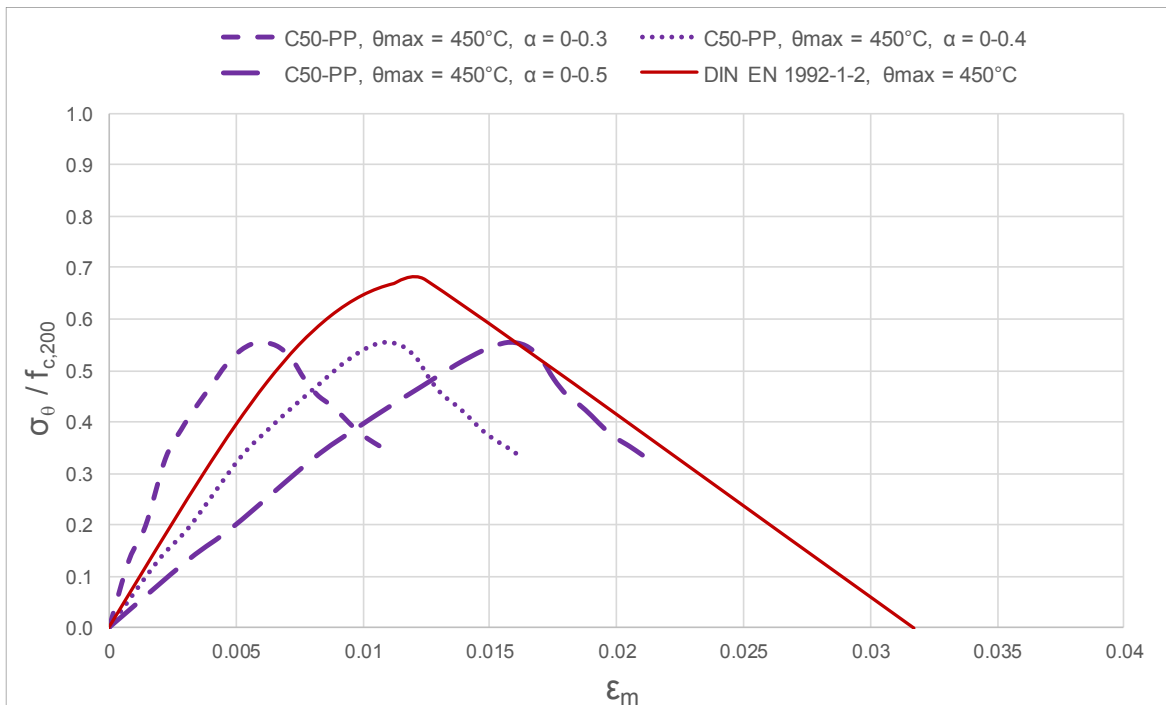


Figure 112: Implicit stress-strain curves at $\theta_{max} = 450^{\circ}\text{C}$ accumulating transient creep with different upper boundaries for C50-PP vs. EN 1992-1-2's stress-strain curve

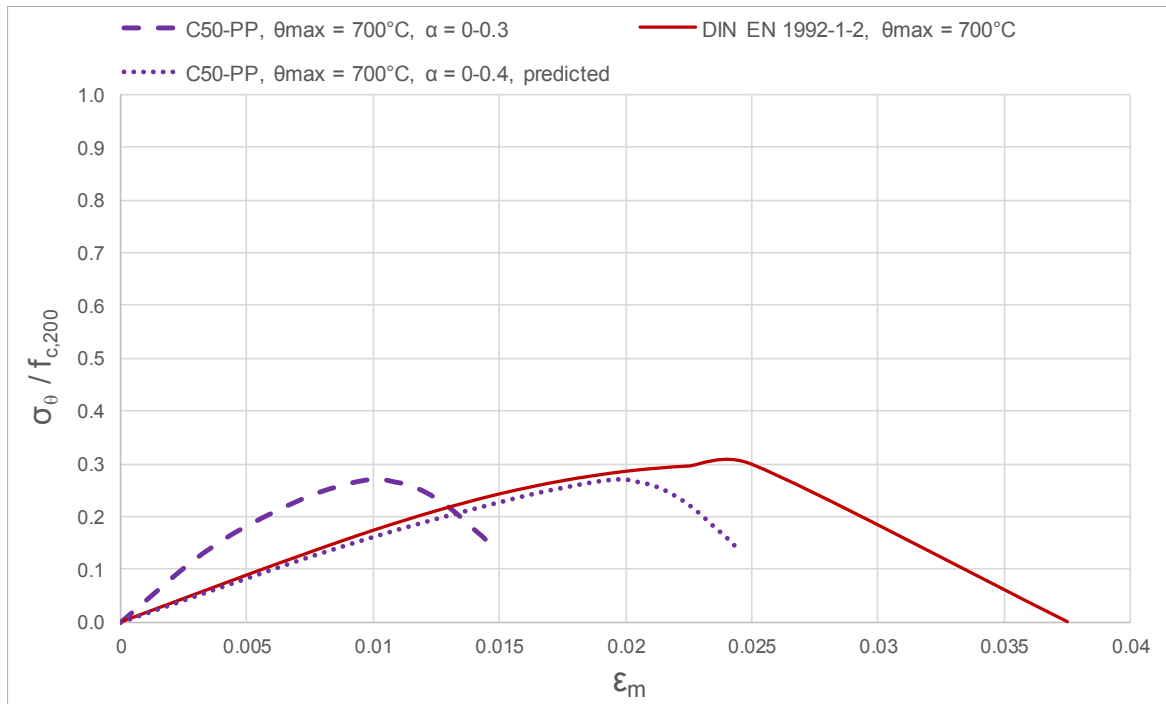


Figure 113: Implicit stress-strain curves at $\theta_{max} = 700^{\circ}\text{C}$ accumulating transient creep with upper boundary of $\alpha = 0.3$ for C50-PP vs. EN 1992-1-2's stress-strain curve

9.14.3 Modulus of Elasticity

For the implicit stress-strain results, slope of a line drawn from the origin to a point on the curve at 40% of the average compressive strength is assumed as the secant modulus of elasticity. The secant modulus of elasticity is estimated for the proposed implicit stress-strain curves considering the upper pre-load levels of $\alpha = 0.3, 0.4$ (predicted) and 0.5 . The relative moduli of elasticity based on different assumptions are plotted in Fig. 114. It can be seen that modulus of elasticity evaluated taking into account transient creep with upper

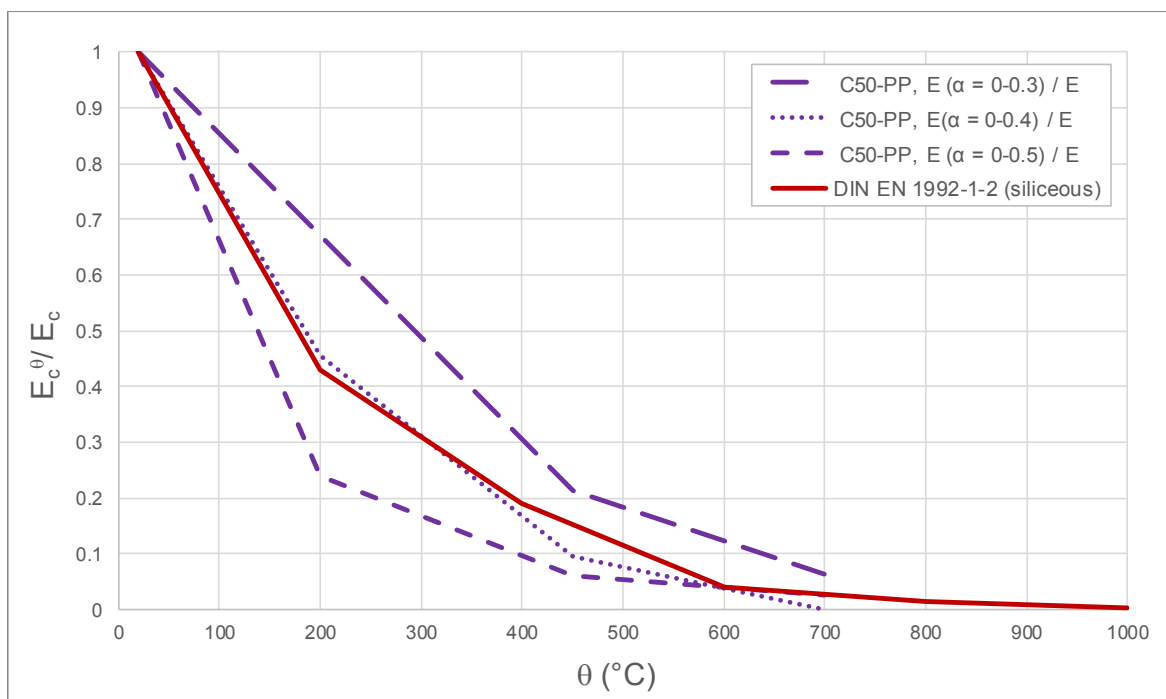


Figure 114: Relative moduli of elasticity extracted from stress-strain curves of C50-PP with upper limit of $\alpha = 0.3$ and lower limit of $\alpha = 0.5$ vs. EN 1992-1-2

load level of $\alpha = 0.4$ is in a very good agreement with the EN 1992-1-2's relative modulus of elasticity curve. The relative modulus of elasticity for $\alpha = 0.3$ and 0.5 give then the upper and lower boundaries of relative modulus of elasticity respectively. Relative modulus of elasticity at 700°C is predicted for $\alpha = 0.5$ and afterward from the average strain values for $\alpha = 0.5$.

9.14.4 Modified EN 1992-1-2 Stress-strain Model for Concrete with Polypropylene Fibres

To propose a model for concrete with PP-fibres that suggests a more practical usage, modifications are implemented into the proposed stress-strain model of EN 1992-1-2. Two modification factors are added into the proposed formula for the ascending branch of the stress-strain curve to estimate the stress-strain curves based on the predicted transient creep values for $\alpha = 0.4$ for C50-PP. The modification factors m and n are added to Eq. 28 as given in Eq. 75.

Further, the strain at peak stress values $\varepsilon_{cl}^{\theta_{max}}$ are modified (reduced) as given in Tab. 26.

$$\frac{\sigma}{f_c^{\theta_{max}} \cdot m} = \frac{3\varepsilon_m}{\varepsilon_{cl}^{\theta_{max}} \left(2 + \left(\frac{\varepsilon_m}{\varepsilon_{cl}^{\theta_{max}}} \right)^{3 \cdot (n=0.567)} \right)} \quad (75)$$

$$m = 1 \quad \text{for } 20 \leq \theta \leq 100^\circ\text{C}$$

$$m = -1.6 \theta \cdot 10^{-3} + 1.16 \quad \text{for } 100 < \theta < 200^\circ\text{C}$$

$$m = 0.840 \quad \text{for } \theta \geq 200^\circ\text{C}$$

In addition, in Tab. 26, the ultimate compressive strains, $\varepsilon_{cul}^{\theta_{max}}$, are evaluated and listed for different temperatures for the descending branch. Both strains given in Tab. 26 are lower than the given values in EN 1992-1-2.

Table 26: Strains at peak stresses and ultimate strains at elevated temperatures for the modified EN 1992-1-2's stress-strain model

θ ($^\circ\text{C}$)	20	100	200	300	400	500	600	700	800	900
$\varepsilon_{cl}^{\theta_{max}}$	0.0025	0.0035	0.0048	0.0073	0.0099	0.0130	0.0168	0.0205	0.0205	0.0205
$\varepsilon_{cul}^{\theta_{max}}$	0.0035	0.0058	0.0100	0.0164	0.0228	0.0263	0.0269	0.0275	0.0303	0.0330

Fig. 115 is illustrative of the results due to the modified material model and the stress-strain curves of C50-PP at elevated temperatures. The results of stress-strain curves based on the proposed formula are further plotted against EN 1992-1-2 curves in Fig. 116. Factor m in Eq. 75 takes account of strength reduction that should be implemented for concrete with PP-fibres.

It is assumed that at ambient temperature, m is equal to 1 as given in EN 1992-1-2. Therefore, this remains constant from ambient temperature to 100°C . Since the tests for C50-PP are performed at $\theta_{max} \geq 200^\circ\text{C}$ and the relative reduction factor of C50-PP to EN 1992-1-2 is at 200°C equal 0.84, a linear interpolation between 1 and 0.84 is considered for m between 100 and 200°C . For the temperatures equal and higher than 200°C , m remains constant and equal to 0.84. Further, the influence of changing m for $\theta_{max} = 200$ and 450°C is illustrated in Fig. 117.

In addition, n modifies the curvature of the ascending branch. Fig. 118 shows the influence of different n values on the curvature of ascending branch for $\theta_{max} = 200$ and 450°C . $n = 0.567$ is assumed for all the temperature levels. To compute n , nonlinear regression method is used. The factor n is computed by considering that the differences between strains in the ascending branch of the test results of C50-PP for $\theta_{max} = 200, 450$ and 700°C and the proposed formula remains under 5% for the corresponding stress levels.

For the descending branch of the proposed model, linear course is assumed from the strain at peak stress to the ultimate strain.

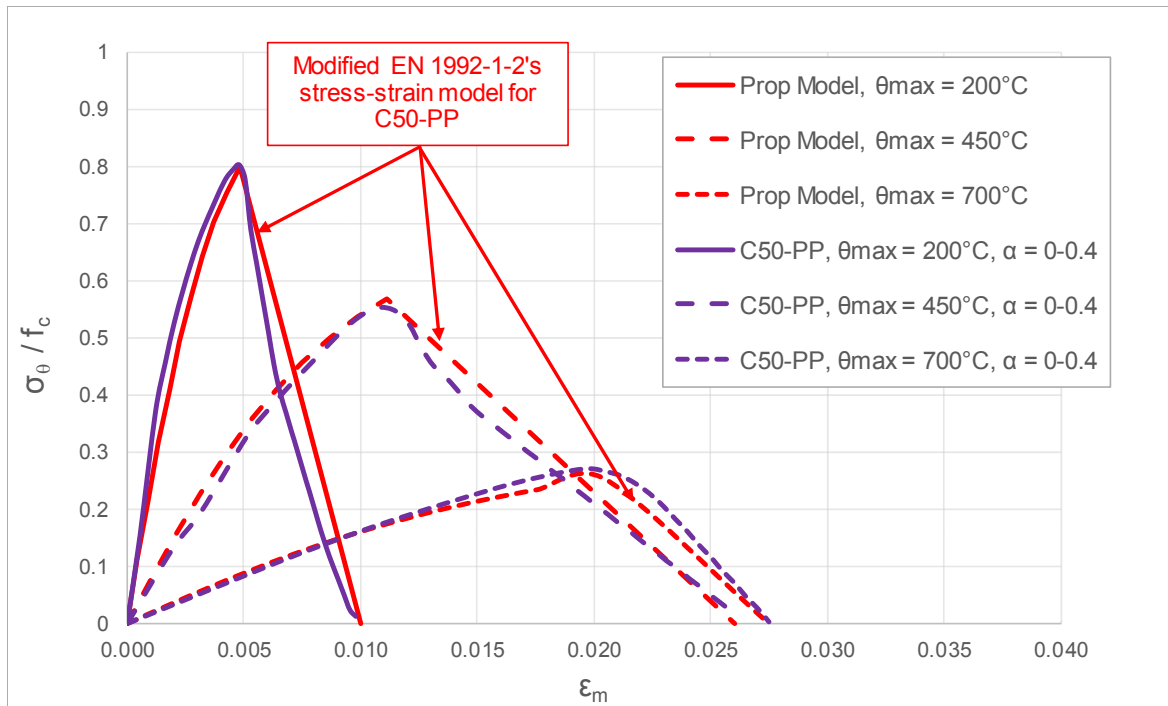


Figure 115: Modified implicit proposed stress-strain curves vs. stress-strain curves of C50-PP

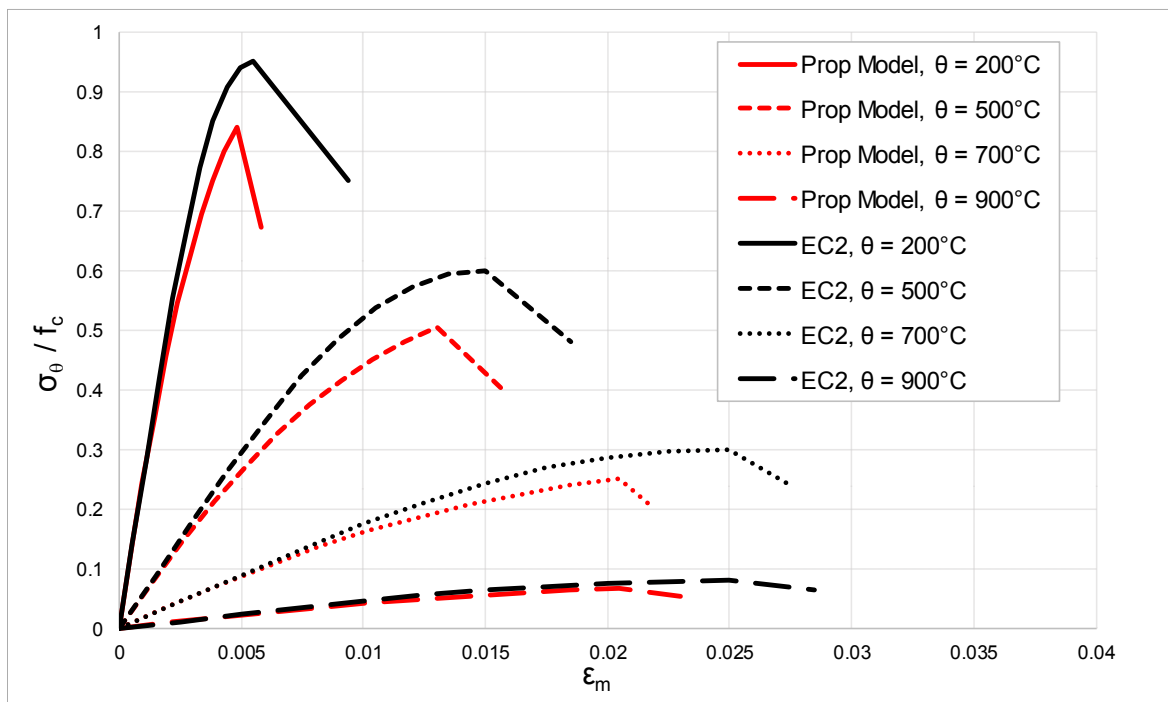


Figure 116: Comparison of the proposed stress-strain model with EN 1992-1-2's model at elevated temperatures

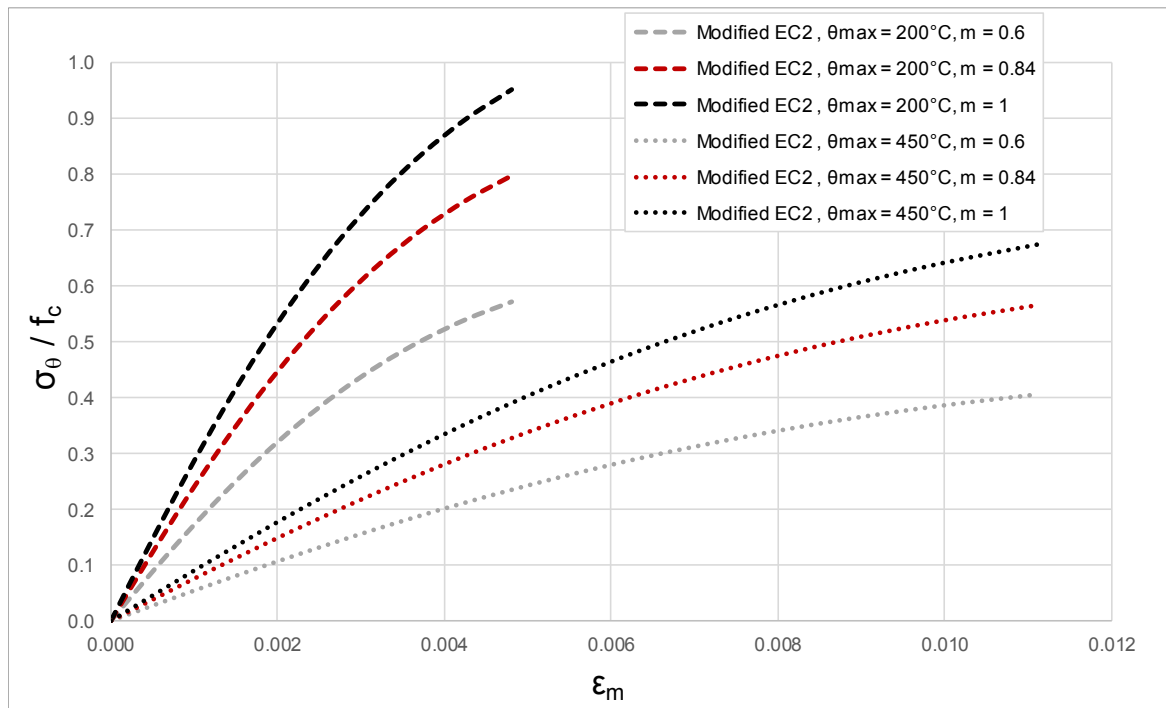


Figure 117: Influence of changing factor m on the stress-strain curves for $\theta_{max} = 200$ and 450°C

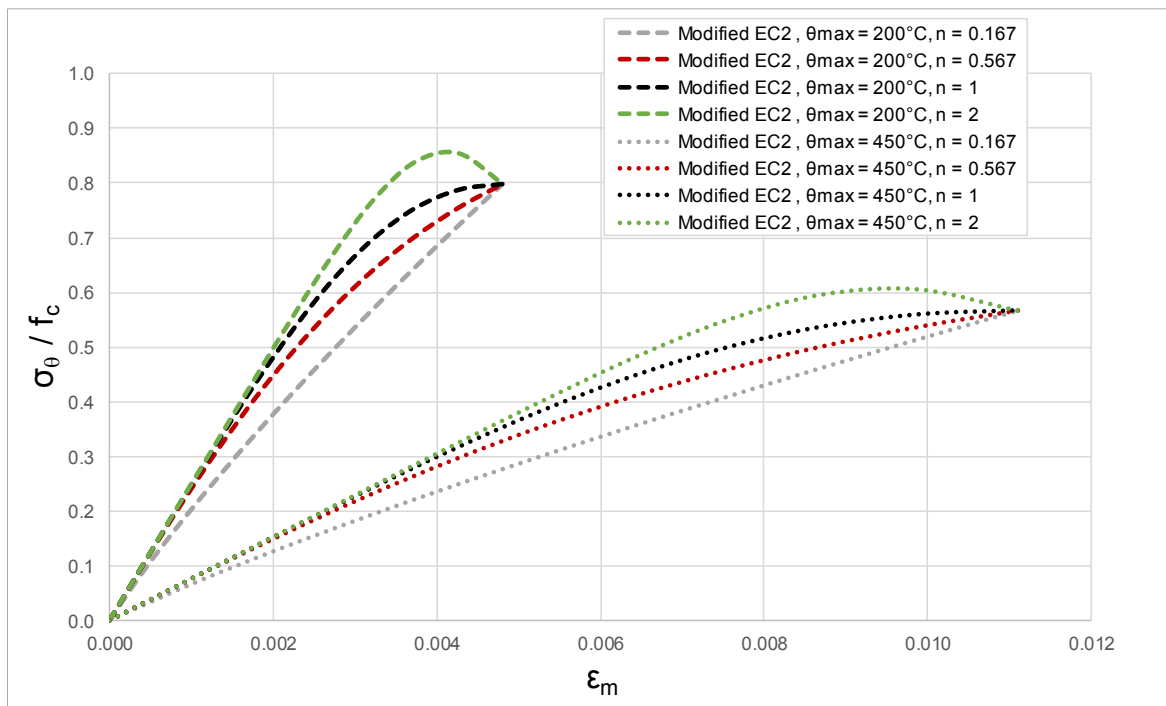


Figure 118: Influence of different n values on the curvature of the ascending branch of stress-strain curves for $\theta_{max} = 200$ and 450°C

10 Structural Analysis of a Cut-and-cover Tunnel under ZTV-ING Fire Using Finite Element Method

10.1 General

To sum up different aspects which might influence the thermo-mechanical analysis of a cut-and-cover tunnel structure exposed to ZTV-ING fire curve, an example of a 2-cell-cut-and-cover reinforced concrete tunnel having PP-fibres in its admixture is investigated later in this chapter. Different parameters that might affect the nonlinear structural analysis of a cut-and-cover tunnel exposed to ZTV-ING are discussed in (Pouran, et al., 2017). The following aspects are dealt with in this chapter:

- General structural mechanics: a short discussion on the general structural mechanics for beam members and Euler Bernoulli and Timoshenko beam theories;
- An insight into the concept of finite element method (FEM) covering elastic, nonlinear material analysis;
- EN 1992-1-1's design concept of reinforced concrete beams at ambient temperatures and level 2 and level 3 concept according to EN 1992-1-2;
- Short explanation on the available element types and strategies in SOFiSTiK (2016) to perform physically nonlinear thermo-mechanical analysis;
- Investigating available benchmark examples and other existing examples for the case of fibre beams at elevated temperatures in SOFiSTiK;
- Performing nonlinear analyses on single-span and two-span beams with different constraints having a rectangular cross-section exposed to fire;
- Investigating a study case of the cut-and-cover tunnel structure by analysing the followings:
 - Initial stress state of structure and cross-section at the beginning of fire;
 - Analysing the cross-sectional variable states parallel with thermal effects;
 - Effect of modification of constitutive concrete material model on the structure level.

10.2 Structural Mechanics

General constitution of theory of structural mechanics for all member types is based on three fundamental equations:

- Equilibrium equation which relates the external forces to the internal forces with a differential equation;
- Kinematic equations. Considering two points on a body, the kinematic equations enable us to distinguish between the observable displacements, translation and rotation, which do not impose internal forces, and relative internal deformation of these points (strains) which induce internal forces. The latter is expressed with set of differential equations;
- Constitutive material law: the constitutive material law states the relationship between stresses and strains of a material based on the material properties collected from experiments. In the case of elastic behaviour, this relation is expressed with algebraic equations.

The solution derived from the combination of these equations must fulfil the dynamics boundary conditions, that shows the stresses on the boundary, \mathbf{O}_r , are compatible with the prescribed boundary forces. Further, geometric boundary conditions must also be met on the boundary that means the displacement on the boundary \mathbf{O}_r (point, line or surface) are compatible with the prescribed displacements. This is illustrated in Fig. 119 in the known Tonti Diagram for all member types.

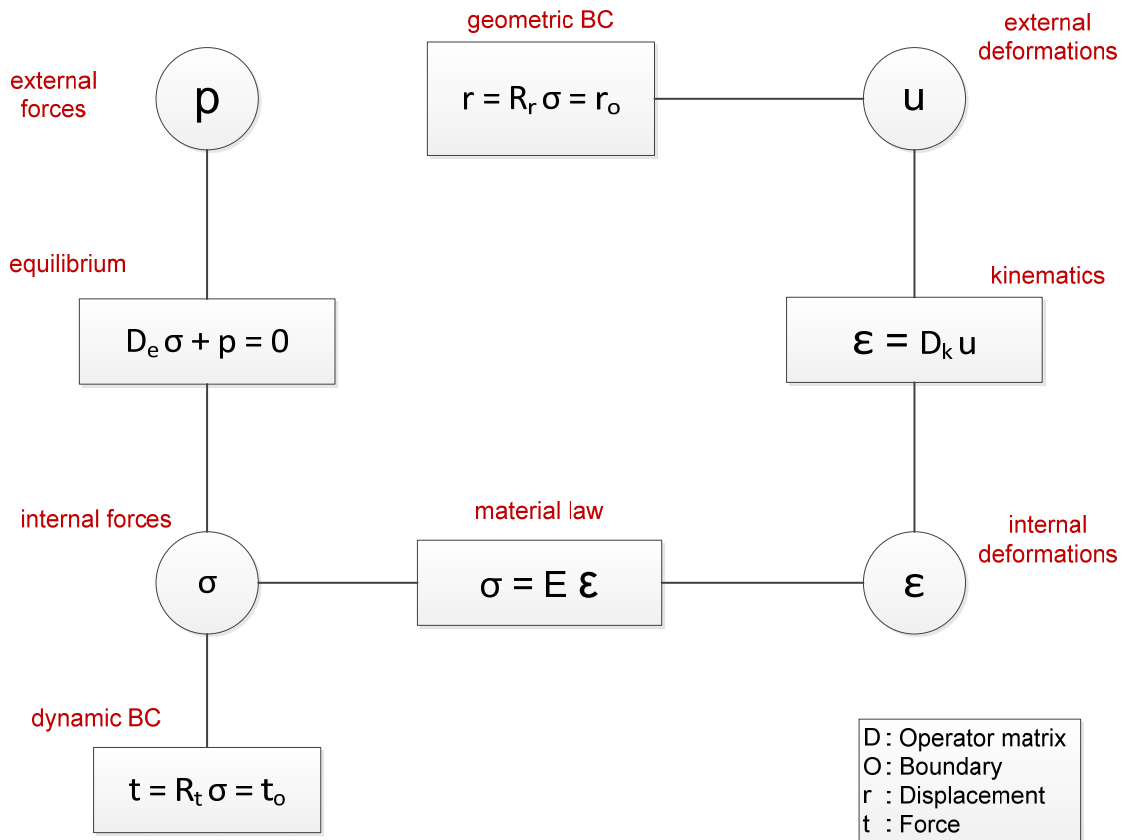


Figure 119: General theory of structural mechanics for all member types (Tonti-scheme)

10.3 Beam Theory according to Euler-Bernoulli and Timoshenko

In case of beam members in a plane, there are three degrees of freedom and correspondingly three internal forces at each section. Normal hypothesis of Bernoulli states the orthogonal line to the cross-section of undeformed beam remains orthogonal after the deformation. This means, the transversal shear strain which distorts the cross-section is not taken into account:

$$\gamma \equiv 0 \quad (76)$$

Later, Timoshenko proposed his theory where he took account of shear. Considering shear deformation, as shown in Fig. 120, the rotation of a beam cross-section is the sum of rotation due to bending and shear strain:

$$\psi = \psi_{bend} + \psi_{shear} = \frac{du_z}{dx} + \gamma \quad (77)$$

The classical bending moment and shear force equations according to Euler-Bernoulli are:

$$M = -EI \frac{d^2 u_z}{dx^2} \quad (78)$$

$$V = -EI \frac{d^3 u_z}{dx^3} \quad (79)$$

To Timoshenko on the other hand, there exists two uncoupled equations:

$$M = -EI \frac{\partial \psi}{\partial x} \quad (80)$$

$$V = -GA \theta = GA \left(\psi - \frac{\partial u_z}{\partial x} \right) \quad (81)$$

The Euler-Bernoulli theory takes account of stiffer beam cross-section. The difference between these two theories decrease for the less shear stiff beams (long beams with small thickness).

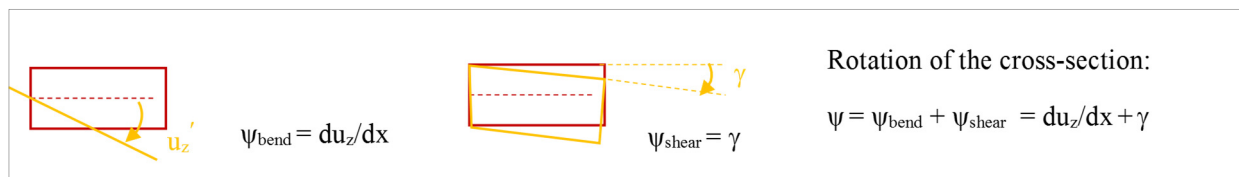


Figure 120: Nodal rotation of a beam member under transverse loading

10.4 An Insight into Finite Element Method

As explained, the structural mechanics is based on three main fundamental equations; equilibrium, kinematics and material law. The combinations of these fundamental equations lead to the governing differential equations that relate the external forces with displacements. Equilibrium in classical structural mechanics is demonstrative of an equilibrium condition in a small element and has a differential form (strong form). To solve the differential governing equations, boundary conditions must be fulfilled. Analytical classical solutions are usually applicable on academic simple structural models made of one member type.

The finite element method (FEM) provides numerical computer based solution to be used for arbitrary combination of member types. It is based on discretization of the structure into different elements and writing down the equilibrium condition for each element ($\mathbf{S}_{loc} = \mathbf{K}_{loc} \cdot \mathbf{V}_{loc}$). Having constructed the element stiffness matrix, \mathbf{K}_{loc} , and nodal degrees of freedom, \mathbf{V}_{loc} , and nodal force vectors, \mathbf{S}_{loc} , and by using Direct Stiffness Method (DSM), the element and nodal matrices are transformed into a global matrix form ($\mathbf{S}_{glob} = \mathbf{K}_{glob} \cdot \mathbf{V}_{glob}$). The solution of the global equation now gives the global nodal degrees of freedom, \mathbf{V}_{glob} , from which we can extract element displacements. From the evaluated nodal degrees of freedom and the local stiffness matrix, we are able to compute the nodal forces of an element.

As explained, FEM starts with the equilibrium condition within an element but it does not start with analytical structural differential formulation, instead it starts with work principle for the considered element. The work principle states that after external forces and internal forces done work on an elastic system, total potential energy of the system remains constant.

We can now assume an axial spring with stiffness k suspended and extended due to a gravity force G as representative of the truss element with the equivalent extensional stiffness EA . The gravity external force G caused a nodal displacement u and axial elongation of spring that induce the internal spring force in the spring, F . Both external works done by G ($W_G = mgz$) and internal work done by F ($W_F = 1/2 ku^2 = 1/2 Fu$) are dependent on the final displacement of u , not the path taken (potential). The work principle states that total potential energy remains constant:

$$W_{tot} = W_{tot}(u) = W_{ext} + W_{int} = const \quad (82)$$

where W_{tot} is the total potential energy, W_{ext} refers to the external work and W_{int} stands for internal work. The first derivation of total potential with respect to u gives us minimum of the total potential and is equivalent to equilibrium:

$$\frac{dW_{tot}}{du} = 0 \quad \Rightarrow -G + k u = -G + F = 0 \quad \Rightarrow F = G \quad (83)$$

FEM starts with the work principle. It is mathematically a variational problem. Writing down the total work done on a simply supported truss with length L subjected to axial external force over the length (Zahlten, 2017).

$$W_{tot} = - \int_0^L \sigma \varepsilon dx + \int_0^L p u dx = minimum \quad (84)$$

That can be stated as $W_{tot} = W_{int} + W_{ext}$.

$$W_{tot} = - \int_0^L \frac{1}{2} EA u'^2 dx + \int_0^L p u dx = minimum \quad (85)$$

The latter is a variational problem. Our desired function which minimizes the functional W_{tot} is our true displacement function $u(x)$. After integration by parts and rearranging the equation:

$$\delta W_{tot} = - \int_0^L (EA u'' + p) \delta u dx + EA u' \delta u \Big|_{x=0}^{x=L} = 0 \quad (86)$$

$$EAu'' + p = 0 \quad (\text{Euler-Lagrange Equation}) \quad (87)$$

The solution of Euler-Lagrange Equation (ELE) yields the desired $u(x)$ function.

Principle of Virtual Displacement (PVD) is the basis of FEM. PVD is a variational problem that yields the equilibrium. PVD states in general that for a body in equilibrium, the sum of virtual work done on the system is equal zero. The virtual displacement imposes virtual internal deformation or strains ($\delta\epsilon$) which does internal work with true stresses σ and virtual displacement (δu) or variation of u which does work with external force p . If we now consider the general form of PVD (example of a work principle) within a domain v :

$$\delta W = - \int_v \sigma \delta\epsilon dv + \int_v p \delta u dv + BT = 0 \quad (88)$$

where BT refers to the boundary terms. PVD yields the equilibrium equation in an integral form (weak form of equilibrium).

FEM starts with elementwise application of direct solution of RITZ method for our variational problem. A displacement function is defined as a sum of test functions $g_i(x)$ weighted by an unknown parameter a_i :

$$y(x) = a_1 g_1(x) + a_2 g_2(x) + \dots \quad (89)$$

Our test function can have different shapes (the quality of solution is dependent on our choice). It must fulfil the geometric boundary condition. The dynamic boundary condition is further fulfilled automatically. We now add our displacement function in general form of variational problem (PVD):

$$\delta W = - \int_v \sigma \delta\epsilon dv + \int_v p \delta u dv \quad (90)$$

The first variation must vanish.

$$\delta y(x) = \delta a_1 [\dots] + \delta a_2 [\dots] + \dots = 0 \quad (91)$$

δa_i and a_i are independent so all the terms in the brackets must be zero. In this way, we might be able to find all a_i parameters from algebraic equations. Moreover, as a result, the displacement function can be found. RITZ solution is an approximating solution; we construct a global equilibrium (weak form) in each element and use our test functions.

After we found the solution of the nodal displacements (extracted from the system nodal degrees of freedom), the course of change for displacements, strains and stresses over different dimensions of an element should be constructed. This is done by choosing shape functions (linear, quadratic or higher orders) based on our choice. They state how the nodal degrees of freedom should be interpolated in different dimensions in relation with all nodal degrees of freedom in an element. In Figs. 121a and 121b, FEM for displacement element formulation is schematically explained with the main points.

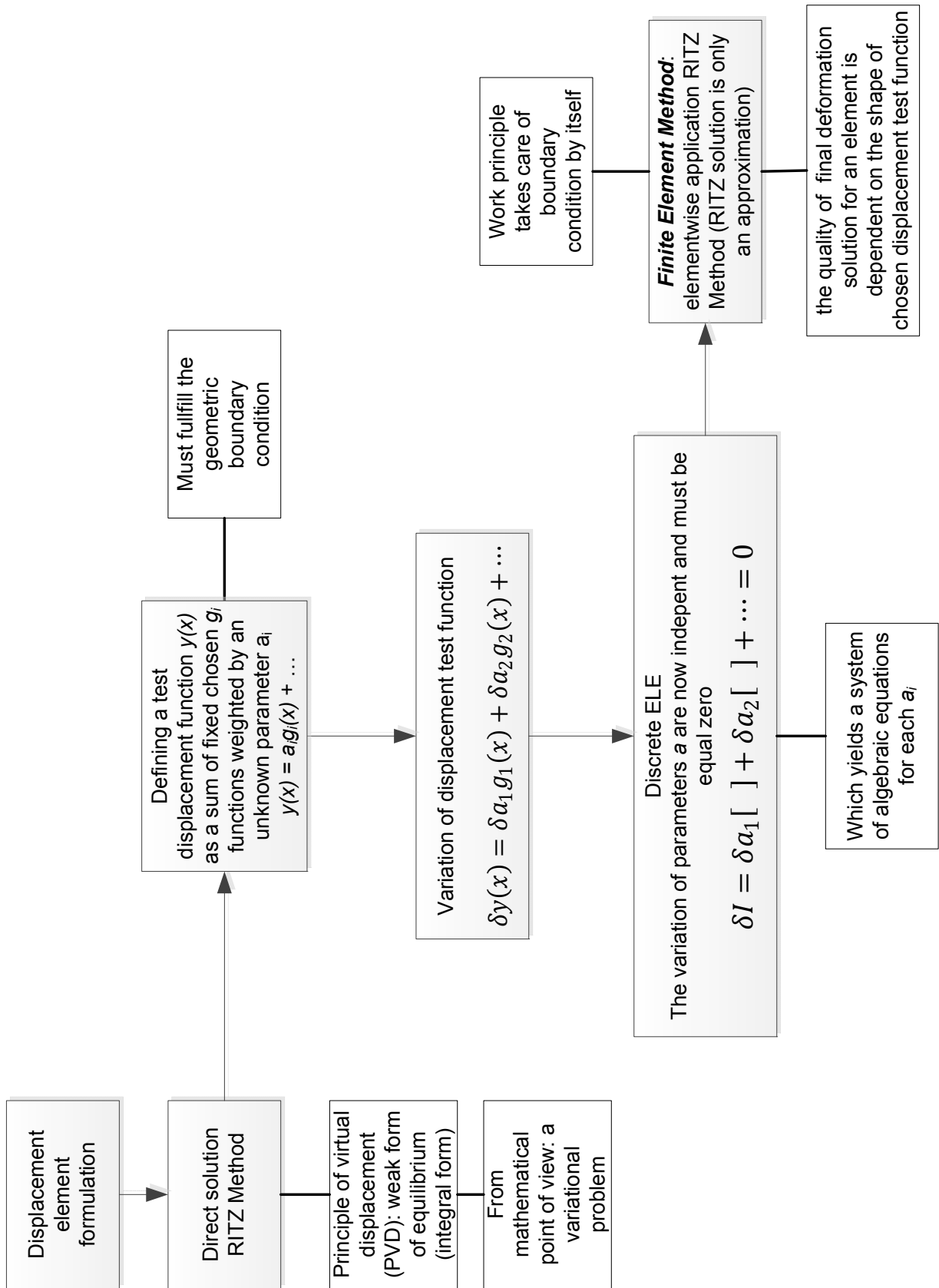


Figure 121a: Scheme of FEM for displacement element formulation

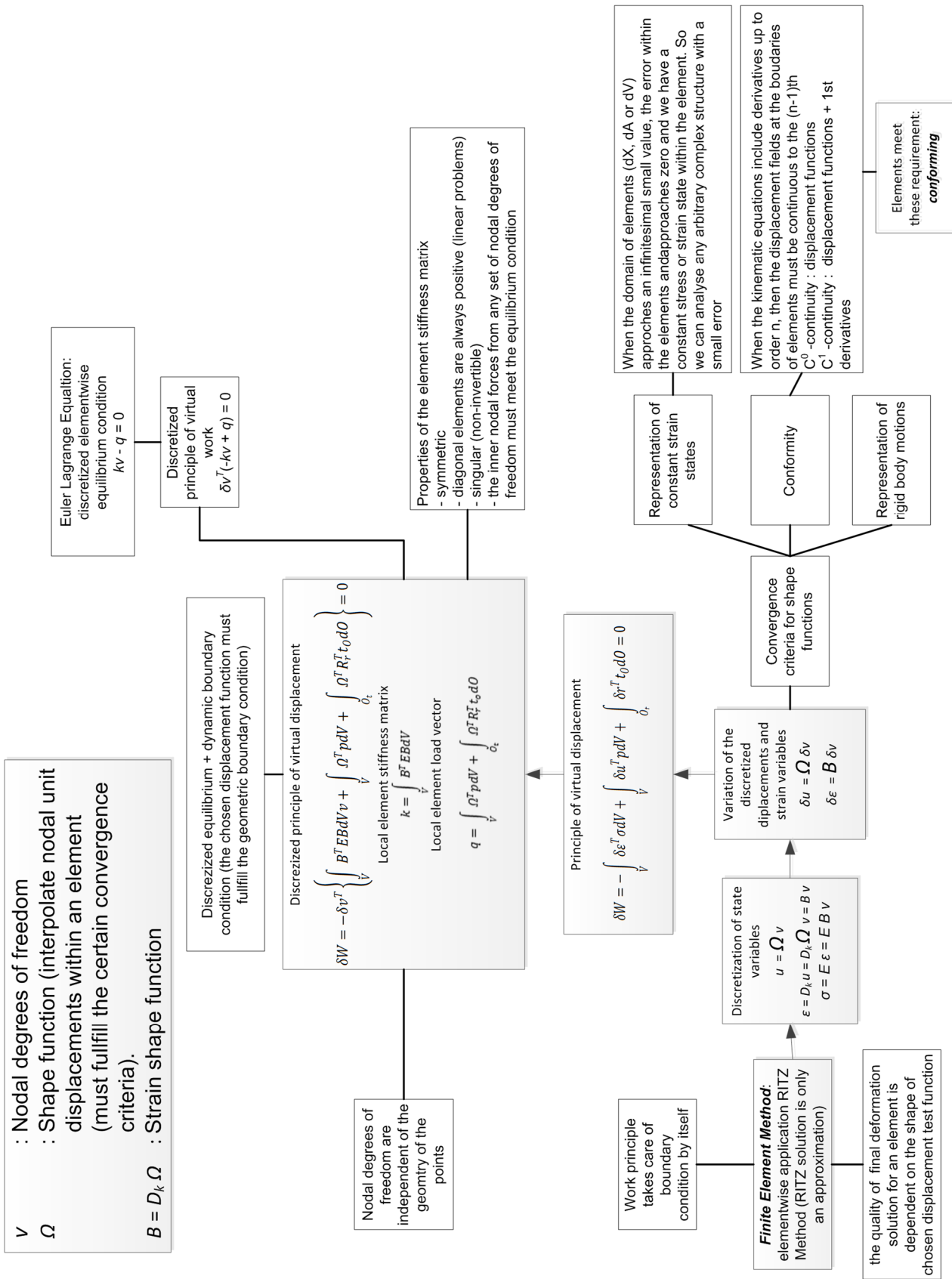


Figure 121b: Scheme of FEM for displacement element formulation

10.4.1 Finite Element Analysis Using Nonlinear Material Properties

The material law states the relationship between the internal deformations and internal forces. This is based (in our case) on the 1-dimensional experimental results. On the other hand, the flexural stresses and strains in case of beam cross-section are the results of force resultants ($M = EI \kappa$). In the case of designing a reinforced concrete beam, codes normally consider linear strain distribution with a simplified nonlinear stress distribution when the crack tensile stresses are exceeded in tension zone. If failure occurs in concrete flexural compression zone, we can expect a sudden (abrupt) brittle failure without any pre-warning.

In case of cross-section under stresses, damages occur internally and increasing of damages might result in local or global failure. By increasing the stress or strain states, there might occur irreversible changes. To perform numerical structural analysis that takes account of reversible and irreversible changes in the cross-section, we need an analysis procedure to take account and accumulate all the damages or changes up to the current state of analysis (history dependent analysis). Therefore, the time dimension must be added to keep the stress and strain variables (internal variables) at the different time points up to the current state. Since we have no direct functional relationship between stresses and strains, the only way is to use incremental material law (nonlinear partial differential form) for each point under consideration (Zahlten, 2000).

For the elastic analysis, we can compute the stresses directly from the material law. For inelastic analysis, the incremental form for the material law can be expressed as:

$$\frac{d\sigma}{d\varepsilon} = \mathbf{E}_T(\sigma, \varepsilon, t) \Rightarrow d\sigma = \mathbf{E}_T(\sigma, \varepsilon, t) d\varepsilon \Rightarrow \sigma = \int_0^{\bar{\varepsilon}} \mathbf{E}_T(\sigma, \varepsilon, t) d\varepsilon \quad (92)$$

Which is mathematically an initial value problem that needs initial stress and strain magnitudes. $\mathbf{E}_T(\sigma, \varepsilon, t)$ is the tangential material matrix of the current state that is history dependent. To solve this, we need a numerical algorithm. The problems are:

- Using an iterative load increment analysis, the solution of internal variables might deviate at each state of our increment from the real solution. This problem can be reduced by having more iterative steps;
- The global iteration algorithms might also have an influence on the result. During each step, irreversible damage might be induced to the solution. Therefore, it is very important that incremental loads be applied to the structure with the same pattern as this happens in the reality so that our incremental nonlinear numerical analysis could simulate the real response of the structure (path dependency nature of solution);
- In case of beam under flexural bending, regarding the real stress-strain situation of each point over the cross-section in an inelastic state, the strain distribution over the cross-section due to our analysis remains no longer linear. The linear strain distribution (considered for design and simplified analytical mechanical analysis) can be therefore violated.

Using nonlinear analysis, the bending moment is no further only dependent on the curvature ($M = EI \kappa$), but it is also dependent on axial and shear strains. This interactive relationship is dependent on the used material law as well as the shape of cross-section.

Having defined the relevant non-linear material relationship, it must be implemented into the FEM. Using an iterative method, displacement of the nodal displacements could be obtained in elastic analysis (Rust , 2015):

$$\mathbf{K} \hat{\mathbf{u}} = \mathbf{f}^{ext} \quad (93)$$

where \mathbf{f}^{ext} gives external forces and $\mathbf{K} \hat{\mathbf{u}}$ refers to the internal forces.

In the linear analysis, \mathbf{K} as explained could be computed. In case of non-linearities (geometric, material or boundary) the equation is not solvable directly. We need to use an iterative method (such as Newton Raphson scheme), increment of the nodal displacement can be achieved by solving the following relation:

$$\mathbf{K}_T \Delta \hat{\mathbf{u}} = \mathbf{f}^{ext} - \mathbf{f}^{int} \quad (94)$$

where internal forces:

$$\mathbf{f}^{int} = \int_V \mathbf{B}^T \boldsymbol{\sigma} dV \quad (95)$$

do not come from the product of stiffness matrix with nodal displacement but from our considered nonlinear defined function but has a nonlinear form (function). The tangential stiffness matrix now can be evaluated using derivation of internal forces:

$$\mathbf{K}_T = \int_V \mathbf{B}^T(\hat{\mathbf{u}}) \frac{\partial \boldsymbol{\sigma}}{\partial \boldsymbol{\varepsilon}} \mathbf{B}(\hat{\mathbf{u}}) dV + \int_V \frac{\partial \mathbf{B}^T(\hat{\mathbf{u}})}{\partial \hat{\mathbf{u}}} \boldsymbol{\sigma} dV \quad (96)$$

In case of material nonlinear analysis, \mathbf{B} is not dependent on the displacements. The derivative of stresses with respect to total strain must be computed for Eq. 94.

FE computes the nodal displacements and from these extract the total strain and stores history variables. At each step, the stress and increment in the variables from the history are computed in the element level using a local or internal iteration. The new internal forces being computed from the internal stresses now take a part in global equilibrium. The internal forces and external forces are not identical at first try. Therefore, the global iteration of displacements are carried out to improve the results iteratively. At each iteration, new displacements and strains from the stresses at integration points are calculated.

10.4.2 Analysis Using Nonlinear Material Properties for Fibre or Layered Elements

In the case of using fibre or layered elements, the integral of internal stresses to the internal resultant forces are carried out numerically using a discretised number of layers over the cross-section. These layers should simulate the results of one-dimensional tests at elevated temperatures. The over the cross-section nonlinear thermal strains and as a result the nonlinear stress state of the cross-section can be implemented in model having a high number of fibres. The higher the number of layers, the better the approximation of the nonlinear stress curve.

10.5 Design of a Reinforced Concrete Beam

10.5.1 At Ambient Temperatures according to EN 1992-1-1

A cross-section in the mid-span of a single simply supported beam under transverse loading is considered. The flexural ultimate limit state design philosophy of EN 1992-1-1 is based on linear strain relation over the beam cross-section. Design is based on first provision of enough reinforcement in the tension zone to provide enough ductility and restrict the depth of concrete compression zone ($x \leq 0.45d$) so that both the maximum yield strain of tensile reinforcement ($\varepsilon_{st} = 0.00217$) and ultimate allowable concrete compressive strain at the farthest fibre of compressive zone are reached.

$$\varepsilon_{st} = \varepsilon_{cu2} \left(\frac{d-x}{x} \right) \quad (97)$$

The design process is schematically illustrated in Fig. 122. The other notations in this section are also graphically shown in this figure. Further, the code gives three compressive stress-strain curves for concrete where the ultimate compressive strain limits for the normal concrete strength class are identical for all models ($\varepsilon_{cu1} = \varepsilon_{cu2} = \varepsilon_{cu3} = 0.0035$).

10.5.2 Fire Design: Simplified Calculation Method or Level 2 to EN 1992-1-2

Flexural design of reinforced concrete beam due to EN 1992-1-1
 $x \leq 0.45d$ to ensure tensile steel yields (no moment redistribution applied)

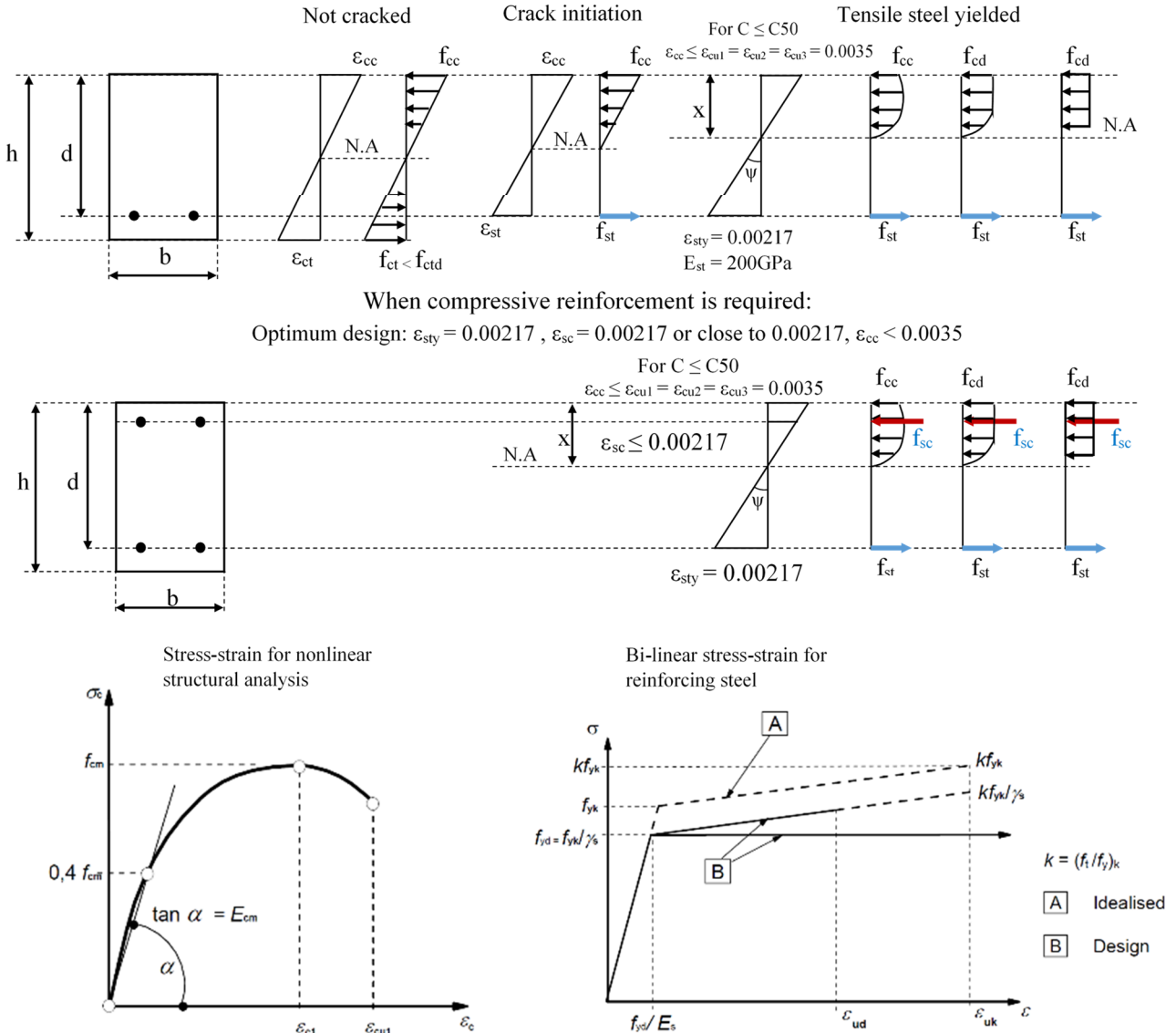


Figure 122: EN 1992-1-1's design philosophy for the reinforced concrete beams

Fire design of a statically determinate single-span beam can be performed using “Zone Method”. For the specific determined fire duration, temperature profiles of the cross-section should be used by having the results of thermal analysis of the cross-section. The cross-section is divided to number of layers or zones toward the centre of the cross-section. The temperature of different layers and the average temperature and strength reduction coefficient $k_{c,\theta}$ of each layer is estimated. For the layers near the exposed side with a very high temperature it is assumed that they are damaged and no longer bearable. Thus, the cross-section is replaced by a reduced cross-section. Further, for the reduced cross-section a new strength is defined based on the temperature in the middle of the cross-section. The strength of reinforcement is reassessed based on the temperature in the middle of reinforcement bars and correspondingly the reduction factor $k_{s,\theta}$ at the considered time. The internal equilibrium of the forces now can be written for the reduced concrete cross-section and the reinforcement with reduced strength as shown in Fig. 123.

Linear strain distribution over the cross-section is assumed with $\varepsilon_{sy,\theta} = \varepsilon_{sy,fi} < 2\%$ (see Fig. 123) for the beam having tensile and compressive reinforcement and $\varepsilon_{c,fi} \leq 0.35\%$ for the concrete in compression zone. $\varepsilon_{sy,fi} = 2\%$ is 10 times larger than $\varepsilon_{sy} = 0.2\%$ at the ambient temperature.

Design of reinforced concrete at ambient temperature where maximum flexural strains of tensile bars $\varepsilon_{st} = 0.2\%$ and maximum compressive strain of concrete $\varepsilon_{cc} = 0.35\%$ reach at the same time is called tension-controlled section. Using the reduced concrete cross-section (Zone Method) with reduced tensile strength of bars where $0.5\% \leq \varepsilon_{st,fi} < 2\%$, the member is considered to be fully ductile (McCormac, et al., 2013).

For continuous beams, EN 1992-1-2 assumes that the moment redistribution from the span to the supports is allowed provided that there is sufficient amount of reinforcement at the supports and the tensile reinforcement is adequately extended into the span to ensure a safe bending moment envelope.

Therefore the moment of resistance at the supports $M_{Rd1,fi}$ or $M_{Rd2,fi}$ (see Fig. 123) can be found based on a simplified equation:

$$M_{Rd,fi} = \left(\frac{\gamma_s}{\gamma_{s,fi}} \right) M_{Ed} \left(\frac{A_{s,prov}}{A_{s,req}} \right) \frac{(d-a)}{d} \quad (98)$$

where γ_s and $\gamma_{s,fi}$ are partial safety factors of reinforcement at ambient and fire situations respectively. M_{Ed} is the applied moment for a single-span beam in the mid-span for cold design according to EN 1992-1-1. $A_{s,prov}$ and $A_{s,req}$ are the area of tensile steel provided and the area of tensile steel required for the design at ambient temperature to EN 1992-1-1 for a single-span beam respectively. a refers to the required average bottom axis distance given in Table 5.5 of EN 1992-1-2 and d is the effective depth of section.

The latter method does not take into account the indirect flexural or axial effects that might be added up to the system from the adjacent fields. Further, there is no simplified check method for the cross-section near the supports to ensure that compressive failure of concrete does not occur at highly elevated temperatures.

10.5.3 Fire Design: Advanced Calculation Method or Level 3 to EN 1992-1-2

The flexural analysis of a statically indeterminate continuous beams in fire situation is based on considering the worst case scenario which might be caused by implementing the thermal indirect effects due to temperature gradients in the affected member and other indirect effects arising from the adjacent members. The latter should be performed by assuming temperature-dependent material properties of the affected zones and taking into account the time-dependent flexural stress and strain variables that might be induced in the system.

Due to higher temperatures at the layers near the fire-exposed side of concrete and internal restraints, internal restraint forces are induced in these layers (or fibres) that are dependent on the applied temperature values and the strength of layers:

$$F_{cc,\theta_l}(f_{c,\theta_l}, \theta_l) = \sigma_{cc,\theta_l} \cdot A_l \quad (99)$$

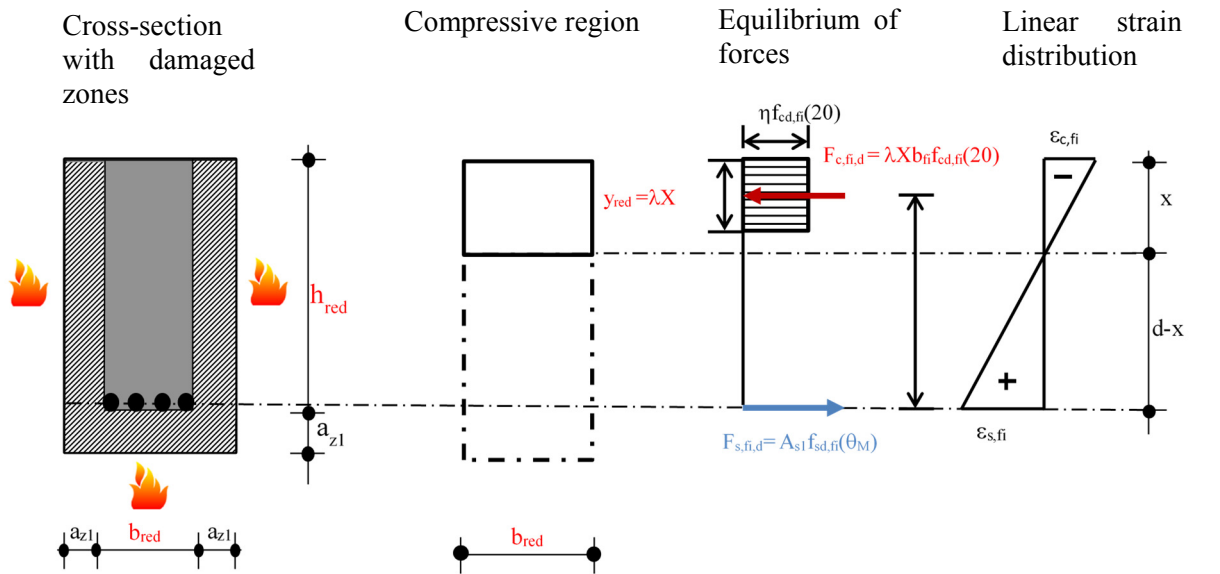
where F_{cc,θ_l} is the restraint axial force of the affected fibre at temperature θ_l in the cross-section near the exposed side. f_{c,θ_l} refers to the strength of the affected fibre at temperature θ_l in the cross-section. θ_l stands for the temperature at the considered layer. σ_{cc,θ_l} and A_l correspond to thermally restraint stress and area of the considered layer respectively.

Figure 124 illustrates two cross-sections of reinforced concrete for a continuous beam, one in the mid-span and the other one at the mid-support in fire situation.

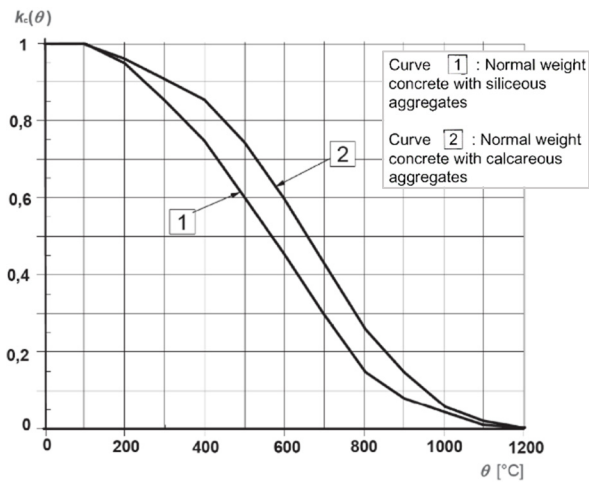
For the cross-section in the mid-span (see Fig. 124), flexural stress and strain have linear distribution at the initial stage of fire where the bottom part is under tension. As the temperature increases in the bottom layers, the local restraint axial forces are induced in the layers affected by elevated temperatures. This causes local compressive stresses in these layers. The new flexural stress-state of the whole cross-section now has two compressive zones at the bottom and upper side of the cross-section. The compressive stress level of the affected layers ($\sigma_{cc,\theta_1}/f_{c,l}$) are low. Using the one-dimensional stress-strain model for the concrete cylinders at elevated temperatures to EN 1992-1-2 with the corresponding stress level, the total strains of these layers are tensile. This means, the strain distribution even with the compressive local state at the bottom of concrete is still tensile and might increase compared to the initial stage.

For the cross-section at the support, the bottom part of cross-section is under compression at the initial stage. As temperatures rise in the affected layers, the local restraint forces are induced and increase the compressive stresses that already existed in these layers. The compressive stress level of the affected layers ($\sigma_{cc,\theta_1}/f_{c,l}$) now is higher. This means on the other hand that the strains due to the high compressive stress level of the affected layers remain compressive and might increase as the stress level goes up.

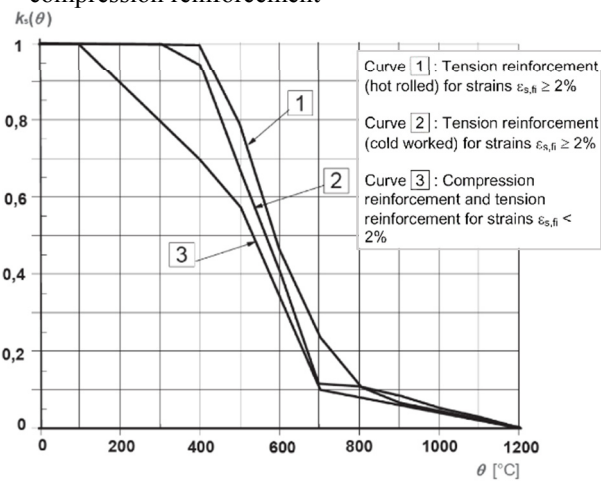
The failure of a member will occur when the plastic hinges form an unstable structure for a ductile member.



Strength reduction coefficient $k_c(\theta)$ for concrete



Strength reduction coefficient $k_s(\theta)$ for tension or compression reinforcement



Moments of resistance $M_{Rd,fi}$ for continuous beams based on the $M_{Ed,fi}$ in the mid-span of single span beam

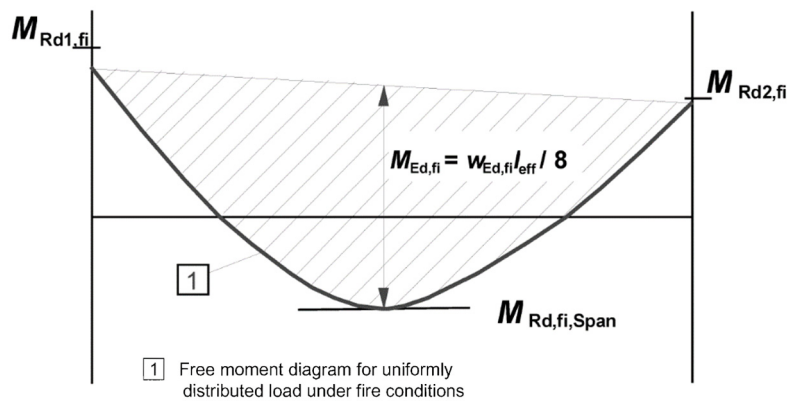
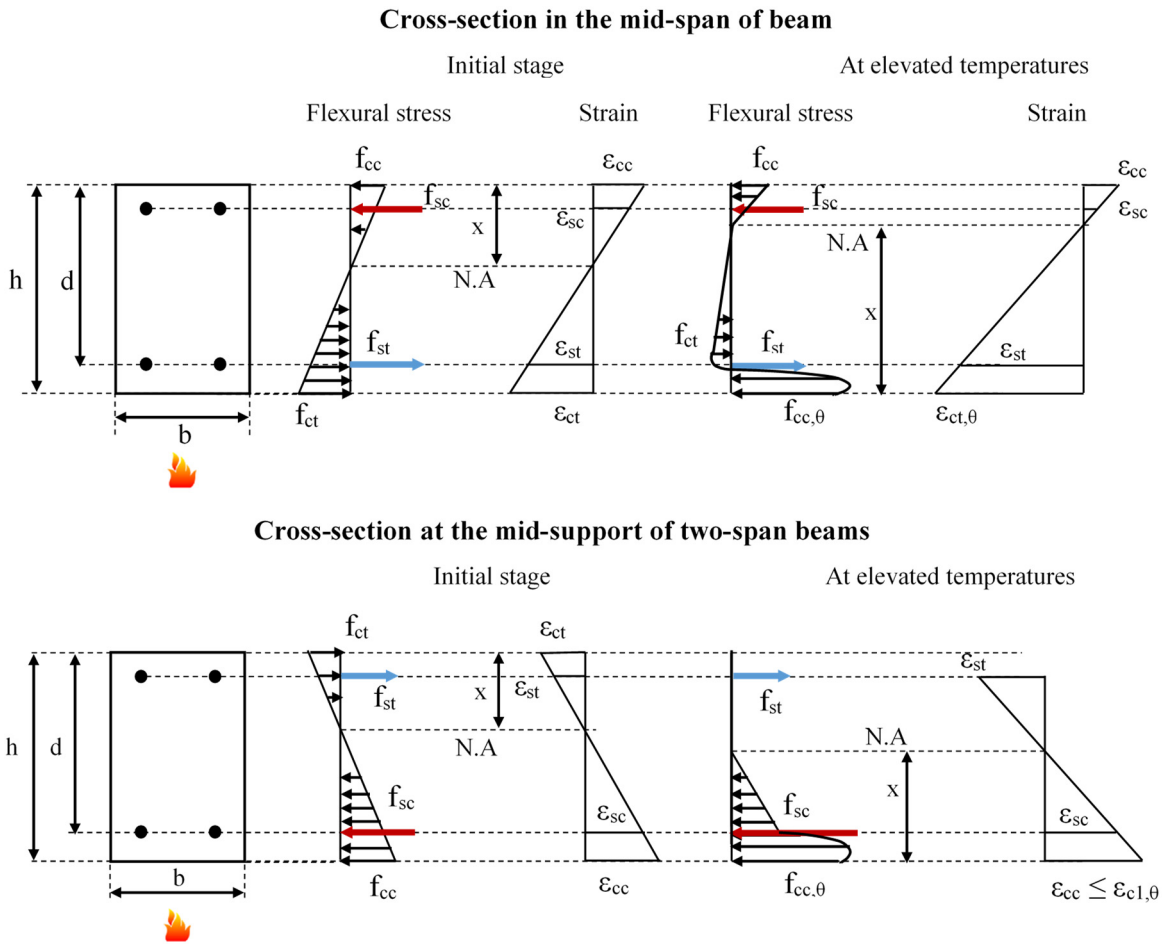


Figure 123: Level 2 design concept according to EN 1992-1-2 for single-span and continuous beams



Stress-strain diagram of concrete at elevated temperatures according to EN 1992-1-2 used for modelling of the affected concrete fibres near the exposed side

Stress-strain diagram of reinforcing steel at elevated temperatures according to EN 1992-1-2 used for the fibres simulating reinforcement

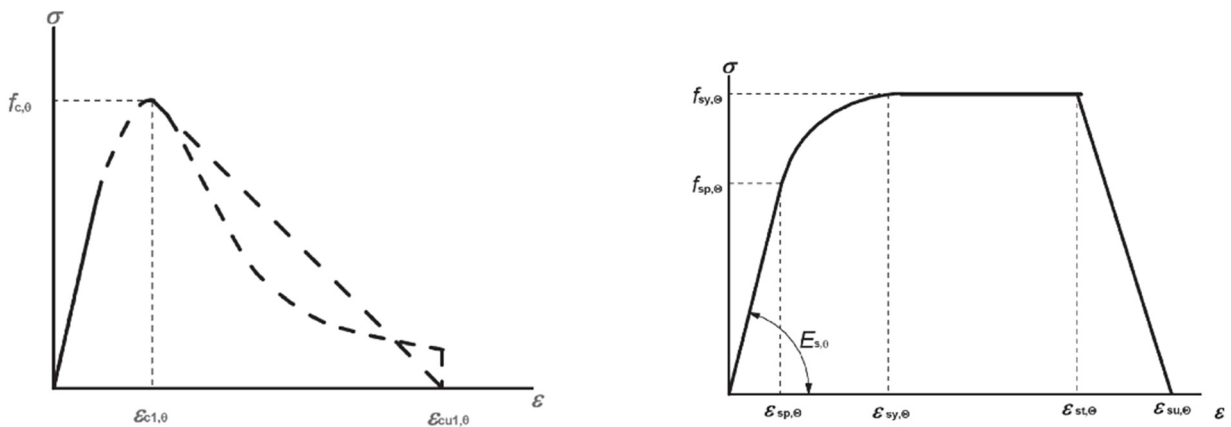


Figure 124: Cross-sectional stress-strains for the reinforced concrete beams and constitutive stress-strain curves for concrete and reinforcements at the elevated temperatures according to EN 1992-1-2

10.6 Analysis of Structure Using Beam Elements in SOFiSTiK

Generally, SOFiSTiK uses three beam formulations:

- Standard beam element: beam with a prismatic cross-section following Timoshenko theory;
- Extended beam element: which is an extended formulation of Timoshenko theory to analyse variable number of beam sections with assigned implicit hinges;
- Fibre beam elements: the linear properties are almost identical to the extended beam elements.

In inelastic state, the internal forces are computed based on the fibre stress distributions. Further, the following characteristics are considered:

- Damage model for crack evolution in the concrete;
- Tension stiffening effects;
- Temperature dependent material properties.

In the element formulation, the following restrictions still exists:

- Fibre element only covers the rectangular cross-section with no eccentricities;
- Imperfection and pre-stressing loads cannot be assigned.

Three program modules are available for (statically determinate or indeterminate) advanced structural analyses of beam structures; ASE (2016), STAR2 (2016) and TALPA (2016). The thermo-mechanical analysis for a reinforced concrete structure (with nonlinear material properties) is only available using fibre elements that are coded in TALPA. This analysis is carried out by defining a primary state (initial-stress state) for each step of analysis that takes into account the variables and damage characteristics of the last state of the cross-section as the initial state of the current step of analysis. The initial analysis must also be carried out using fibre elements. Nonlinear (material) thermo-mechanical process is performed by implementing absolute temperatures on the fibres at each time step and adding the local effects to the initial state of variables for the current step of analysis (programmed by user).

10.6.1 Material Nonlinear Fibre Beam Analysis for Fire Situation

The temperature-dependent material properties and constitutive concrete material model in SOFiSTiK can be only implemented in the analysis using fibre beam elements. The initial variable states at the beginning of fire, can also only be imported from a physical nonlinear analysis under the transverse loading with fibre beams. In other words, there is no algorithm to import initial-variable states from other beam formulations into the fibre beam. The stress and strain states of cross-section of the elements then should be imported to the next step of analysis. This is performed in the program module TALPA, solely. The problem here is that fibre beam elements do not work flawlessly when it comes to the analysis of the beam systems under transverse loading for statically indeterminate systems. This will be further discussed in different case studies. In Fig. 125, the schematic of the possibilities in program TALPA to perform nonlinear material analysis (including iteration methods, acceleration strategies) is illustrated.

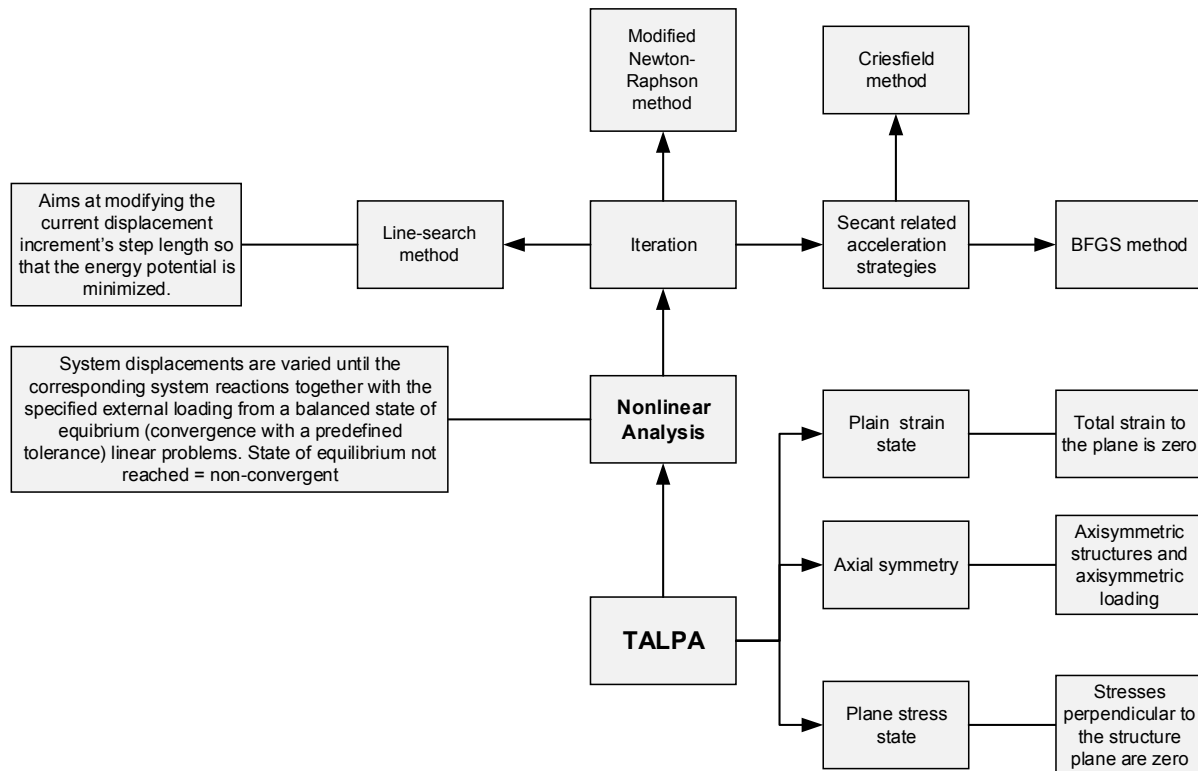


Figure 125: TALPA's scheme in performing nonlinear (material) analysis

10.6.2 Benchmark Examples for Fibre Beams Exposed to Elevated Temperatures in SOFiSTiK

To investigate and understand the main considerations behind the thermo-mechanical analyses performed in SOFiSTiK, all the benchmark examples (designated with BE) in the area of elevated temperatures using fibre beams are extracted from TALPA (2016), and given in Tab. 27. Three out of four examples are the statically determinate systems, BE32, BE33, BE34 (single beams) that are steel and plain concrete subjected to uniformly distributed temperature difference ΔT_N . The last two, simulate compression of the plain concrete based on EN 1992-1-2 material model to the failure using stress-controlled compression (BE33) and displacement-controlled compression (BE34). Further, the stress and strain states along the beams are illustrated from SOFiSTiK in this table. The uniform total strains are based on EN 1992-1-2 being sum of mechanical and thermal strains (do not simulate the compression tests directly). These components are given in Tab. 27 being in agreement with EN 1992-1-2's model. The fourth example (BE35) is to analyse a steel beam with fixed supports at each end exposed to ΔT_N and ΔT_M . For an element in the mid-span of this beam mechanical strain and thermal strain have the same absolute magnitude for the steel. Further, there is no validated benchmark example found for a plain or reinforced concrete beam structure in SOFiSTiK for statically determinate and indeterminate beams using fibre elements. It should be noted that none of these examples cover a fibre beam condition under transverse loading (flexure under transverse loads) and simultaneously cross-section under nonlinear temperature profile over the cross-section.

Table 27: Benchmark examples in SOFiStiK using fibre-beam elements

Data name/title	System	Code/material	Cross-section	Selected load cases/combination of load cases	Mechanical strain at θ (‰)	Thermal strain (‰)	Total strain (‰)	Axial or flexural stresses (MPa)
BE32: Thermal_extension.dat Thermal extension of structural steel in case of fire		MNO1: EN 1993-1-1, S 355 Example 4: Annex CC, DIN EN 1992-1-1 2/NA:2010-03		LC 206: $\Delta T_N = 880$ K				
BE33: Temperature_compression_n.dat Work laws in case of fire for concrete and structural steel		MNO2: EN 1992-1-1 Concrete: C20 Example 5: Annex CC, DIN EN 1992-1-1 2/NA:2010-03		LC12: $P = 1$ kN LC2: $\Delta T_N = 1$ K LC1303: 13.5 · LC12 + 380 · LC2				
BE34: capacity.dat Ultimate bearing capacity of concrete and steel under fire		MNO2: EN 1992-1-1 Concrete: C20 Example 6: Annex CC, DIN EN 1992-1-1 2/NA:2010-03		LC2: $\Delta T_N = 1$ K LC12: $U = 1$ LC1400: 580 · LC2 LC1401: (PLC = 1400), 2.5 · LC12				
BE35: Restraining_forces.dat Calculation of restraining forces in members in case of fire		MNO1: Steel, $F_{yk} = 650$ MPa, $E_s = 210$ GPa Example 7: Annex CC, DIN EN 1992-1-1 2/NA:2010-03		LC200: $\Delta T_N = 100$ K + $\Delta T_M = 200$ K				

10.7 Further Proposed Examples of Fibre Beams Exposed to Elevated Temperatures in SOFiSTiK

There are three other reinforced concrete examples proposed in SOFiSTiK as guide examples exposed to fire (or generally to elevated temperatures) and other actions. These are illustrated in Tab. 28 (designated with the data name) with a selected force, stress and strain state. First example is a straight beam with two fixed supports (fire-temp-nonl_vex.dat) under different thermal actions. In this example, only a reinforced fibre beam under a nonlinear temperature distribution is analysed in one step considering linear and nonlinear material properties. Considering a nonlinear temperature profile in the cross-section for this case as given in Tab. 28 with a maximum temperature of 500°C, the computed flexural stresses and strain states are demonstrated in the mid-span. The thermal strain at the exposed side for 500°C is 7.19 ‰ that corresponds to thermal strain in EN 1992-1-2. The latter corresponds to the fibre temperatures directly and has the same pattern as temperature distribution. The mechanical compressive strain is further computed by SOFiSTiK so that their sum with thermal strains become zero at fibres. The compressive stresses of fibres, on the other, hand are dependent on the fibre strengths.

The two other proposed examples cover tunnel circular cross-sections. The first one (ring-of-fire.dat) considers $\Delta T_N = 30$ and $\Delta T_M = 20$ K over the cross-section and it remains in the elastic state for both stress and strain variables.

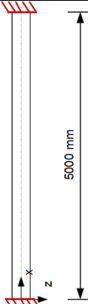
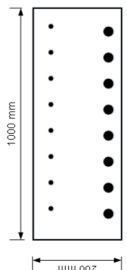
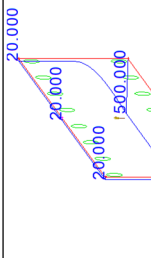
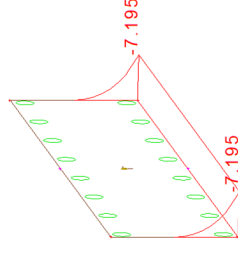
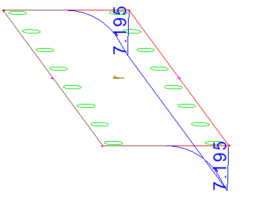
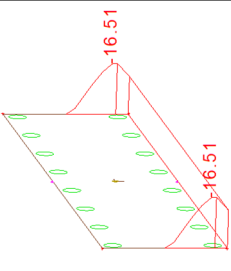
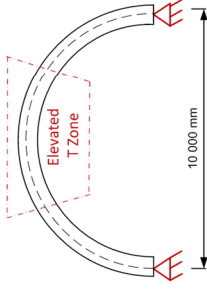
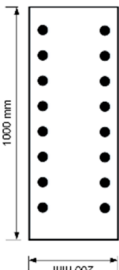
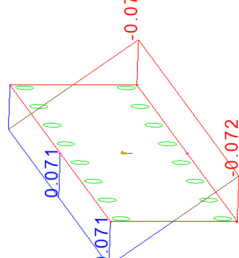
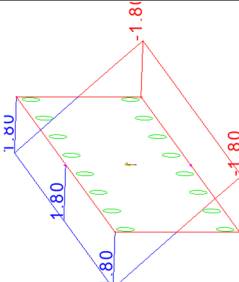
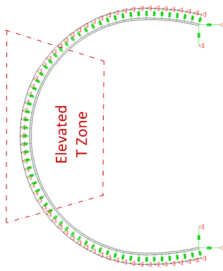
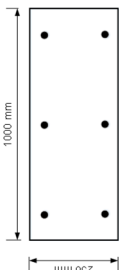
The last example (Tunnel-fire.dat) is a circular tunnel section, partially, under nonlinear temperature profile (see the elevated T zone in Tab. 28). Here, a step-wise material nonlinear analysis by considering the initial states is considered. The results of forces, cross-sectional stresses and strains and minimum fibre strains for the system and a cross-section in the middle of tunnel are illustrated for $t = 0, 3, 5, 30$ and 60 minutes in Tab. 29a and 29b.

Step-wise analysis of the first five minutes:

- $t = 0$, the cross-section in the middle of the tunnel section, is under positive bending with a linear strain distribution. The bottom fibres are under tension;
- $t = 3$ minutes, relative axial restraint compressive stresses for each fibre under elevated temperatures are computed and added to the lowest fibres with a maximum stress of -6.97 MPa. The current mechanical equilibrium state of the cross-section is now constructed. The compressive mechanical strains due to the current compressive thermally induced stress is computed according to EN 1992-1-2 concrete stress-strain material model (accumulating transient strain component). Thermal strains are separately computed for the fibres with the maximum strain of 1.61‰ for 183°C. The total strains in the fibres are then computed by adding the both strain components at the elevated temperatures plus the initial strain component of the fibre. It should be noted, that there is NO option found to illustrate the total strain-state of the fibres at the elevated temperature in SOFiSTiK;
- $t = 5$ minutes, the final state of variable of the preceding step is taken into account as the initial state for the current step. The same procedure is performed as for $t = 3$ minutes.

It should be further noted that with increase of time, the bending moment diagram is shifted upward. It is due to the negative bending moment (local positive z inward the tunnel) caused by increasing compressive stresses near the exposed side (see Tab. 29b for $t = 60$ minutes).

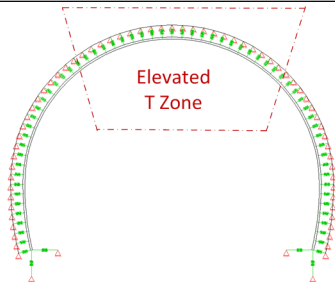
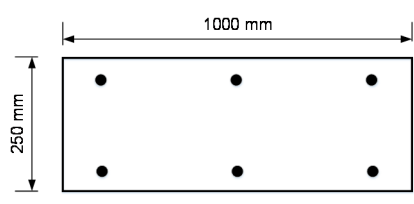
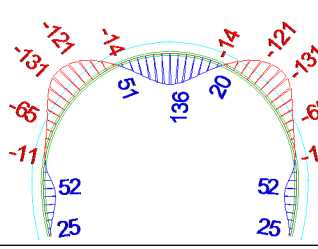
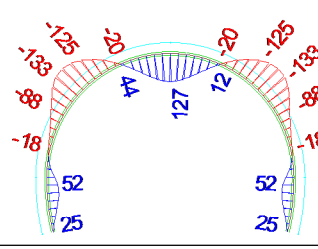
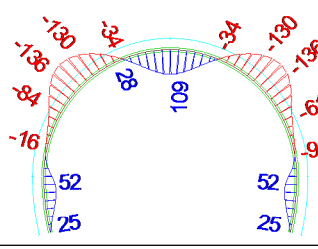
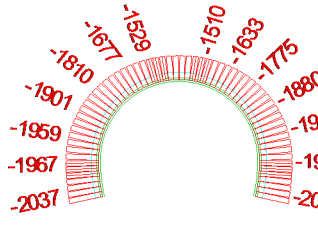
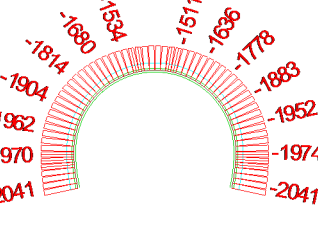
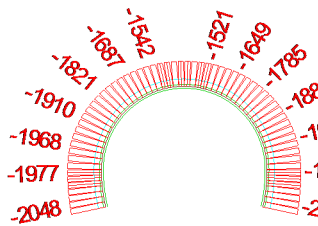
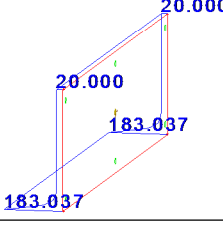
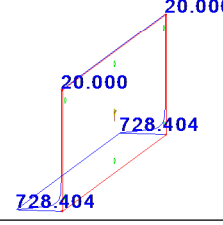
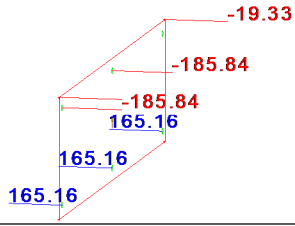
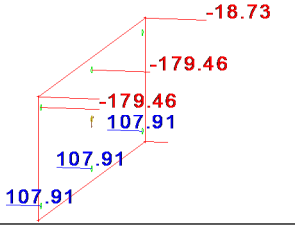
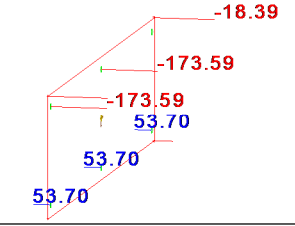
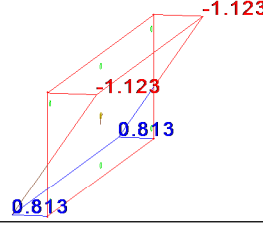
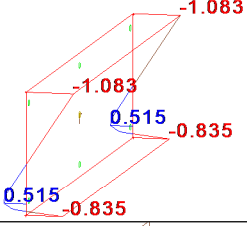
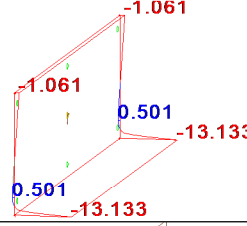
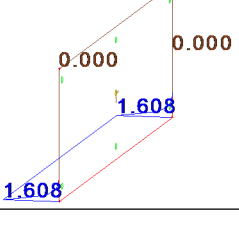
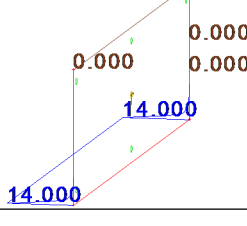
Table 28: Examples of fibre beams exposed to the elevated temperatures and other actions in SOFiStiK

Data name	System	Cross-section	Selected load cases/combination of load cases	Mechanical strain (%)	Thermal strain (%)	Axial or flexural stresses (MPa)
Fire-temp-nonl_ve x.dat			 LC205: Nonlinear temp profile with $T_{z=200} = 500^{\circ}\text{C}$			
Ring-of-fire.dat			LC102: $\Delta T_N = 30\text{ K} + \Delta T_M = 20\text{ K}$			
Tunnel-fire.dat						

The results are given in details in Tab. 30 for different time steps.

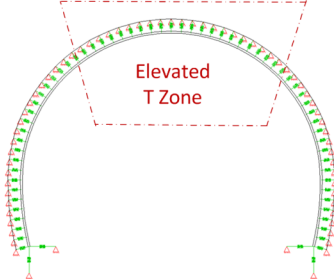
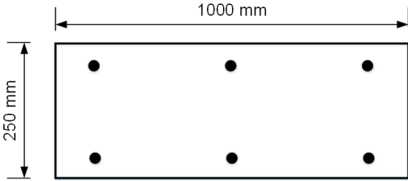
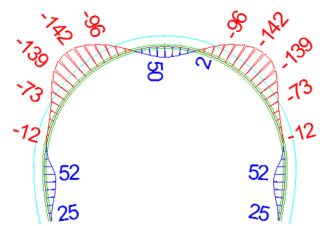
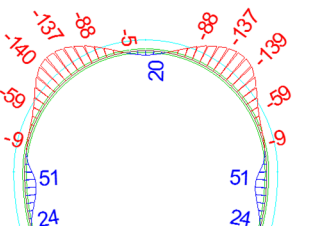
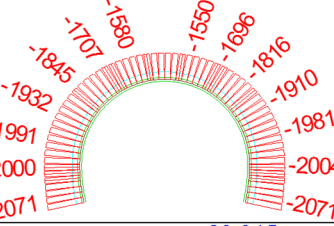
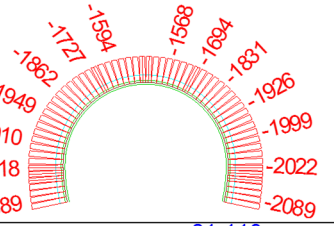
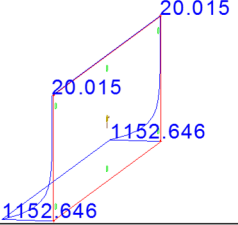
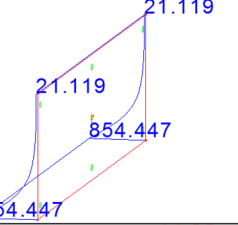
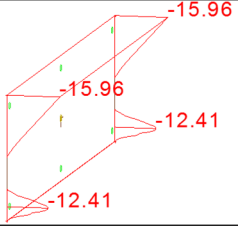
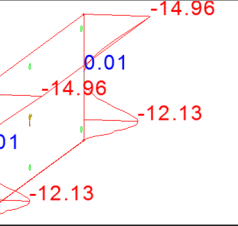
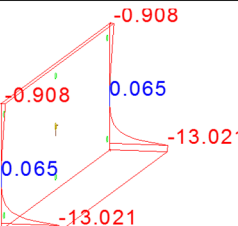
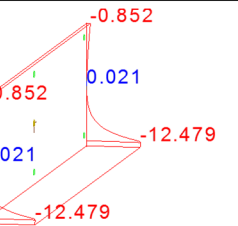
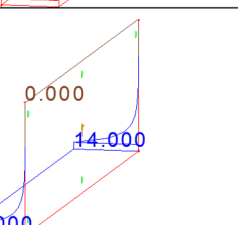
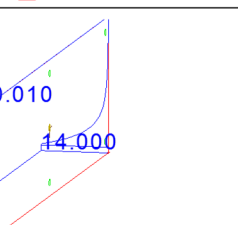
Structural Analysis of a Cut-and-cover Tunnel under ZTV-ING Fire Using Finite Element Method

Table 29a: Different induced effects for a tunnel example exposed to fire in SOFiSTiK from $t = 0$ to $t = 5$ minutes

	Structure		Cross-section
Tunnel-fire.dat			
Time (min)	0	3	5
Bending moment (kNm)			
Axial force (kN)			
Temperature profile (°C)			
Stress of concrete and reinforcement (MPa)			
Mechanical strain of cross-section (%)			
Thermal strain (%)			

Structural Analysis of a Cut-and-cover Tunnel under ZTV-ING Fire Using Finite Element Method

Table 29b: Different induced effects for a tunnel example exposed to fire in SOFiSTiK from $t = 30$ to $t = 60$ minutes

	Structure	Cross-section
Tunnel-fire.dat		
Time (min)	30	60
Bending moment (kNm)		
Axial force (kN)		
Temperature profile (°C)		
Stress of concrete and reinforcement (MPa)		
Mechanical strain of cross-section (%)		
Thermal strain (%)		

10.8 Case Studies for Straight Fibre Beams at Elevated Temperatures Using SOFiSTiK

10.8.1 Single-span Beam under Transverse Loading and Exposed to Fire (Cases 1-4)

Six examples of straight beams exposed to fire analysed using fibre beam elements based on EN 1992-1-2's material model in SOFiSTiK are given in Tab. 30. The first four examples are single-span beams with different support conditions at each end (cases 1 to 4 with 200 elements) and the last two are simply-supported-two-span beams. All the examples are performed to couple thermo-mechanical effects step-wise (at $t = 0, 5$ and 10 minutes) with (or without) other mechanical effects. These have an identical uniform reinforced concrete cross-section over their lengths with concrete strength class of C30/37. Changes in thermally induced compressive stresses from 0 to 10 minutes follows the same concept as from 10 to 30 minutes. Therefore, it is assumed that investigation from 0 to 10 minutes provides sufficient information on course of changes in thermally induced strains and stresses. Fire load is the same for all six cases. These examples are foreseen to discuss the results of fibre-beam analysis and can be related later to an example of a cut-and-cover tunnel cross-section under ZTV-ING fire exposure. The results of bending and axial forces, beam displacements in local x and z directions, cross-sectional flexural stresses, mechanical strains and thermal strains are given at $t = 0, 5$ and 10 minutes for each example in Tabs. H1 to H4 (in Annex H for the first four cases) and in Tabs. 32 and 33 (for the cases 5 and 6). A cross-section in the middle of span for the first four examples are considered and a cross-section at the mid-support for the last two examples.

10.8.2 Two-span Beam under Transverse Loading and One Span Exposed to Fire (Case 5)

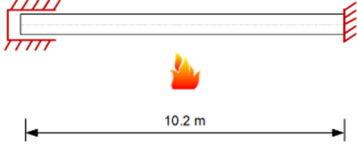
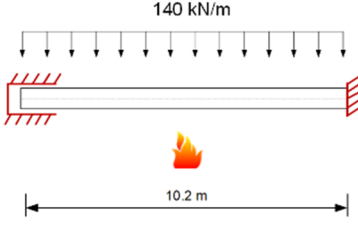
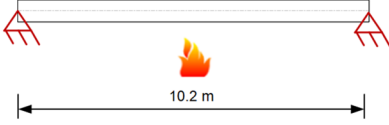
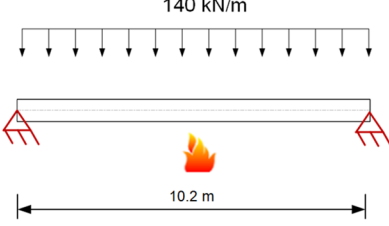
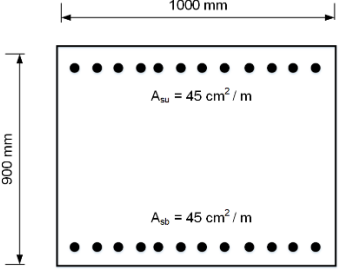
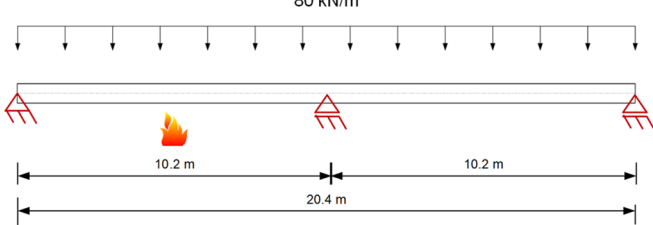
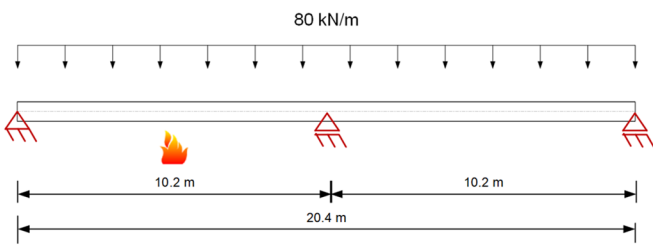
Case 5 refers to a two-span-continuous beam where one span is exposed to fire. The span length is similar to the corresponding length for an example of cut-and-cover tunnel investigated in this chapter. In case of two-span simply supported beam, it can be seen (in Tab. 31) that the axial forces close to the mid-support and close to the left support (axially restraint) give the highest deviations. This deviation increases during the fire. Further, on the bending moment inflection points during the fire, the values of error increase drastically. Considering the flexural stresses over the mid-span at the beginning of fire, the bottom fibres are under compression. The strain state of bottom fibres are also compressive. At $t = 5$ and 10 minutes, the magnitude of compressive fibres restraint-stresses increases and at the same time the magnitude of the total strain on these fibres increases (total strain = (+) thermal strain + (-) mechanical strain). In this case, the magnitude of both flexural compressive stress and compressive total strain increase at the fibres near the exposed side at the mid-span as time elapses. Two checks should be carried out: whether the cross-section has sufficient reinforcement on the top side and that the cross-section does not fail due to the excessive compressive strain of concrete in the compression zone.

10.8.3 Two-span Beam under Transverse Loading and One Span Exposed to Fire with 20% Strength Reduction (Case 6)

Case 6 has identical properties as case 5 but the concrete strength is 20% reduced. This case is investigated to show the influence of strength reduction on the global nonlinear structural analysis. The results of compressive tests for concrete cylinders with PP-fibres show a maximum strength reduction of approximately 20% compared to EN 1992-1-2 compressive strengths. Therefore, the previous example is considered with 20% strength reduction to investigate the influence on the flexural response of the beam. Comparing the bending moment results of the reduced strength case 6 with case 5 (see, Tab. 32), the result of bending moments over the mid-span and mid-support from each case may deviate at maximum of 2.2%. Deflection in the mid-span of the exposed side (left span) might vary up to 8%. This on the other hand means, the reduction in concrete strength might influence the flexural stress response of the physically

nonlinear analysis at the elevated temperature to a low extent, whereas deflection of the beam due to a lower stiffness during the fire decreases to a larger extent.

Table 30: Case studies for nonlinear (material) analysis of reinforced concrete beams using different boundary conditions and loads

No of case	System and loads	Material properties and cross-section
1*		C30/37 S 500 $f_c = 30 \text{ MPa}$
2*		
3*		
4*		
5		
6		$f_c = 24 \text{ MPa}$ (20% reduced strength compared to case 5) S 500
* system variable states are given in Annex H		

Structural Analysis of a Cut-and-cover Tunnel under ZTV-ING Fire Using Finite Element Method

Table 31: Results of nonlinear analysis of a two-span beam under transverse loading and one span exposed to fire (case 5)

Time (min)	0	5	10
Temperature profile			
Bending moment (kNm)			
Axial force (kN)			
Beam displacement in local z (mm)			
Total curvature k_y			
Flexural stress (MPa)			
Mechanical strain (‰)			
Thermal strain (‰)			

Table 32: Comparison of nonlinear results of two-span beam under transverse loading and one span exposed to fire with an identical system with only difference of 20% strength reduction in concrete (case 6)

Time (min)	0	5	10
Bending moment (kNm)			
Beam displacement in local z (mm)			

10.9 Analysis of a Two-cell-cut-and-cover Tunnel Exposed to Fire

In this section, different aspects of fire design of a two-cell-cut-and-cover tunnel structure are discussed up to 30 minutes after the fire initiation. The considered section of tunnel structure (1-m strip of section), as shown in Fig. 126, has polypropylene fibres in its mixture and is elastically bedded from three sides. The tunnel is first designed for the serviceability and ultimate limit states for the most critical criteria that might appear in the ambient temperature according to EN 1992-1-1 design philosophy. The latter is under different corresponding actions as given in Fig. 127. The designed system now must be verified for the ultimate limit state (failure) in the event of fire (occurred in the left cell) by considering partial safety factors for this accidental design situation. Correspondingly, thermal effects are coupled with the other mechanical effects. In this case, the most critical relevant criteria induced by coupling of restraining flexural and axial stresses (thermal effects) with the corresponding stresses induced by other actions. The analyses have been carried out for two types of models in SOFiSTiK ((Pouran, et al., 2014) and (Pouran, et al., 2015)); fibre-beam model and layered-plate model (both for a 1-m strip), see Fig. 128. Considering a strip of the tunnel section as representative for flexural behaviour of the tunnel structure is a conservative assumption as there is no resistance to the lateral strains for the beam model. In reality, therefore, the flexural behaviour of the tunnel is stiffer. In Tab. 33, the ground properties are given. Further, different actions assumed to be relevant for the considered tunnel are listed in Tab. 34. All applied load cases on the tunnel are explicitly illustrated in Annex I (Figs. I1 to I10).

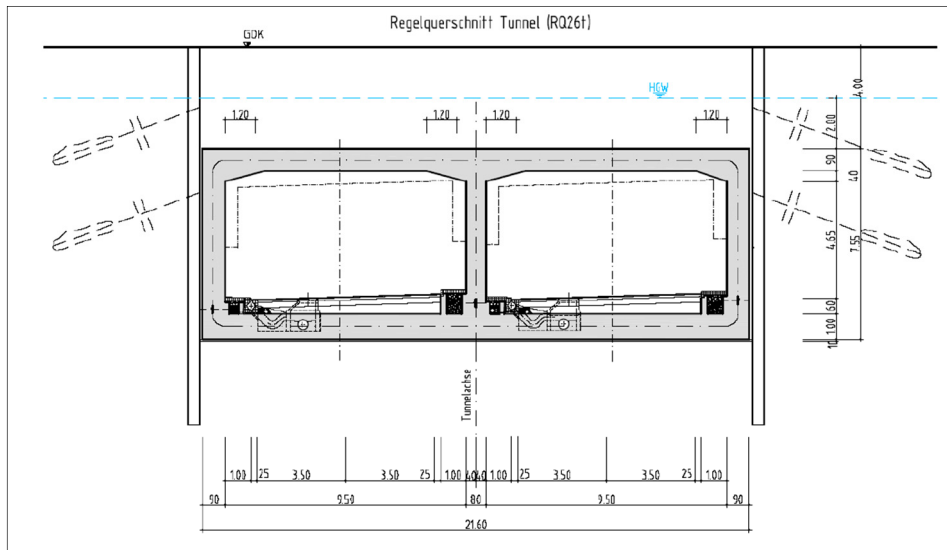


Figure 126: Section of a two-cell-cut-and-cover tunnel

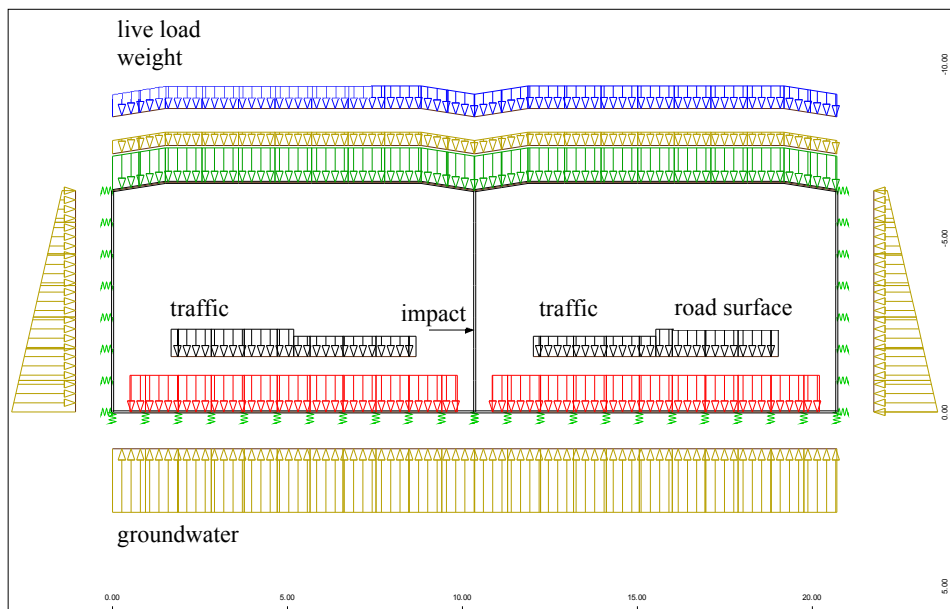


Figure 127: Tunnel section under different actions

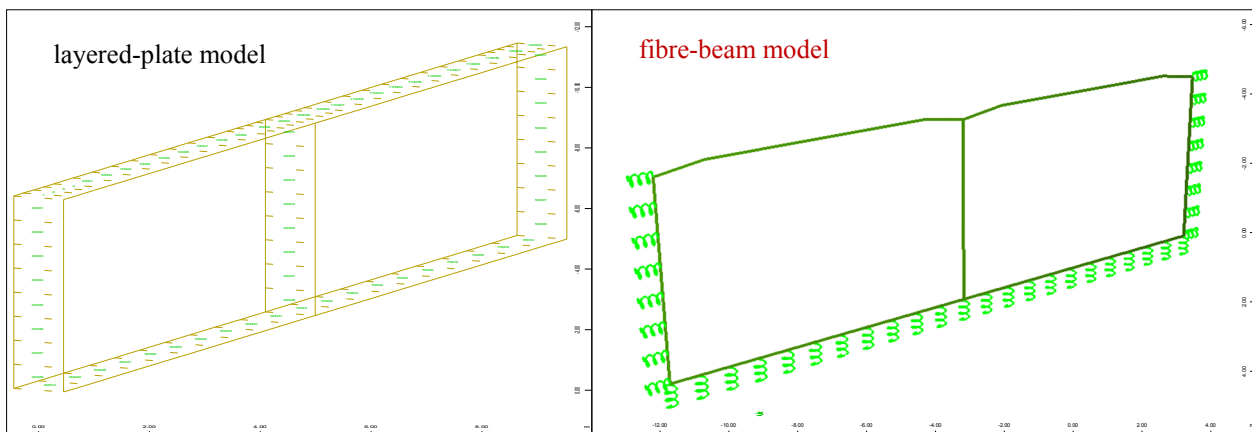


Figure 128: Layered-plate model and fibre-beam model

Table 33: Ground properties

Density γ_d/γ_m dry/moist	Friction angle φ [°]	Cohesion c [kN/m ²]	Elastic modulus [MN/m ²]	Vertical/horizontal bedding [kN/m ³]
21/22	35	0	50	50

Table 34: Designation of actions, load cases and normative references for used in structural analysis of the tunnel

Types of action	Load case no	Normative references for partial safety factors in ambient temperatures	Corresponding figure in Annex I
Self weight of lining, g_l	1	DIN EN 1990/NA:A1	I1
Weight of filling, g_{fill}	2		I2
Earth surcharge load, g_{es}	3		I3
Weight of pavement, g_{pav}	4		I4
Vehicular live load at top ground surface, $q_{v,top}$	5	EN 1990:2002	I5
Soil pressure, g_{soil}	6	DIN EN 1990/NA:A1	I6
Vehicular live load in the tunnel, $q_{v,in}$	7	EN 1990:2002	I7
Water, g_{wa}	8	DIN EN 1054	I8
Temperature change in winter, ΔT_{win}	9	ZTV-ING, section 5.2	I9
Temperature change in summer, ΔT_{sum}	10		I10

10.10 Tunnel Structure at the Beginning of Fire

To design the tunnel for fire situation, it is of main importance to investigate the worst critical state of the cross-section for the existing structure with respect to the fire situation. Since the probability of occurring of fire in the two cells simultaneously is very low, it is assumed that fire might only appear in one of the cells. Further, it is assumed that the asphalts or other protective surface layers protect the base lining of the tunnel from fire. Thus, fire (ZTV-ING fire exposure) acts on three members.

Due to the symmetric pattern of both structure and loading, the envelop of bending moments for the ultimate limit state design has a symmetric shape (see Fig. 129). With respect to the flexural-stress state, two points on the upper beams, over the mid-wall and over the external wall, are critical. This is due to the fact that in the event of fire, the restraining-flexural stresses induce a negative bending moment over the span (when the local z direction is inward). This will shift the bending moment diagram upwards. The flexural capacity

(plastic capacity) of the points over the mid-wall and external wall might be reached prior to the other points. The maximum values of bending moments according to two structural models are illustrated in Fig. 129. The latter occurs for the combination of action with vehicular live load as a leading variable action in the fire situation.

Considering a cross-section in the upper beam close to the mid-wall and external wall, the bottom fibres are under compression whereas the top fibres are under tension.

The experimental results for the cylinders with pre-load levels accordingly (up to 30%) showed improvement of the concrete strength at elevated temperatures. Therefore, it can be expected that these fibres have less reduction in strength during the fire situation.

Further, the compressive stress-strain model is constructed by accumulating the transient creep with the maximum load level of $\alpha = 0.4$.

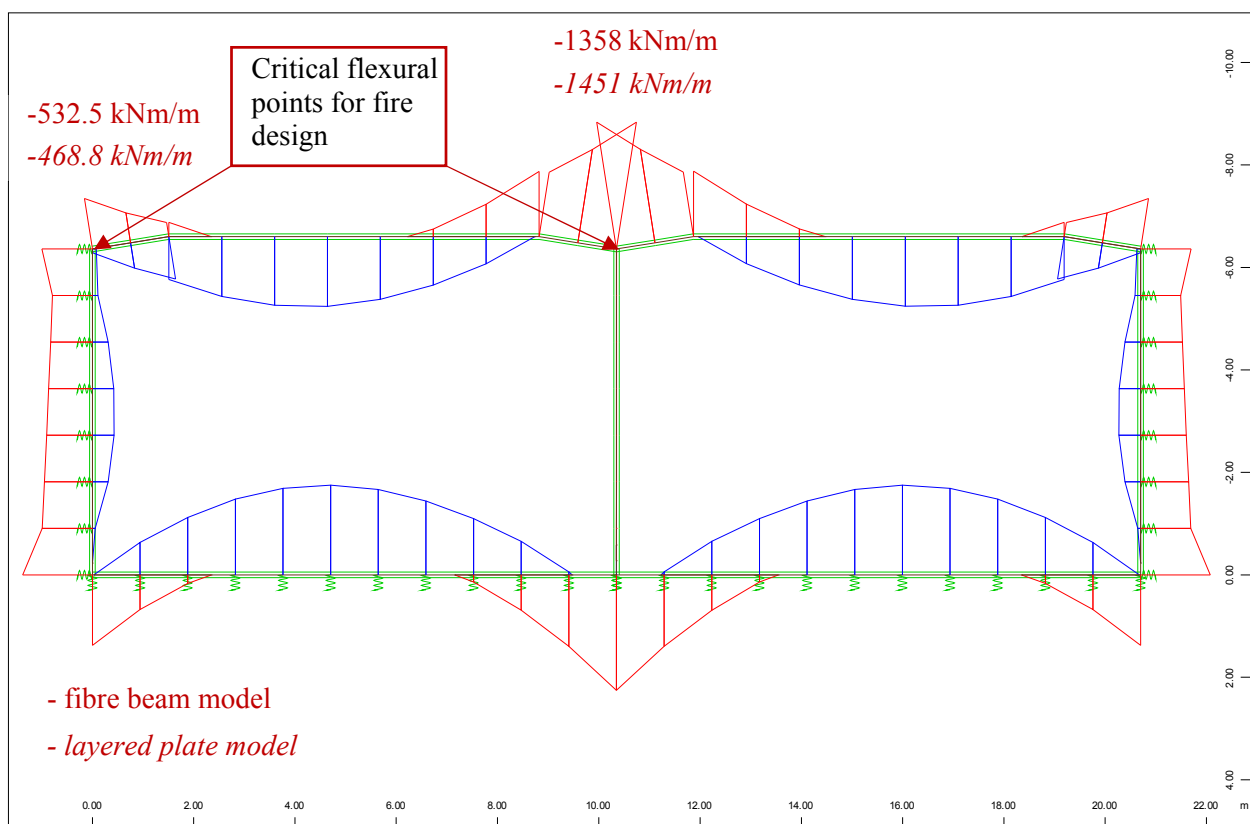


Figure 129: Envelop of bending moments for ULS design at ambient temperature

10.11 Physical Nonlinear Structural Analysis of Tunnel for Fire Situation Using SOFiSTiK

To perform nonlinear analysis for the tunnel structure for fire situation, the procedure should be investigated from different points of view. The followings are accordingly the main different points that play a role in this analysis:

Global structural:

- Slabs are rigidly connected with walls and extended in the longitudinal direction of the tunnel. Model with a strip of the structure does not take into account the lateral restraint that exist in the reality and shows a softer behaviour;
- Using Timoshenko beam theory takes account of shear deformations in the formulation and might therefore be more accurate;
- Using EN 1992-1-2's concrete constitutive material model in a statically indeterminate beam, the stresses of each fibre is computed separately for each fibre corresponding to the applied temperature for the fully flexural or axial restraint situations.

Material:

- Using EN 1992-1-2's concrete constitutive material model for a flexural response of statically indeterminate systems with much higher heating rates in the fibres close to the exposed side, the validity of should be verified via experimental efforts;
- The cooling phase is excluded in this work as the analyses were performed without considering the real stiffening of the structure at the time of analysis;
- It is assumed that there is 2 kg/m³ polypropylene fibres in the concrete mixture and therefore the potential of spalling is low (Pistol, et al., 2012) and correspondingly these effects are neglected.

Modelling in SOFiSTiK:

- Nonlinear (material) analysis is carried out to couple the mechanical effects existing in the ambient temperature with fire partial safety factors with thermal effects;
- The nonlinear (physical) structural analysis is based on the amount of used reinforcement at the beginning of the analysis. In this regard, there is no algorithm which import different reinforcement ratios for an optimum design of the cross-section at the elevated temperatures. The reinforcement ratios are therefore user defined and are based on experience and the expected stress states at elevated temperatures. The problem here is that in contrast to the normal design, here the stress and strain states of the fibres in the cross-sections are not compatible.

The cross-sectional stress-strain behaviour of the roof in the fire-exposed cell computed using the fibre elements are similar to the case studies. Therefore, here, the flexural-stress state, the mechanical strain and thermal strain of these two cross-sections are shown in Fig. 130 and discussed only for $t = 0$ and 30 minutes. Further, for the layered-plate model, the bending moments and axial forces are illustrated in Annex J for $t = 0, 10, 30, 40$ and 90 minutes.

In nonlinear physical analysis of the tunnel with the left cell under fire (all the three members exposed to the ZTV-ING fire curve except for the floor), due to the temperature differences over the cross-section, negative bending moments (considering the local z direction is inward) arise. The ultimate state fire design of the tunnel requires that the failure does not occur for the specified duration. Further, as explained the

stress-state response of concrete fibres is not compatible with their strain state. In addition, Figure 130 shows the bending moment of the left cell of the tunnel at the beginning and at $t = 30$ minutes of the fire spread as critical bending moment state. As shown in this figure, the compressive stress level of the bottom fibres of cross-sections near the external and internal supports are about 0.1 and 0.3 respectively at the beginning of fire. The following issues should be dealt with, checked and avoided:

- The critical temperature of the reinforcement in the tensile zone should not be exceeded. (BAST, 2015) considers a critical temperature of 300°C and a minimum cover requirement of 6 cm for cut-and-cover tunnels. This on the other hand means, reducing the potential of occurrence of the collapse mechanism by still having a ductile member behaviour in the fire situation. Further, (BAST, 2015) requires that the residual deformations remain so small that the serviceability of the structure is not limited after the fire. The latter means control of deflection and crack limits;
- In case of cross-sections near the external and internal supports, the cross-sections' strain states should be checked so that due to the excessive compressive strains that might be induced in the fibres near the exposed side, compressive failure of concrete does not occur;
- Amount and length of tensile reinforcement for the cross-sections near the internal and external supports should be sufficient to provide a ductile behaviour.

In case of the cross-section in the mid-span, the bottom part of cross-section is under tension in the beginning of the fire (see Fig. 131). At $t = 10$ minutes, the compressive fibre stresses activated locally induce a negative bending moment. The choice of 10 minutes fire duration in Fig. 131 is only for the sake of explanation on changes in the strain and stress states of the cross-section during fire. On the other hand, the compressive stress level of the bottom fibres is low and therefore the corresponding mechanical strains for the existing temperatures are lower than thermal strains of these fibres. Therefore, although we have a local compressive stress acting over the fibres, the total strain is tensile on the bottom fibres and may increase during the fire situation. This means, the curvature and deflection may increase. In addition, residual deflections and cracks should be checked for the post usage of the structure.

For the cross-section of the beam near the mid-support, the bottom fibres are under compression in the beginning of fire with the maximum compressive strain of -0.34 ‰ (see Fig. 131). At $t = 10$ minutes, the fibres near the exposed side have a higher compressive stress level. This results in increase of mechanical strain due to EN 1992-1-2 model that exceeds the thermal strain of these fibres. Thus, the total compressive strain of the bottom fibres increases compared to the initial state ($t = 0$). This might result in increasing of compressive strain in the bottom fibres and correspondingly increase in the curvature. Further, the tensile reinforcement on the top should be sufficient to provide ductile behaviour and allow the redistribution of the bending moments.

The strain-state of the bottom fibres of the cross-section near the mid-support at the elevated temperatures can be estimated by superposition of mechanical strains and thermal strains. Mechanical strains at the elevated temperatures are dependent on the stress level of the corresponding fibre. Therefore, having estimated the compressive stress level of the considered fibre, the compressive mechanical strains can be evaluated by using the constitutive stress-strain model at the elevated temperatures. Figure 132 shows the corresponding compressive mechanical strains for $\alpha = 0.3$ for the both EN 1992-1-2 and proposed models at $\theta_{max} = 400, 500$ and 600°C . Further, the magnitude of thermal strains of the fibres at these temperatures are shown in Fig. 133.

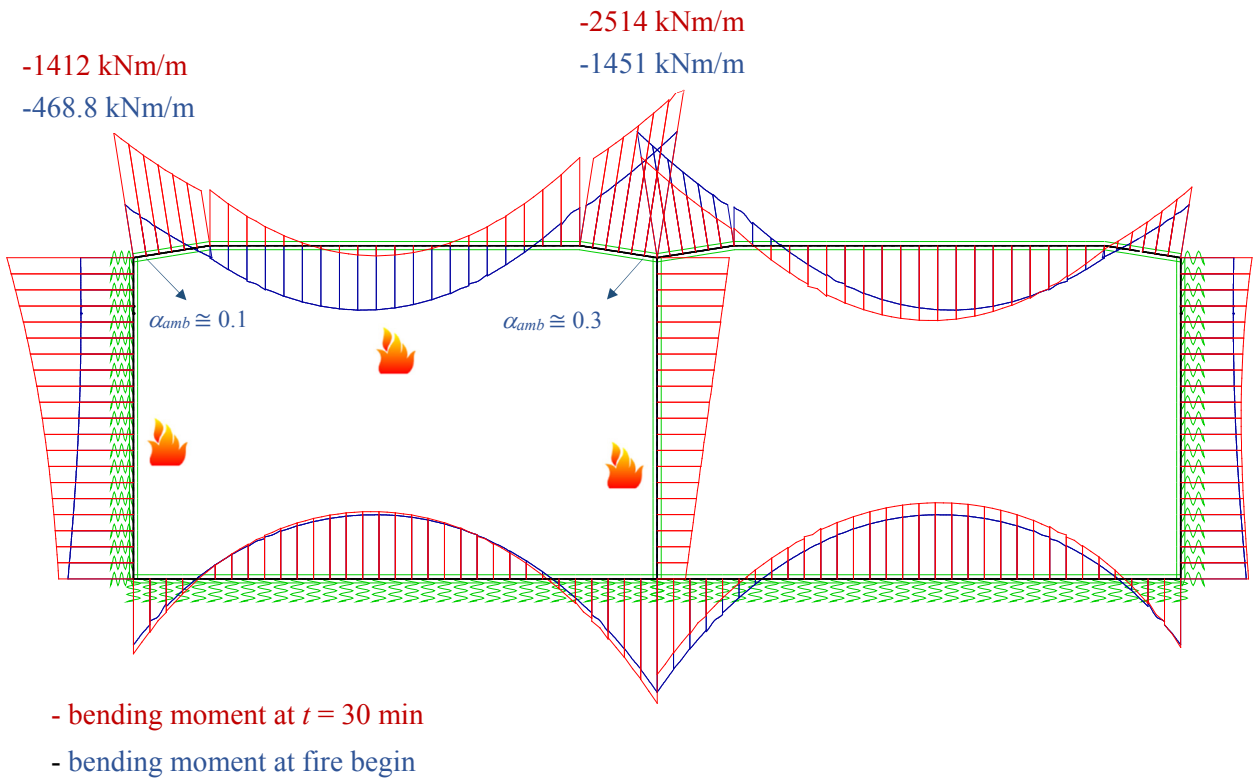


Figure 130: Bending moments at $t = 0$ and $t = 30$ minutes

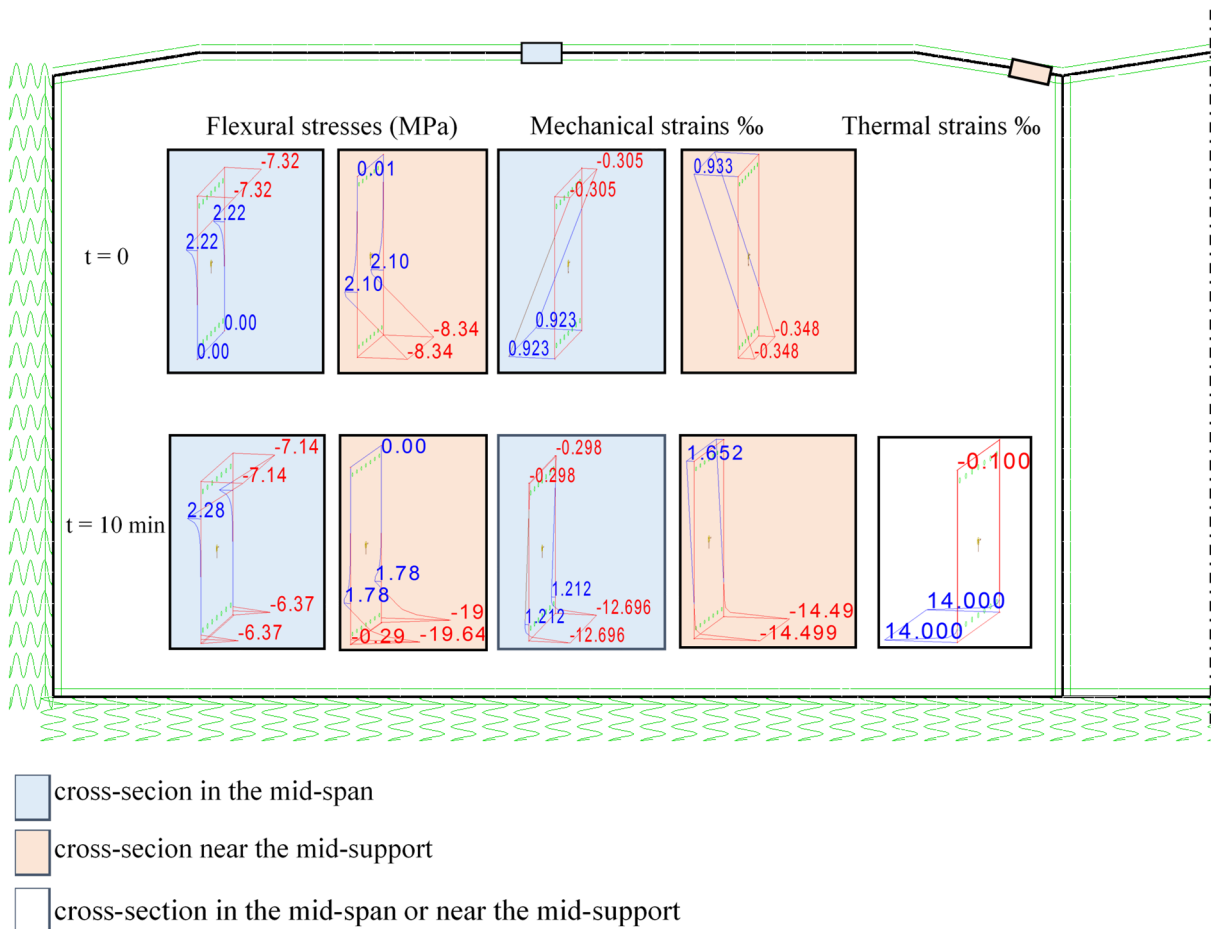


Figure 131: Cross-sectional-variable states at $t = 0$ and $t = 10$ minutes for the fire-exposed cell of the tunnel

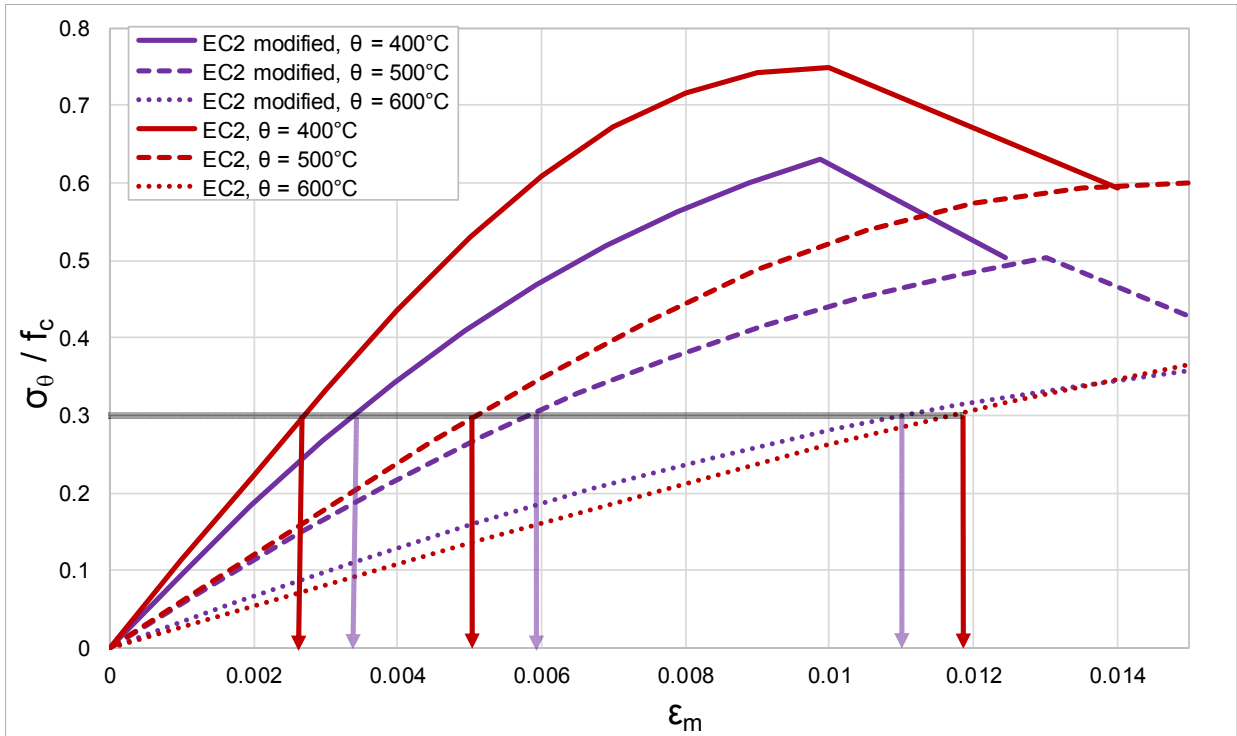


Figure 132: Compressive mechanical strains at load level $\alpha = 0.3$ from the constitutive EN 1992-1-2's model and the proposed model for $\theta_{max} = 400, 500$ and 600°C

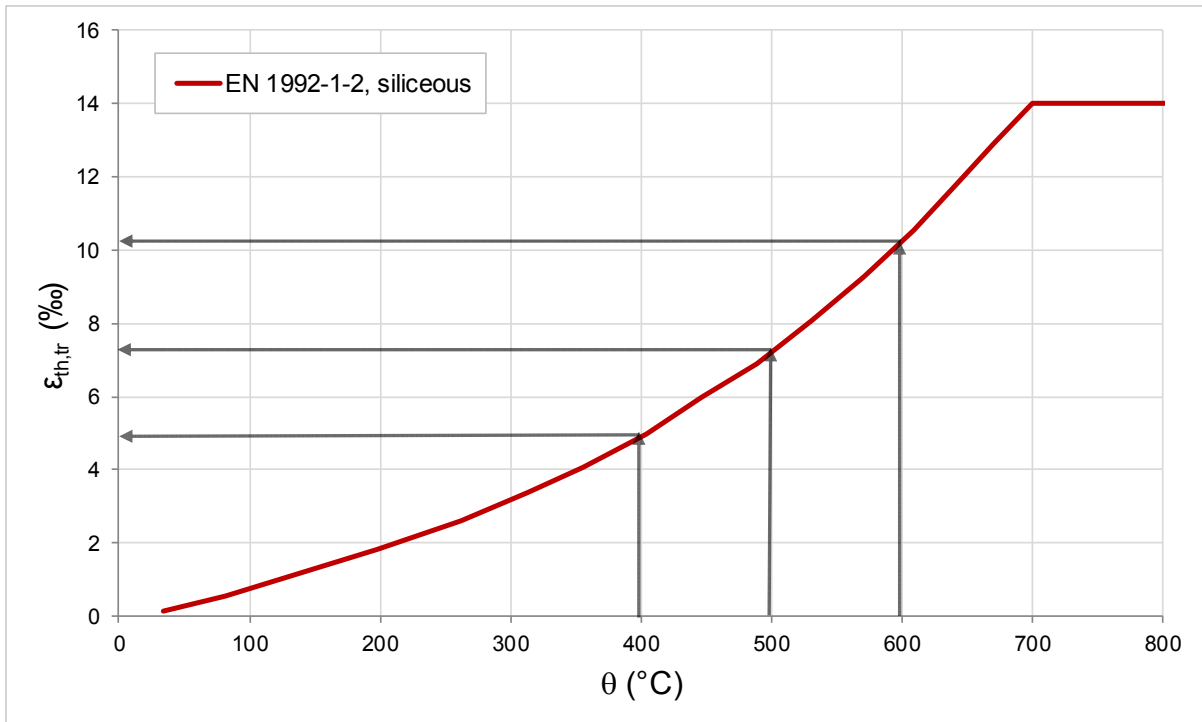


Figure 133: Thermal strain according to EN 1992-1-2 model for $\theta_{max} = 400, 500$ and 600°C

The mechanical strains for $\alpha = 0.1, 0.3$ and 0.4 are evaluated for the both constitutive models for $\theta_{max} = 200-700^\circ\text{C}$ and plotted in Fig. 134 along with thermal strain according to EN 1992-1-2 and the upper boundary of the mechanical strains (strain at peak stress + transient creep) according to EN 1992-1-2.

$\alpha = 0.1$:

The mechanical strains, $\epsilon_{m,\alpha=0.1}$, for the both models are almost identical up to 500°C . Beyond this temperature, $\epsilon_{m,\alpha=0.1}$ according to EN 1992-1-2 is higher than the proposed model. $\epsilon_{m,\alpha=0.1}$ is constantly smaller than thermal strains up to 700°C that means the total strain at the elevated temperature always remains tensile under this stress level.

$\alpha = 0.3$:

$\epsilon_{m,\alpha=0.3}$ according to the proposed models are slightly higher than EN 1992-1-2's values up to approximately 550°C . Beyond this temperature the normative values are higher than the proposed model. Further, for both models, beyond the mentioned temperature, $\epsilon_{m,\alpha=0.3}$ are higher than the thermal strains. This means, at the higher temperatures, the total compressive strains might reach large values.

For the cross-section near the mid-support, above 550°C the excessive compressive total strain may cause increase in the curvature. The corresponding mechanical strains based on the proposed model are smaller in this range and can be treated as favourable in analysing the system deflections.

$\alpha = 0.4$:

The mechanical strains according to the proposed models are higher than EN 1992-1-2's values up to approximately 500°C . Due to the lower strength of the proposed model, the critical temperature lays approximately between 500 and 550°C whereas for EN 1992-1-2 this is at about 600°C .

Further, for $400-500^\circ\text{C}$, the mechanically-induced strains are higher than the thermal strains for the proposed model. This is for EN 1992-1-2's model in the range of $500-600^\circ\text{C}$.

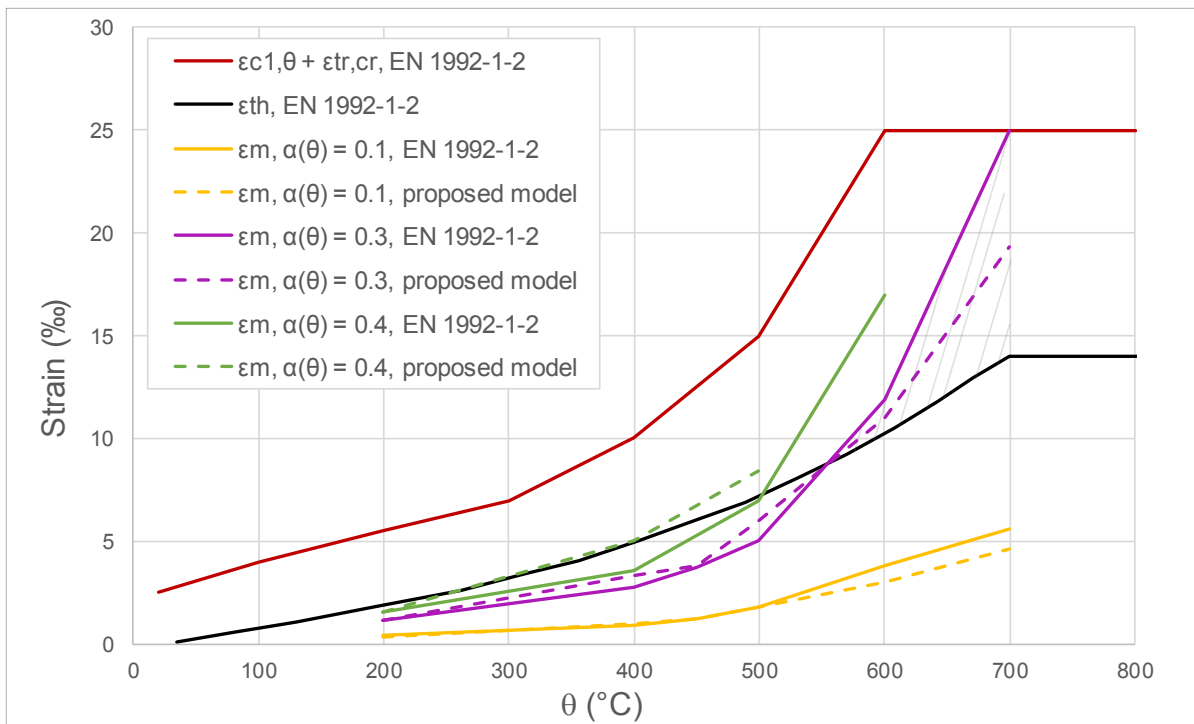


Figure 134: Mechanical strains of cross-section fibres for $\alpha = 0.1, 0.3$ and 0.4 corresponding to EN 1992-1-2's model and the proposed model vs. thermal strains

11 Conclusions and Outlook

Different conclusions regarding various aspects of this study can be made based on area of investigation.

Temperature fields in a cut-and-cover tunnel cross-section:

- An approach is proposed in chapter 2 to compute the temperature values in the thermally affected zone of a cross-section of a cut-and-cover tunnel under normative ZTV-ING fire exposure that can be used in the practice.

Heating rate in a tunnel member and in the cylinder specimens, thermal incompatibilities and stresses in the cylinder specimens:

- The maximum heating rate of 86 K/min under ZTV-ING and a maximum value of 29 K/min under ISO fire show that the heating rate in tunnel structures can be approximately three times larger than the one in residential structures. Using the specified heating rates by RILEM recommendations (RILEM TC 129-MHT, 1998), $R \leq 4$ K/min, in experiment on cylinder specimen, the material model might not give any realistic estimation of first layers up to 6-7 cm from the exposed side;
- (RILEM TC 129-MHT, 1998) recommends the heating rates of $R \leq 4$ K/min for concrete cylinder specimens with diameters $d \geq 60$ mm by taking into account the independent thermal material properties. The values of $\Delta\theta$ shows a good agreement between the two assumptions (dependent and independent thermal material properties) for heating rates $R \leq 4$ K/min. For $R > 4$ K/min the assumption of independent thermal material properties leads to more pronounced deviation and therefore are not reliable.

Thermal stresses and thermal incompatibilities in the cylinder specimens:

- The results of coupled thermo-mechanical analysis of cylinder specimen, without considering the stiffness and strength changes in EN 1992-1-2, can give almost exact values for θ_m up to 100°C;
- The stress distribution resulting from the coupled thermo-mechanical analysis of cuboid using fibre-enhanced quadrilateral elements can be used to enhance the results from cylinder model for temperatures up to 200°C. Further, the ratio of compressive stresses of the layers near the exposed side to the centre of cuboid reduces with time and temperature. This means that influence of thermal effects or thermal incompatibilities reduce with time and more predominantly should be assumed up to 200°C;
- The results of both stress analyses show that the differences in the compressive stresses between a point on the surface of concrete elements and a point in the centre may generally exceed the value of $0.2 f_c$ (7 MPa for the selected concrete class). This leads to more predominant thermal incompatibilities for the specimens, specially, under low load levels for temperatures up to 200°C.

Comparing test results with EN 1992-1-2 and EN 1994-1-2 and influence of addition of Polypropylene fibres on the thermo-mechanical behaviour of the concrete at elevated temperatures:

From steady tests

- The relative strength of the concrete specimens of four batches are higher than the proposed values in EN 1992-1-2 at elevated temperatures except for 200°C. At 200°C all four batches have lower relative strengths compared to EN 1992-1-2;
- At 200°C, the relative strength reduction of C50-PP is higher than C50;
- The relative strains at peak stresses of C50-PP and C50 are almost equal for all the temperatures;

- The results of relative modulus of elasticity from the tests show that C50-PP has the lowest values and build the lower boundary;
- Relative residual concrete strengths from the tests are larger than EN 1994-1-2's values with exception of 200°C;
- At 200°C, relative residual concrete strength of C50-PP is considerably lower than C50.

From transient tests

- The higher the strength of concrete, the lower is the free thermal elongation of the concrete;
- Free elongation of C50-PP is lower than C50;
- The values of transient strains of the loaded specimens were generally lower for C50-PP compared to C50.

Implicit material model

- A modified implicit material model for the concrete with PP-fibres by assuming a predicted $\alpha = 0.4$ and the strain at peak stress values for the tests is developed. The peak stresses, strains at peak stresses and ultimate strains according to the modified model are smaller than EN 1992-1-2's corresponding values for the elevated temperatures;
- The relative modulus of elasticity values for the constitutive stress-strain curves from the tests with PP-fibres under $\alpha = 0.4$ were in a very good agreement with EN 1992-1-2's values.

Structural analysis of a cut-and-cover tunnel exposed to ZTV-ING fire exposure curve:

- Different case studies are discussed to investigate the results of step-wise thermo-mechanical nonlinear (physical) analysis of reinforced concrete beams in SOFiSTiK.

Analysis of a cross-section in the mid-span of a cut-and-cover tunnel exposed to the fire

- The mechanical compressive stresses induce mechanical strains on the fibres near the exposed side during the fire. The compressive induced strains on the fibres are smaller than the thermal strains induced in these fibres. Although there exists compressive local stresses on these fibres, due to their low level, the total strains are tensile during fire.

Analysis of a cross-section over the mid-wall of a cut-and-cover tunnel exposed to the fire

- In the beginning of fire, the fibres near the exposed side are under compression. During the fire situation, the compressive local stresses are induced. This results in increase of compressive load level of each fibre. The high compressive load level of the fibres at elevated temperatures may lead to excessive compressive mechanical strains which results in higher total compressive strains of these fibres;
- For $\alpha = 0.1$, the mechanical strains at this stress level is constantly smaller than thermal strains up to 700°C according to the EN 1992-1-2 and proposed models. This means at the elevated temperature, there only exists elongation in the affected fibres;
- Due to existing compressive stresses on the fibres near the exposed side at the beginning of fire, it can be assumed (according to the test results) that these fibres have higher strength at the elevated temperatures for the maximum stress level of $\alpha = 0.3$;
- For $\alpha = 0.3$, above 550°C, excessive compressive total strains are induced in the affected fibres. This may cause increase in the curvature. The corresponding mechanical strains based on the proposed model are beyond 550°C smaller and can be treated as favourable in analysing the system deflections;

- For $\alpha = 0.4$, the mechanical induced strains are higher than the thermal strains for the proposed model for 400-500°C. This is for EN 1992-1-2's model in the range of 500-600°C. The latter means a higher allowance of the total compressive strain according to the EN 1992-1-2's model.

Reduction in the strength of fibres

- 20% percentage reduction in the fibre strength has a small influence on the flexural response in the nonlinear fibre beam analysis;

Reduction in the strains at peak stresses of fibres

- The reduced strain at peak stress values (in the modified model) used for the fibres result in decrease of mechanical strains at the elevated temperatures. As a result, beyond approximately 500°C, and under $\alpha(\theta) = 0.3$, a compressive total strain state of the fibres are expected and these values are smaller than the corresponding values from EN 1992-1-2's model.

Outlook

- Correctness of the assumption that the material model in EN 1992-1-2 based on 1D small-scale tests and a low heating rate can be used for flexural response of a tunnel member with much higher heating rates should be investigated;
- Small-scale tests with $\alpha = 0.4$ should be carried out for the concrete with the same mixture as used for C50-PP to validate the predicted results;
- The results of nonlinear flexural analysis of the beams with fibre elements exposed to ZTV-ING fire exposure using EN 1992-1-2's implicit model should be validated with the large-scale experimental test results.

Bibliography

Abrams M-S Compressive Strength of Concrete at Temperatures to 1600F [Journal] / Special Publication . - 1971. - Vol. 25. - pp. 33-58.

Anderberg Y Mechanical Behaviour at Fire of Concrete and Hyperstatic Concrete Structures [Report] / Division of Structural Mechanics and Concrete Construction. - Lund : Lund Institute of Technology, 1976.

Anderberg Y and Thelandersson S Stress and deformation characteristics of concrete at high temperatures. Lund Institute of Technology. Division of Structural Mechanics and Concrete Construction, 1976.

ANSYS. - Version 17.2, 2016.

Arnault P, Ehm H and Kruppa J Rapport Expérimental sur les Essais avec des Feux Naturels Exécutés dans la Petite Installation-Maizières-Les-Metz. Doc. CECM-3/73-II-F [Report] / Convention Européenne de la Construction Métallique. - Puteaux , 1973.

Balazs G-L and Lubloy E Compressive strength of fire exposed fibre reinforced concrete [Conference] / 8th RILEM International Symposium on Fibre Reinforced Concrete: Challenges and Opportunities, BEFIB 2012. - 2012.

Bamonte P and Monte F Modeling R/C Columns in Fire According to Different Constitutive Models for Heated Concrete [Book Section] / Structures in Fire: Proceedings of the Sixth International Conference. - [s.l.] : DEStech Publications, Inc, 2010.

BAST Bundesanstalt für Straßenwesen Zusätzliche Technische Vertragsbedingungen und Richtlinien für Ingenieurbauten (ZTV-ING) Teil 5 "Tunnelbau" und Teil 3 "Massivbau", Abschnitt 1 "Beton". - 2015.

Bazant Z-P and Chern J-C Stress-induced thermal and shrinkage strains in concrete. [Journal] / Journal of engineering mechanics. - 1987. - 10 : Vol. 113. - pp. 1493-1511.

Beard A and Carvel R The Handbook of Tunnel Fire Safety [Book]. Thomas Thelford, 2005.

Behnood A and Ghandehari M Comparison of compressive and splitting tensile strength of high-strength concrete with and without polypropylene fibers heated to high temperatures [Journal] / Fire Safety Journal. - 2009. - 8 : Vol. 44. - pp. 1015-1022.

Boström L, Wickström U and Adl-Zarrabi B Effects of specimen size and loading conditions on spalling of concrete [Journal] / FIRE AND MATERIALS. - 2007. - Vol. 31. - pp. 173-186.

Castillo C and Durrani A-J Effect of Transient High Temperature on High-Strength Concrete [Journal] / ACI Materials. - 1990. - 1 : Vol. 87. - pp. 47-53.

Chang Y-F, Chen Y-H; Shew M-S and Yao G-C Residual stress--strain relationship for concrete after exposure to high temperatures [Journal] / Cement and Concrete Research. - 2006. - 10 : Vol. 36. - pp. 1999-2005.

Dehn F, Nause P, Juknat M, Orgass M and König A Brand- und Abplatzverhalten von Faserbeton in Straßentunneln, Berichte der Bundesanstalt für Straßenwesen, Heft B73 [Report]. - Bergisch Gladbach : Wirtschaftsverlag NW, 2010.

Dehn F, Kotthof I, Neumann N, Hegemann K, Heide U and Schmidt J Brandversuche in Tunneln, Heft 1103 [Report] / Forschung Straßenbau und Straßenverkehrstechnik. - 2013.

Diederichs U, Jumppanen UM and Penttala V Material Properties of High Strength Concrete at Elevated Temperatures [Book Section] / IABSE 13th congress. - Helsinki : [s.n.], 1988.

Furamura F, Abe T, Shinohara Y, Tomaturo K, Kuroha K and Kokubo I Mechanical Properties of High Strength Concrete at High Temperatures [Book Section] / Proceedings, 4th Weimar Workshop on High Strength Concrete . - Weimar, 1995.

Gernay T and Franssen J-M A Comparison Between Explicit and Implicit Modelling of Transient Creep Strain in Concrete Uniaxial Constitutive Relationships [Conference] / Proceedings of the Fire and Materials 2011 Conference. Interscience Communications Ltd, 2011.

Gernay T and Franssen J-M Consideration of transient creep in the Eurocode constitutive model for concrete in the fire situation [Conference] / Sixth International Conference Structures in Fire . - [s.l.] : DEStech Publications, Inc, 2010.

Guo Z and Shi X Experiment and Calculation of Reinforced Concrete at Elevated Temperatures [Book]. - [s.l.] : Elsevier, 2011.

Harte R, Krätzig W-B, Noh, S-Y and Petryana, Y-S On progressive damage phenomena of structures [Journal] / Computational Mechanics. - 2000. - Vol. 25. - pp. 404-412.

Hertz Kristian Heat-induced Explosion of Dense Concretes [Report]. - Lyngby : Institute of Building Design, 1984.

Horiguchi T, Sugawara T and Saeki N Fire resistance of hybrid fiber reinforced high strength concrete [Conference] / 6th International RILEM Symposium on Fibre Reinforced Concretes. - 2004.

Huisman Sven, Weise F, Meng B and Schneider U Influence of polypropylene fibres on the thermal strain of high strength concrete at high temperatures [Journal] / Journal of Structural Fire Engineering. - 2011. - 3 : Vol. 2. - pp. 173-180.

Huisman S, Weise F, Meng B and Schneider U Transient strain of high strength concrete at elevated temperatures and the impact of polypropylene fibers [Journal] / Materials and Structures. - 2012. - 5 : Vol. 45. - pp. 793-801.

Huisman Sven Materialverhalten von hecfestem Beton unter thermomechanischer Branspruchung [Book]. - 2010.

Khennane A and Baker G Uniaxial model for concrete under variable temperature and stress [Journal] / Journal of Engineering Mechanics. - 1993. - 8 : Vol. 119. - pp. 1507-1525.

Khoury G-A, Algar S, Felicetti R and Gambarova P Mechanical Behaviour of HPC and UHPC Concretes at High Temperatures in Compression and Tension [Conference] / ACI Internation Conference on "State-of-the-art" in High Performance Concrete. - Chicago, 1999.

Khoury G-A, Grainger B-N and Sullivan P-J-E Strain of concrete during first heating to 600°C under Load [Journal] / Magazine of Concrete Research. - 1985. - Vol. 37. - pp. 195-215.

Khoury G-A, Grainger B-N and Sullivan P-J-E Transient thermal strain of concrete: literature review, conditions within specimen and behaviour of individual constituents [Journal] / Magazine of concrete research. - 1985. - 132 : Vol. 37. - pp. 131-144.

Khoury G-A, Sullivan P-J-E and Grainger B-N Radial temperature distributions within solid concrete cylinders under transient thermal states. [Journal] / Magazine of concrete research . - 1984. - 128 : Vol. 36. - pp. 146-156.

Khoury G-A Effect of fire on concrete and concrete structures [Journal]. Progress in Structural Engineering and Materials, 2000. - Vol. 2. - pp. 429-447.

Lam Eddie S-Sh, Wu B and Ho Ivy F-Y Monotonic and Cyclic Behavior of High-Strength Concrete with Polypropylene Fibers at High Temperature. [Journal] / ACI Materials Journal. - 2012. - 3 : Vol. 109. - pp. 323-330.

Li Y-H and Franssen J-M Test results and model for the residual compressive strength of concrete after a fire [Journal] // Journal of Structural Fire Engineering. - 2011. - 1 : Vol. 2. - pp. 29-44.

Li X, Chen N, Li J, He X and Liu H Effect of Temperature and Strain Rate on Deformation Behavior of Invar 36 Alloy [Journal] / Acta Metall Sin. - 2017.- 2 : Vol. 53. - pp. 968-974.

Lie T-T Structural fire protection [Book]. - New York : American Society of Civil Engineers, 1992.

McCormac J-C and Brown R-H Design of reinforced concrete [Book]. John Wiley & Sons, 2013. - Vol. 9.

Moore D, Lennon T and Wang Y Designers' guide to EN 1991-1-2, 1992-1-2, 1993-1-2 and 1994-1-2: handbook for the fire design of steel, composite and concrete structures to the eurocodes. Thomas Telford Services Ltd., 2007

Naus D-J The Effect of Elevated Temperature on Concrete Materials and Structures- a Literature Review [Report]. Oak Ridge National Laboratory (ORNL), 2006.

Peter C PhD Thesis, Tragverhalten von Verkehrstunneln im Brandfall mit einer Innenschale aus PP-Faserbeton. - Wuppertal : Bergische Universitaet Wuppertal, 2016.

Phan L-T High-strength Concrete at High Temperature- an Overview [Conference] / Utilization of High Strength/High Performance Concrete, 6th International Symposium Proceedings. - 2002. - pp. 501-518.

Phan L-T and Carino N-J Mechanical Properties of High-strength Concrete at Elevated Temperatures. U.S. Department of Commerce, National Institute of Standards and Technology, 2001.

Pickardt R, Bose T and Schäfer W Beton-Herstellung nach Norm: Arbeitshilfe für Ausbildung, Planung und Baupraxis [Book]. - Erkrath : Verlag Bau+ Technik GmbH, 2006.

Pistol K, Weise F and Meng B Polypropylen-Fasern in Hochleistungsbetonen [Journal] / Beton-und Stahlbetonbau. - 2012. - 7 : Vol. 107. - pp. 476-483.

Pliya P, Baucour A-L and Noumowe A Contribution of cocktail of polypropylene and steel fibres in improving the behaviour of high strength concrete subjected to high temperature [Journal] / Construction and building materials. - 2011. - 4 : Vol. 25. - pp. 1926-1934.

Poon C-S, Shui Z-H and Lam L Compressive behavior of fiber reinforced high-performance concrete subjected to elevated temperatures [Journal] / Cement and Concrete Research. - 2004. - 12 : Vol. 34. - pp. 2215-2222.

Pouran O and Harte R Nonlinear Structural Analysis of Cut-And-Cover Tunnels Exposed to Fire [Conference] / Applications of Structural Fire Engineering ASFE'15. - Dubrovnik : 2015. - pp. 43-48.

Pouran O and Harte R A Simplified Method to Design Cooling Tower Shells for Fire Situation [Conference] / International Symposium on Industrial Chimneys and Cooling Towers. - Rotterdam : 2016. - pp. 353-362.

Pouran O and Harte R Influence of heating rate and thermal incompatibilities on the test results of concrete cylinder specimens with polypropylene fibres under heating [Conference] / international conference of applications of structural fire engineering (ASFE 2017). - Manchester : CRC Press, 2017. - pp. 63-72.

Pouran O and Harte R Prüfgutachten HH 02/14-1 zum Forschungsprogramm Straßenwesen FE 15.0582/2013/FRB Erprobung des rechnerischen Brandschutznachweises für Tunnel in offener Bauweise [Report]. - 2014.

Pouran O, Harte R and Peter Carsten Parameters affecting the structural analysis of a tunnel structure exposed to fire [Journal] / Acta Polytechnica CTU Proceedings. - 2017. - Vol. 7. - pp. 47-51.

RakMK B4 High Strength Concrete Supplementary Rules and Fire Design RakMK B4 (Finnish). Concrete Association of Finland, 1993.

RILEM Recommendation of RILEM TC-HTC: mechanical concrete properties at high temperatures-modelling and applications [Journal] / Materials and Structures. - 2007. - pp. 841-853.

RILEM TC 129-MHT RILEM TC 129-MHT: Test Methods for Mechanical Properties of Concrete at High Temperatures - Recommendation: Part 7: Transient Creep for service and accident conditions [Journal] / Materials and Structures. - 1998. - Vol. 31. - pp. 290-295.

Rust W Non-Linear Finite Element Analysis in Structural Mechanics [Book]. Springer, 2015.

Schneider U, Schneider M and Franssen J-M Consideration of nonlinear creep strain of siliceous concrete on calculation of mechanical strain under transient temperatures as a function of load history [Conference] / Fifth International Conference Structures in Fire. - 2008. - pp. 463-476.

Schneider U Concrete at High Temperatures - A General Review [Journal] / Fire Safety Journal. - 1988. - Vol. 13. - pp. 55-68.

Schneider U, Diederichs U and Weiß R Hochtemperaturverhalten von Festbeton, Sonderforschungsbereich 148 - Brandverhalten von Bauteilen. TU Braunschweig, 1977.

Schneider U Behaviour of Concrete at High Temperature / Heft 337, Deutscher Ausschuss fuer Stahlbeton. - Munich : Wilhelm Ernst & Sohn, 1982.

Schneider U Behaviour of concrete under thermal steady state and non-steady state conditions [Journal] / Fire and Materials. - 1976. - 3 : Vol. 1. - pp. 103-115.

Schlüter A Passive Fire Protection for Tunnels: Guidelines, Parameters, Reality and suitable Measures [Journal] / Tunnel. - 7 2014. - pp. 22-33.

Shi X, Tan T-H, Tan K-H and Guo Z Concrete Constitutive Relationships under Different Stress-temperature Paths [Journal] / Journal of Structural Engineering. - 2002. - 12 : Vol. 128. - pp. 1511-1518.

SOFiSTiK: Teddy, Version 16.09. - 2016.

SOFiSTiK: ASE General Static Analysis of Finite Element Structures, ASE Manual, Version 2016-9, SOFiSTiK AG, Oberschleissheim, Germany.

SOFiSTiK: HYDRA Seepage and Thermal Analysis, HYDRA Manual, Version 2016-5, SOFiSTiK AG, Oberschleissheim, Germany.

SOFiSTiK: STAR2 Statics of Beam Structures 2nd Order Theory, STAR2 Manual, Version 2016-9, SOFiSTiK AG, Oberschleissheim, Germany.

SOFiSTiK: TALPA 2D Finite Elements in Geotechnical Engineering, TALPA Manual, Version 2016-8, SOFiSTiK AG, Oberschleissheim, Germany.

Terro M-J Numerical modeling of the behavior of concrete structures in fire [Journal] / ACI Structural Journal. ACI, 1998. - 2 : Vol. 95.

Yang H, Lin Y, Hsiao C and Liu J-Y Evaluating residual compressive strength of concrete at elevated temperatures using ultrasonic pulse velocity [Journal] / Fire Safety Journal . - 2009. - 1 : Vol. 44. - pp. 121-130.

Youssef M-A and Mofteh N General stress-strain relationship for concrete at elevated temperatures [Journal] / Engineering Structures. - 2007. - 10 : Vol. 29. - pp. 2618-2634.

Zahlten W Lecture notes on "The Finite Element Method". - Wuppertal : Bergische Universität Wuppertal, 2017.

Zahlten W Lecture notes on higher mechanics 1, "Nonlinear Methods". - Wuppertal : Bergische Universität Wuppertal, 2000.

Normative References

- DIN EN 12390-3:2009 Testing hardened concrete - Part 3: Compressive strength of test specimens, July 2009
- DIN EN 12390-7:2009 Testing hardened concrete - Part 7: Density of hardened concrete, July 2009
- DIN EN 12390-13:2014 Testing hardened concrete - Part 13: Determination of secant modulus of elasticity in compression, June 2014
- EN 1991-1-2:2002 Actions on structures - Part 1-2: General actions - Actions on structures exposed to fire, November 2002
- EN 1991-1-5:2003 Actions on structures - Part 1-5: General actions - Thermal actions, November 2003
- EN 1992-1-1:2004 Design of concrete structures - Part 1-1: General rules and rules for buildings, December 2004
- EN 1992-1-2:2004 Design of concrete structures - Part 1-2: General rules – structural fire design, December 2004
- EN 1994-1-2:2005 Design of composite steel and concrete structures - Part 1-2: General rules - structural fire design, August 2005
- ZTV-ING Zusätzliche Technische Vertragsbedingungen und Richtlinien für Ingenieurbauten, Teil 5 Tunnelbau, Abschnitt 2 offene Bauweise, März 2012

Annex A: One-dimensional Heat Transfer in a Wall

In reality, the most cases of heat transfer are three-dimensional. In case of a medium with a predominant temperature change and thus heat transfer in one direction, the temperature change or heat transfer can be assumed negligible in other directions. Since the three-dimensional heat transfer equations can be easily derived from case of one dimensional heat transfer, the one-dimensional heat transfer process is here assumed. The Fouriers' law of heat conduction states that the rate of heat conduction through a concrete wall is proportional to the temperature difference across the wall and the area of wall normal to the heat transfer direction and is inversely proportional to the thickness of wall.

$$\dot{Q}_x = -kA_x \frac{d\theta}{dx}, \quad \dot{Q}_y = -kA_y \frac{d\theta}{dy}, \quad \dot{Q}_z = -kA_z \frac{d\theta}{dz} \quad (100)$$

where k is the thermal conductivity of concrete, A is the normal area of wall to the direction of heat transfer and $\frac{d\theta}{dx}$ is temperature gradients in x direction.

The heat conduction vector can be written in rectangular coordinates as:

$$\vec{Q}_n = \dot{Q}_x \vec{i} + \dot{Q}_y \vec{j} + \dot{Q}_z \vec{k} \quad (101)$$

In thermal analysis, concrete is assumed to be an isotropic material and thus the change in material properties is assumed to be the same in all directions. So the thermal conductivity is simplified and there is no need to express thermal conductivities as a tensor quantity.

Assuming a one-dimensional transient heat transfer in a cube element as representative of wall or slab, an energy balance on a thin element with thickness of Δx at a short time interval of Δt for variable conductivity (function of temperature) can be stated as:

$$\left(\begin{array}{c} \text{Rate of} \\ \text{heat conduction} \\ \text{at } x \end{array} \right) - \left(\begin{array}{c} \text{Rate of} \\ \text{heat conduction} \\ \text{at } x + \Delta x \end{array} \right) + \left(\begin{array}{c} \text{Rate of} \\ \text{heat generation} \\ \text{inside the element} \end{array} \right) = \left(\begin{array}{c} \text{Rate of change} \\ \text{of energy content} \\ \text{of the element} \end{array} \right) \quad (102)$$

or

$$\dot{Q}_x - \dot{Q}_{x+\Delta x} + \dot{E}_{gen,element} = \frac{\Delta E_{element}}{\Delta t} \quad (103)$$

$$\dot{Q}_x - \dot{Q}_{x+\Delta x} + \dot{e}_{gen} A \Delta x = \rho c A \Delta x \frac{\theta_{t+\Delta t} - \theta_t}{\Delta t} \quad (104)$$

By assuming uniform heat generation in a homogenous material, \dot{e}_{gen} , is the constant rate of heat generation per unit volume (a volumetric phenomenon and therefore specified per unit volume W/m^3), ρ is the density and c is specific heat (ρc indicates the capability of heat storage of concrete). By dividing the both sides by $A \Delta x$ and taking limit of $\Delta x \rightarrow 0$ and $\Delta t \rightarrow 0$ the equation becomes:

$$\frac{1}{A} \frac{\partial}{\partial x} (kA \frac{\partial \theta}{\partial x}) + \dot{e}_{gen} = \rho c \frac{\partial \theta}{\partial t} \quad (105)$$

where A is in the case of wall constant and therefore the equation becomes:

$$\text{Variable conductivity: } \frac{\partial}{\partial x} (k \frac{\partial \theta}{\partial x}) + \dot{e}_{gen} = \rho c \frac{\partial \theta}{\partial t} \quad (106)$$

The thermal conductivity of concrete is dependent on the temperature and therefore it changes in x corresponding to the changes of θ . By considering a constant thermal conductivity:

Constant conductivity: $\frac{\partial^2 \theta}{\partial x^2} + \frac{\dot{e}_{gen}}{k} = \frac{1}{\alpha} \frac{\partial \theta}{\partial t}$ (107)

where α is the thermal diffusivity: $\alpha = \frac{\text{Heat conducted}}{\text{Heat stored}} \frac{k}{\rho c} \left(\frac{m^2}{s} \right)$ (108)

Thermal diffusivity is indicative of how fast heat propagates in the concrete. Assume a dried concrete (moisture content = 0%) and temperature dependent material properties of concrete according to EN 1992-1-2 (including upper and lower limits of thermal conductivities). The upper values of thermal diffusivity of concrete, α_u , reduce from the maximum of 9.43E-07 to 2.69E-07 (m²/s) and the lower limits, α_l , from 6.44E-07 to 2.46E-07 (m²/s) for temperatures between 20 to 1200°C respectively (see Fig. A1). This means the rate of heat penetration in the concrete decreases with the increase in temperature.

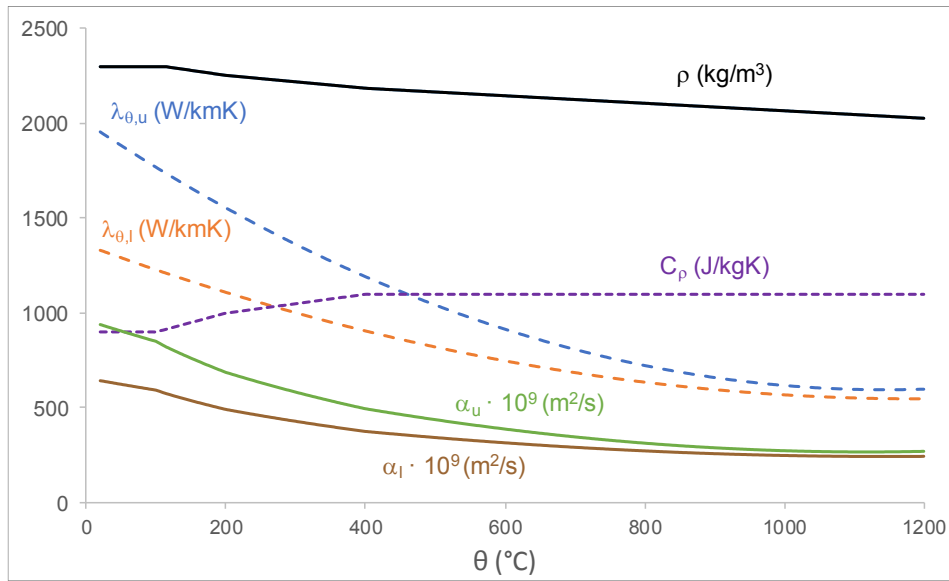


Figure A1: Upper and lower limits of thermal diffusivities based on EN 1992-1-2 temperature dependent material properties

Annex B: Spalling of Cylinder Specimens under Uniaxial Compressive Load

Table B1: Test results acc. to (Hertz, 1984) for HSC cylinder specimens under axial compressive load at elevated temperatures for concrete with Silica Fumes and without Silica Fumes in the mix

Authors	Comp strength ambient (MPa)	Diameter x height cylinder (mm)	Nr of tests	Nr of spall	Spall temp or range (°C)	Water/cement w/c	Silica Fumes (Kg/m ³)	Type and amount of additive (Kg/m ³) or % of vol	Heating and cooling rate (°C/min)	Test type
(Hertz, 1984)	169.1	100 x 200	---	0		X ¹	✓	---	1	Comp strength unstressed
	119.2		---	2	450, 650	X	✓	---		
	146.4		---	3	350, 450, 650	X	✓	---		
	177		---	0		X	---	---		
	200		---	0		X	---	---		
	175		---	0		X	---	Steel fibres 1.5%		
	191		---	0		X	---	Steel fibres 1.5%		
	171		---	2	400, 600	X	---	Steel fibres 3%		
	185		---	1	600	X	---	Steel fibres 3%		
	130	57 x 100	---	0		X	---	---	1	Comp strength unstressed
	173		---	0		X	---	---		
	165		---	0		X	---	Steel fibres 1.5%		
	167		---	0		X	---	Steel fibres 1.5%		
	151		---	0		X	---	Steel fibres 3%		
	154		---	0		X	---	Steel fibres 3%		
	175	28, 57	---	0		X	---	---	1	Comp strength unstressed
	188		---	0		X	---	Steel fibres 1.5%		
	166		---	0		X	---	Steel fibres 1.5%		
	174		---	0		X	---	Steel fibres 3%		
	156		---	0		X	---	Steel fibres 3%		
	158		---	0		X	---	Steel fibres 1.5%		

¹ Unknown or not found

Annex B: Spalling of Cylinder Specimens under Uniaxial Compressive Load

Table B2: Test results acc. to (Diederichs, et al., 1988), (Castillo, et al., 1990) and (Furamura, et al., 1995) for HSC cylinder specimens under axial compressive load at elevated temperatures

Authors	Comp strength ambient (MPa)	Diameter x height of cylinder (mm)	Nr of tests	Nr of spall	Spall temp or range (°C)	Water/cement w/c	Silica Fumes (Kg/m ³)	Type and amount of additive (Kg/m ³) or % of vol	Heating and cooling rate (°C/min)	Test type
(Diederichs, et al., 1988)	106.6	80 x 300	X	---	---	X	53	---	2	$\epsilon_{tr,tot}$
	91.8		X	---	---	X	---	Fly ash, 157		
	84.5		X	---	---	X	---	Blast slag furnace cement		
	32.9		X	---	---	X	X	---		
	X	X	X	X	X	X	X	X	32	X
(Castillo & Durrani, 1990)	31.1	51 x 102	X	X	X	0.68	---	X	7-8	Comp strength unstressed
	62.8		X	X	X	0.32	---	F superplasticizer to ASTM with no fly ash		Comp strength stressed
	89		X	All. 1/3 at 320 – 360°C	700		---			
(Furamura, et al., 1995)	21	50 x 100	45	---	---	0.58	---	X	1	Comp strength unstressed
	42		45	---	---	0.41	---	X		
	60		24	---	---	0.32	---	X		

Annex B: Spalling of Cylinder Specimens under Uniaxial Compressive Load

Table B3: Test results acc. to (Phan, et al., 2001) for HSC cylinder specimens under axial compressive load at elevated temperatures for concrete with and without Silica Fumes and with different water/cement ratios in the mixes

Authors	Comp strength ambient (MPa)	Diameter x height of cylinder (mm)	Nr of tests	Nr of spall	Spall temp or range (°C)	Water/cement w/c	Silica Fumes (Kg/m ³)	Type and amount of additive (Kg/m ³) or % of vol	Heating and cooling rate (°C/min)	Test type
(Phan, et al., 2001)	98	100 x 200	3	0	---	0.22	10% of cement mass	X	5	Comp strength stressed
			3	3	450		10% of cement mass	X		Comp strength unstressed
			5 from 300°C 3 from 450°C	1 from 300°C 3 from 450°C	1 at 300 3 at 450		10% of cement mass	X		Residual strength unstressed
	88	100 x 200	3	3	600	0.33	10% of cement mass	X	5	Comp strength stressed
			4	4	1 at 450 3 at 600		10% of cement mass	X		Comp strength unstressed
			4 for 300°C 3 for 450°C	1 from 300°C 0 from 450°C			10% of cement mass	X		Residual strength unstressed
	75	100 x 200	3	3	600	0.33	---	X	5	Comp strength stressed
			3	3	600		---	X		Comp strength unstressed
			3	0	---		---	X		Residual strength unstressed
	50	100 x 200	3	0	---	0.57	---	X	5	Comp strength stressed
			3	0	---		---	X		Comp unstressed
			3	0	---		---	X		Residual strength unstressed

Annex B: Spalling of Cylinder Specimens under Uniaxial Compressive Load

Table B4: Test results acc.to (Huismann, 2010) for HSC cylinder specimens under axial compressive load at elevated temperatures for concrete with Silica Fumes with different heating rates

Authors	Compressive strength ambient (MPa)	Diameter x height of cylinder (mm)	Concrete with PP		Concrete without PP		Spall temp or range (°C)	Vol of PP (Kg/m ³)	Water/cement w/c	Silica Fumes (Kg/m ³)	Type and amount of additive (Kg/m ³) or % of vol	Heating and cooling rate (°C/min)	Test type
			Nr of tests	Nr of spall	Nr of tests	Nr of spall							
(Huismann, 2010)	113	100 x 300	1	---	---	---	---	2	0.32	63.8	Superplasticizer	0.2	Thermal strain
	110	100 x 300	---	---	2	---	---	---	0.32	63.8	Superplasticizer	1	Thermal strain
	110		---	---	1	X	X	---					$\epsilon_{tr,tot}$ $\alpha = 0.1$
	110		---	---	1	X	X	---					$\alpha = 0.2$
	110		---	---	1	X	X	---					$\alpha = 0.3$
	113		2	---	---	---	---	2					$\epsilon_{tr,tot}$ $\alpha = 0.1$
	113		2	---	---	---	---	2					$\epsilon_{tr,tot}$ $\alpha = 0.2$
	113		2	---	---	---	---	2					$\alpha = 0.3$
	113		3	---	---	---	---	2					$\alpha = 0.4$
	113		2	---	---	---	---	2					$\alpha = 0.5$
	113		2	---	---	---	---	2					$\alpha = 0.6$
	113	2	---	---	---	---	2	$\alpha = 0.7$					
	110	100 x 300	---	---	1	1	400	---	0.32	63.8	Superplasticizer	15	Thermal strain
	113		3	---	---	---	---	---					Thermal strain
	113		3	---	---	---	---	---					$\epsilon_{tr,tot}$ $\alpha = 0.2$
	110	100 x 300	---	---	X	All tests $\alpha > 0.1$	325	---	0.32	63.8	Superplasticizer	1	Stress strain stressed

Annex B: Spalling of Cylinder Specimens under Uniaxial Compressive Load

Table B5: Test results acc. to (Huismann, et al., 2012) for HSC cylinder specimens under axial compressive load at elevated temperatures for concrete with Silica Fumes

Authors	Comp strength ambient (MPa)	Diameter x height of cylinder (mm)	Concrete with PP		Concrete without PP		Spall temp or range (°C)	Vol of PP (Kg/m ³)	Water/cement w/c	Silica Fumes (Kg/m ³)	Type and amount of additive (Kg/m ³ or % of vol)	Heating and cooling rate (°C/min)	Test type
			Nr of tests	Nr of spall	Nr of tests	Nr of spall							
(Huismann, et al., 2012)	110	100 x 300	---	---	X	---	---	---	0.32	63.8	Superplasticizer 17.4	1	Thermal strain
	110		---	---	X	---	---	2					
	113		X	---	---	---	---	---					
	113		X	---	---	---	---	2					
	110	100 x 300	---	---	X	All of tests with $\alpha > 0.1$	325	---	0.32	63.8	Superplasticizer 17.4	1	$\epsilon_{r,tot}$
	113		X	0	---	---	---	2					$\epsilon_{r,tot}$

Annex C: Mass Loss of Batches

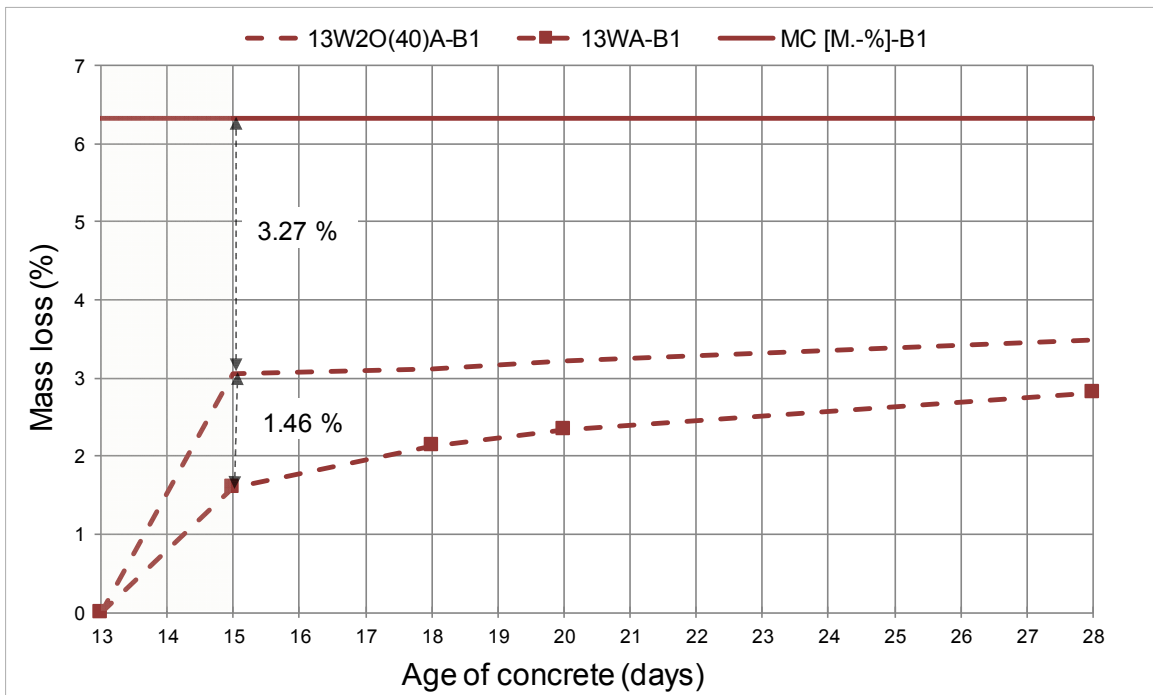


Figure C1: Relative mass loss to the 13-day old saturated specimen for 13W2O(40)-B1 and 13WA-B1 specimens

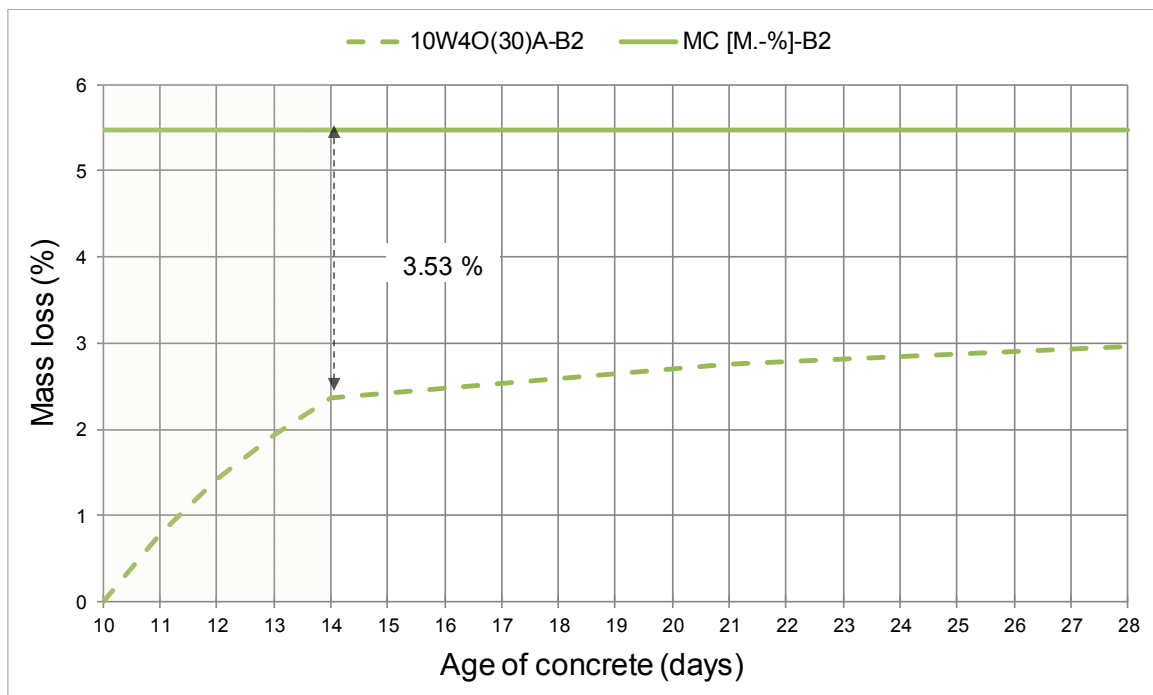


Figure C2: Relative mass loss to the 10-day old saturated specimen and total moisture content (M.- %) for batch 2

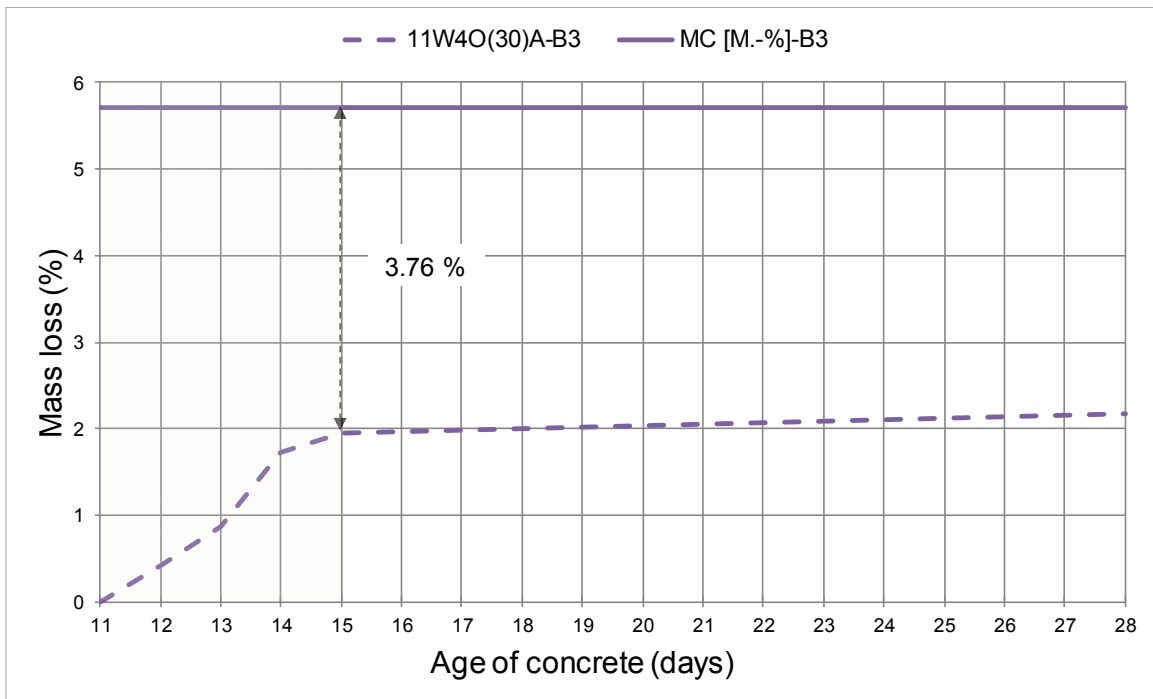


Figure C3: Relative mass loss to the 11-day old saturated specimen and total mass loss (M.- %) for batch 3

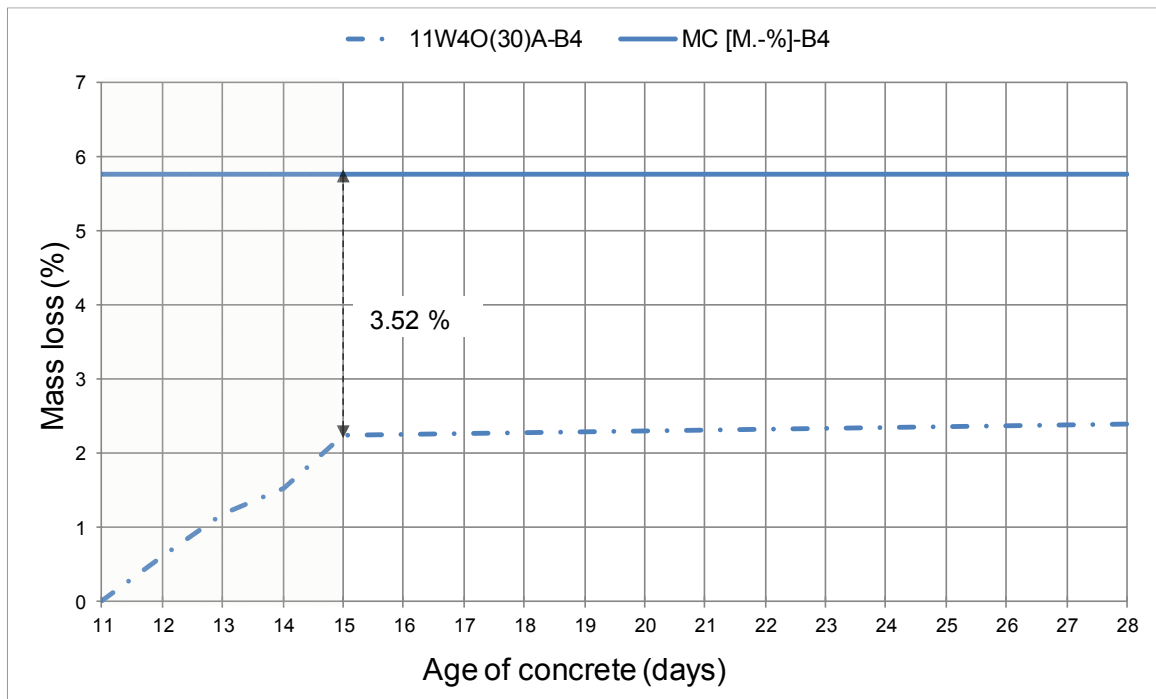


Figure C4: Relative mass loss to the 11-day old saturated specimen and total mass loss (M.- %) for batch 3

Annex D: Stress-strain Curves at Ambient Temperature

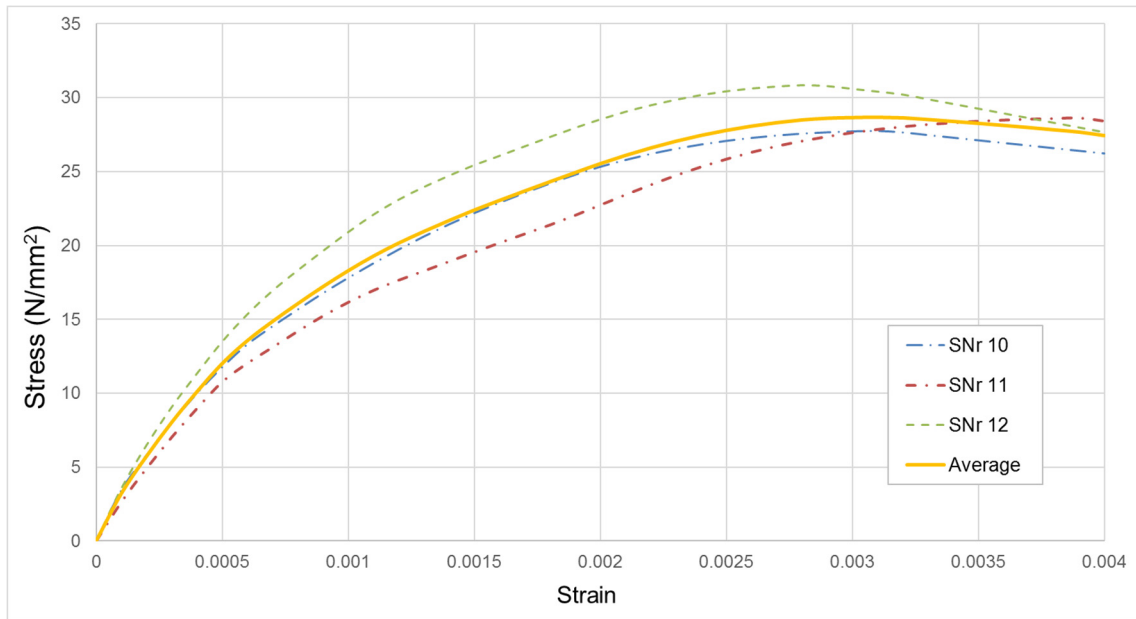


Figure D1: Stress-strain for 90-day-old cylinder specimens from batch 1

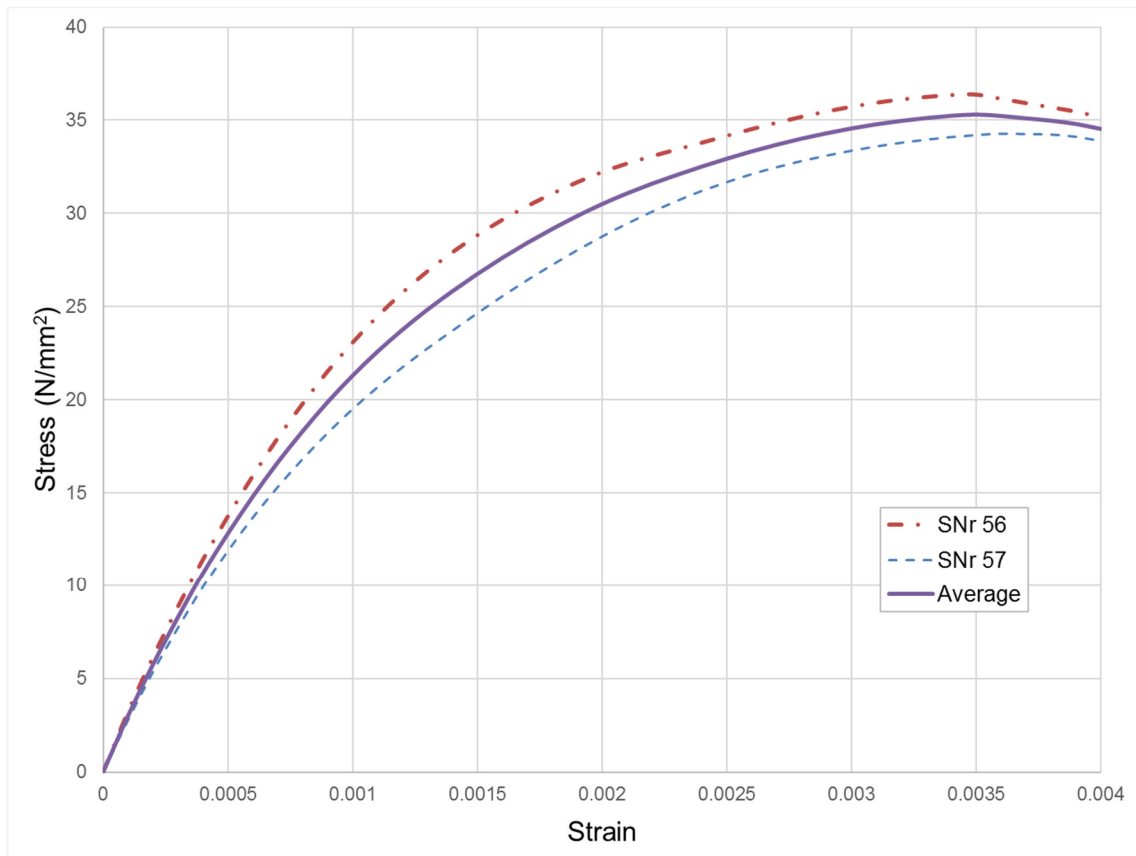


Figure D2: Stress-strain for 90-day-old cylinder specimens from batch 2

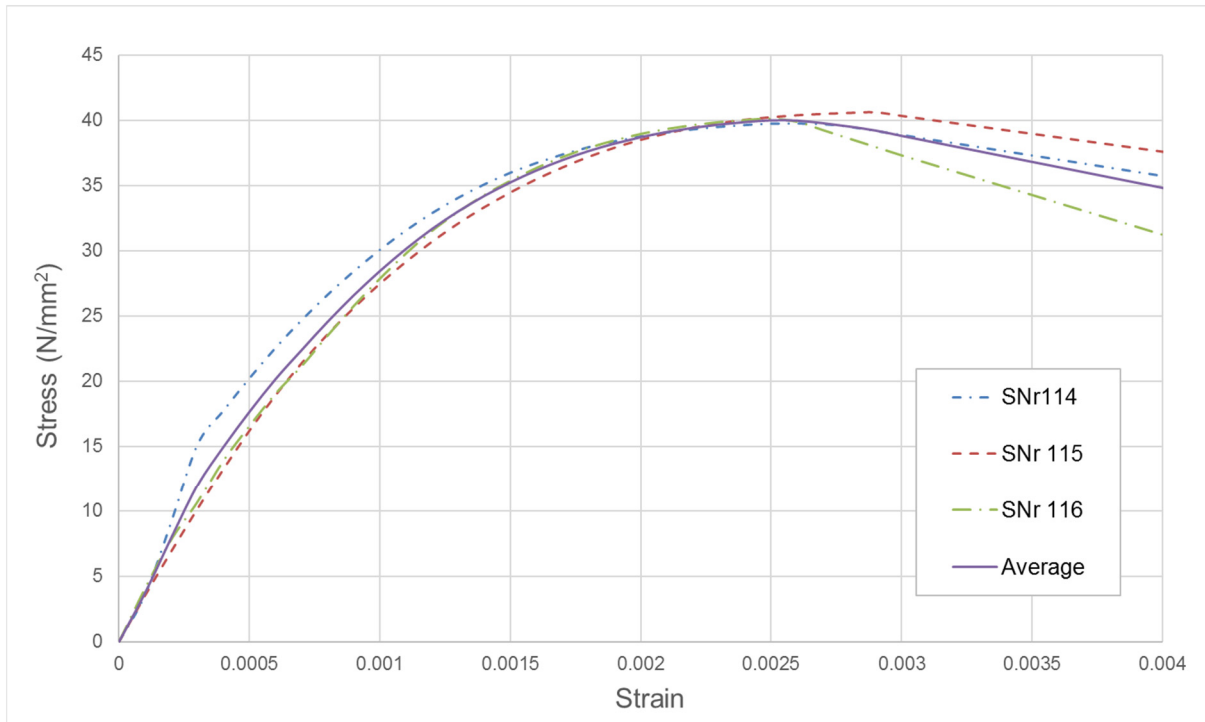


Figure D3: Stress-strain for 28-day-old cylinder specimens from batch 3

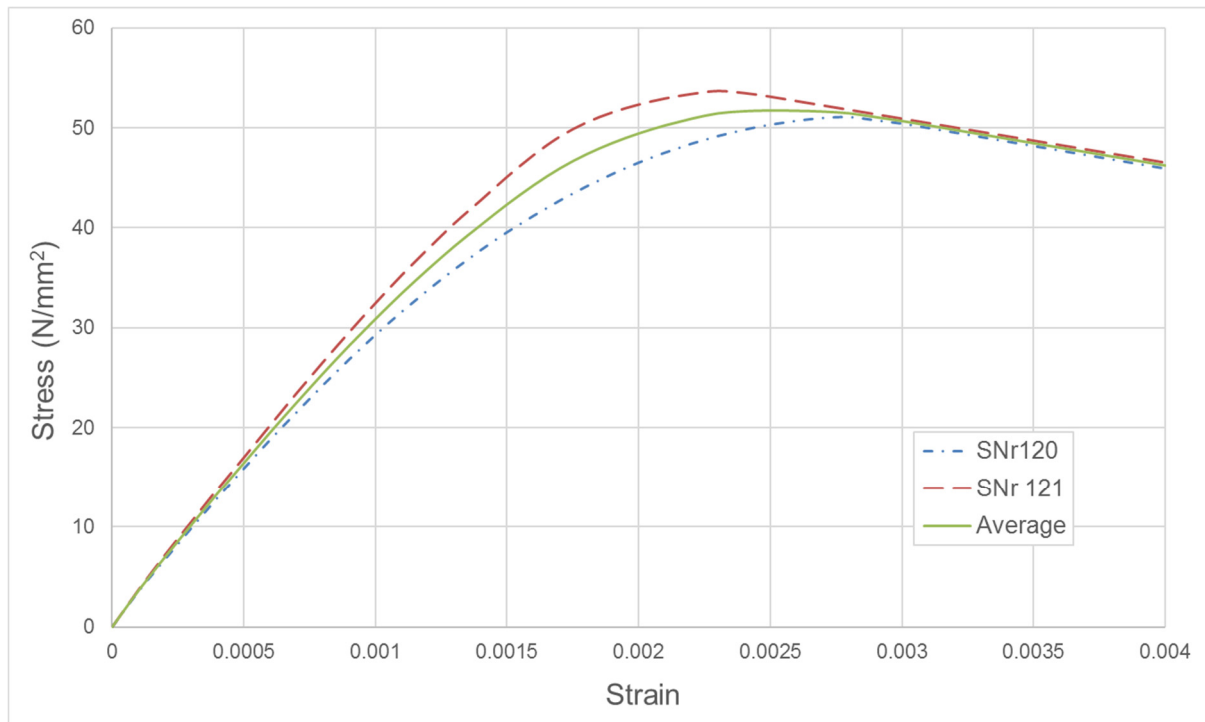


Figure D4: Stress-strain for 90-day-old cylinder specimens from batch 3

Annex D: Stress-strain Curves at Ambient Temperature

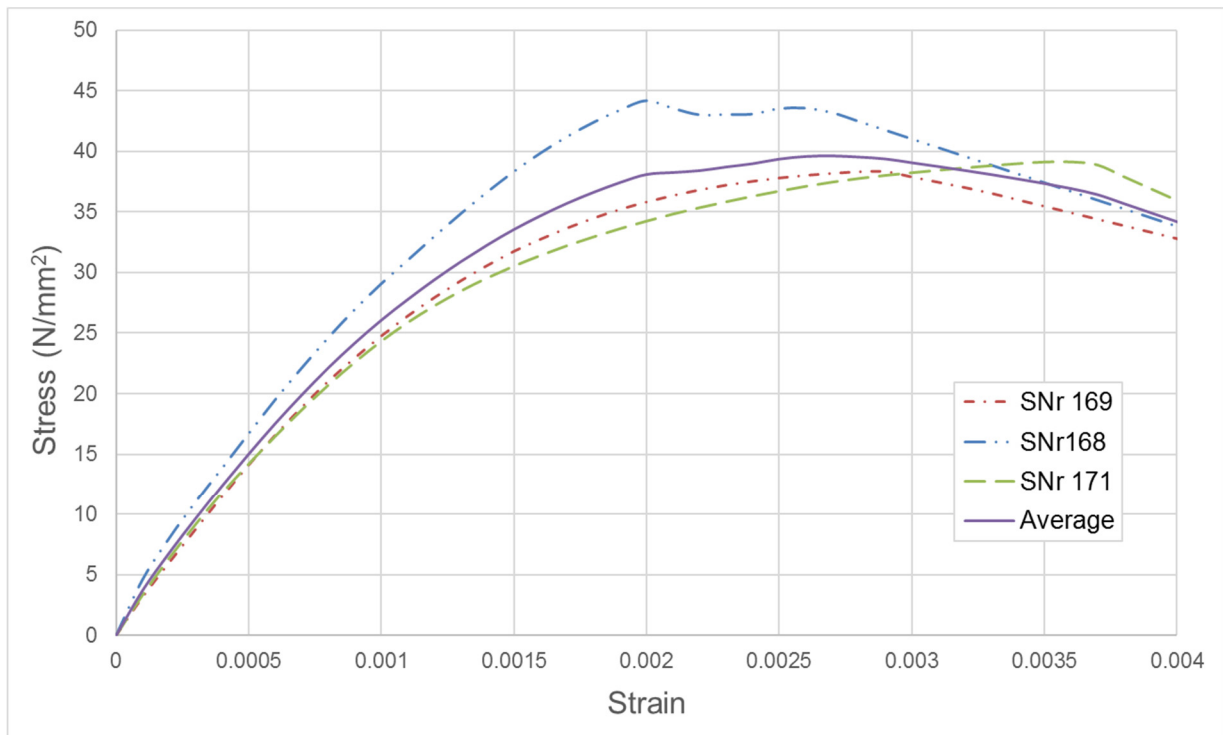


Figure D5: Stress-strain for 28-day-old cylinder specimens from batch 4

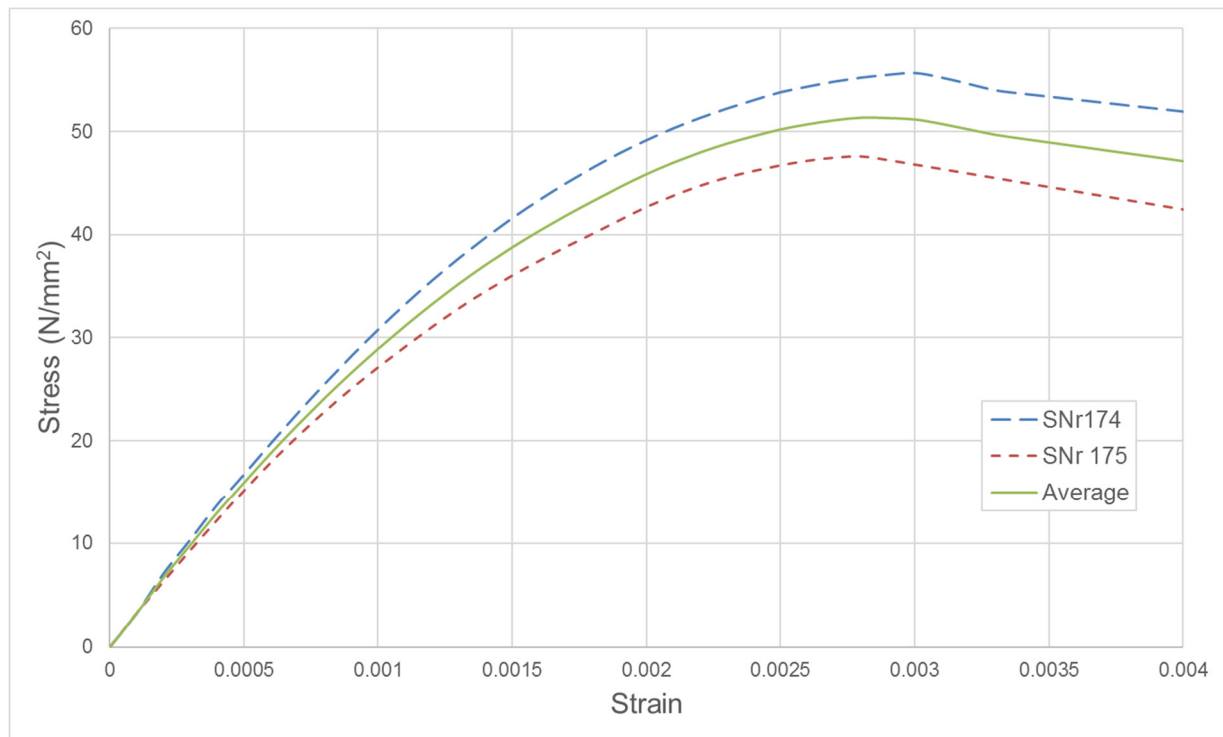


Figure D6: Stress-strain for 90-day-old cylinder specimens from batch 4

Annex E: Characteristics of Cylinder Tests

Table E1: Tests performed on batches 1 and 2

Batch Nr.	Test Nr.	$f_{c,28}$	$f_{c,90}$	$f_{c,200}$	E-test	Dried out
1	1					✓
	2					✓
	3					✓
	4					✓
	5					✓
	6					✓
	7	✓				
	8	✓				
	9	✓				
	10			✓		
	11			✓		
	12			✓		
	13			✓	✓	
	14			✓	✓	
	38				✓	
	39				✓	
	2	50	✓			
51						✓
52		✓				
53		✓			✓	
54		✓			✓	
55		✓			✓	
56				✓		
57				✓		
60						✓
71				✓		
72				✓		
73					✓	
74					✓	
75					✓	
87					✓	
88				✓		

Annex E: Characteristics of Cylinder Tests

Table E2: Tests performed on batches 1 and 2

Batch Nr.	Test Nr.	$f_{c,28}$	$f_{c,90}$	$f_{c,200}$	E-test	Dried out
3	114	✓				
	115	✓				
	116	✓				
	117	✓			✓	
	118	✓			✓	
	119	✓			✓	
	120		✓			
	121		✓			
	122				✓	
	124				✓	
	125				✓	
	134			✓		
	135			✓		
	140					✓
	141					✓
	142					✓
	143					✓
	144					✓
164				✓		
4	168	✓				
	169	✓				
	170	✓			✓	
	171	✓				
	172	✓			✓	
	173	✓			✓	
	174		✓			
	175		✓			
	176				✓	
	177				✓	
	189			✓		
	190			✓		
	191			✓		
	196			✓		
	209					✓
	210					✓
	211					✓
	212					✓
213					✓	
214					✓	

Annex F: Results of Temperature Measurements for the Prisms

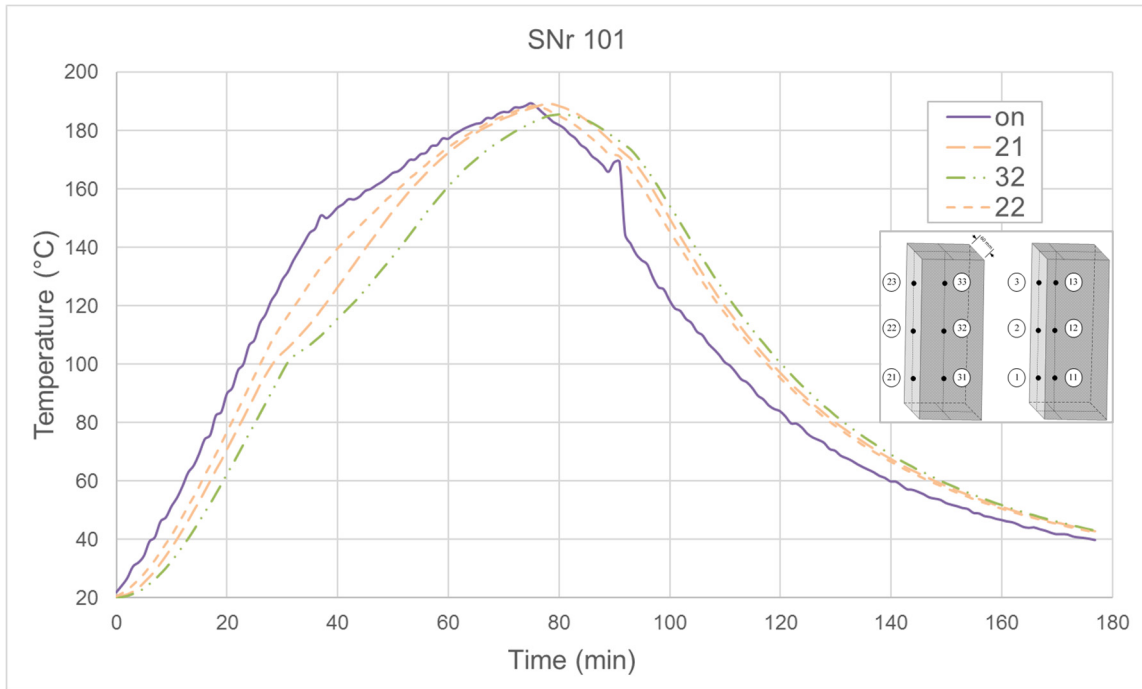


Figure F1: Temperatures in specimen 101 up to max approximate temperature of 190°C

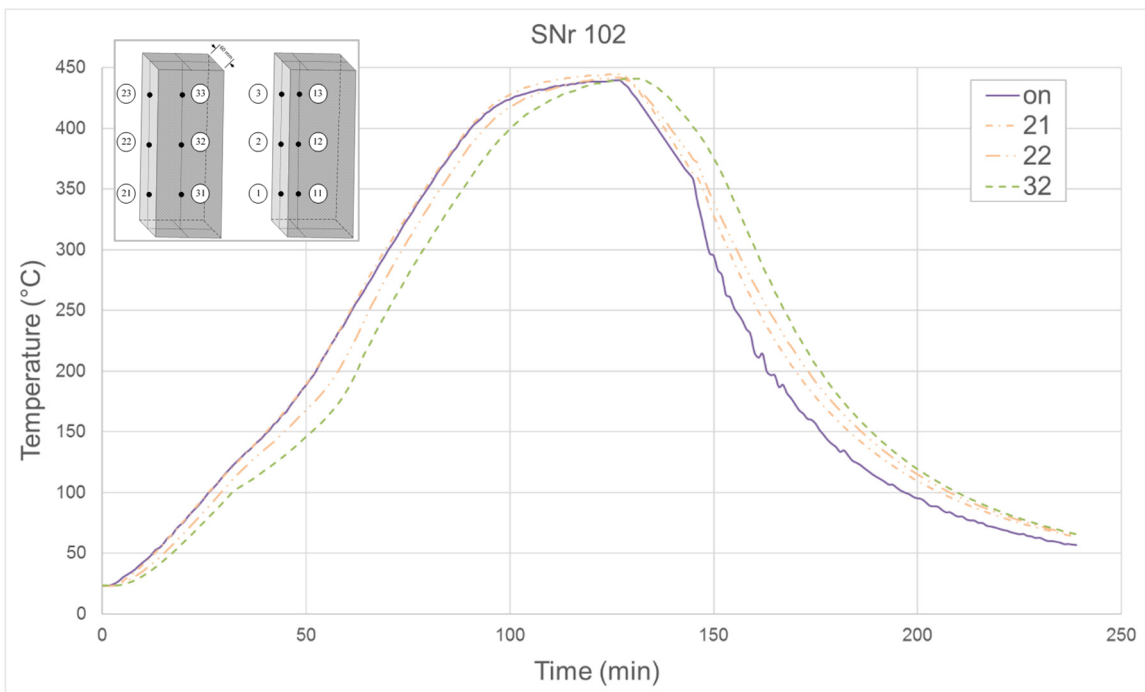


Figure F2: Temperatures in specimen 102 up to max approximate temperature of 440°C

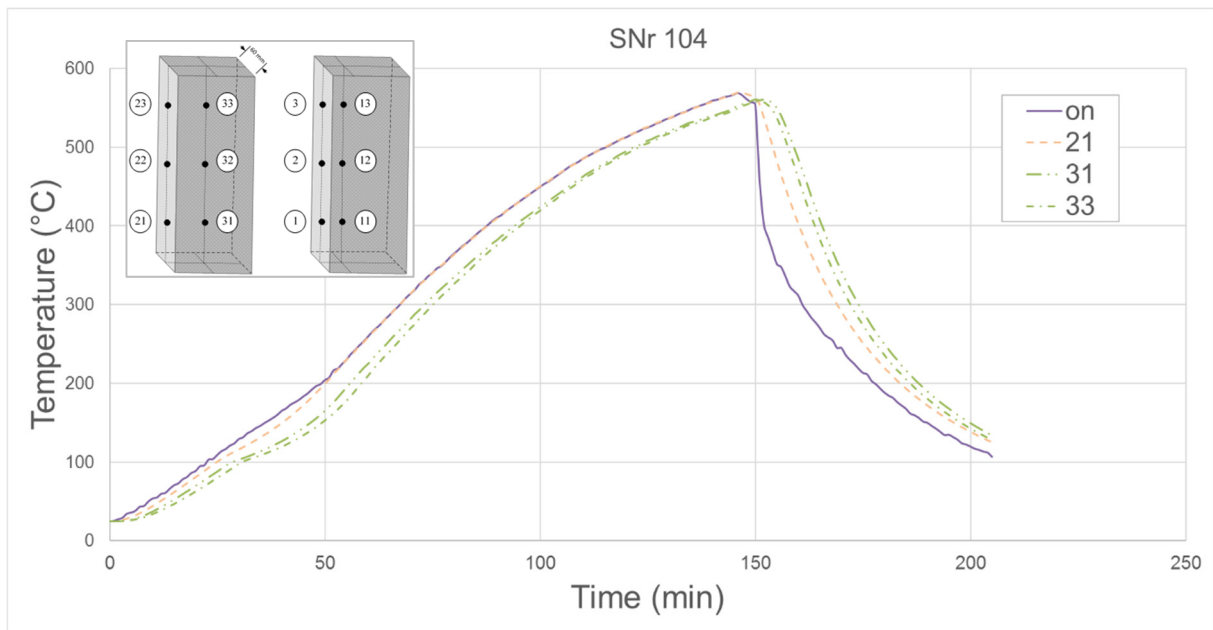


Figure F3: Temperatures in specimen 104 up to max approximate temperature of 560°C

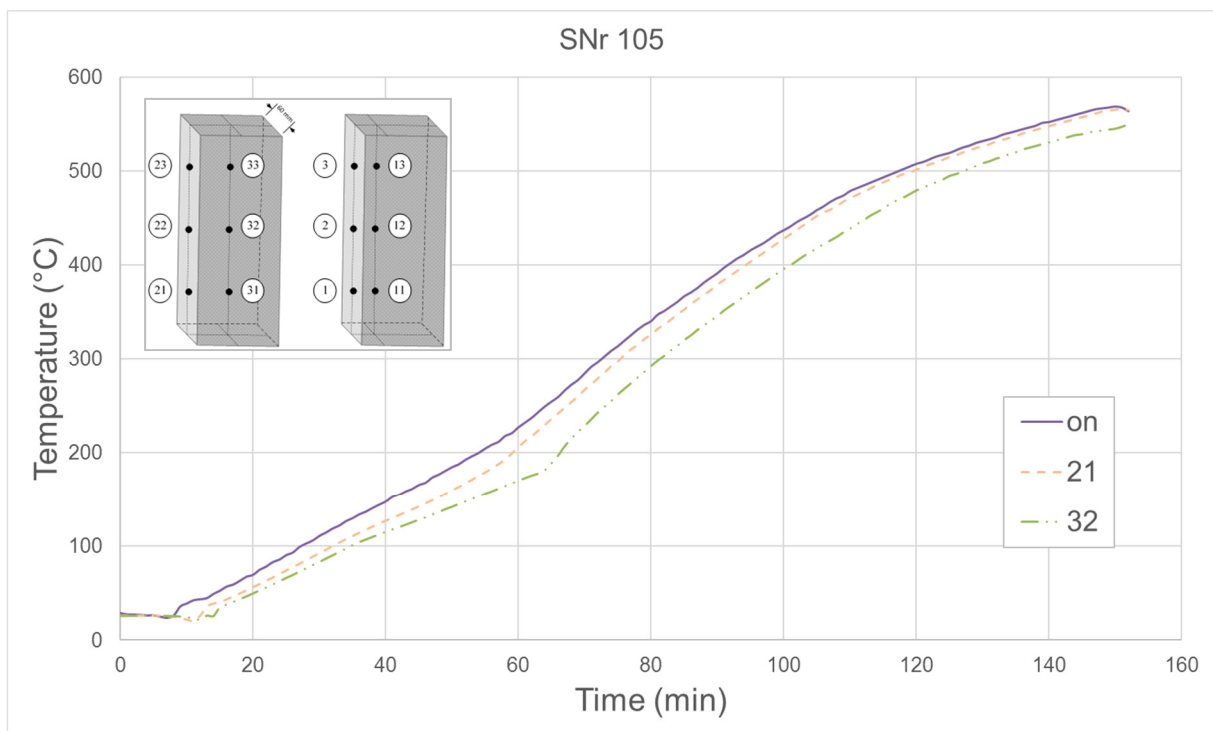


Figure F4: Temperatures in specimen 105 up to max approximate temperature of 570°C

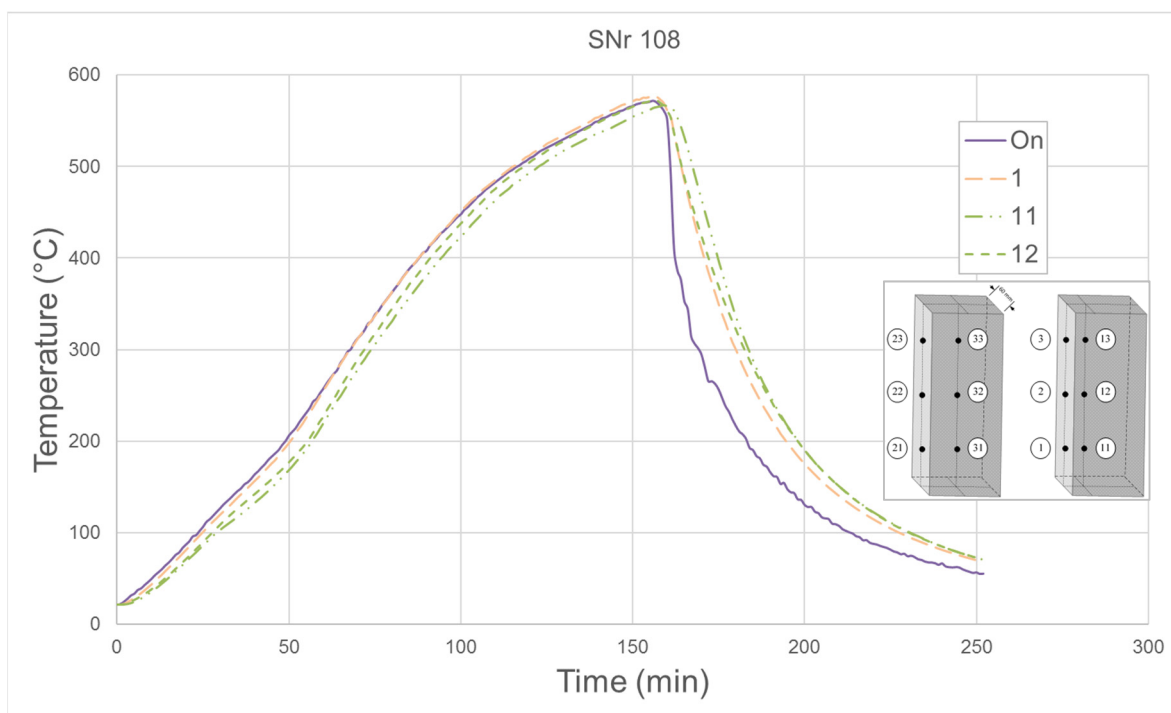


Figure F5: Temperatures in specimen 108 up to max approximate temperature of 570°C

Annex G: Thermal Incompatibilities in Specimens with Polypropylene Fibres under Heating

G.1 Introduction

EN 1992-1-2's material model is based on the results of ISO-fire exposure curve that is used for fire design of building structures. Application of this model is limited according to EN 1992-1-2. On the other hand, in the event of fire in a cut-and-cover tunnel, the fire growth stage might occur in a very high rate. By assuming the section of tunnel under fire as a compartment, the flash-over can take place in a very short period of time. Temperature might reach a higher maximum value due to explosion of one or more vehicles compared to the ISO-fire exposure curve extracted based on the fire load for residential structures. Fire also starts to disappear, relatively, in a quicker manner.

The stress-strain curve proposed by EN 1992-1-2 for concrete exposed to elevated temperatures is designed for the concrete without PP-fibres and is applicable for the heating rates between 2 to 50 K/min. The effects of adding PP-fibres to the concrete mixture on the behaviour of concrete at elevated temperatures have been inconsistent according to different authors. By performing concrete tests at elevated temperatures, one of the most important points is to find the extent of reliability of results. Further, in order to find the uniform temperature distribution in the cylinder concrete specimens under compressive load during heating, (RILEM TC 129-MHT, 1998) limits the use of heating rates dependent on the radius of cylinder to $R \leq 4$ K/min. The high value of heating rates results in thermal incompatibilities or as called by (Khoury, et al., 1985) structural effects that might influence the strain results. Due to temporary tensile stresses at the centre of specimens, the results of transient strain tests might be not accurate especially for the specimens with a load factor $\alpha < 0.2$ ($0.2 f_c$) during the heating up procedure. In this section, the results of the thermal and thermo-mechanical analyses of a cylinder concrete specimen under heating are introduced in accordance with the requirements arising from the thermal analysis of an element of tunnel structure.

G.2 Thermal Analysis and Transient Heat Transfer

From thermo-dynamics point of view, we can assume that for the both cases of a tunnel element and a cylinder specimen, the volume change in the concrete is negligible and changes in internal energy are only function of variable temperatures through the concrete with time. In case of concrete cylinder specimens with diameter less than 60 mm and heated, it should be noted that for low heating rates $R \leq 1$ K/min, the heat flux has small changes at a time through the concrete. When temperature changes with time not with the position in the concrete, a lumped system may also give an acceptable estimation of heat transfer.

G.3 Boundary Conditions

There are commonly four types of boundary conditions that can be assumed: specified temperature, specified heat flux, convection, and radiation boundary conditions. In case of cylinder specimen, as the temperature change rate on the specimen boundaries are controlled, the specified temperature boundary condition is assumed relevant and more conservative. However, for the sake of investigation, the combined convection and radiation boundary condition has been assumed for all thermal analyses of members and specimens.

Transient Heat Transfer of a Concrete Cylinder Specimen

If we now consider a thin shell element within the concrete cylinder specimen with a thickness of Δr having height of L then an energy balance on this thin cylinder element during a short time interval of Δt can be expressed as:

$$\frac{1}{r} \frac{\partial}{\partial r} \left(rk \frac{\partial \theta}{\partial r} \right) + \dot{e}_{gen} = \rho c \frac{\partial \theta}{\partial t} \quad (109)$$

In the absence of a heat source, the latter equation becomes:

$$\text{Variable conductivity } \frac{1}{r} \frac{\partial}{\partial r} \left(rk \frac{\partial \theta}{\partial r} \right) = \rho c \frac{\partial \theta}{\partial t} \quad (110)$$

$$\text{Constant conductivity } \frac{1}{r} \frac{\partial}{\partial r} \left(r \frac{\partial \theta}{\partial r} \right) = \frac{1}{\alpha} \frac{\partial \theta}{\partial t} \quad (111)$$

where r is the radius of cylinder. It should be noted that the area normal to the direction of heat transfer is at any location $A = 2\pi rL$, where L refers to the height of cylinder and A is dependent on r and varies corresponding to the location. The above equations can be extended to three-dimensional form as:

$$\text{Variable conductivity } \rho c \frac{\partial \theta}{\partial t} = \frac{1}{r} \frac{\partial}{\partial r} \left(kr \frac{\partial \theta}{\partial r} \right) + \frac{1}{r^2} \frac{\partial}{\partial \varphi} \left(k \frac{\partial \theta}{\partial \varphi} \right) + \frac{\partial}{\partial z} \left(k \frac{\partial \theta}{\partial z} \right) \quad (112)$$

$$\text{Constant conductivity } \frac{1}{\alpha} \frac{\partial \theta}{\partial t} = \frac{1}{r} \frac{\partial}{\partial r} \left(r \frac{\partial \theta}{\partial r} \right) + \frac{1}{r^2} \frac{\partial}{\partial \varphi} \left(\frac{\partial \theta}{\partial \varphi} \right) + \frac{\partial}{\partial z} \left(\frac{\partial \theta}{\partial z} \right) \quad (113)$$

Fourier parabolic second-order partial differential equation:

$$\frac{1}{\alpha} \frac{\partial \theta}{\partial t} = \frac{1}{r} \frac{\partial}{\partial r} \left(r \frac{\partial \theta}{\partial r} \right) + \frac{1}{r^2} \frac{\partial^2 \theta}{\partial \varphi^2} + \frac{\partial^2 \theta}{\partial z^2} \quad (114)$$

For the case of concrete cylinder under heating in the laboratory, it is possible to adjust the boundary conditions that the changes in temperatures in both z and φ directions are negligible. This can be done by applying approximately a uniform temperature condition on the curved surface of specimen for a given time and by this minimizing the axial temperature difference. Assuming that the latter is ruling the condition in the practice, Eq. 114 can be assumed to be only function of radius of specimen and time. Thus, it becomes:

$$\frac{\partial \theta}{\partial t} = \alpha \left(\frac{\partial^2 \theta}{\partial r^2} + \frac{1}{r} \frac{\partial \theta}{\partial r} \right) \quad (115)$$

Initial boundary condition: the initial temperature is assumed to be 0 and as the solution is found for the equation, the ambient temperature can be added to the equation:

$$\theta(r) = 0 \text{ for } t = 0 \quad (116)$$

Boundary condition: the values of boundary conditions are absolute temperatures on the surface of specimen and are linear function of time:

$$\theta(r = r_{max} = a) = R t \text{ for } \theta > 0 \quad (117)$$

where R is the heating rate.

Eq. 115 can be solved using Laplace transformation and changes the equation to an ordinary differential equation:

$$\theta(r, t) = R \left(t - \frac{a^2 - r^2}{4\alpha} \right) + \frac{2R}{\alpha a} \sum_{n=1}^{\infty} e^{-\alpha A_n^2 t} \frac{J_0(r a_n)}{a_n^3 J_1(a a_n)} \quad (118)$$

where J_0 and J_1 are the so called first-kind Bessel function having orders of 0 and 1, and where $\pm a_n$, $n = 1, 2, \dots$ are the roots of $J_0(a a_n) = 0$. The second part of equation has a negative exponential which means the contribution from this part reduces with the increase of time and is representative of contribution of the initial transients. Therefore, the contribution of the second part of Eq. 118 can be neglected:

$$\theta(r, t) = R \left(t - \frac{a^2 - r^2}{4\alpha} \right) \quad (119)$$

Providing that R and α are constant, the equation indicates that after a period of time after start of heating, the radial temperature difference becomes constant. By assuming the latter which is based on the study of (Khoury, et al., 1985), RILEM (RILEM TC 129-MHT, 1998) considers the maximum allowable radial temperature difference to be:

$$\Delta\theta = \frac{Ra^2}{4\alpha} \quad (120)$$

This leads to the uniform course of temperature profile change after a short period of time and linear temperature increase rate of any two points on the radius of cylinder with time.

G.4 Thermal Analysis of Cylinder Specimen

Thermal analyses for a cylinder specimen with radius of $r = 30$ mm and height of $L = 180$ mm have been carried out by HYDRA (2016) as solver and analysis program in SOFiSTiK (2016) and ANSYS (2016). This has been done by using three different heating rates, $R = 4, 14$ and 24 K/min and the maximum temperature of 900°C . For the thermal analyses with ANSYS model, the assumption of constant thermal diffusivity due to (RILEM TC 129-MHT, 1998) and (Khoury, et al., 1984) are made and for the model with SOFiSTiK, dependent material properties according to EN 1992-1-2 have been taken into account. The results of temperature increase at a point on the cylinder surface ($r = 30$ mm) and in the middle of cylinder ($r = 0$) are shown in Fig. G1. The result of ANSYS, as it was expected, shows a linear temperature increase rate. This is not the case for the SOFiSTiK results as the temperature dependent material properties are assumed. The differences between temperature values at each point according to ANSYS and SOFiSTiK outputs, $\Delta\theta$, are larger for the heating rates greater than 4 K/min (see Fig. G2). For $\Delta\theta$ values, there is an ignorable deviation for $R \leq 4$ K/min between the temperature values according to output of each software. Further, the decrease in the slope of line representing temperature values according to SOFiSTiK at 100°C shows the sudden increase in the value of heat capacity of concrete and therefore decrease in thermal diffusivity. The results of thermal analysis performed by SOFiSTiK have been considered as the more realistic and accurate model for the stress analysis.

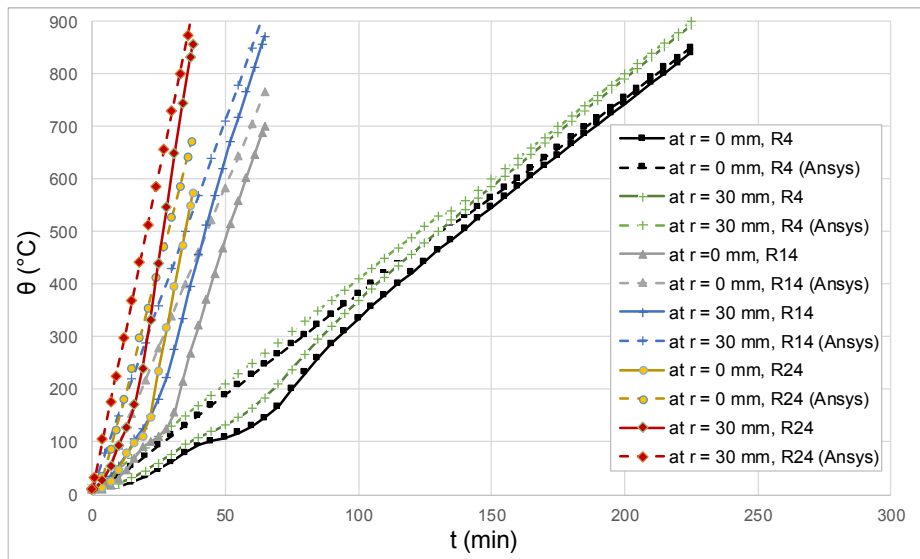


Figure G1: Temperature values at the points located on the surface and center of cylinder

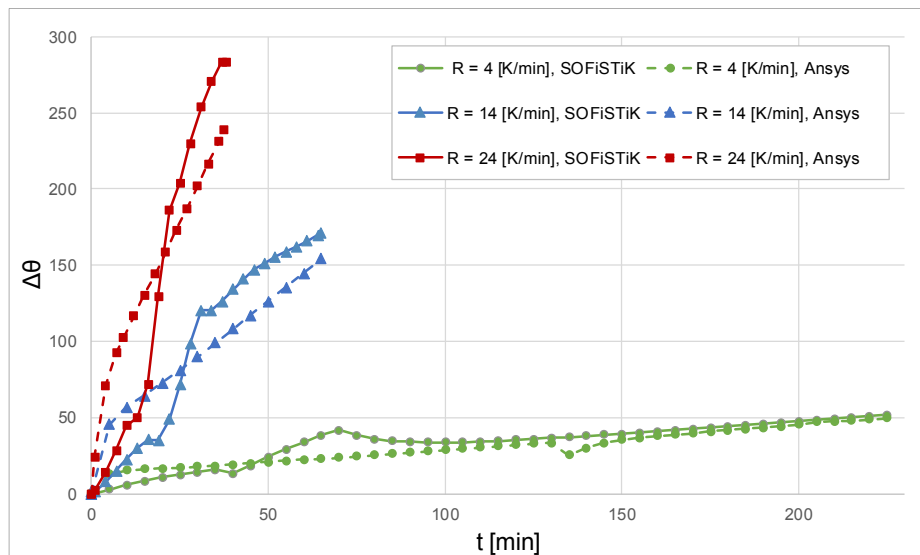


Figure G2: Temperature differences between the points on the surface and center of cylinder

G.5 Stress Analysis of Cylinder

In order to be able to investigate and analyse the influence of the evaluated temperature results on the thermo-mechanical behaviour of the concrete cylinder specimen, there is no advanced method available which can simulate and couple the effects due to microscopic phenomenon of complex components of concrete such as pore pressure, drying shrinkage, chemical reactions and relaxation with the elevated temperatures at different points within concrete. Using macroscopic EN 1992-1-2's implicit material model to investigate the thermal effects and stress analysis on a cylinder specimen without considering the microscopic and local phenomenon is not therefore rational.

Considering the former argument, there is no straightforward method to analyse thermal effects or stresses on the material behaviour. The following procedure is used to investigate and grasp a better understanding

of the effects of temperature gradients within such a concrete cylinder specimen. The procedure is based on the combination of the following available methodologies and observations:

- Analysis of restraint forces using coupled-thermo-mechanical analysis of a concrete cylinder exposed to different heating rates via volume elements by excluding the variation of concrete strength and stiffness due to elevated temperatures. This might give a good estimation of temperatures up to 100°C and a view of influence of the thermal stresses and temperature gradient for temperatures up to 200°C. It is to be noted in concrete with sufficient amount of PP-fibres, the moisture transport is accelerated in temperature range between 200 and 250°C. In this case, the pore pressure is dominant for the mentioned temperature range in vicinity of concrete surface;
- Analysis of variation in stress distribution using fibre-enhanced quadrilateral elements based on multi-layered strain model according to (Harte, et al., 2000) representing a cuboid of 60 x 60 x 180 mm (material model is according to EN 1992-1-2). This might help to give an overview of the influence of thermal stresses and temperature gradient for concrete with sufficient amount of PP-fibres. It is to be noted the course of variation in stresses can be related to temperature ranges up to 200°C and the phase where the specimen is almost dried out, which is dependent on the moisture content and heating rate.

G.6 Restraint Forces Using Volume Model

It is assumed even for the concrete cylinder specimens with a low level of load such as 0.1 MPa to 0.2 f_c , there exists high level of constraints on the boundary surfaces to loading machine. Constraints at the interface with loading machine are shown in Fig. G3. C35/45 class of concrete is used for the analysis. The result of the 3D model generated via SOFiSTiK by using ISO8 three-dimensional solid elements, to overcome the problem of singularities and make the best approximation for restrained forces at constraints, are presented. This is due to the fact that the coupled-thermo-mechanical analysis in SOFiSTiK can be performed by using direct import of temperature fields in the structural volume model whereas in ANSYS it is the user's task to mesh the model for transient thermal and structural analyses separately which might result in incompatibilities in evaluating stresses. Further, the model meshing properties are listed in Tab. G1. In this analysis, the nonlinear material properties are assumed whereas the thermal effects on the stiffness and strength of concrete and excessive thermally induced strains are excluded. For mechanical analysis thermal loads are defined and implemented in structural model and analysed for each 5-minute-time intervals.

The result of nodal forces at constraints in the centre of cylinder ($r = 0$) and on the concrete surface ($r = 30$ mm) along the axis of cylinder (designated by global Z direction) for three heating rates are shown in Fig. G4. It is to be noted that the maximum nodal forces achieved on the surface of concrete is almost identical as the temperature values are almost the same on these nodes at the maximum temperatures value (θ_m). The latter is due to the fact that the thermally induced changes in the stiffness and strength are not considered in the model.

Restraint forces for all three groups on the nodes with $r = 0$ mm after the period of 5 minutes are tensile. Further the values of compressive stresses are illustrated in Fig. G5 for different heating rates after 5 minutes for all heating rates and at $t = 50, 15$ and 10 minutes for $R = 4, 14$ and 24 K/min respectively. The latter is specified to analyse the stresses up to maximum temperature, θ_m , of 240°C . It should be noted that for temperatures above 100°C , the maximum compressive stresses at the first layer of elements closed to the exposed surfaces are overestimated as the changes in stiffness matrix of concrete elements are not properly considered.

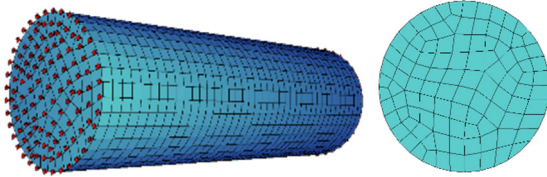


Figure G3: Constraints and mesh of cylinder specimen

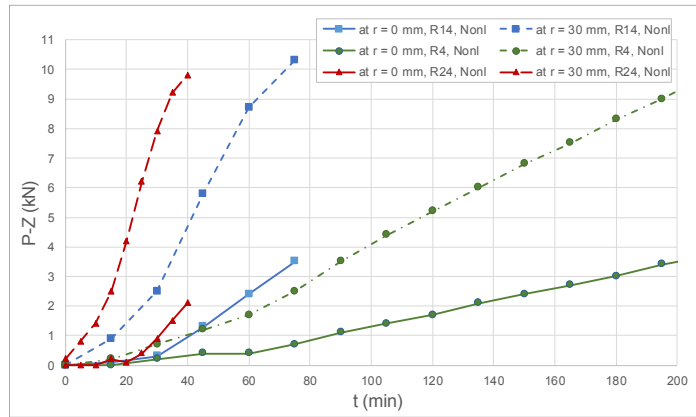


Figure G4: Nodal restraint forces at constraints along the axis of cylinder for heating rates 4, 14 and 24 K/min

Annex G: Thermal Incompatibilities in Specimens with Polypropylene Fibres under Heating

Table G1: Mesh properties of the cylinder specimen

Types of elements	ISO8 three dimensional solid	ISO4 quadrilateral (boundaries)
Number of elements	4080	1644
Progression factor		1.1
Minimum size of mesh [mm]		1

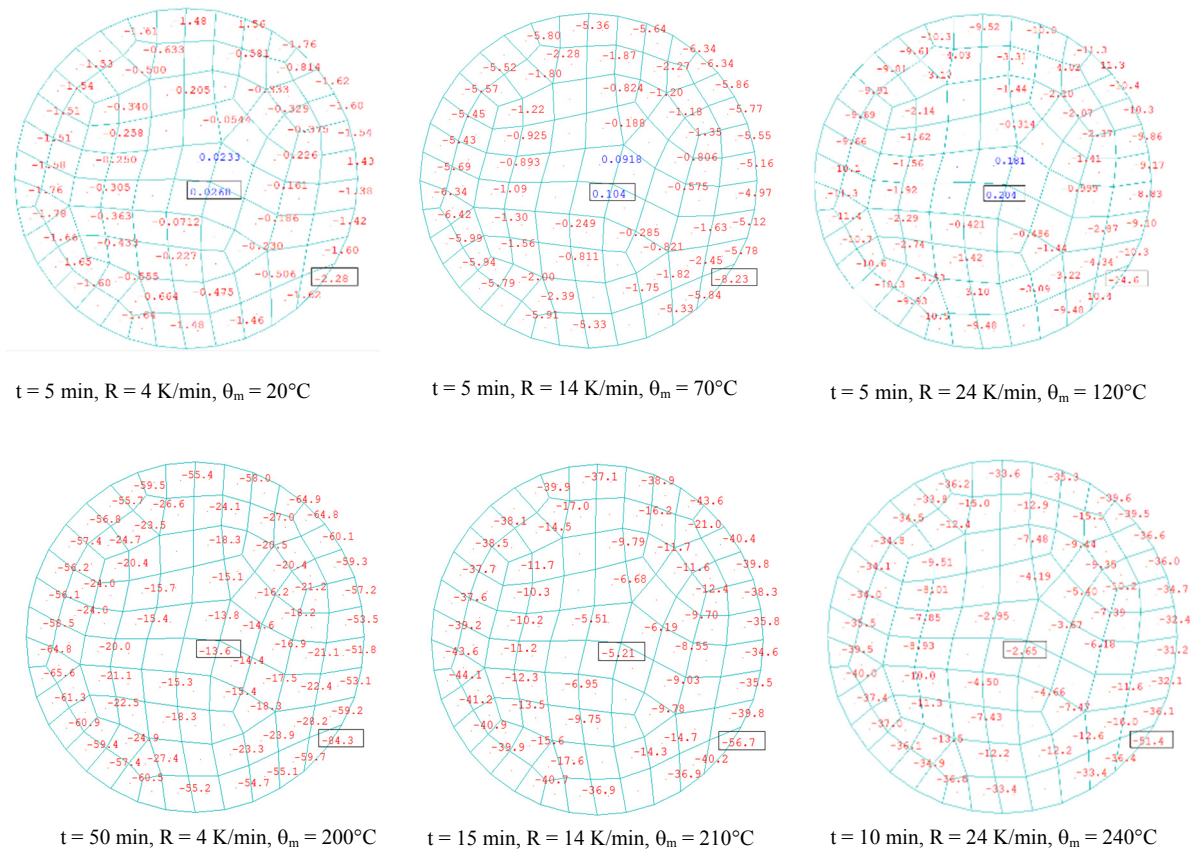


Figure G5: Compressive stresses from the element average values along the axis of cylinder

Further, the differences in the compressive stresses between a point on the surface of concrete and in the centre at $t = 5 \text{ min}$ for heating rates $R = 4, 14$ and 24 are 2.3, 8.33 and 14.8 MPa respectively. This might result in thermal incompatibilities for specimens especially when they are under low load levels. Using the levels (corresponding to pre-load level) of 0.1 MPa to $0.2f_c$ which is for the selected concrete class 7 MPa, thermal incompatibilities due to difference in thermal stresses along the cylinder axis should be expected up to θ_m of 200°C .

G.7 Variation in Stress Distribution using Fibre-enhanced-quadrilateral-plate Elements

A cuboid of $60 \times 60 \times 180 \text{ mm}$ as shown in Fig. G6 has been assumed by generating series of quad elements making a plane of $60 \times 180 \text{ mm}$ (as an approximate alternative for the cylinder specimen) with parallel layers of planes located symmetrically up to 30 mm normal to each side of quads' plane. The parallel layers implement the variation in the material properties induced by elevated temperatures as well as strains due to EN 1992-1-2's model.

The disadvantage of the model is that in case of restraint cylinder element, where there is no strain in the reality, the excessive flexural nonlinear strains cannot be controlled. However, the variation in stress distribution might give an overview of thermal stress behaviour of concrete cylinder specimen (having PP-fibres) for temperatures up to 200°C and after the specimen is dried out.

Fig. G7 indicates the variation of thermal stress along with temperature distribution for $R = 4$ K/min after 15, 45, and 90 minutes. The distribution of thermally induced stresses at 15 minutes follow the same parabolic pattern as the temperature distribution over the thickness. It is due to the fact that, in this

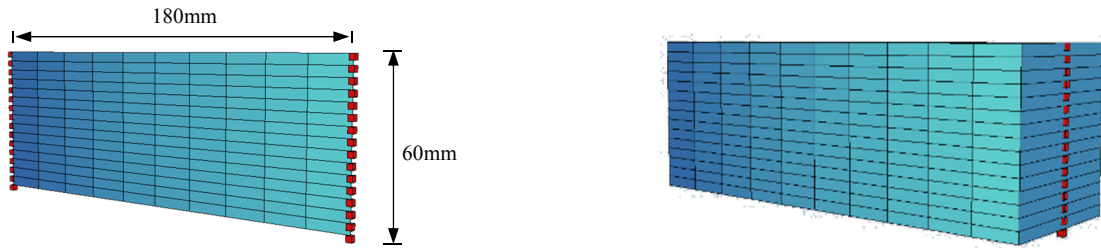


Figure G6: Plane of quadrilateral elements (left) and fibre-enhanced plate elements (right)

temperature range, the fibres close to the exposed side still have their full strength and ratio of compressive stresses in this regions to the compressive stresses in the centre are therefore higher. As temperature increases, thermal diffusivities of layers with higher temperatures decrease in a higher rate than those with lower temperatures towards centre. The ratio of compressive stress of the layers near the exposed side to the compressive stresses in the centre of cuboid reduces with the increase of time and temperature. This is due to the loss of strength in these layers. For the temperature ranges up to 200°C the stress distribution can be assumed to have the similar shape as temperature distribution. It is to be noted the compressive stress values occurred in farthest fibres from centre at θ_m of approximately 248°C (see Fig. G7) are significantly smaller compared to the corresponding stresses at $\theta_m = 200^\circ\text{C}$.

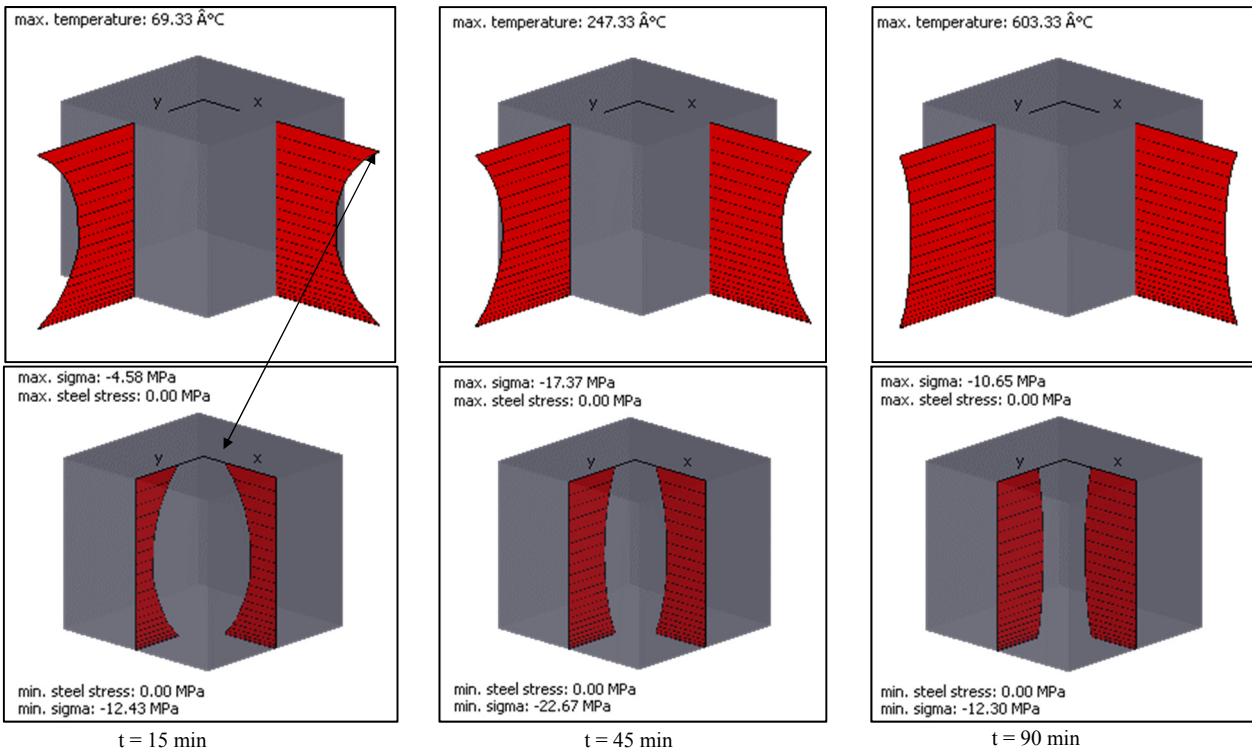


Figure G7: Compressive stress distribution using nonlinear analysis via fibre-enhanced plate model

Annex H: Cross-section and System Variable States for the Reinforced Concrete Beams under Fire (Study Cases)

Table H1: Nonlinear results of beam with a fixed and a vertically and rotationally restraint support exposed to fire (case 1)

Time (min)	5	10	30
Temperature profile			
Bending moment (kNm)			
Beam displacement in local x (mm)			
Flexural stress (MPa)			
Mechanical strain (‰)			
Thermal strain (‰)			

Annex H: Cross-section and System Variable States for the Reinforced Concrete Beams under Fire (Study Cases)

Table H2: Nonlinear results of beam with a fixed and a vertically and rotationally restraint support under transverse loading and fire action (case 2)

Time (min)	0	5	10
Temperature profile			
Bending moment (kNm)			
Beam displacement in local x (mm)			
Beam displacement in local z (mm)			
Total curvature k_y			
Flexural stress (MPa)			
Mechanical strain (‰)			
Thermal strain (‰)			

Annex H: Cross-section and System Variable States for the Reinforced Concrete Beams under Fire (Study Cases)

Table H3: Nonlinear results of an axially restraint beam exposed to fire (case 3)

Time (min)	5	10	30
Temperature profile			
Axial force (kN)			
Beam displacement in local z (mm)			
Total curvature k_y			
Flexural stress (MPa)			
Mechanical strain (%)			
Thermal strain (%)			

Annex H: Cross-section and System Variable States for the Reinforced Concrete Beams under Fire (Study Cases)

Table H4: Nonlinear results of axially restraint beam under transverse loading and fire action (case 4)

Time (min)	0	5	10
Temperature profile			
Bending moment (kNm)			
Axial force (kN)			
Beam displacement in local z (mm)			
Total curvature k_y			
Flexural stress (MPa)			
Mechanical strain (‰)			
Thermal strain (‰)			

Annex I: Actions on the Tunnel

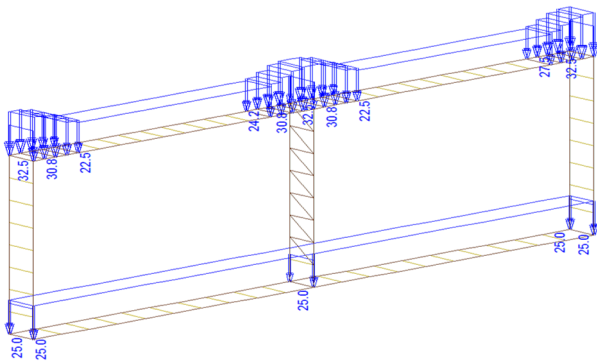


Figure 11: Load case 1 (LC 1) self weight

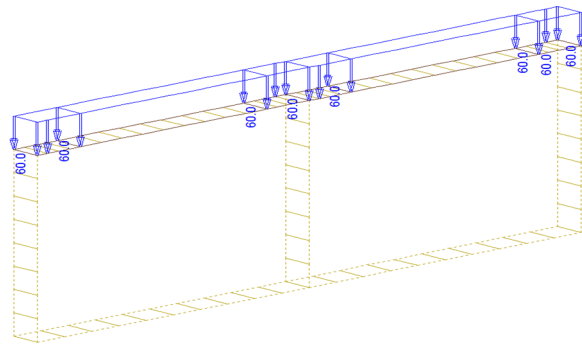


Figure 12: Load case 2 (LC 2) weight of filling

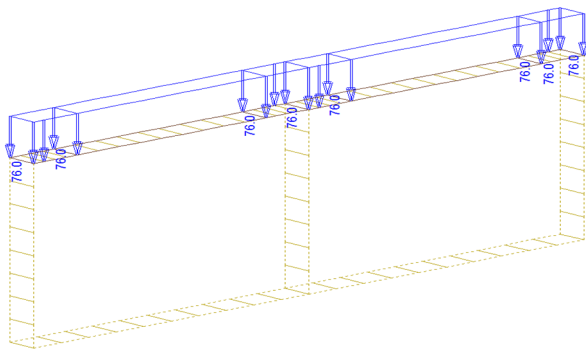


Figure 13: Load case 3 (LC 3) earth surcharge load

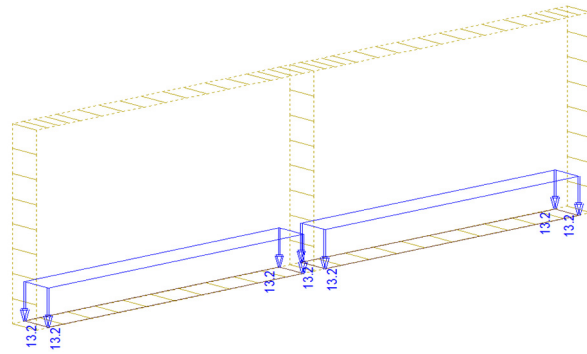


Figure 14: Load case 4 (LC 4) weight of road pavement

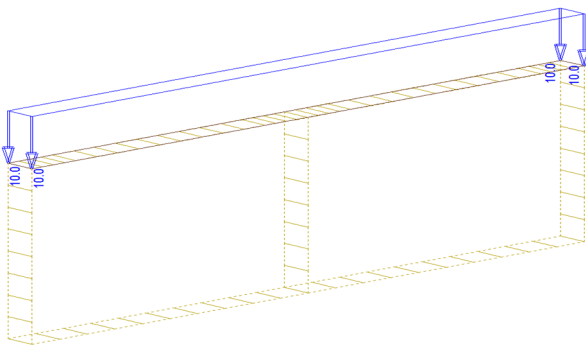


Figure 15: Load case 5 (LC 5) vehicular live load at top ground surface

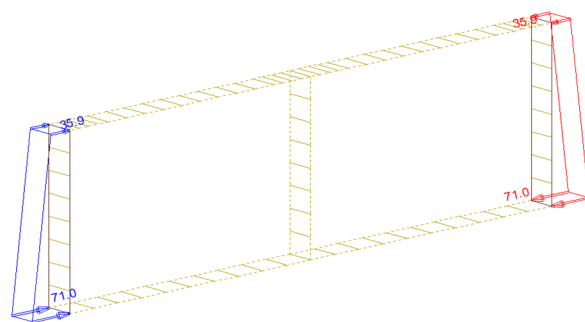


Figure 16: Load case 6 (LC 6) soil pressure

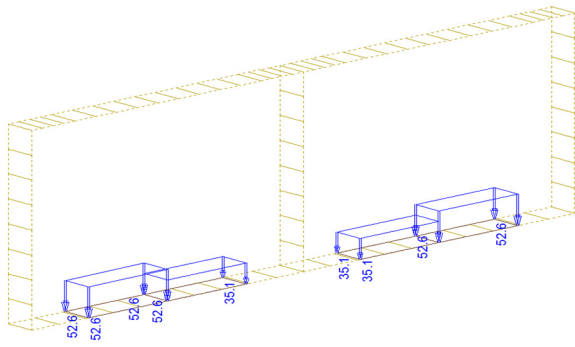


Figure I7: Load case 7 (LC 7) vehicular live load in the tunnel

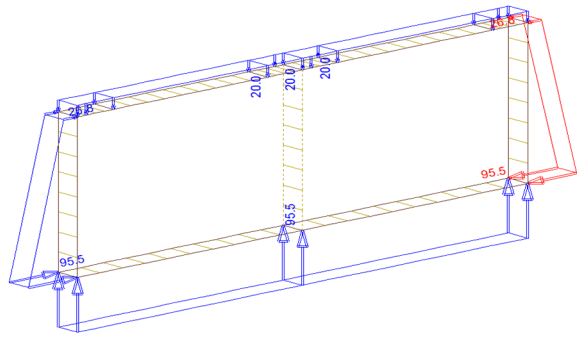


Figure I8: Load case 8 (LC 8) ground water

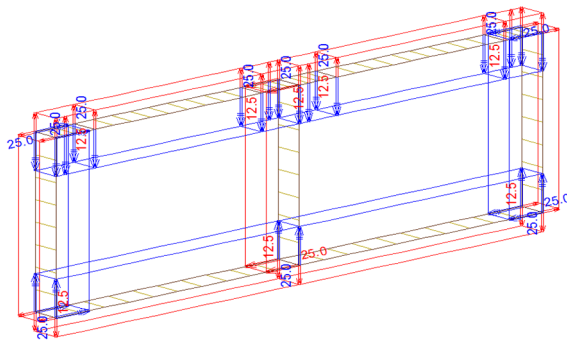


Figure I9: Load case 9 (LC 9) temperature change in winter

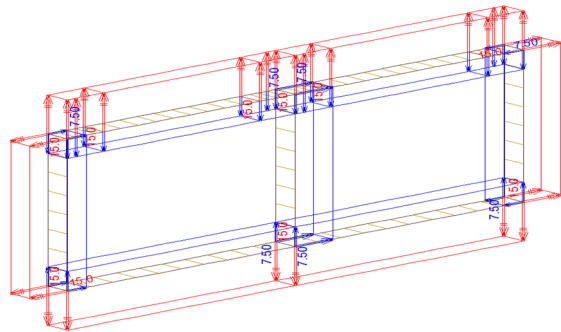


Figure I10: Load case 10 (LC 10) temperature change in summer

Annex J: Bending Moments and Axial Forces of the Tunnel from Nonlinear Thermo-mechanical Analysis of the Plate Model

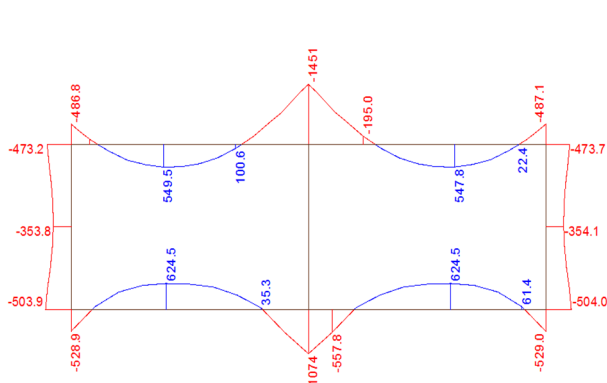


Figure J1: Bending moments at $t = 0$

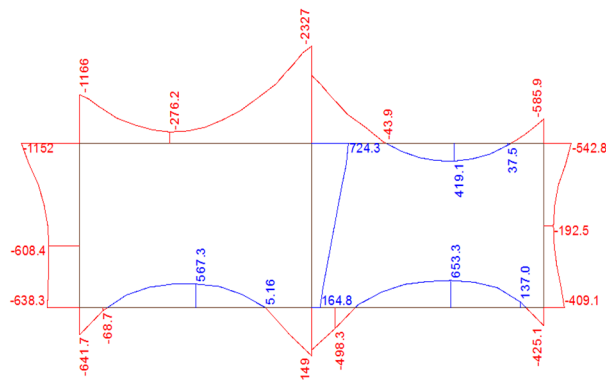


Figure J2: Bending moments at $t = 10$ min

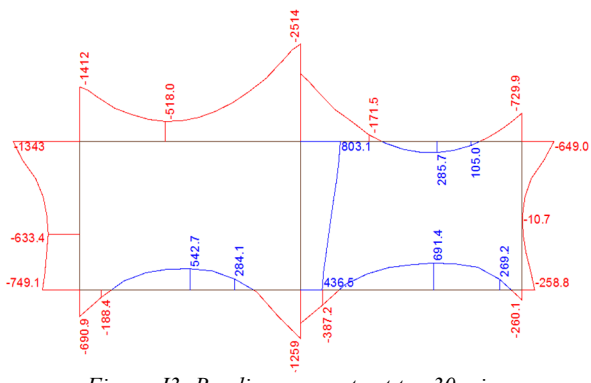


Figure J3: Bending moments at $t = 30$ min

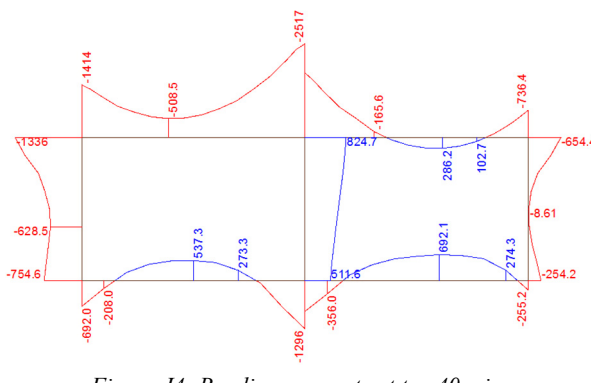


Figure J4: Bending moments at $t = 40$ min

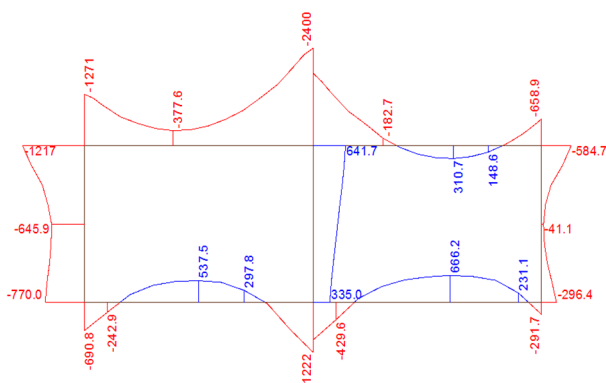


Figure J5: Bending moments at $t = 90$ min

Annex J: Bending Moments and Axial Forces of the Tunnel from Nonlinear Thermo-mechanical Analysis of the Plate Model

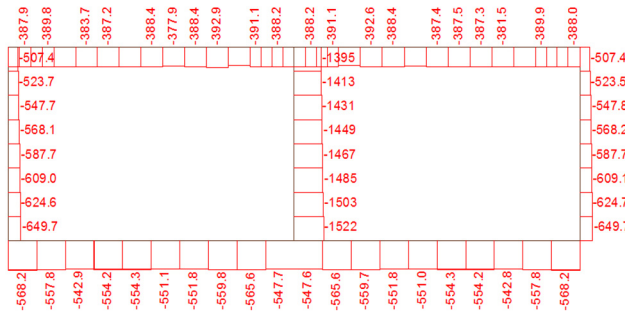


Figure J6: Axial forces at $t = 0$

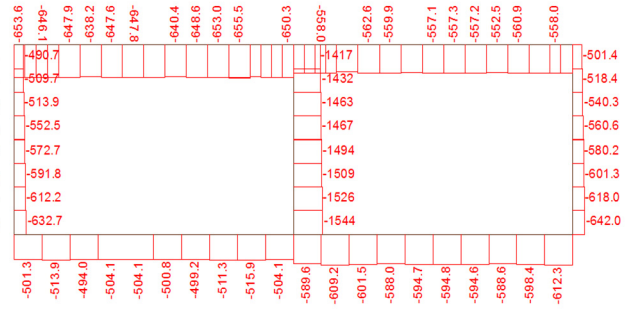


Figure J7: Axial forces at $t = 10$ min

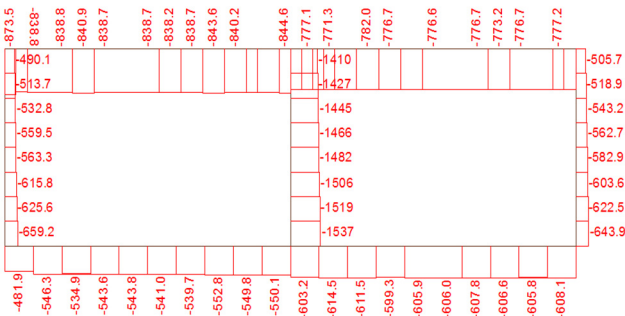


Figure J8: Axial forces at $t = 30$ min

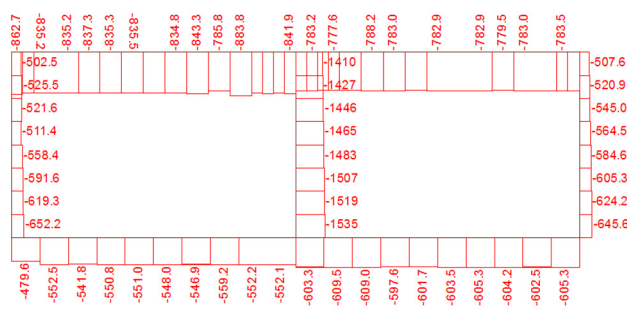


Figure J9: Axial forces at $t = 40$ min

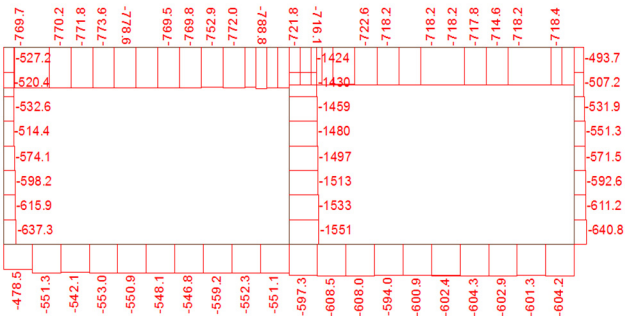


Figure J10: Axial forces at $t = 90$ min

Lebenslauf

Persönliche Daten

Nachname	Pouran
Vorname	Omid
Geburtstag	07.01.1983
Nationalität	Iranisch
E-Mail	Pouran@uni-wuppertal.de

Schulbildung

1997 – 2000	Adib Non-Profitable High-School, Teheran, Iran
2000 – 2001	Peyvand High-School and Pre-University, Teheran, Iran

Ausbildung

2002 – 2006	Universitätsgrad im Hoch- und Tiefbau an der Islamischen Azad Universität
2006 – 2009	Universitätsabschluss der Naturwissenschaften (Bachelor of Science) im Bauingenieurwesen an der Islamischen Azad Universität
2009 – 2010	Master of Science im konstruktiven Ingenieurbau an der Manchester Universität, Manchester, UK
Seit 04/2012 – 2018	Doktorand am Lehrstuhl für Statik und Dynamik der Tragwerke der Bergischen Universität Wuppertal

Berufserfahrung

08/2012 – 03/ 2013	Wissenschaftliche Hilfskraft an der Fakultät 5 – Abt. Bauingenieurwesen, Statik und Dynamik der Tragwerke
2013-2014	Mitarbeiter in Krätzig & Partner Ingenieurgesellschaft für Bautechnik mbH
2013-2018	Wissenschaftlicher Mitarbeiter an der Fakultät 5 – Abt. Bauingenieurwesen, Statik und Dynamik der Tragwerke

Curriculum Vitae

Personal Data

Surname	Pouran
First Name	Omid
Date of Birthday	07.01.1983
Nationality	Iranian
E-Mail	Pouran@uni-wuppertal.de

Education

1997 – 2000	Adib Non-Profitable High-School, Tehran, Iran
2000 – 2001	Peyvand High-School and Pre-University, Tehran, Iran
2002 – 2006	Associate of Science Program in Civil Construction, Islamic Azad University
2006 – 2009	Bachelor of Science (BSc) in Civil Engineering, Islamic Azad University
2009 – 2010	Master of Science (MSc) in Structural Engineering, The University of Manchester of Manchester, Manchester, UK
Since 04/2012 – 2018	PhD Candidate at Bergischen Universität Wuppertal

Work Experience

08/2012 – 03/ 2013	Scientific Assistant at Faculty 5 – Department of Civil Engineering, Institute for Statics and Dynamics of Structures
2013-2014	Proof Engineer and Supervisor at Krätzig & Partner, Ingenieurgesellschaft für Bautechnik mbH
2013-2018	Teaching and Research Assistant at Faculty 5 – Department of Civil Engineering, Institute for Statics and Dynamics of Structures

List of Author's Publications

Pouran O and Harte R Influence of heating rate and thermal incompatibilities on the test results of concrete cylinder specimens with polypropylene fibres under heating. In: Proceedings of the international conference of applications of structural fire engineering (ASFE 2017), Manchester/United Kingdom, 7-8 Sept. 2017, 63-72

Pouran O, Harte R and Peter C Parameters affecting the structural analysis of a tunnel structure exposed to fire. In: Acta Polytechnica CTU Proceedings 7 (2016): 48-52.

Pouran O and Harte R A Simplified Method to Design Cooling Tower Shells for Fire Situation. In: Industrial Chimneys & Cooling Towers. Proc. of International Conference ICCT2016, Rotterdam/Netherlands, Bergische Universität Wuppertal, 2016, 353- 362

Pouran O, Harte R and Peter C Parameters Affecting the Structural Analysis of a Tunnel Structure Exposed to Fire. Acta Polytechnica CTU Proceedings 1 (2016).

Harte R and Pouran O Comparison of Design and Analysis of Cooling Towers and Concrete Chimneys. Journal of the International Association for Shell and Spatial Structures IASS, March 2016, Vol.57, No. 1, 25-33

Harte R, Kaemmer K and Pouran O Zur Berechnung und Bemessung von Kühltürmen und Industrieschornsteinen. In: Höffer, R., Hölscher, N. (Hrsg.) Festschrift Prof. Dr.-Ing. J. Niemann. Ruhr-Universität Bochum, 2015, 67-75

Pouran O and Harte R Thermal Effects in Design of Reinforced Concrete Structures. In: Proc. of Annual Conference on Research in Civil Engineering, Architecture and Stable Environment ACRCEAS 2015, Tehran/Iran, December 15, 2015, 117-118

Pouran O, Harte R and Peter C Nonlinear Structural Analysis of Cut-And-Cover Tunnels Exposed to Fire. In: Proc. of Applications of Structural Fire Engineering ASFE'15, Dubrovnik, 2015, 43-48

Harte R and Pouran O Comparison of Design Strategies for Concrete Chimneys and Cooling Towers: CICIND Report Vol. 31, No. 2, 2015, 103-107

Harte R and Pouran O Interaction and Intersection in Research and Development of Cooling Towers and Concrete Chimneys. In: Industrial Chimneys & Cooling Towers. Proc. of International Conference ICCT2014, Prague/Czech Republic, Bergische Universität Wuppertal, 2014, 199-208